

DISS. ETH NO. 30242

**SOLUTE MIXING AND CHAOTIC TRANSPORT IN
UNSATURATED POROUS MEDIA**

A thesis submitted to attain the degree of

DOCTOR OF SCIENCES
(Dr. sc. ETH Zurich)

presented by

ANDRÉS FELIPE VELÁSQUEZ PARRA

Master of Science in Civil Engineering,
ETH Zurich

born on 29.04.1992

accepted on the recommendation of

Prof. Dr. Roman Stocker, examiner
Prof. Dr. Joaquín Jiménez-Martínez, co-examiner
Prof. Dr. Marco Dentz, co-examiner
Dr. Michele Griffa, co-examiner
Prof. Dr. Rubén Juanes, co-examiner

2024

ACKNOWLEDGMENTS

The development and completion of a Doctoral Thesis is always the result of a network of support and collaboration, which I was fortunate to have around me throughout these five and a half years. First of all, I would like to thank Prof. Dr. Joaquín Jiménez-Martínez for his invaluable guidance and support over all these years. It has been a privilege to grow professionally in his group and to learn from his unlimited love for science. I would also like to thank Prof. Dr. Roman Stocker for his guidance as Doctoral Supervisor and for his encouragement to always pursue bigger goals. A special thanks to Dr. Michele Griffa for his unconditional support and mentoring since the first day and for his essential role in the successful completion of this thesis. I also want to thank the additional members of my Doctoral Committee, Prof. Dr. Marco Dentz and Prof. Dr. Rubén Juanes, for the very fruitful discussions over the past years and for serving as co-examiners of this doctoral thesis. I would also like to thank Dr. Tomás Aquino, Prof. Tanguy Le Borgne, Prof. Yves Méheust, Dr. Matthias Willmann, and Dr. Federica Marone for the external scientific collaborators during this period. A special mention to Matthias for his constant mentoring during my teaching activities, which I cherish very much. Also to Federica for her support and scientific inputs.

Big thanks also to all past and current members of the SEP group. To Ishaan, Dorothee, Xueyi, Sandra, Max, Zahra, and Lucas for all the shared experiences and for creating such a beautiful work environment. Also to past and present members of the Stocker Lab, with special mention to Juanita, Estelle, and Jen for bringing so much joy to the day-by-day life over the past years.

Nothing would have been possible without the constant efforts and encouragement of my family, specially of my mother, father, sister, aunt, and grandma, who have managed to feel very close in spite of the distance. To Tata, Andrés, Maira, Felipe, Brandón, Juan, Marce, Andrés, Karen, Pepe, Ursi, Sebi, Joanna, Ante, and Martin, thank you very much for always being there. To Alejandro for nourishing my growing passion for music during four years already. And last but not least, to Joel for brightening up my days and joining me along the way.

Andrés Velásquez-Parra
March 2024

ABSTRACT

Porous media are ubiquitous in the environment. It is a structural component of living organisms, being present in plants, tissues, and biofilms, and also of abiotic systems, such as soils. The latter stands out for its high environmental relevance, as it mediates the effects on the subsurface of processes occurring in the atmosphere. The unsaturated region of soils, extending from the surface until the deeper aquifers, is key in this exchange, as it controls the fate of solutes, pollutants, and nutrients entering the subsoil. This region is characterized by the combined presence of more than one fluid phase in the pore space, which translates into high spatial heterogeneity and large inherent topological complexity. As a result, some of the most relevant physical processes taking place in this region are not fully understood yet. Fluid flow and solute transport are examples of such processes, whose study has been constrained by the difficulty in both accessing these systems in a non-invasive manner and in observing and quantifying them at the required spatial and temporal resolutions.

This doctoral thesis aims to provide a mechanistic understanding of the control of saturation (fraction of the pore volume occupied by the liquid phase) on the processes of fluid flow and solute transport in porous media. This was achieved through an extensive numerical and theoretical investigation at the pore scale, deeply rooted in previous experimental work. In particular, the use of synchrotron X-ray micro-tomography allowed overcoming the technical challenges mentioned above by allowing real-time observation of the movement, spreading, and mixing of an injected solute in a porous medium at different degrees of saturation and under different flow rates.

Results on the impact of saturation on flow revealed an enhancement in the flow redistribution upon a decrease in saturation. This manifested itself in the stronger formation of backbones of preferential flow and in larger dead-end regions of very low velocity. The latter contributed largely to a marked change of scaling in the velocity distribution and to a sharp transition to enhanced anomalous transport, visible already after a slight desaturation in the system. A theoretical framework is presented, which successfully captured these variations from structural properties in unsaturated porous media. Results from the synchrotron X-ray experiments showed that this enhanced solute dispersion at lower saturation imparts larger amounts of deformation to the solute plume, which renders the mixing of transported solute with the resident solution more

efficient. Similar outcomes were obtained upon an increase in the injection flow rate under a constant saturation degree. A fully resolved 3D numerical investigation of flow allowed explaining the physical mechanisms behind this interplay. Lower saturation alters the connectivity of the system, enhancing the streamlines convergence in the pore space and leading to backbone formation. This results in a strengthened helical flow inside the liquid phase, with large values of helicity density linked to strong streamlines deformation in the form of intensive folding and braiding. This suggests the simultaneous presence of shear- and vorticity-dominated deformation regions in the pore space, whose combination is ultimately responsible for the enhanced solute plume deformation quantified from the experimental data. Based on additional transport simulations performed on the same 3D geometries, we conclude on the occurrence of chaotic advection and chaotic mixing in the system, as initially suggested by the strong braiding and folding of streamlines visible in the vicinity of air clusters and solid boundaries. As indicated by the Lyapunov exponents, computed from the solute plume deformation reconstructed for all tested conditions, the strength of chaos in the liquid phase is enhanced upon both a decrease in saturation and an increase in flow rate.

The study presented in this thesis is a major leap forward in our understanding of the physical mechanisms behind the larger flow field heterogeneity and enhanced transport dynamics characteristic of unsaturated porous media. The results here presented are relevant for a wide range of environmental and industrial applications, being especially useful in investigations on mixing and reactive transport under multiphase conditions. The outcome of this thesis will likely motivate further research in the field and will contribute to the study of complex systems and additional processes of high environmental and industrial relevance.

ZUSAMMENFASSUNG

Poröse Medien sind allgegenwärtig in der Umwelt. Sie sind Hauptbestandteil sowohl von Lebenswesen, wobei sie in Pflanzen, Geweben, und Biofilme zu finden sind, wie auch von abiotischen Systemen, z.B. Böden. Die Letzteren zeichnen sich durch ihre Relevanz bei vielen Umweltprozessen aus, da sie sämtliche Auswirkungen aller auf der Atmosphäre vorkommenden Prozesse auf den Untergrund vermitteln. Die ungesättigte Bodenzone, die sich von der Oberfläche bis zu den tiefen Grundwasserleitern erstreckt, spielt dabei eine Hauptrolle. Sie kontrolliert das Geschick aller in den Untergrund reinfließenden Substanzen, wie z.B. Schadstoffen und Nährstoffen. Diese Zone zeichnet sich durch das gemeinsame Anwesen von mehreren Phasen im Porenraum, bzw., Flüssigkeiten und Gasen, was zu hoher Heterogenität und zu grosser topologischer Komplexität führt. Als Folge dessen sind heutzutage einige der wichtigsten physikalischen Prozesse in dieser Zone noch nicht wohlverstanden. Dazu gehören die Flüssigkeitsströmung und der Transport gelöster Stoffe, deren Erforschung bisher hauptsächlich durch experimentelle Herausforderungen verhindert worden ist. Insbesondere haben sich das nicht-invasive Testen von porösen Medien sowie die experimentelle Beobachtung solcher Prozesse mit der erforderlichen Zeit- und Raumauflösung als technisch sehr komplex erwiesen.

Diese Doktorarbeit hat als Hauptziel, ein mechanistisches Verständnis der Kontrolle der Sättigungszahl (der von Flüssigkeiten, bzw. Wasser, besetzten Anteil des Porenvolumens) auf die Flüssigkeitsströmung und auf den Transport gelöster Stoffe zu gewinnen. Dies wurde durch eine intensiv numerische und theoretische Erforschung im Porenmasstab erreicht, die auf früherer experimenteller Arbeit beruht. Insbesondere hat die Anwendung von Synchrotron-Röntgenmikrotomographie dabei geholfen, die oben erwähnten technischen Herausforderungen zu überwinden. Diese Technik hat die direkte Erfassung der Bewegung, der Verbreitung, und der Vermischung eines injizierten Stoffes innerhalb des Porenraums bei verschiedenen Sättigungszahlen und bei verschiedenen Durchflussgeschwindigkeiten ermöglicht.

Unsere Ergebnisse haben eine Verstärkung der Strömungsverteilung nach einer Senkung der Sättigungszahl gezeigt. Dies hat sich in der Entwicklung sowohl von stärkerer Vorzugsströmung entlang kanalartiger Poren als auch von grösseren Stauzonen tiefer Fliessgeschwindigkeiten erwiesen. Diese Stauzonen haben ebenfalls bloss nach einer leichten Senkung der Sättigungszahl eine

markante Veränderung in der Form der Geschwindigkeitsverteilung verursacht, die mit einem Übergang zu verstärkten anomalen Transportprozessen einhergegangen ist. Dem hier gezeigten theoretischen Model ist es gelungen, solche Änderungen anhand struktureller Eigenschaften des porösen Mediums vorherzusagen. Ergebnisse aus der Synchrotron-Röntgenmikrotomographie haben bestätigt, dass diese verstärkte mechanische Dispersion des Stoffes eine hohe Verformung der Stofffahne hervorruft, die seine Vermischung mit dem vorher liegenden Porenwasser verbessert. Eine ähnliche Auswirkung ergibt sich aus der Erhöhung der Durchflussgeschwindigkeiten bei unveränderter Sättigungszahl. Anhand einer numerischen Studie haben wir die physikalischen Mechanismen erklärt, die für diese Wechselwirkung verantwortlich sind. Eine tiefere Sättigungszahl ändert die Konnektivität des porösen Mediums, was die Konvergenz von Strömungslinien innerhalb des Porenraums und die Bildung von kanalartigen Poren fördert. Als Folge dessen entsteht eine starke Schraubenströmung in der flüssigen Phase, die mit einer hohen Helizität und mit einer starken Strömungslinienverformung verbunden ist. Diese Verformung zeigt sich vor allem als intensives Falten und Verflechten. Dies weist auf die dominierende Rolle von entweder Scherung oder Vortizität bei der lokalen Verformung innerhalb des Porenraums hin. Ihre Kombination erklärt die starke Verformung des injizierten Stoffes, die in den dazugehörigen Experimenten beobachtet wurde. Mithilfe von numerischen Simulationen von Stofftransport, die in den selben Geometrien der Experimente durchgeführt wurden, haben wir die Entwicklung von chaotischer Advektion und chaotischer Vermischung im Porenraum erforscht, die von dem früher erkannten Falten und Verflechten von Strömungslinien in der Nachbarschaft von Gas- und Festkörperoberflächen angedeutet wurde. Als ermittelte Lyapunov-Exponenten zeigten, die aus der Stofffahnenverformung für alle getesteten Fälle berechnet wurden, führt eine Senkung in der Sättigungszahl zu einer Verstärkung von Chaos in der flüssigen Phase.

Die in dieser Doktorarbeit gezeigte Forschung stellt einen wesentlichen Schritt für das Verständnis der physikalischen Mechanismen dar, die die grosse Heterogenität des Strömungsfeldes und den verstärkten Stofftransport erklären, durch die ungesättigte poröse Medien sich auszeichnen. Unsere Ergebnisse können bei zahlreichen Industrie- und Umweltprozessen breite Anwendung finden. Insbesondere sind sie in der Forschung von Vermischungsprozessen und reaktivem Stofftransport in mehrphasigen Medien von grosser Bedeutung. Die Ergebnisse von dieser Doktorarbeit wirken motivierend für die weitere Forschung in diesem Fachbereich, und sie tragen ebenfalls zur künftigen Untersuchung von komplexen Systemen und von zusätzlichen hochrelevanten Prozessen für die Umwelt und für die Industrie bei.

CONTENTS

Acknowledgments	iii
Abstract	v
Zusammenfassung	vii
List of Figures	xxx
List of Tables	xxxiii
1 Introduction	1
1.1 Flow and transport in porous media	2
1.1.1 The occurrence of anomalous transport	4
1.2 The process of mixing	6
1.2.1 Solute’s plume deformation and control on mixing	6
1.2.2 Advances in pore-scale 3D imaging for flow and transport in porous media	8
1.3 Chaotic advection and chaotic mixing	9
1.4 Thesis objective and research questions	12
2 Sharp transition to anomalous transport in unsaturated porous media	25
2.1 Introduction	27
2.2 Methods	28
2.2.1 Numerical flow simulations	28
2.2.2 Particle tracking simulations	29
2.3 Prediction of unsaturated flow distribution	29
2.3.1 Impact of saturation on flow velocities	29
2.3.2 Theoretical flow model	30
2.4 Prediction of advective transport	37
2.5 Conclusions and outlook	39
Appendix 2.A Porous medium structure and flow	45
Appendix 2.B Theoretical model for flow and velocity PDFs	47
2.B.1 Full formulation considering three-dimensional effects	48
2.B.2 Two-dimensional limit	50
2.B.3 Model parameters and regime scalings	52
Appendix 2.C Particle tracking simulations and the CTRW model	52
3 Phase saturation control on vorticity enhances mixing in porous media	59
3.1 Introduction	61
3.2 Methods	63

3.2.1	Synchrotron X-ray micro-tomography experiments	63
3.2.2	Experimental concentration calibration	67
3.2.3	Image analysis	68
3.2.4	Solute advance front reconstruction	69
3.2.5	Numerical simulations of flow	69
3.3	Theoretical concepts and metrics	70
3.3.1	Variance of the concentration field	70
3.3.2	Euler characteristic	71
3.3.3	Helicity density	72
3.3.4	Q-Criterion	72
3.4	Results and discussion	73
3.4.1	Lower saturation enhances mixing via a stronger solute front deformation	73
3.4.2	Dependence of mixing on hydrodynamics and air clusters volume	78
3.4.3	Backbone formation promotes helicity	80
3.4.4	Larger shear- and vorticity-dominated deformation at lower saturation degree	84
3.5	Conclusions	86
	Appendix 3.A Experimental concentration calibration	97
	Appendix 3.B Numerical flow simulations	102
	Appendix 3.C Power function regression of the evolution in time of the solute plume’s front deformation	105
	Appendix 3.D Movie captions	106
	3.D.1 Movie S1.	106
	3.D.2 Movie S2.	107
	Appendix 3.E Additional Supplementary Material	108
4	Chaotic advection and chaotic mixing in unsaturated porous media	115
4.1	Introduction	117
4.2	Materials and methods	120
4.3	Results and discussion	122
4.3.1	Solute plume deformation as a function of saturation	123
4.3.2	Solute mixing as function of saturation	126
4.3.3	Control of saturation on the chaos strength	127
4.4	Conclusions and outlook	131
	Appendix 4.A Reconstruction and quantification of the solute’s plume deformation	137
	Appendix 4.B Exponential function regressions	141
	Appendix 4.C Additional Supplementary Material	146

5	Discussion, Conclusions and Outlook	149
5.1	General discussion	149
5.1.1	Control of liquid phase saturation on both fluid flow and solute dispersion in porous media	149
5.1.2	Control of saturation on solute mixing and solute plume deformation	151
5.1.3	Chaotic advection and chaotic mixing in unsaturated porous media	154
5.2	Conclusions and contributions to the research field	156
5.3	Outlook and possible future research directions	158
	Curriculum Vitae	165

LIST OF FIGURES

Figure 1.1	Schematic of the repeated occurrence of flow branching and merging resulting from the topological complexity of porous media, i.e., Baker’s flow. The increase in the interface between mixing solutions after repeated cycles of branching and merging is depicted (adapted from Lester et al. (2016) and Carrière (2007)).	10
Figure 2.1	Velocity fields obtained from Stokes flow numerical simulations, displayed in terms of the velocity magnitude v normalized by its mean value \bar{v} , for (a) $S_w = 1.00$ and (b) $S_w = 0.71$. The colorbar is common to subfigures (a) and (b), with red colors indicating high velocities and blue colors low velocities. Regions where $\log_{10}(v/\bar{v}) \leq -1$ are shown in the darkest blue tone. The solid phase (circular obstacles) is shown in gray and air clusters in black. Subfigures (c) and (d) show the partition of the velocity field into two types of flow structures: (i) backbone or preferential paths, depicted in red, and (ii) dead-end regions of low velocity, depicted in blue, for $S_w = 0.83$ and $S_w = 0.71$, respectively. The inset in subfigure (d) depicts the geometry of a dead-end region, with ℓ representing the dead-end region’s depth.	30
Figure 2.2	Numerical (continuous lines) and predicted (dashed lines) probability density functions (PDF) for (a) Eulerian velocities and (b) pore flow rates, normalized by their respective average values \bar{v} and \bar{q} , for $S_w = 1.00, 0.83, 0.77,$ and 0.71 . The log-log scale highlights the scaling of low magnitudes; the power law scalings are shown for visual reference. Semi-log insets highlight the exponential behavior at high magnitudes.	31

- Figure 2.3 PDF of the dead-end areas p_A for (a) $S_w = 0.83$, (b) $S_w = 0.77$, and (c) $S_w = 0.71$. For all three cases, p_A is well approximated by a Pareto PDF (Eq. 2.9) describing power-law decay. Corresponding values of the fitting parameter γ describing a power law decay $\propto A^{-1-\gamma}$, which decreases with decreasing liquid phase saturation, are also shown. Quantities are non-dimensionalized with respect to the area a_m^2 associated with the average pore-throat aperture. 34
- Figure 2.4 Advective dispersion σ_x^2 in time for $S_w = 1.00, 0.83, 0.77$, and 0.71 . Time is normalized by the advective time $t_a = \lambda/\bar{v}$ over the mean pore size λ . The plot compares σ_x^2 from the particle tracking analysis (continuous lines) with σ_x^2 from a CTRW approach computed using the predicted velocity PDF $p_E(v)$ (dashed lines). Scalings for a ballistic ($\sigma_x^2 \sim t^2$) and a Fickian ($\sigma_x^2 \sim t^1$) regime are also displayed for reference. 38
- Figure 2.5 Velocity fields obtained from Stokes flow numerical simulations, displayed in terms of the velocity magnitude v normalized by its mean value \bar{v} , for (a) $S_w = 1.00$, (b) $S_w = 0.83$, (c) $S_w = 0.77$, and (d) $S_w = 0.71$. The color scale is common to all panels, with red colors indicating high velocities and blue colors low velocities. Regions where $\log_{10}(v/\bar{v}) \leq -1$ are shown in the darkest blue tone. The solid phase (circular obstacles) is shown in gray and air clusters in black. More accentuated backbone and dead-end regions are induced with decreasing liquid phase saturation. 46
- Figure 2.6 Partition of the velocity field for (a) $S_w = 0.83$, (b) $S_w = 0.77$, and (c) $S_w = 0.71$ into two types of flow structures: (i) backbone or preferential paths of high velocity, depicted in red, and (ii) dead-end regions or stagnation zones of low velocity, depicted in blue. The number and size of dead-ends increase as liquid phase saturation decreases. The ratio f of dead-end area to the total area of the pore space is reported for each case. 47

Figure 2.7	(a) Close view of the velocity field for $S_w = 0.71$, highlighting the velocity field within a dead-end region. An observation cross-section is depicted as a continuous line. (b) Velocity variation over the depth of a dead-end region, here parallel to the y -axis, along the observation cross-section shown in (a). The velocity decays exponentially as a function of depth.	48
Figure 2.8	Spatial distribution of liquid-phase velocities v within each pore throat in the medium along the direction y transverse to the local main flow direction at each throat, under fully-saturated conditions ($S_w = 1.00$). Velocities are normalized by the maximum velocity v_{\max} at each pore throat and y coordinates are normalized by the corresponding pore throat size a . The plot highlights the variability of the velocity profile across pore throats. The color map represents the pore throat size, with dark blue tones corresponding to small pore throats and yellow colors representing large ones. The continuous line represents the mean velocity profile described by Eq. 2.16. The dashed line shows a parabolic (i.e., Poiseuille) velocity profile (Eq. 2.26), found only in the smaller pore throats.	49
Figure 2.9	(a) Eulerian velocity PDFs and (b) local flow rate PDFs for all analyzed saturation degrees $S_w = 1.00, 0.83, 0.77$, and 0.71 . Continuous lines represent the data from Stokes flow simulations; dashed lines represent full numerical computation of the integral representation of the theoretical PDFs discussed in Section 2.3.2; and circular markers represent the analytical low- and high-magnitude regime scalings. Plots are non-dimensionalized according to the mean velocity \bar{v} and the mean pore flow rate \bar{q} of the numerical data set, respectively.	53
Figure 2.10	Auto-correlation functions ρ of the longitudinal velocities, as a function of longitudinal distance x normalized by the mean pore size λ , for $S_w = 1.00, 0.83, 0.77$, and 0.71	54

Figure 2.11	<p>Temporal evolution of advective longitudinal dispersion σ_x^2. Time has been non-dimensionalized by the advective time t_a for each saturation. (a) Comparison of dispersion from particle tracking simulations (continuous lines) with dispersion obtained from CTRW using the numerical Eulerian velocity PDFs (dash-dotted lines). (b) Comparison of σ_x^2 from CTRW using the numerical Eulerian velocity PDFs (dash-dotted lines) and from CTRW using the velocity PDFs from the theoretical model (dotted lines). Scalings for ballistic ($\sigma_x^2 \sim t^2$) and Fickian ($\sigma_x^2 \sim t^1$) regimes are shown as visual guides.</p>	55
-------------	--	----

Figure 3.1 Concentration field and mixing quantification from synchrotron X-ray micro-tomography experiments. a) 3D reconstruction of the tested porous medium. Only three-quarters of the sample are displayed to allow the visualization of the gas phase (air, shown in cyan) inside of the pore space for the experiment performed at $S_w = 0.82$. b) Concentration field expressed in units of mole per unit of volume (molar concentration, M) for the experiment performed at $S_w = 0.82$ with a flow rate $q = 0.25 \text{ mm}^3 \text{ s}^{-1}$ at time $t = 50.4 \text{ s}$ after the tracer entered the sample. All concentration values lower than 0.15 M are not displayed for improved visualization. For the same purpose, the air phase is also not shown, whereas the solid phase of borosilicate glass grains is shown as grey transparency. Only three-quarters of the sample are displayed to better visualize the concentration differences inside the pore space. The white arrow indicates the main flow direction. The formation of a backbone of preferential flow is indicated on the upper right portion of the sample. c) Evolution of the variance of the concentration field, σ_c^2 , in time for all five transport experiments. The values of σ_c^2 have been corrected by the variance at time $t = 0 \text{ s}$, $\sigma_{c,t=0}^2$. d) Rate of change of σ_c^2 over time, $\partial(\sigma_c^2 - \sigma_{c,t=0}^2)/\partial t$, as computed from the results shown in panel c). For panels c) and d), different line types correspond to different injection flow rates, whereas different line colors correspond to different saturation degrees. Note that, in that regard and for facilitating experiment comparison, we have grouped together $S_w = 0.76$ and $S_w = 0.75$ given their very similar saturation degree.

Figure 3.2

Analysis of the solute front deformation over time, as a function of the saturation degree. a) Deformation over time of the plume's advancing front, here represented by the isosurface of 50% of concentration, shown at the time instants $t = 30$ s (in light red) and $t = 60$ s (in yellow), for the experiment performed at $S_w = 0.92$ and flow rate $q = 0.25 \text{ mm}^3 \text{ s}^{-1}$ (refer to Movie S2 in the Supplementary Material, Appendix 3.D, for a visualization of the entire time series). The solid phase of borosilicate glass grains is not displayed to improve the visualization, while the gas phase (air) is shown in semi-transparent cyan. The white arrow indicates the main flow direction. b) Temporal evolution of the area of the advancing front, A , normalized by the area computed at the initial time of the deformation analysis, A_0 . Different line types correspond to different injection flow rates, whereas different line colors correspond to different saturation degrees. Note that, in that regard and for facilitating experiment comparison, we have grouped together $S_w = 0.76$ and $S_w = 0.75$ given their very similar saturation degree. The respective power law fitting curves are displayed with dot lines for all cases except for $S_w = 0.92$, which is the only case that reaches a plateau at later times. Scalings for both a ballistic ($A/A_0 \sim t^1$) and a Fickian ($A/A_0 \sim t^{0.5}$) regime are displayed for visual reference.

Figure 3.3 Hydrodynamic characterization and air clusters volume distribution as a function of saturation degree. a) Probability density function (PDF) of the liquid flow velocity magnitude, $p(v)$, computed in each case via 3D flow Finite Elements Method (FEM)-based numerical simulations. $p(v)$ has been normalized by the corresponding average velocity magnitude value, \bar{v} . $p(v)$ for the additional case $S_w = 1.00$ is also included. The Log-Log scale highlights the scaling of the low-velocity magnitudes, with exact power-law scalings also shown for visual reference only. A semi-Log plot is shown in the inset to display the exponential behavior at high-velocity magnitudes. b) PDF of the volume of air clusters, $p(V_a)$, for all experiments. $p(V_a)$ is expressed in units of μm^3 . The minimum volume considered corresponds to that of an average pore of size $\bar{\xi} = 30 \mu\text{m}$. The power-law scaling V_a^{-2} is shown for visual reference. In both panels, different line types correspond to different injection flow rates, whereas different line colors correspond to different saturation degrees. Note that, in that regard, we have grouped together $S_w = 0.76$ and $S_w = 0.75$ given their very similar saturation degree. 79

Figure 3.4 Euler characteristic, χ , of the liquid phase, as a function of saturation degree S_w , computed for every experiment at a single time step chosen at about half of its duration. Results were obtained in each case from binary tomographic images of the liquid phase of the entire sample (liquid phase mask, see Figure 3.7 in Appendix 3.A). A fully saturated condition $S_w = 1.00$ is also displayed for comparison. The best fitting line is displayed black dotted. The color criteria used for the markers follows the same one used in Figures 3.1c, 3.1d and 3.2b. 81

Figure 3.5

Analysis of the occurrence of helical flow in the pore space. a) Variation of the average absolute helicity density, $\langle |h| \rangle$, with S_w , for the three experimental injection flow rates $q = 0.125, 0.25, \text{ and } 0.50 \text{ mm}^3 \text{ s}^{-1}$. The conditions investigated experimentally are displayed with squared markers, whereas additional numerically simulated conditions are shown with circular markers. The dotted lines describe the linear trend obtained for the variation of $\langle |h| \rangle$ with S_w . The color criteria corresponds to that of Figures 3.1c, 3.1d and 3.2b. b) and c) show different streamlines deformation patterns induced by the occurrence and enhancement of helical flow in the system. These results correspond to the experiment performed at $S_w = 0.75$ and $q = 0.125 \text{ mm}^3 \text{ s}^{-1}$, with numerically generated streamlines colored based on the absolute local helicity ($\log_{10}(|h|)$) and with the air phase imaged experimentally displayed in semi-transparent cyan. The borosilicate glass grains are not displayed to improve visibility. White ribbon arrows describe the deformation pattern common to the different groups of streamlines: b) depicts the braiding of streamlines in the neighbourhood of an air bubble (see red streamlines on the left) and the absence of it for streamlines travelling along a backbone (see grey streamlines on the right); c) depicts the convergence of two groups of streamlines into the same backbone, with one group experiencing strong braiding and folding (red tones) and the other one showcasing no strong streamline deformation (grey tones).

Figure 3.6 Impact of the saturation degree on how topology controls the solute plume deformation. a) Average positive and negative Q -criterion, $\langle Q \rangle$, as a function of S_w , for the three experimental injection flow rates, $q = 0.125, 0.25,$ and $0.50 \text{ mm}^3 \text{ s}^{-1}$. The conditions investigated experimentally are displayed with squared markers, whereas additional conditions, created numerically only, are shown with circular markers. The dotted lines describe the linear trends obtained for the variations of the respective indexes as a function of S_w . b) PDF of the Q -criterion, $p(Q)$, for the experimental cases only, plus the case $S_w = 1.00$, included for comparison. Different line types correspond to different injection flow rates, whereas different line colors correspond to different saturation degrees. Note that, in this regard, we have grouped together $S_w = 0.76$ and $S_w = 0.75$ given their very similar saturation degree. In both panels, we have indicated with grey shaded areas the range of Q -values associated to vorticity-dominated deformation. 85

Figure 3.7 Graphical summary of the image analysis protocol used for the post-processing and quantitative evaluation of the reconstructed transport experiments. The protocol was also used for the analysis of the calibration tomograms. All processes depicted here were performed in 3D, i.e., considering all slices in the image stack representing every tomogram, hence taking into account 3D connectivity and continuity of the different material phases. For every step, both the software used and the corresponding plugin(s) are listed. 99

Figure 3.8 Summary of the experiment calibration process. a) Calibration curve relating the tomographic voxel value (i.e., phase contrast intensity), V , and the solute concentration, c , obtained following the procedure described in Appendix 3.A. All thirteen pairs of points used for the calibration are shown in blue markers and represent the average voxel value of the calibration tomogram, V_i , and their corresponding concentration values. The error bars represent the standard deviation of the voxel values, S_{V_i} , for every calibration tomogram. The obtained linear relationship is shown in the magenta dashed line. Red dashed lines represent the 99% confidence intervals obtained for the concentration estimation. The resulting linear equation is also shown. b) Variation in the median absolute deviation from the median value (MAD) of a sample of voxel values, with the increasing number of sampled voxels. This was used for estimating the representative statistical sample size, to be used for defining the confidence intervals shown in a). MAD-values stabilize around a value of 500 voxels for all cases. 101

Figure 3.9 Scalar fields of the resultant velocity magnitude in the liquid phase obtained from the steady-state Stokes flow simulations, displayed as the logarithm of the velocity magnitude v , $\log_{10}(v)$. The color bar is common to all panels, with lighter colors depicting larger velocity magnitudes. Regions where $\log_{10}(v) < -7.0$ are depicted in black and those where $\log_{10}(v) > -2.5$ are shown in the brightest yellow. All five experimental cases are shown together and described by their corresponding liquid phase saturation degree S_w and injection flow rate q . The fully saturated case $S_w = 1.00$ is also shown for reference. Three-quarters of the sample are displayed in all cases to better visualize the inner flow structures. The white arrows indicate the main flow direction. 103

Figure 3.10 Scalar fields of the vorticity magnitude ω in the liquid phase obtained from the steady-state Stokes flow simulations. The color bar is common to all panels, with lighter colors depicting larger vorticity magnitudes. Regions where $\omega > 100 \text{ s}^{-1}$ are shown in the brightest yellow. All five experimental cases are shown together and described by their corresponding liquid phase saturation degree S_w and injection flow rate q . The fully saturated case $S_w = 1.00$ is also shown for reference. Three-quarters of the sample are displayed in all cases to visualize the inner scalar field magnitudes better. The white arrows indicate the main flow direction. 104

Figure 3.11 Probability density function, $p(\xi)$, of the pore size, ξ , computed for the porous medium made of sintered irregularly shaped borosilicate glass grains, used in all transport experiments. A 3D rendering of the tomographic reconstruction of the entire sample is shown in Figure 3.12b. The distribution was obtained by using the Pore Size Distribution algorithm, available on the Xlib plugin library (Münch 2022) on the free-source software ImageJ. From this distribution, we computed the average pore size, $\bar{\xi} = 30 \mu\text{m}$ 108

Figure 3.12 Setup for the transport experiments + X-ray tomography measurements, as implemented at the TOMCAT beamline of the Swiss Light Source (SLS), Paul-Scherrer Institute (Villigen, Switzerland). a) Shows a schematic representation of the experimental setup, with an indication of the two injection lines, and the installation of pressure sensors both at the inlet and at the outlet lines. b) Shows, in the upper panel, the general setup and the porous medium sample location relative to the X-ray beam. The lower right panel shows a close-up of the flow cell, with the gas and liquid injection lines at the bottom, the outlet line at the top, and the central cylindrical part containing the sample. A 3D rendering of the tomographic reconstruction of the entire sample is shown in the lower left panel, depicting the heterogeneous shape of the solid grains, with the whole sample resembling a sandy soil in terms of grain size and bulk porosity. 109

Figure 3.13

Alternative representation of the experimental results. a) Variance of the concentration field, σ_c^2 , against the dimensionless time, τ , for all five transport experiments. The values of σ_c^2 have been corrected by the variance at time $t = 0$ s, $\sigma_{c,t=0}^2$. τ is expressed as $\tau = t/t_{\text{adv}}$, where the advective time $t_{\text{adv}} = \bar{\xi}/\bar{v}$ is the time required for the flow to bridge the average pore size $\bar{\xi}$ at the average flow velocity \bar{v} . b) Evolution over the dimensionless time τ of the area of the advancing front, A , normalized by the area computed at the initial time of the deformation analysis, A_0 . The respective power law fitting curves are displayed with dot lines for all cases except for $S_w = 0.92$, which is the only case that reaches a plateau at later times. On both panels, different line types correspond to different injection flow rates, whereas different line colors correspond to different saturation degrees. Note that, in that regard and for facilitating experiment comparison, we have grouped together $S_w = 0.76$ and $S_w = 0.75$ given their very similar saturation degree. 110

Figure 3.14 Skewness, $\gamma_{1,p(Q)}$, of the probability density function of the Q -criterion as a function of the liquid phase saturation degree S_w . Cases tested experimentally are displayed with squared markers. Additional cases derived from numerical flow simulations to generate one flow field for every combination of saturation degree and injection flow rate, q , tested experimentally are included and shown in circular markers. Note that, for this purpose, we have grouped together $S_w = 0.75$ at $q = 0.50 \text{ mm}^3 \text{ s}^{-1}$ and $S_w = 0.76$ at $q = 0.125 \text{ mm}^3 \text{ s}^{-1}$ given their very similar saturation degree, meaning that we simulated only one additional case for $S_w = 0.76$ at $q = 0.25 \text{ mm}^3 \text{ s}^{-1}$. This grouping is also reflected in the color criteria of the markers, which corresponds to that used in Section 3.4 (see Figure 3.6) and represents the saturation degree plotted on the x -axis. However, $S_w = 0.75$ and $S_w = 0.76$ are not considered identical conditions in terms of saturation, given the different spatial arrangement of air clusters inside the pore space obtained in both cases. Results indicate that $\gamma_{1,p(Q)}$ is exclusively controlled by the saturation degree, i.e., the spatial heterogeneity of the porous medium, whereas changes in the imposed flow conditions on the same system do not affect the skewness of the distribution. The latter behavior is observed in the overlapping between the squared and circular markers. This concludes on the exclusive control of saturation, and in particular of the spatial distribution of the gas phase (air) in the pore space, on defining the main mechanism locally deforming the solute plume as it spreads through the pore space, i.e., shear-dominated or vorticity-dominated deformation. 111

Figure 3.15 Variations in the mechanisms of flow deformation as function of connectivity. a) Variation of the average absolute helicity density, $\langle|h|\rangle$, with the Euler characteristic χ , for the three experimental injection flow rates $q = 0.125, 0.25,$ and $0.50 \text{ mm}^3 \text{ s}^{-1}$. b) Average positive and negative Q -criterion, $\langle Q \rangle$, as a function of χ , for the three experimental injection flow rates, $q = 0.125, 0.25,$ and $0.50 \text{ mm}^3 \text{ s}^{-1}$. The grey shaded area indicates the range of Q -values associated with shear-dominated deformation. On both panels, the conditions investigated experimentally are displayed with squared markers, whereas additional numerically simulated conditions are shown with circular markers. The dotted lines describe the linear trend obtained for the variation of both metrics with χ . The color criteria corresponds to that employed in Section 3.4. . . . 112

Figure 4.1 Main outputs from the two steady-state transport scenarios solved numerically. Results for a porous medium with a saturation degree $S_w = 0.82$ and with an injection flow rate $q_1 = 0.125 \text{ mm}^3\text{s}^{-1}$ are displayed. a) Solute's plume deformation, i.e., deformation of the isosurface of the 1% of concentration, 3D-rendered in yellow, as reconstructed from the low-diffusivity transport scenario ($D_S = 1 \times 10^{-12} \text{ m}^2\text{s}^{-1}$). In addition, the air phase volume is 3D-rendered in transparent cyan and the porous medium boundaries are shown as a transparent cylinder. The pore space boundaries on the inlet's cross section are highlighted in white, with the surface region of the chosen injection pore on the inlet's cross-sectional plane highlighted in magenta. b) Solute's concentration field inside the sample, expressed in units of solute moles per unit of volume (molar concentration, M), as obtained from the diffusive transport scenario ($D_H = 1.929 \times 10^{-9} \text{ m}^2\text{s}^{-1}$). All concentration values below 0.01 M are displayed in the darkest blue. In addition, only the solid phase's volume is 3D-rendered in transparent grey. Only three-quarters of the sample are displayed to improve the visualization of the concentration gradients inside the sample. In both panels, the white arrow indicates the main flow direction. See Figures 4.5, 4.7 and 4.8 in the Appendix, for the remaining cases. 121

Figure 4.2 Evolution of the relative length of the solute's plume front, ℓ/ℓ_0 , with travel distance along the z -axis, for all pairs of conditions S_w - q considered in this study. All the results stemmed from the low-diffusivity simulations, i.e., performed with a diffusion coefficient $D_S = 1 \times 10^{-12} \text{ m}^2\text{s}^{-1}$, in which no variation in ℓ/ℓ_0 upon changes in q for the same S_w was observed. The plume's front is represented through the isosurface of the concentration field with value equal to 1% of the injection concentration (1.0 M). ℓ represents the plume's length over an x - y cross-sectional plane at a certain z . The results have been expressed as a relative deformation by dividing ℓ by the isosurface length at $z = 0 \text{ }\mu\text{m}$, ℓ_0 . This explains the offset along the y -axis for all the curves. Results for every observation plane are shown as markers, whereas the corresponding exponential regressions are shown as continuous lines. Different colors correspond to different saturation degrees. In both panels, the type of scaling described by ℓ/ℓ_0 as a function of z is displayed. 124

Figure 4.3 Mixing analysis for the two transport scenarios considered in this work. a) Evolution of the mixing volume, $M_V(D_S)$, along the main flow direction, z , for all tested S_w cases based on the transport scenario defined by $D_S = 1 \times 10^{-12} \text{ m}^2\text{s}^{-1}$. Values for M_V have been computed over an x - y cross-section plane moving along z . Different colors correspond to different S_w values. b) and c) Evolution of $M_V(D_H)$ along z for $S_w = 0.92$ and $S_w = 0.76$, respectively, based on results for the transport scenario defined by $D_H = 1.929 \times 10^{-9} \text{ m}^2\text{s}^{-1}$. Results for the three tested flow rates are shown in different colors. In addition, the evolution of M_V along z for the low-diffusivity case D_S (i.e., $M_V(D_S)$) is shown also in each panel for comparison. In all panels, results for every observation plane along z are shown as markers, whereas the corresponding exponential regressions are shown as continuous lines. 127

Figure 4.4 Variation of the exponential scaling rate parameter, α , as function of the saturation degree, S_w , for the different injection flow rates, q , as obtained from the regression performed on the results of the numerical simulations of transport for a) the relative increase in plume's deformation (isosurface transversal deformation), ℓ/ℓ_0 , b) the mixing volume for the low-diffusivity scenario, $M_V(D_S)$, and c) the mixing volume for the diffusive scenario, $M_V(D_H)$. d) Variation in the Lyapunov exponent, λ , as function of S_w and q , computed from the data in a) as $\lambda = \alpha_{\ell/\ell_0} \bar{v}$. The color labelling corresponds to that employed in Figures 4.2 and 4.3. Different markers are assigned to different flow rates. 129

Figure 4.5 Solute's plume deformation, i.e., deformation of the isosurface of the 1% of concentration, as reconstructed from the numerical simulations performed for the low-diffusivity transport scenario ($D_S = 1 \times 10^{-12} \text{ m}^2\text{s}^{-1}$), for all five saturation degrees considered in this study. In all cases, the air phase is shown in cyan transparency, the sample boundaries are shown as a transparent cylinder, and the inlet's cross section at the top is shown in white, where the injection pore is highlighted in magenta. The color assigned to every isosurface in each panel corresponds to the color map employed in Section 4.3 for every saturation degree. The white arrows represent the main flow direction. 139

Figure 4.6 Graphical summary of the quantification of the solute's plume deformation, i.e., deformation of the isosurface of the 1% of concentration. a) Isosurface generated for the porous medium characterized by a saturation degree $S_w = 0.92$. The systems bounds are depicted as a transparent cylinder, and three x - y planes, located along z at $198 \mu\text{m}$ (purple), $1300 \mu\text{m}$ (blue), and $2642 \mu\text{m}$ (green) from the injection point, are displayed. The white arrow represents the main flow direction. b), c), and d) show the 2D sections resulting from the intersection of these three x - y planes with the porous medium, respectively. They show the resulting pore space cross section as white lines, and the intersection with the isosurface of the 1% of concentration as single curves in the same color as the corresponding plane. The ensemble of these single curves represent the transverse deformation of the plume across the pore space. The length scale in panel b) is common for panels b), c), and d). 140

Figure 4.7 Concentration field inside of the porous medium, expressed in units of mole per unit of volume (M), for the saturation degrees $S_w = 1.00, 0.92,$ and 0.89 , as obtained from the numerical simulations performed for the diffusive transport scenario ($D_H = 1.929 \times 10^{-9} \text{m}^2\text{s}^{-1}$). For all cases, results for the highest flow rate, $q_1 = 0.500 \text{mm}^3\text{s}^{-1}$, and for the lowest one, $q_3 = 0.125 \text{mm}^3\text{s}^{-1}$, are shown in the left and the right column, respectively. The color bar is common to all panels, where all concentration values below 0.01M are displayed in the darkest blue. In addition, only the solid phase is shown in grey transparency, and only three-quarters of the sample are shown to better visualize the concentration gradients inside the sample. The white arrows represent the main flow direction. . . 143

- Figure 4.8 Concentration field inside of the porous medium, expressed in units of mole per unit of volume (M), for the saturation degrees $S_w = 0.82$ and 0.76 , as obtained from the numerical simulations performed for the diffusive transport scenario ($D_H = 1.929 \times 10^{-9} \text{ m}^2\text{s}^{-1}$). For all cases, results for the highest flow rate, $q_1 = 0.500 \text{ mm}^3\text{s}^{-1}$, and for the lowest one, $q_3 = 0.125 \text{ mm}^3\text{s}^{-1}$, are shown in the left and the right column, respectively. The color bar is common to all panels, where all concentration values below 0.01 M are displayed in the darkest blue. In addition, only the solid phase is shown in grey transparency, and only three-quarters of the sample are shown to better visualize the concentration gradients inside the sample. The white arrows represent the main flow direction. 144
- Figure 4.9 Evolution of the mixing volume, $M_V(D_H)$, along the main flow direction, z , for all five saturation degrees considered in the study, based on the results of the numerical simulations for the diffusive transport scenario defined by $D_H = 1.929 \times 10^{-9} \text{ m}^2\text{s}^{-1}$. Values for $M_V(D_H)$ have been computed over a x - y cross-section plane moving along z , and are displayed as markers in every panel. The corresponding exponential regressions are shown as continuous lines. In each panel, results for the three tested flow rates are shown in different colors. In addition, the evolution of M_V along z for the low-diffusivity case D_S is also shown for comparison in each case. 145
- Figure 4.10 Comparison between the computed exponential regression parameters α_{ℓ/ℓ_0} and $\alpha_{M_V(D_S)}$, obtained from the isosurface deformation ℓ/ℓ_0 , and the mixing volume, $M_V(D_S)$, data sets for every saturation degree, respectively. Both data sets are linked to the low-diffusivity transport scenario. The dashed line corresponds to the linear equation of unitary slope. Results expose the large variation induced on the exponential growth rate of the mixing volume over travel distance upon a small change in the corresponding growth rate of the isosurface deformation. 146

LIST OF TABLES

Table 2.1	Model parameters. The parameters employed to model the flow and velocity PDFs are the ratio f of dead-end areas to total pore space area, the Pareto exponent γ of the dead-end area PDF, and the characteristic pore flow rate q_c . The characteristic velocity $v_c = q_c / (ha_m)$ is also reported. The CTRW transport model requires the tortuosity χ and the longitudinal correlation length ζ_x of Lagrangian velocities.	55
Table 3.1	Summary of the flow characterization for all experiments reported in this study, and additionally also for the case $S_w = 1.00$, which was built up from the combination of the segmented tomograms of the liquid (KI solution) and the gas (air) phase. Values reported here were computed from the numerical flow simulations. Flow descriptors include the injection flow rate, q , the mean fluid flow velocity, \bar{v} , the Péclet number, Pe , the capillary number, Ca , and the total number of injected pore volumes during the entire experiment, PV . For the computation of both Pe and Ca , we used the average properties of the KI solution over the range of concentrations chosen for the experiments (0.06 M to 0.90 M) and at a temperature of 25°C.	74

Table 3.2	<p>Results of the regression performed for the evolution in time of the area A of the isosurface of 50% of concentration, i.e., solute plume's front. The regression follows the equation $Y = \beta t^\alpha$, where $Y = A/A_0$, being A_0 the isosurface area at time $t = 0$ s, and β and α are the parameters of the power function. The regression was performed using the least-squares method over the logarithmic values of Y and t, that is, over the linear equation $\ln Y = \ln \beta + \alpha \ln t$ (see Appendix 3.C). The Pearson correlation coefficient, R^2, obtained in every case for the regression is also reported. Results indicate an increase in the power law scaling, α, due to both a decrease in saturation degree, S_w, under constant injection flow rate of the solute, q, and an increase in q at very similar S_w.</p>	107
Table 4.1	<p>Summary of the flow and transport characterization for all thirty conditions reported in this study based on results of the numerical flow simulations. These conditions are characterized by the saturation degree, S_w, the injection flow rate, q, with $q_1 = 0.125$, $q_2 = 0.250$ and $q_3 = 0.500 \text{ mm}^3 \text{ s}^{-1}$, and the diffusion coefficient, D_i, where $D_H/D_S \approx 2000$. Reported descriptors include the mean fluid flow velocity, \bar{v}, expressed in units of $\times 10^{-4} \text{ m s}^{-1}$, and the dimensionless Péclet numbers, $Pe(D_H)$ and $Pe(D_S)$, linked to the two transport scenarios defined by D_H and D_S, respectively.</p>	123
Table 4.2	<p>Summary of the exponential regression (see Eq. 4.4) performed on the results obtained from the numerical simulations for the low-diffusivity transport scenario, for all saturation degrees considered. Two main data sets are included, namely, the isosurface deformation, ℓ/ℓ_0, and the mixing volume, $M_V(D_S)$. Both of them did not show any dependency on the injection flow rate, q, given the high Péclet numbers achieved, $Pe(D_S) > 2000$. Reported variables include the exponential regression parameters α_{ℓ/ℓ_0} and $\alpha_{M_V(D_S)}$ [μm^{-1}], and β_{ℓ/ℓ_0} [-] and $\beta_{M_V(D_S)}$ [$\times 10^4 \mu\text{m}^2$], and also the dimensionless symmetric Mean Absolute Percentage Error (sMAPE).</p>	142

Table 4.3	Summary of the exponential regression (see Eq. 4.4) performed on the results obtained from the numerical simulations for the diffusive transport scenario, namely, the mixing volume, $M_V(D_H)$. Results for all five saturation degrees, S_w , and for all three injection flow rates, q_1 , q_2 , and q_3 , considered in the study are reported. For each data set, the exponential regression parameters, $\alpha_{M_V(D_H)}$ [μm^{-1}], and $\beta_{M_V(D_H)}$ [$\times 10^4 \mu\text{m}^2$], together with the dimensionless symmetric Mean Absolute Percentage Error (sMAPE), are reported.	146
-----------	---	-----

INTRODUCTION

Porous media belong to some of the most ubiquitous systems found in nature. They are the building block of tissues and organs in a plethora of living organisms (Khanafar and Vafai 2022), form essential features in plants (Dadmohammadi and Datta 2022; Dullien 1991), and even describe the basic aggregation mechanism of several microorganisms in the form of biofilms (Kurz et al. 2023). In addition, porous media are an essential component of abiotic factors in the environment, being soils the most abundant example, which mediate mass and energy fluxes. In all these cases, porous media is described by a volume, i.e., pore-space, hosted inside a solid matrix or skeleton in the form of small interstices connected to each other. This leads to structures of high topological complexity that serve as hosts for a variety of physical, chemical, and biological processes.

Soils represent an interesting case of study given their role in controlling the effects of processes taking place in the atmosphere on those occurring in the subsurface. In particular, the unsaturated region of soils, which is located between the soil surface and the deeper aquifers, is essential for this exchange. This region is characterized by the presence of more than one fluid phase in the pore space (water and air), what is usually referred to as unsaturated. It controls both the distribution of any substance entering the subsoil and the mixing of this substance with other fluid phases already present in the pore space, as the solute moves and spreads through the pore space. Hence, it plays a major role in controlling the fate of solutes, pollutants, or nutrients in the subsoil. In particular, it acts as filter and buffer for contaminants (Burauel and Baßmann 2005). This region is thus of paramount importance for a series of environmental and industrial applications, which include groundwater and soil remediation (Cunningham et al. 2003; Lahav et al. 2010; Sebilo et al. 2013; Williams et al. 2009), artificial groundwater recharge (Bouwer 2002; Dillon 2005), radioactive waste disposal (Winograd 1981), agricultural irrigation (Rockström et al. 2009; Sebilo et al. 2013; Valdes-Abellan et al. 2017), and energy storage (Barbier 2002), among

others. However, our understanding of the physical mechanisms controlling fluid flow and solute transport and mixing in these environments is rather limited, which has impaired our capacity to develop effective predicting tools and optimize some of the above-mentioned applications. This is mainly due to the large degree of physical heterogeneity characterizing these systems, which arise from both the complex spatial organization and the intricate interactions of the different fluid phases at the pore scale, i.e., at the scale of the liquid- or gas-filled voids between solid grains, at which intrinsically fluid flow, solute transport, and mixing occur (Dentz et al. 2011). In addition, the high technical complexity of accessing these micro-scale systems in a non-invasive manner and imaging these processes at the required spatial and temporal resolutions has represented a major bottleneck in their study.

This doctoral thesis presents a systematic study on the control of the spatial heterogeneity, expressed through the saturation degree, S_w , i.e., the relative occupancy of the liquid phase in the pore space, on the processes of fluid flow and solute transport and mixing at the pore scale. It combines experimental, numerical, and theoretical approaches to understand the physical mechanisms behind them, providing new tools for their prediction and up-scaling, and for the further study of other related processes also taking place in such environments. The results of this study can also find application in other type of multiphase systems of high environmental and industrial relevance, such as deep aquifers, where geological CO₂ sequestration is carried out (Szulczewski et al. 2012), and static mixers, commonly operated under the presence of immiscible phases in the process industry (Valdés et al. 2022).

1.1 FLOW AND TRANSPORT IN POROUS MEDIA

Under the conditions most commonly found in nature, flow through porous media at the pore scale is usually classified as Stokes flow, which is characterized by laminar flow conditions at very low Reynolds numbers, $Re \ll 1.0$. This describes a fluid flow strongly dominated by viscous forces, with negligible impact of inertial effects. From a simplification of the Navier-Stokes equation, and under the consideration of incompressible flow conditions, the Stokes flow field can be expressed as

$$0 = -\nabla P + \mu \nabla^2 v + F, \quad (1.1)$$

where ∇P is the pressure gradient, μ is the dynamic viscosity of the fluid, v is the fluid velocity, and F represents any additional body force acting on the moving fluid.

Transport in porous media results from the combination of a series of single processes, some of which are strongly linked to the flow field just described. They are most commonly summarized in the form of the Advection-Dispersion equation, which expresses the variation in time of the concentration of a transported species c . It is commonly written as

$$\frac{\partial c}{\partial t} = D\nabla^2 c - v\nabla c + R, \quad (1.2)$$

where R represents all solute mass sources and sinks, e.g., as result of reaction or degradation processes, $v\nabla$ represents the advective transport component, i.e., the solute movement with the underlying flow field, and $D\nabla^2 c$ represents the contributions from both solute dispersion and molecular diffusion to the change of solute concentration over time. Solute dispersion is strongly associated with the underlying flow field, as it results from velocity gradients acting on neighbouring parcels of fluid, causing solute deformation and solute spreading across the pore space. Contrastingly, diffusion is entirely independent of the flow conditions and originates from concentration gradients built up in the pore space, resulting in an increase in the volume occupied by the solute over time as diffusion smooths out concentration differences existing between two miscible solutions. This definition of transport has been widely used in the classical formulations of solute transport at the continuum (Darcy scale). However, the use of average parameters for describing the pore space does not allow for taking into account the effects of pore space heterogeneity on the quantification and prediction of solute dispersion and mixing. This impossibility is even more pronounced in the case of unsaturated porous media, which display larger degrees of heterogeneity due to the presence of several material phases in the pore space (Jiménez-Martínez et al. 2017). As a consequence, classical models applied in unsaturated porous media assume the instantaneous complete mixing of entering solutes with the resident solution and/or the full displacement of the existing pre-event water by the entering one, which has been shown to not be accurate based on laboratory and field studies (Berkowitz et al. 2004; Brooks et al. 2010; Silliman et al. 2002). **This imposes the need for further research to develop accurate model formulations for the study of flow and transport in porous media, and in particular of unsaturated systems.**

1.1.1 *The occurrence of anomalous transport*

Recent studies, mainly based on micro- and millifluidics experiments and on pore-scale numerical simulations, have shown the impossibility of describing accurately solute transport and mixing in porous media by direct application of Eq. 1.2 (Berkowitz et al. 2006; Bijeljic et al. 2011; Levy and Berkowitz 2003). They have identified the occurrence of the so-called anomalous transport in the time evolution of solute's plume spreading and mixing. This is usually characterized by breakthrough curves, i.e., time series of the solute concentration at fixed locations, that display early arrival and long tailing, resulting in non-symmetric solute plume spreading (Berkowitz et al. 2006; Bordoloi et al. 2022) and in non-Fickian evolution of mixing in time (de Anna et al. 2014). Such findings have been reported even for very simplified porous geometries, described by narrow pore size distributions, and under fully saturated conditions, in which the intrinsic structural heterogeneity of the pore space is still much smaller than that found under natural conditions (Bordoloi et al. 2022; de Anna et al. 2014). Both experimental and numerical investigations, both in 2D and 3D, and considering both natural and artificial porous media, have revealed the dominant role of the local fluid flow velocity variations in shaping this transport response. In particular, the role of velocity intermittency, i.e., the temporal variation of Lagrangian velocities and accelerations along single streamlines as they move through the pore space, has been highlighted as main driver on the development of anomalous transport (de Anna et al. 2014; de Anna et al. 2013; Holzner et al. 2015; Kang et al. 2014), since it is associated with changes in the correlation structure of flow velocities across the pore space. This intermittent behavior stems itself from the morphological heterogeneity and the connectivity of the porous medium, which lead to the formation of regions of high and low flow velocity in the vicinity of pore throats and larger pore bodies, respectively (de Anna et al. 2014; Holzner et al. 2015). Depending on the topology of the pore space, isolated portions of pore bodies can even act as dead-end regions, where flow is mostly rotational and transport is dominated by molecular diffusion (Bordoloi et al. 2022). This leads to long-tailed non-symmetric distributions of residence times of discrete solute particles across the pore space, characteristic of anomalous transport.

The occurrence of a double flow structure (Holzner et al. 2015), characterized by the combined presence of a backbone of high flow velocities and dead-end regions of low flow velocity, has been shown to be enhanced under unsaturated conditions (de Gennes 1983), altering the underlying flow field and leading to broader distributions of flow velocities inside the pore space (Birkholzer and

Tsang 1997; Datta et al. 2013; Guédon et al. 2019; Jiménez-Martínez et al. 2017; Nützmann et al. 2002). An increase in both the resulting tortuosity and the solute fingering formation has been observed (Jiménez-Martínez et al. 2015; Jiménez-Martínez et al. 2017), leading to ballistic dispersion regimes at earlier times that differ from the expected Fickian behavior predicted with classical formulations. However, the impact of the increased porous space heterogeneity on solute transport remains controversial. Studies across different observation scales have reported both an increase (Aziz et al. 2018; Bromly and Hinz 2004; Haga et al. 1999; Jiménez-Martínez et al. 2017; Nützmann et al. 2002) and a decrease (Birkholzer and Tsang 1997; Vanderborght and Vereecken 2007) of dispersivity with decreasing liquid phase saturation. Some investigations have also reported non-monotonic variations of dispersivity with saturation characterized by a critical saturation degree, below which dispersivity starts decreasing again (Raouf and Hassanizadeh 2013). **A systematic investigation on the impact of saturation on the solute dispersion regimes over relevant time scales is thus necessary and has not been reported yet. Moreover, an understanding of the physical mechanisms behind the control of saturation on changes in the solute transport response at the pore scale is still missing.**

Advances in the development of analytical models for the prediction of flow and transport in porous media have mainly centered around the study of fully saturated systems. They have attempted to include the effects of pore-scale heterogeneity on transport across scales (Lasseux et al. 2021), through application of dual-domain mass transfer models (Liu and Kitanidis 2012), pore-network models (Bijeljic and Blunt 2007), and more widely, of Continuous Time Random Walk (CTRW) models (Berkowitz et al. 2006; Bijeljic et al. 2011; de Anna et al. 2013; Kang et al. 2014; Le Borgne et al. 2011; Levy and Berkowitz 2003; Puyguiraud et al. 2021). They have succeeded at providing better predictive tools than Eq. 1.2 through the addition of correlation schemes for the flow velocities and/or travel times of single advected particles, allowing for a closer representation of the solute breakthrough curves and of the early- and long-time dispersion scalings in the pore space (Kang et al. 2014; Le Borgne et al. 2011; Puyguiraud et al. 2021). However, they usually require a previous description of the underlying flow field. Recent investigations have provided important contributions for relating flow velocity distributions with properties of the medium structure, for example, by identifying the dominant role of spatial correlations on the resulting flow distribution and by implementing this on models for prediction of flow across the system (Alim et al. 2017). **However, the adaptation of flow and dispersion predicting models to unsaturated porous media has not been straightforward due to the not yet fully understood interactions among the different material**

phases occupying the pore space. In particular, the impact of the non-wetting phase (a gas phase in the case of the unsaturated region of soils) on variations in the velocity field and on the resulting solute dispersion and mixing remains elusive, being essential for an accurate prediction of fluid-fluid (homogeneous) and fluid-solid (heterogeneous) reactions under multiphase conditions.

1.2 THE PROCESS OF MIXING

Mixing is a key process in the transport of solutes through porous media, as it is ultimately responsible for the increase in the volume occupied by the solute plume in the pore space. This occurs due to the action of molecular diffusion, which smooths out concentration gradients existing at the interface between the mixing solutions (Danckwerts 1952; Kitanidis 1994; Ottino 1989). Although diffusion occurs in the absence of flow, the diffusive flux is largely enhanced in the presence of flow. Local velocity differences lead to solute dispersion, contributing to the stretching of the plume and therefore, to the increase of the interface between the two miscible solutions (de Anna et al. 2014; Jha et al. 2011; Jiménez-Martínez et al. 2015; Jiménez-Martínez et al. 2016). Hence, mixing is an essential process in the occurrence of chemical reactions in the pore space (Aquino et al. 2023; Markale et al. 2021).

1.2.1 *Solute's plume deformation and control on mixing*

Previous studies, most of which have been performed under 2D conditions, at both Darcy scale (Basilio Hazas et al. 2022; Chiogna et al. 2016; Cirpka et al. 2015; de Barros et al. 2012; Rolle et al. 2009) and pore-scale (de Anna et al. 2014; Jiménez-Martínez et al. 2015; Markale et al. 2021), have attempted to describe the physical mechanisms behind the occurrence of mixing. They have centered on the quantification of mixing from concentration fields obtained either experimentally (de Anna et al. 2014; Hasan et al. 2020; Jiménez-Martínez et al. 2015; Jiménez-Martínez et al. 2016; Markale et al. 2021; Van Offenwert et al. 2019) or numerically (Cirpka et al. 2015; Jha et al. 2011; Puyguiraud et al. 2021) using descriptors such as the mixing volume (de Anna et al. 2014), the mixing degree (Jha et al. 2011; Jiménez-Martínez et al. 2016), the dilution index (Kitanidis 1994), the variance of the concentration field (Jha et al. 2011), or the scalar dissipation rate (Jiménez-Martínez et al. 2015). In all these cases, these metrics exhibit non-Fickian scalings of the evolution of mixing at early times, commonly characterized by ballistic and/or superdiffusive scalings. Generally,

these studies have relied on the quantification of the solute front deformation to explain this enhanced mixing process, displaying in all cases a close correlation with the scale of mixing over time, i.e., non-Fickian growth rates of deformation up to characteristic diffusion times, after which the coalescence of material lines leads to diffusion dominated transport regimes (Le Borgne et al. 2015; Le Borgne et al. 2013). In particular, studies performed under unsaturated conditions have shown the enhancement of the solute front deformation upon a decrease in liquid phase saturation (Jiménez-Martínez et al. 2015; Jiménez-Martínez et al. 2016), highlighting the control of the increased morphological heterogeneity within the pore space on the amount of deformation exerted on the solute plume as it moves through it. This has been linked to the combined presence of preferential flow paths and stagnation zones, as described in Section 1.1.1, which also leads to larger concentration gradients at the interface between these two flow regions, rendering mixing more efficient. **However, the large majority of these studies has relied on 2D observations, not allowing to take into account the effects of 3D pore space connectivity on the analysis of solute deformation and mixing.**

Additional 2D and 3D studies, performed at Darcy-scale under fully saturated conditions, have attempted to explain the physical mechanisms behind the enhanced solute plume's deformation through the analysis of secondary flow motions in the pore space (Chiogna et al. 2015; Chiogna et al. 2016; Chiogna et al. 2014; Cirpka et al. 2015; de Barros et al. 2012; Ye et al. 2020; Yu et al. 2015). By using both numerical and experimental approaches, they have exposed the occurrence of helical flow and twisted streamlines in systems characterized by an anisotropic permeability tensor (Bakker and Hemker 2004; Chiogna et al. 2014; Yu et al. 2015), which has been linked to larger plume deformation and an increased plume dilution. They have also provided important contributions for the quantification of the former through the successful application of topological descriptors in mixing investigations. On one hand, they have managed to identify the relevant deformation mechanisms acting locally across the pore space through computation of vortex identification indexes, such as the Okubo-Weiss parameter (de Barros et al. 2012; Geng et al. 2020; Okubo 1970; Weiss 1991) and the Q -criterion (Geng et al. 2020; Hunt et al. 1988). These are expressed as a function of the local deformation tensor and allow the local identification of shear-dominated and vorticity-dominated deformation regions, i.e., a quantification of the local excess of rotation strain rate relative to the shear strain rate. On the other hand, these studies have also managed to characterize streamlines deformation by applying descriptors of both the spatial complexity and the strength of secondary flows across the pore space, such as the helicity density

(Chiogna et al. 2015; Chiogna et al. 2016; Cirpka et al. 2015; Moffatt 1992; Sposito 2001; Yu et al. 2015), which directly relates the velocity and vorticity vector fields existing in the system. In general, these studies have highlighted the importance of the topological uniqueness of porous systems in controlling solute plume deformation, and have shed light on the important role of rotational deformation on mixing enhancement. **However, similar investigations at the pore scale and under the presence of several material phases in the pore space have not been reported yet, given both the complexity of experimentally observing these processes at the temporal and spatial scale required to capture the interactions among all material phases, and the high computational cost of similar numerical investigations.**

1.2.2 *Advances in pore-scale 3D imaging for flow and transport in porous media*

Recent technological advances have allowed the novel application of different imaging techniques in 3D flow and transport studies in porous media. This has been possible thanks to improvements in the spatial and temporal resolution achieved with these techniques, in the computational tools required for the gathering and post-processing of experimental information, and in the fabrication techniques employed for generating artificial porous media. Some of these techniques include Magnetic Resonance Imaging (MRI) (Lehoux et al. 2016; Markale et al. 2021; Song 2013), high-resolution laser imaging (Heyman et al. 2021; Heyman et al. 2020; Souzy et al. 2020), and X-ray micro-tomography (Armstrong et al. 2016; Boon et al. 2017; Chen et al. 2021; Hasan et al. 2020; Van Offenwert et al. 2019), which have been applied either for direct visualization of the physical processes themselves, or for providing the working geometry for further numerical investigations. The cited studies, whose large majority has focused on fully saturated systems, have either relied on artificial and simplified porous media made of circular beads of constant or varying diameter (Hasan et al. 2020; Heyman et al. 2020; Markale et al. 2021), or, to a lesser extent, on natural systems consisting of either sand packing or rock cores (Chen et al. 2021; Lehoux et al. 2016; Van Offenwert et al. 2019). They have reported important insights on both flow and transport processes. MRI experiments have provided new ground for more accurate descriptions of particle dispersion in sand-like porous systems (Lasseux et al. 2021), and it has also been employed in investigations on unsaturated porous media to analyze the impact of wetting-phase saturation on fluid-fluid chemical reactions, directly linked with the process of transport and mixing of reactants across the pore space (Markale et al. 2021). High-resolution laser imaging has been applied with success for imaging the movement of small

fluorescent particles used for the reconstruction of experimental flow fields (Souzy et al. 2020). Additionally, groundbreaking studies of transport under low-diffusivity conditions have also been reported after the application of this technique, which has allowed a detailed reconstruction of the transversal deformation of a solute injected punctually in a fully saturated porous medium composed of glass beads (Heyman et al. 2021; Heyman et al. 2020). Nevertheless, X-ray micro-tomography has been the most exploited technique for 3D transport investigations in recent years. Laboratory-based micro-tomography has enabled imaging the advance of a tracer through artificial and natural porous media (Van Offenwert et al. 2019). However, this study has been limited by the spatial and temporal resolutions achieved in such experimental facilities, which are not high enough to effectively map dispersion and mixing dynamics at the pore scale. This has largely limited the applicability of this technique from laboratory-based campaigns to the acquisition of porous geometries for further use in numerical investigations (Guédon et al. 2019; Kang et al. 2014; Puyguiraud et al. 2021). Such studies have unveiled important mechanisms behind the non-Fickian scalings of plume spreading over time and on the relevance of velocity and acceleration intermittency on solute spreading, allowing for their implementation in improved analytical models for dispersion and transport prediction. X-ray micro-tomography at the high spatial and temporal resolutions required for porous media transport investigations can only be carried out in synchrotron facilities. Such studies have been reported only very recently, on one hand focusing on transport in unsaturated porous media through direct imaging of the movement and mixing of a tracer, providing a characterization of incomplete mixing at the pore scale (Hasan et al. 2020); and on the other hand, for the analysis of hysteresis in the hydrodynamic dispersion of fully saturated sandy soils during cycles of imbibition and drainage (Chen et al. 2021). **However, the use of these imaging techniques for the study of mixing in unsaturated porous media, especially aimed at providing a mechanistic understanding of the impact of saturation on solute mixing and on the reported enhanced mixing efficiency, still remains largely unexplored.**

1.3 CHAOTIC ADVECTION AND CHAOTIC MIXING

The technical advances described in Section 1.2.2, together with improvements in computational power during the last decades, have offered new research opportunities for understanding solute transport in porous media. Recent studies have described the inherent nature of porous media to promote chaotic flow dynamics (Lester et al. 2013), which have been more commonly associated

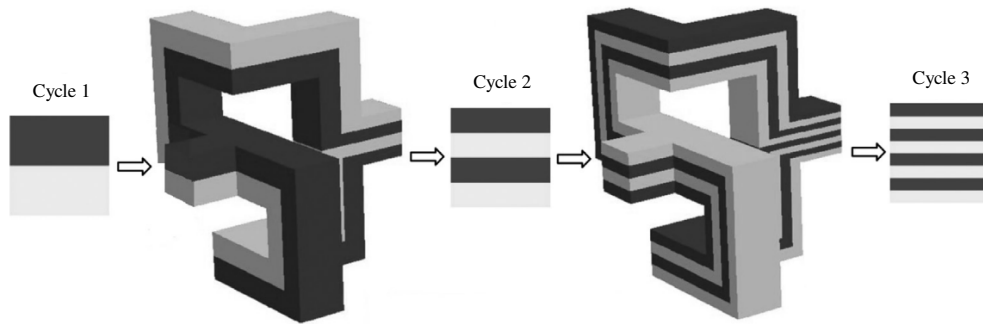


Figure 1.1: Schematic of the repeated occurrence of flow branching and merging resulting from the topological complexity of porous media, i.e., Baker's flow. The increase in the interface between mixing solutions after repeated cycles of branching and merging is depicted.¹

with turbulent flow. Numerical investigations have shed light on the inherent capacity of 3D porous systems to promote the exponential divergence of fluid particles as they are advected through the pore space, which is a main feature of chaotic systems, despite the existence of laminar flow conditions. This trend differs from the algebraic scales of dispersion and mixing usually reported from 2D experimental and numerical investigations (de Anna et al. 2014; Jha et al. 2011; Jiménez-Martínez et al. 2015), and it is associated to the presence of a third degree of freedom in the system (Metcalf et al. 2022). This exponential divergence leads to complex fluid particle trajectories (Aref 1984; Ottino 1989), which translates into enhanced solute plume deformation, leading to the rapid generation of small-scale structures over which diffusive mass transfer occurs more efficiently. As a consequence, mixing is enhanced (Aref 2002). This exponential growth of material lines in porous media arises from the combined effect of two deformation mechanisms, namely, stretching and folding, both hallmarks of chaotic advection. They are induced in porous media by the repeated branching and merging of material lines taking place along pore throats in the vicinity of solid boundaries, i.e., baker's flow (Carrière 2007; Lester et al. 2013). This is better shown in Figure 1.1, where the increase in the interface length between both mixing solutions after repeated cycles of branching and merging is depicted. This larger mixing interface in time, together with an increase in the concentration gradients sustained along this boundary, ultimately renders mixing more efficient.

¹ Reprinted and adapted from Lester et al. (2016) with permission from Elsevier, and from Carrière (2007) with permission from AIP Publishing.

Some of the Darcy-scale studies discussed in Section 1.2.1, which investigated the physical mechanisms behind solute plume deformation, have already reported some signs of chaotic advection. The experimental investigation of Yu et al. (2015) reported the occurrence of twisted streamlines linked to helical flow, which resulted in increased lateral mass exchange. This has been backed up by numerical investigations, where stretching and folding have been quantified and associated with mixing enhancement (Chiogna et al. 2015; Chiogna et al. 2016; Cirpka et al. 2015). Twisting leads to braiding between neighbouring streamlines, which reflects characteristics of the flow topology (Thiffeault and Finn 2006) and constitutes an essential mechanism for the occurrence of exponential deformation of material lines and ultimately of chaos (Boyland et al. 2000; Metcalfe et al. 2022). **However, these studies have not presented a direct assessment of chaos through the quantification of either the deformation of material lines and/or the divergence of neighbouring streamlines.** Advances in such quantification in porous media have been reported mostly from pore-scale studies. Experimental studies are very scarce and have only been reported recently (Heyman et al. 2021; Heyman et al. 2020) after successful application of high-resolution laser imaging via high-precision refractive index matching on a porous media composed of transparent borosilicate glass spheres. It allowed observing the movement of a fluorescent dye injected punctually under low-diffusivity conditions, enabling the reconstruction of the lateral deformation of the plume over distance. Results exposed the exponential scaling of the solute deformation due to strong stretching and folding, and values for the Lyapunov exponent, λ , characterizing this deformation, were reported. This index measures the rate of exponential divergence of neighbouring parcels of fluid, being a proxy for the growth of a material line with time (Ottino 1990). Hence, it informs on the strength of chaos in the system (Lester et al. 2016). It is expressed as

$$\lambda = \lim_{t \rightarrow \infty} \frac{1}{t} \ln \frac{\ell(t)}{\ell_0}, \quad (1.3)$$

where $\ell(t)$ is the size of the material line at any given time, t , expressed as a relative deformation compared to the initial length ℓ_0 . Most of the current understanding of the physical mechanisms behind chaotic advection and chaotic mixing in porous media comes from numerical and analytical investigations. They have pointed out the dominant role of the topological complexity intrinsic to these systems in controlling the repeated separation and reattachment of fluid at the contact with solid interfaces (Lester et al. 2014; Lester et al. 2016). In particular, the formation of stagnation points in the skin friction field on

these solid boundaries gives place to the development of stable and unstable manifolds, both of which are responsible for the strong deformation imposed on the fluid further downstream in the form of intense stretching and folding (Lester et al. 2014; Lester et al. 2016). **Nevertheless, these studies have been exclusively performed under fully saturated conditions and in very simplified porous systems. An investigation on the strength of chaotic advection and chaotic mixing in more heterogeneous systems and on the impact of the saturation degree on these chaotic dynamics through direct quantification of the rate of solute deformation has not been reported yet.** Such an investigation would widen our knowledge on the enhanced solute mixing and solute transport in systems of high environmental relevance, such as the unsaturated region of soils. In addition, they could support ongoing research at the large scale that aims at exploiting the advantages of chaotic mixing for subsurface processes, such as groundwater remediation (Cho et al. 2019; Mays and Neupauer 2012; Neupauer et al. 2014) and biodegradation (Bagtzoglou and Oates 2007).

1.4 THESIS OBJECTIVE AND RESEARCH QUESTIONS

The overarching goal of this doctoral thesis is to gain a deep understanding of the control of the saturation degree on the processes of fluid flow and solute transport in porous media, and on the physical mechanisms controlling this dependency. We aim to apply these findings both in the prediction of fluid flow, solute dispersion, and mixing through the characterization of processes such as solute plume deformation and chaotic advection and chaotic mixing under unsaturated conditions. Considering the different knowledge gaps identified in the previous sections, we propose the following research questions, addressed during the development of this doctoral thesis:

1. What is the control of liquid phase saturation on the processes of fluid flow and solute dispersion in porous media? and what mechanisms contribute to their prediction?
2. How does the saturation degree impact the process of solute plume deformation and solute mixing in porous media? and what are the physical mechanisms behind this response?
3. How does saturation influence the occurrence of chaotic advection and chaotic mixing in porous media? and how does this relate to the observed solute plume deformation?

We address these research questions with a combination of experimental, numerical, and analytical work. This is summarized in three publications, which constitute the core of this document. The document is organized as follows:

- *Chapter 1* presents a summary of the state-of-the-art in the study of flow and transport processes in porous media, and it also summarizes the main goal and research questions of this thesis. It highlights the main contributions in the field from a multi-scale perspective, both on fully saturated and unsaturated porous media, and it aims at revealing the main knowledge gaps in the field, and for unsaturated conditions in particular.
- *Chapter 2* deals with the study of the impact of liquid phase saturation on fluid flow and dispersion in porous media, addressing Research Question No. 1. It is based on a 2.5D numerical and analytical investigation, rooted in previous millifluidic experiments (Jiménez-Martínez et al. 2017), that allowed identifying the impact of an additional immiscible (gas) phase in the pore space, i.e., air bubbles, on flow reorganization and solute dispersion. The former is observed in the formation and enhancement of the double-flow structure (Holzner et al. 2015) upon a reduction in the saturation degree of the system, that is, the formation of backbones of high flow velocity and larger dead-end regions of low flow velocity. This chapter exposes the dominant role of the physical heterogeneity added by the immiscible phase, and in particular by the size distribution of the dead-end regions, in shaping the dispersion dynamics of the transported solute. Based on these findings, we propose an analytical model for the prediction of the flow redistribution, i.e., probability density functions (PDF) of flow rate and velocity, as a function of the saturation degree. We combine this analytical formulation with a Continuous Time Random Walk model to extend its applicability for the prediction of the anomalous dispersion scalings observed from numerical particle tracking simulations. This work provides an important contribution to the fluid flow and solute transport prediction from morphological and structural properties of the pore space, addressing also the physical mechanisms involved in such interplay. This work has been published as Velásquez-Parra, A., T. Aquino, M. Willmann, Y. Méheust, T. Le Borgne, and J. Jiménez-Martínez. (2022). "Sharp transition to strongly anomalous transport in unsaturated porous media." In: *Geophysical Research Letters* 49, e2021GL096280.
- *Chapter 3* addresses Research Question No. 2 by means of an extensive experimental and numerical investigation of the process of mixing in un-

saturated porous media. This study relies on previous 4D synchrotron X-ray micro-tomography experiments performed at the beamline for Tomographic Microscopy and Coherent Radiology Experiments (TOMCAT) at the Paul-Scherrer Institute in Villigen, Switzerland. They allowed the real-time observation of the spreading and mixing of an injected solute in a porous medium resembling a sandy soil at unprecedented spatial and temporal resolutions for such an investigation. Both the impact of the sample's saturation degree and of the solute's injection flow rate were tested during the experimental campaign. In this chapter, I present the results of an intensive image-analysis protocol to post-process the experimental data, supported by additional numerical simulations of flow built up on geometries reconstructed from the samples tested and imaged experimentally. This allowed both the reconstruction of the experimental concentration fields and of the solute front deformation, i.e., the interface where mixing between the injected and the resident solution takes place, and the numerical generation of the corresponding flow fields, respectively. Results revealed an enhancement of mixing both upon a decrease in saturation and with an increase in the injection flow rate. This was associated with an increase in the solute plume's front deformation. We explain the latter by analyzing the impact of lower liquid phase saturation on connectivity changes in the pore space through the computation of different topological indexes, which describe the morphological heterogeneity of the pore space (Euler characteristic) and the occurrence of secondary flow motions in the system (helicity density). By combining these analyses with vortex-identification criteria (Q -criterion), which help identify shear-dominated and vorticity-dominated flow deformation regions across the pore space, we were able to describe the physical mechanisms explaining the enhanced solute front deformation, and thus, the enhanced mixing efficiency observed and quantified from our experiments. This study provides important insights into the role of pore space heterogeneity, and of its variation upon change in saturation, in driving solute front deformation and mixing under unsaturated conditions. In addition, it exposes the potential of synchrotron-based X-ray micro-tomography for the study of transport in porous media. This investigation has been accepted for publication as Velásquez-Parra, A., F. Marone, R. Kaufmann, M. Griffa, and J. Jiménez-Martínez. (2024). "Phase saturation control in vorticity enhances mixing in porous media". In: *Water Resources Research*.

- *Chapter 4* presents the results from a numerical investigation aimed at both complementing the results summarized in Chapter 3 and addressing Research Question No. 3. It is based on steady-state numerical simulations of flow and transport on the same porous media tested experimentally in Chapter 3. By implementing a punctual injection of a miscible tracer, we focus on the quantification of its rate of transversal deformation and of its rate of mixing as it moves along the main longitudinal direction, to characterize the occurrence of chaotic advection and chaotic mixing in 3D porous systems under unsaturated conditions. These two processes were investigated by simulating conditions of low-diffusivity and also those tested in the reference experiments, respectively, which was achieved by varying the diffusion coefficient of the injected solute. Five different saturation degrees and three different flow rates were considered for each of these two transport scenarios, resulting in a total of thirty fully resolved 3D flow and transport simulations. Results allowed the reconstruction of the mixing interface between the injected solute and the resident solution and the generation of concentration fields for all conditions. These were used for the computation of the growth rate of both the plume deformation and the mixing volume over travel distance, respectively. Results revealed chaotic scalings for both metrics, i.e., exponential growth rates, which were enhanced both upon a decrease in saturation and upon an increase in the injection flow rate, independently of the diffusivity of the mixing solutions for the dimensions of the domain. Results also allowed the computation of the Lyapunov exponent as a function of time for all conditions, providing a direct quantification of chaos. The obtained results are explained relying on the main findings presented in Chapters 2 and 3 on the impact of the system's heterogeneity on solute dispersion and mixing. This study presents for the first time a quantification of the strength of chaos in unsaturated porous media, explaining the impact of the saturation degree and of the imposed flow dynamics on chaotic advection and chaotic mixing. The corresponding publication has been submitted to *Environmental Science and Technology* as Velásquez-Parra, A., F. Marone, M. Griffa, and J. Jiménez-Martínez, J. (2024). "Chaotic transport of solutes in unsaturated porous media".
- *Chapter 5* discusses the main findings presented in previous chapters with the aim of concluding on the overarching goal of the doctoral thesis. It also discusses future research perspectives on the field, using our key findings and the state-of-the-art presented in Chapter 1 as a starting point.

BIBLIOGRAPHY

- Alim, K., S. Parsa, D. A. Weitz, and M. P. Brenner (2017). "Local pore size correlations determine flow distributions in porous media." In: *Physical Review Letters* 119, p. 144501.
- Aquino, T., T. Le Borgne, and J. Heyman (2023). "Fluid-solid reaction in porous media as a chaotic restart process." In: *Physical Review Letters* 130, p. 264001.
- Aref, H. (1984). "Stirring by chaotic advection." In: *Journal of Fluid Mechanics* 143, pp. 1–21.
- Aref, H. (2002). "The development of chaotic advection." In: *Physics of Fluids* 14, pp. 1315–1325.
- Armstrong, R. T., J. E. McClure, M. A. Berrill, M. Rücker, S. Schlüter, and S. Berg (2016). "Beyond Darcy's law: The role of phase topology and ganglion dynamics for two-fluid flow." In: *Physical Review E* 94, p. 043113.
- Aziz, R., V. Joekar-Niasar, and P. Martinez-Ferrer (2018). "Pore-scale insights into transport and mixing in steady-state two-phase flow in porous media." In: *International Journal of Multiphase Flow* 109, pp. 51–62.
- Bagtzoglou, A. C. and P. M. Oates (2007). "Chaotic advection and enhanced groundwater remediation." In: *Journal of Materials in Civil Engineering* 19, pp. 75–83.
- Bakker, M. and K. Hemker (2004). "Analytic solutions for groundwater whirls in box-shaped, layered anisotropic aquifers." In: *Advances in Water Resources* 27, pp. 1075–1086.
- Barbier, E. (2002). "Geothermal energy technology and current status: An overview." In: *Renewable and Sustainable Energy Reviews* 6, pp. 3–65.
- Basilio Hazas, M., F. Ziliotto, M. Rolle, and G. Chiogna (2022). "Linking mixing and flow topology in porous media: An experimental proof." In: *Physical Review E* 105, p. 035105.
- Berkowitz, B., A. Cortis, M. Dentz, and H. Scher (2006). "Modeling non-fickian transport in geological formations as a continuous time random walk." In: *Reviews of Geophysics* 44, RG2003.
- Berkowitz, B., S. E. Silliman, and A. M. Dunn (2004). "Impact of the capillary fringe on local flow, chemical migration, and microbiology." In: *Vadose Zone Journal* 3, pp. 534–548.
- Bijeljic, B. and M. J. Blunt (2007). "Pore-scale modeling of transverse dispersion in porous media." In: *Water Resources Research* 43, W12S11.

- Bijeljic, B., S. Rubin, H. Scher, and B. Berkowitz (2011). "Non-fickian transport in porous media with bimodal structural heterogeneity." In: *Journal of Contaminant Hydrology* 120-121, pp. 213-221.
- Birkholzer, J. and C.-f. Tsang (1997). "Solute channeling in unsaturated heterogeneous porous media." In: *Water Resources Research* 33, pp. 2221-2238.
- Boon, M., B. Bijeljic, and S. Krevor (2017). "Observations of the impact of rock heterogeneity on solute spreading and mixing." In: *Water Resources Research* 53, pp. 4624-4642.
- Bordoloi, A. D., D. Scheidweiler, M. Dentz, M. Bouabdellaoui, M. Abbarchi, and P. de Anna (2022). "Structure induced laminar vortices control anomalous dispersion in porous media." In: *Nature Communications* 13, p. 3820.
- Bouwer, H. (2002). "Artificial recharge of groundwater: hydrogeology and engineering." In: *Hydrogeology Journal* 10, pp. 121-142.
- Boyland, P. L., H. Aref, and M. A. Stremler (2000). "Topological fluid mechanics of stirring." In: *Journal of Fluid Mechanics* 403, pp. 277-304.
- Bromly, M. and C. Hinz (2004). "Non-fickian transport in homogeneous unsaturated repacked sand." In: *Water Resources Research* 40, W07402.
- Brooks, J. R., H. R. Barnard, R. Coulombe, and J. J. McDonnell (2010). "Ecohydrologic separation of water between trees and streams in a Mediterranean climate." In: *Nature Geoscience* 3, pp. 100-104.
- Burauel, P. and F. Baßmann (2005). "Soils as filter and buffer for pesticides — experimental concepts to understand soil functions." In: *Environmental Pollution* 133, pp. 11-16.
- Carrière, P. (2007). "On a three-dimensional implementation of the Baker's transformation." In: *Physics of Fluids* 19, p. 118110.
- Chen, Y., H. Steeb, H. Erfani, N. K. Karadimitriou, M. S. Walczak, M. Ruf, D. Lee, S. An, S. Hasan, T. Connolley, N. T. Vo, and V. Niasar (2021). "Nonuniqueness of hydrodynamic dispersion revealed using fast 4D synchrotron X-ray imaging." In: *Science Advances* 7, eabj0960.
- Chiogna, G., O. A. Cirpka, M. Rolle, and A. Bellin (2015). "Helical flow in three-dimensional nonstationary anisotropic heterogeneous porous media." In: *Water Resources Research* 51, pp. 261-280.
- Chiogna, G., O. A. Cirpka, and P. A. Herrera (2016). "Helical flow and transient solute dilution in porous media." In: *Transport in Porous Media* 111, pp. 591-603.
- Chiogna, G., M. Rolle, A. Bellin, and O. A. Cirpka (2014). "Helicity and flow topology in three-dimensional anisotropic porous media." In: *Advances in Water Resources* 73, pp. 134-143.

- Cho, M. S., F. Solano, N. R. Thomson, M. G. Trefry, D. R. Lester, and G. Metcalfe (2019). "Field trials of chaotic advection to enhance reagent delivery." In: *Groundwater Monitoring and Remediation* 39, pp. 23–39.
- Cirpka, O. A., G. Chiogna, M. Rolle, and A. Bellin (2015). "Transverse mixing in three-dimensional nonstationary anisotropic heterogeneous porous media." In: *Water Resources Research* 51, pp. 241–260.
- Cunningham, A. B., R. R. Sharp, R. Hiebert, and G. James (2003). "Subsurface biofilm barriers for the containment and remediation of contaminated groundwater." In: *Bioremediation Journal* 7, pp. 151–164.
- Dadmohammadi, Y. and A. K. Datta (2022). "Food as porous media: a review of the dynamics of porous properties during processing." In: *Food Reviews International* 38, pp. 953–985.
- Danckwerts, P. V. (1952). "The definition and measurement of some characteristics of mixtures." In: *Applied Scientific Research* 3, pp. 279–196.
- Datta, S. S., H. Chiang, T. S. Ramakrishnan, and D. A. Weitz (2013). "Spatial fluctuations of fluid velocities in flow through a three-dimensional porous medium." In: *Physical Review Letters* 111, p. 064501.
- De Anna, P., J. Jiménez-Martínez, H. Tabuteau, R. Turuban, T. Le Borgne, M. Derrien, and Y. Méheust (2014). "Mixing and reaction kinetics in porous media: An experimental pore scale quantification." In: *Environmental Science and Technology* 48, pp. 508–516.
- De Anna, P., T. Le Borgne, M. Dentz, A. M. Tartakovsky, D. Bolster, and P. Davy (2013). "Flow intermittency, dispersion, and correlated continuous time random walks in porous media." In: *Physical Review Letters* 110, p. 184502.
- De Barros, F. P., M. Dentz, J. Koch, and W. Nowak (2012). "Flow topology and scalar mixing in spatially heterogeneous flow fields." In: *Geophysical Research Letters* 39, p. L08404.
- De Gennes, P. G. (1983). "Hydrodynamic dispersion in unsaturated porous media." In: *Journal of Fluid Mechanics* 136, pp. 189–200.
- Dentz, M., T. Le Borgne, A. Englert, and B. Bijeljic (2011). "Mixing, spreading and reaction in heterogeneous media: a brief review." In: *Journal of Contaminant Hydrology* 120, pp. 1–17.
- Dillon, P. (2005). "Future management of aquifer recharge." In: *Hydrogeology Journal* 13, pp. 313–316.
- Dullien, F. A. L. (1991). *Porous media - Fluid transport and pore structure*. 2nd ed. Academic Press. Chap. 1. Pore Structure, pp. 5–155.
- Geng, X., M. C. Boufadel, K. Lee, and C. An (2020). "Characterization of pore water flow in 3-D heterogeneous permeability fields." In: *Geophysical Research Letters* 47, e2019GL086879.

- Guédon, G. R., F. Inzoli, M. Riva, and A. Guadagnini (2019). "Pore-scale velocities in three-dimensional porous materials with trapped immiscible fluid." In: *Physical Review E* 100, p. 043101.
- Haga, D., Y. Niibori, and T. Chida (1999). "Hydrodynamic dispersion and mass transfer in unsaturated flow." In: *Water Resources Research* 35, pp. 1065–1077.
- Hasan, S., V. Niasar, N. K. Karadimitriou, J. R. Godinho, N. T. Vo, S. An, A. Rabbani, and H. Steeb (2020). "Direct characterization of solute transport in unsaturated porous media using fast X-ray synchrotron microtomography." In: *Proceedings of the National Academy of Sciences of the United States of America* 117, pp. 23443–23449.
- Heyman, J., D. R. Lester, and T. Le Borgne (2021). "Scalar signatures of chaotic mixing in porous media." In: *Physical Review Letters* 126, p. 34505.
- Heyman, J., D. R. Lester, R. Turuban, Y. Méheust, and T. Le Borgne (2020). "Stretching and folding sustain microscale chemical gradients in porous media." In: *Proceedings of the National Academy of Sciences of the United States of America* 117, pp. 13359–13365.
- Holzner, M., V. L. Morales, M. Willmann, and M. Dentz (2015). "Intermittent lagrangian velocities and accelerations in three-dimensional porous medium flow." In: *Physical Review E* 92, p. 013015.
- Hunt, J., A. Wray, and P. Moin (1988). "Eddies, streams, and convergence zones in turbulent flows." In: *Center for Turbulence Research, Proceedings of the Summer Program*, pp. 193–208.
- Jha, B., L. Cueto-Felgueroso, and R. Juanes (2011). "Fluid mixing from viscous fingering." In: *Physical Review Letters* 106, p. 194502.
- Jiménez-Martínez, J., P. de Anna, H. Tabuteau, R. Turuban, T. Le Borgne, and Y. Méheust (2015). "Pore-scale mechanisms for the enhancement of mixing in unsaturated porous media and implications for chemical reactions." In: *Geophysical Research Letters* 42, pp. 5316–5324.
- Jiménez-Martínez, J., T. Le Borgne, H. Tabuteau, and Y. Méheust (2017). "Impact of saturation on dispersion and mixing in porous media: Photobleaching pulse injection experiments and shear-enhanced mixing model." In: *Water Resources Research* 53, pp. 1457–1472.
- Jiménez-Martínez, J., M. L. Porter, J. D. Hyman, J. W. Carey, and H. S. Viswanathan (2016). "Mixing in a three-phase system : Enhanced production of oil-wet reservoirs by CO₂ injection." In: *Geophysical Research Letters* 43, pp. 196–205.
- Kang, P. K., P. de Anna, J. P. Nunes, B. Bijeljic, M. J. Blunt, and R. Juanes (2014). "Pore-scale intermittent velocity structure underpinning anomalous transport through 3-D porous media." In: *Geophysical Research Letters* 41, pp. 6184–6190.

- Khanafer, K. and K. Vafai (2022). "Chapter 1 - Applications of porous media in biological transport modeling." In: *Modeling of Mass Transport Processes in Biological Media*. Ed. by S. Becker, A. V. Kuznetsov, F. de Monte, G. Pontrelli, and D. Zhao. Academic Press, pp. 1–15.
- Kitanidis, K. (1994). "The concept of the dilution index." In: *Water Resources Research* 30, pp. 2011–2026.
- Kurz, D. L., E. Secchi, R. Stocker, and J. Jimenez-Martinez (2023). "Morphogenesis of biofilms in porous media and control on hydrodynamics." In: *Environmental Science and Technology* 57, pp. 5666–5677.
- Lahav, O., M. Kochva, and J. Tarchitzky (2010). "Potential drawbacks associated with agricultural irrigation with treated wastewaters from desalinated water origin and possible remedies." In: *Water Science and Technology* 61, pp. 2451–2460.
- Lasseux, D., F. Valdés-Parada, and B. Wood (2021). "Recent developments in upscaling and characterization of flow and transport in porous media." In: *Advances in Water Resources* 150, p. 103886.
- Le Borgne, T., D. Bolster, M. Dentz, P. de Anna, and A. Tartakovsky (2011). "Effective pore-scale dispersion upscaling with a correlated continuous time random walk approach." In: *Water Resources Research* 47, W12538.
- Le Borgne, T., M. Dentz, and E. Villermaux (2015). "The lamellar description of mixing in porous media." In: *Journal of Fluid Mechanics* 770, pp. 458–498.
- Le Borgne, T., M. Dentz, and E. Villermaux (2013). "Stretching, coalescence, and mixing in porous media." In: *Physical Review Letters* 110, p. 204501.
- Lehoux, A. P., S. Rodts, P. Faure, E. Michel, D. Courtier-Murias, and P. Coussot (2016). "Magnetic resonance imaging measurements evidence weak dispersion in homogeneous porous media." In: *Physical Review E* 94, p. 053107.
- Lester, D. R., G. Metcalfe, and M. G. Trefry (2013). "Is chaotic advection inherent to porous media flow?" In: *Physical Review Letters* 111, p. 174101.
- Lester, D. R., G. Metcalfe, and M. G. Trefry (2014). "Anomalous transport and chaotic advection in homogeneous porous media." In: *Physical Review E* 90, p. 063012.
- Lester, D. R., M. G. Trefry, and G. Metcalfe (2016). "Chaotic advection at the pore scale: Mechanisms, upscaling and implications for macroscopic transport." In: *Advances in Water Resources* 97, pp. 175–192.
- Levy, M. and B. Berkowitz (2003). "Measurement and analysis of non-Fickian dispersion in heterogeneous porous media." In: *Journal of Contaminant Hydrology* 64, pp. 203–226.
- Liu, Y. and P. K. Kitanidis (2012). "Applicability of the Dual-Domain model to nonaggregated porous media." In: *Ground Water* 50, pp. 927–934.

- Markale, I., G. M. Cimmarusti, M. M. Britton, and J. Jiménez-Martínez (2021). "Phase saturation control on mixing-driven reactions in 3D porous media." In: *Environmental Science and Technology* 55, pp. 8742–8752.
- Mays, D. C. and R. M. Neupauer (2012). "Plume spreading in groundwater by stretching and folding." In: *Water Resources Research* 48.
- Metcalfe, G., D. Lester, and M. Trefry (2022). "A primer on the dynamical systems approach to transport in porous media." In: *Transport in Porous Media* 146, pp. 55–84.
- Moffatt, H. K. (1992). "Helicity in laminar and turbulent flow." In: *Annual Review Fluid Mechanics* 24, pp. 281–312.
- Neupauer, R. M., J. D. Meiss, and D. C. Mays (2014). "Chaotic advection and reaction during engineered injection and extraction in heterogeneous porous media." In: *Water Resources Research* 50, pp. 1433–1447.
- Nützmänn, G., S. Maciejewski, and K. Joswig (2002). "Estimation of water saturation dependence of dispersion in unsaturated porous media: experiments and modelling analysis." In: *Advances in Water Resources* 25, pp. 565–576.
- Okubo, A. (1970). "Horizontal dispersion of floatable particles in the vicinity of velocity singularities such as convergences." In: *Deep-Sea Research and Oceanographic Abstracts* 17, pp. 445–454.
- Ottino, J. M. (1989). *The Kinematics of mixing: stretching, chaos, and transport*. Cambridge, England: Cambridge University Press.
- Ottino, J. M. (1990). "Mixing, chaotic advection, and turbulence." In: *Annual Review Fluid Mechanics* 22, pp. 207–254.
- Puyguraud, A., P. Gouze, and M. Dentz (2021). "Pore-scale mixing and the evolution of hydrodynamic dispersion in porous media." In: *Physical Review Letters* 126, p. 164501.
- Raouf, A. and S. M. Hassanizadeh (2013). "Saturation-dependent solute dispersivity in porous media: Pore-scale processes." In: *Water Resources Research* 49, pp. 1943–1951.
- Rockström, J., M. Falkenmark, L. Karlberg, H. Hoff, S. Rost, and D. Gerten (2009). "Future water availability for global food production: The potential of green water for increasing resilience to global change." In: *Water Resources Research* 45, W00A12.
- Rolle, M., C. Eberhardt, G. Chiogna, O. A. Cirpka, and P. Grathwohl (2009). "Enhancement of dilution and transverse reactive mixing in porous media: Experiments and model-based interpretation." In: *Journal of Contaminant Hydrology* 110, pp. 130–142.

- Sebilo, M., B. Mayer, B. Nicolardot, G. Pinay, and A. Mariotti (2013). "Long-term fate of nitrate fertilizer in agricultural soils." In: *Proceedings of the National Academy of Sciences* 110, pp. 18185–18189.
- Silliman, S. E., B. Berkowitz, J. Simunek, and M. T. V. Genuchten (2002). "Fluid flow and solute migration within the capillary fringe." In: *Ground Water* 40, pp. 76–84.
- Song, Y. Q. (2013). "Magnetic resonance of porous media (MRPM): A perspective." In: *Journal of Magnetic Resonance* 229, pp. 12–24.
- Souzy, M., H. Lhuissier, Y. Méheust, T. Le Borgne, and B. Metzger (2020). "Velocity distributions, dispersion and stretching in three-dimensional porous media." In: *Journal of Fluid Mechanics* 891, A16.
- Sposito, G. (2001). "Topological groundwater hydrodynamics." In: *Advances in Water Resources* 24, pp. 793–801.
- Szulczewski, M. L., C. W. MacMinn, H. J. Herzog, and R. Juanes (2012). "Lifetime of carbon capture and storage as a climate-change mitigation technology." In: *Proceedings of the National Academy of Sciences of the United States of America* 109, pp. 5185–5189.
- Thiffeault, J. L. and M. D. Finn (2006). "Topology, braids and mixing in fluids." In: *Philosophical Transactions of the Royal Society A: Mathematical, Physical and Engineering Sciences* 364, pp. 3251–3266.
- Valdés, J. P., L. Kahouadji, and O. K. Matar (2022). "Current advances in liquid–liquid mixing in static mixers: a review." In: *Chemical Engineering Research and Design* 177, pp. 694–731.
- Valdes-Abellan, J., J. Jiménez-Martínez, L. Candela, D. Jacques, C. Kohfahl, and K. Tamoh (2017). "Reactive transport modelling to infer changes in soil hydraulic properties induced by non-conventional water irrigation." In: *Journal of Hydrology* 549, pp. 114–124.
- Van Offenwert, S., V. Cnudde, and T. Bultreys (2019). "Pore-scale visualization and quantification of transient solute transport using fast microcomputed tomography." In: *Water Resources Research* 55, pp. 9279–9291.
- Vanderborght, J. and H. Vereecken (2007). "Review of dispersivities for transport modeling in soils." In: *Vadose Zone Journal* 6, pp. 29–52.
- Weiss, J. (1991). "The dynamics of enstrophy transfer in two-dimensional hydrodynamics." In: *Physica D: Nonlinear Phenomena* 48, pp. 273–294.
- Williams, K., A. Kemna, M. J. Wilkins, and J. Druhan (2009). "Geophysical monitoring of coupled microbial and geochemical processes during stimulated subsurface bioremediation." In: *Environmental Science and Technology* 43, pp. 6717–6723.

- Winograd, I. (1981). "Radioactive waste disposal in thick unsaturated zones." In: *Science* 212, pp. 1457–1464.
- Ye, Y., G. Chiogna, C. Lu, and M. Rolle (2020). "Plume deformation, mixing, and reaction kinetics: An analysis of interacting helical flows in three-dimensional porous media." In: *Physical Review E* 102, p. 013110.
- Yu, Y., G. Chiogna, O. A. Cirpka, P. Grathwohl, and M. Rolle (2015). "Experimental evidence of helical flow in porous media." In: *Physical Review Letters* 115, p. 194502.

SHARP TRANSITION TO ANOMALOUS TRANSPORT IN UNSATURATED POROUS MEDIA

This chapter has been published on January 19 2022 as: Velásquez-Parra, A., T. Aquino, M. Willmann, Y. Méheust, T. Le Borgne, & J. Jiménez-Martínez (2022). “Sharp transition to strongly anomalous transport in unsaturated porous media”. In: *Geophysical Research Letters* 49, e2021GL096280. <http://doi.org/10.1029/2021GL096280>

Key Findings:

- The presence of an immiscible phase in porous media leads to an abrupt shift in the scaling of the liquid phase velocity distribution.
- Dispersion is quasi-Fickian in saturated systems, but becomes quasi-ballistic under even slightly unsaturated conditions.
- We predict flow and advective transport based on phase distribution and porous medium geometry.

Authors’ contribution: *A. Velásquez-Parra:* conceptualization, numerical analysis, theoretical development, data analysis, paper writing; *T. Aquino:* theoretical development, paper writing; *M. Willmann:* conceptualization, numerical analysis, data analysis; *Y. Méheust:* theoretical development, paper writing; *T. Le Borgne:* theoretical development, paper writing; *J. Jiménez-Martínez:* conceptualization, supervision, paper writing.

This is a post-print of the paper, differing from the published version only in terms of layout and formatting. Reprinted with permission from John Wiley & Sons Publications and the American Geophysical Union.

ABSTRACT

The simultaneous presence of liquid and gas in porous media increases flow heterogeneity compared to saturated flows. However, the impact of saturation on flow and transport has so far remained unclear. The presence of gas in the pore space leads to flow reorganisation. We develop a theoretical framework that captures the impact of that reorganization on pore-scale fluid velocities. Preferential flow is distributed spatially through a backbone and flow recirculation occurs in flow dead-ends. We observe, and predict theoretically, that this previously-identified flow structure induces a marked change in the scaling of the velocity probability density function compared to the saturated configuration, and a sharp transition to strongly anomalous transport. We develop a transport model using the continuous time random walk theory that predicts advective transport dynamics for all saturation degrees. Our results provide a new modeling framework linking phase heterogeneity to flow heterogeneity in unsaturated media.

PLAIN LANGUAGE SUMMARY

The unsaturated zone, where water and air coexist in the pore space, extends between the soil surface and the groundwater level. Its pronounced structural heterogeneity induces complex flow patterns, which lead to rich solute transport behaviors. Inputs (precipitation) and outputs (evaporation and deep drainage) induce spatio-temporal variability in water saturation (i.e., fraction of the pore space occupied by water), which impacts flow, transport, and biochemical reactions. It has been observed that water-unsaturated conditions lead to a strong separation of flow in regions of high velocity, where most of the fluid is transported, and regions of low velocity. We identify the spatial distribution and size of the low-velocity regions as key control features on water flow and transport of dissolved chemical species, leading to transport behaviors that differ from those described by classical transport formulations. We use these findings to develop a theoretical framework that allows us to predict flow and advective transport under unsaturated conditions, based on parameters that describe the heterogeneity in phase distribution within the pore space and that are directly linked to the geometry of the system. These results represent a decisive step towards the prediction of fate and transport phenomena from structural properties in unsaturated porous media.

2.1 INTRODUCTION

Unsaturated porous media, where liquid and gas phases coexist, play a central role in a broad range of environmental and industrial applications, including contaminant transport (Lahav et al. 2010; Sebilo et al. 2013), artificial groundwater recharge (Bouwer 2002), underground gas storage (Panfilov 2010), radioactive waste disposal (Winograd 1981), and energy storage (Barbier 2002), among others. Previous studies have shown that under saturated conditions, i.e., for single-phase flow, structural heterogeneity in the solid phase is sufficient to induce anomalous transport (de Anna et al. 2013; Holzner et al. 2015; Kang et al. 2014; Le Borgne et al. 2011; Morales et al. 2017; Moroni et al. 2007; Stoop et al. 2019). This typically translates to early solute arrival and longer tailing at a given control plane, as well as non-Fickian scaling of spatial solute spreading (Berkowitz et al. 2006; Bijeljic et al. 2011), all features that cannot be described using classical transport formulations.

In unsaturated porous media, the presence of several immiscible or partially-miscible fluid phases in the pore space induces complex flow topologies, increasing flow tortuosity and resulting in more extreme high and low velocities (Birkholzer and Tsang 1997; Datta et al. 2013; de Gennes 1983; Jiménez-Martínez et al. 2017; Nützmann et al. 2002; Wildenschild and Jensen 1999). The consequences of this heterogeneity for solute transport properties remain controversial. Both an increase (Aziz et al. 2018; Bromly and Hinz 2004; Haga et al. 1999; Padilla et al. 1999) and a decrease (Birkholzer and Tsang 1997; Vanderborght and Vereecken 2007) of dispersion with decreasing saturation have been reported. However, these studies have resorted to continuum/effective-scale theories, where the use of locally-averaged velocity values does not reflect the complexity of the pore-scale velocity field.

Here, we use images from millifluidic experiments and pore-scale numerical simulations to derive a new theoretical framework linking medium structure parameters and saturation degree (S_w , fraction of the pore volume occupied by the liquid) to the probability density function (PDF) of both flow rate through pore throats and velocities, and to anomalous transport dynamics. We identify a previously-unknown abrupt change in the velocity statistics, which become much broader even for low desaturations. Our theory is built on the partition of the pore space into two contrasting structures, a backbone of preferential flow paths, and dead-end regions of low velocity. While the backbone/dead-end structure is known since the work of de Gennes (1983), dead-ends were simply assumed to have zero velocities, and its direct impact on velocity statistics remained unknown. Our theory elucidates the mechanisms leading to the

observed transition and predicts the change exerted by the presence of dead-ends on the velocity PDF scaling for unsaturated systems, compared to fully saturated conditions. Using a continuous time random walk (CTRW) approach, parameterized according to the theoretical velocity PDFs, we predict a transition from quasi-Fickian to highly anomalous, quasi-ballistic transport in unsaturated systems, in agreement with resolved simulations.

2.2 METHODS

2.2.1 Numerical flow simulations

We employ experimental images of a quasi two-dimensional (2D) porous medium characterizing the arrangement of two immiscible phases (water and air) under different S_w (1.00, 0.83, 0.77, and 0.71) (Jiménez-Martínez et al. 2017) and simulate flow at the pore scale. Experiments were performed for low capillary numbers, hence the air clusters (non-wetting phase) remain immobile (Tang et al. 2019). Under these conditions, variations in the viscosity of the non-wetting phase are not relevant. The dimensions of the system are 132 mm \times 87 mm, and its thickness (vertical gap) $h = 0.5$ mm. The average pore throat width (shortest distance between grains) $a_m = 1.17$ mm, and the mean pore size (meeting point of pore throats) $\lambda = 1.85$ mm, leading to a porosity of 0.71, similar to that reported in other studies addressing 2D systems (Andrade, Jr. et al. 1997; Tallakstad et al. 2009).

We numerically simulate 2D steady-state Stokes flow, in which the flow of water around the solid grains and air bubbles is exclusively controlled by viscous dissipation. The effect of the third dimension on depth-averaged flow is introduced in the Stokes equation through a Darcy-like term (Ferrari et al. 2015) representing the drag force exerted on the liquid by the upper and lower walls in the experimental configuration (Jiménez-Martínez et al. 2017). A constant flow rate of $1.375 \text{ mm}^3\text{s}^{-1}$ for the saturated case and $0.277 \text{ mm}^3\text{s}^{-1}$ for the unsaturated cases is imposed at the inlet (Jiménez-Martínez et al. 2017). Atmospheric pressure is imposed at the outlet. We assign a no-slip boundary condition to solid–liquid interfaces and a slip boundary condition to liquid–gas interfaces, i.e., zero longitudinal stress is imposed along these interfaces rather than a zero velocity (Kazemifar et al. 2016).

2.2.2 Particle tracking simulations

To investigate the consequences of our velocity analysis for advective transport, we also perform advective particle tracking simulations to allow for a numerical quantification of dispersion. We perform a flux-weighted injection of 10^4 particles along the inlet boundary of the porous medium, over an area with a length equal to the medium width in the y -direction and a width equal to the average grain size (i.e., 0.83 mm) along the x -axis. Particle positions are tracked isochronically over fixed time steps Δt (t -Lagrangian sampling). For $S_w = 1.00$, $\Delta t = 0.05 t_a$, where $t_a = \lambda/\bar{v}$ is the advective time over the mean pore size λ at the mean velocity \bar{v} . For the unsaturated cases, Δt ranges between $0.021 t_a$ and $0.029 t_a$. A 100-times finer time discretization is introduced at early times to improve resolution in the ballistic dispersion regime.

2.3 PREDICTION OF UNSATURATED FLOW DISTRIBUTION

2.3.1 Impact of saturation on flow velocities

While the simulated velocity fields exhibit limited variability under saturated conditions (Figure 2.1a), the flow heterogeneity is strongly enhanced in the unsaturated case (Figure 2.1b). The introduction of air induces a partition of the flow field into two flow structures (de Gennes 1983): a backbone of preferential flow paths, and dead-end regions (velocity is non-zero (Jiménez-Martínez et al. 2015; Jiménez-Martínez et al. 2017)) that branch out from the backbone (Figure 2.1c and 2.1d). For the Eulerian velocity PDF $p_E(v)$, this reorganization of flow compared to the saturated case leads to an increase in the probability of low velocities (Figure 2.2a), as they are not only encountered close to the solid–liquid interfaces but also within dead-end regions (Figure 2.1b). This is described by the sharp transition from a plateau for $S_w = 1.00$ to a power-law-like behavior for $S_w < 1.00$. High velocities follow an exponential trend, in agreement with existing literature (Datta et al. 2013), and can be characterized by a saturation-dependent characteristic velocity v_c .

We partition the flow field into backbone and dead-end regions (Figure 2.1c and 2.1d) by selecting a velocity threshold at the transition between the power-law and exponential velocity regimes. Results suggest a more accentuated flow separation with lower saturation, where dead-end regions increase both in size and number as S_w decreases, and where the dead-end area PDF p_A decays as a power-law (Figure 2.3). Note that previous studies in 2D porous media have analyzed air cluster area distributions, rather than fluid dead-end area

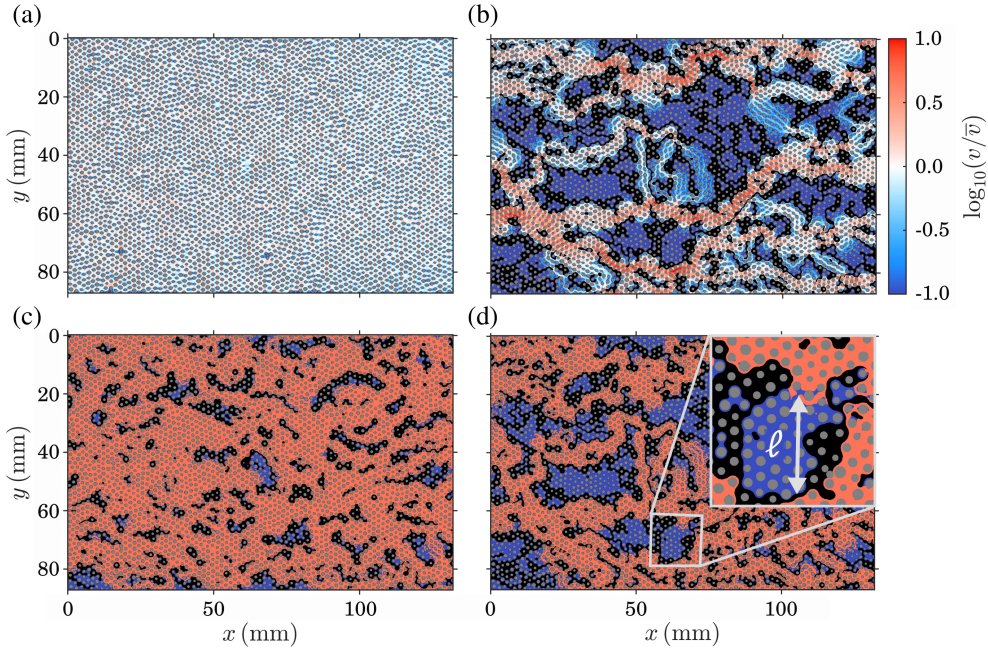


Figure 2.1: Velocity fields obtained from Stokes flow numerical simulations, displayed in terms of the velocity magnitude v normalized by its mean value \bar{v} , for (a) $S_w = 1.00$ and (b) $S_w = 0.71$. The colorbar is common to subfigures (a) and (b), with red colors indicating high velocities and blue colors low velocities. Regions where $\log_{10}(v/\bar{v}) \leq -1$ are shown in the darkest blue tone. The solid phase (circular obstacles) is shown in gray and air clusters in black. Subfigures (c) and (d) show the partition of the velocity field into two types of flow structures: (i) backbone or preferential paths, depicted in red, and (ii) dead-end regions of low velocity, depicted in blue, for $S_w = 0.83$ and $S_w = 0.71$, respectively. The inset in subfigure (d) depicts the geometry of a dead-end region, with ℓ representing the dead-end region's depth.

distributions, and found a power-law behavior with an exponential cutoff at large cluster sizes (Jiménez-Martínez et al. 2017; Tallakstad et al. 2009).

2.3.2 Theoretical flow model

To derive a theoretical framework for $p_E(v)$, we first consider the local flow rate through a pore throat, or pore flow rate q . It is computed by integrating flow velocities over the cross section of the pore throat. For all unsaturated conditions, the PDF of pore flow rates over the ensemble of throats $p_Q(q)$ shows a scaling similar to that of $p_E(v)$ for both low and high magnitudes (Figure 2.2a).

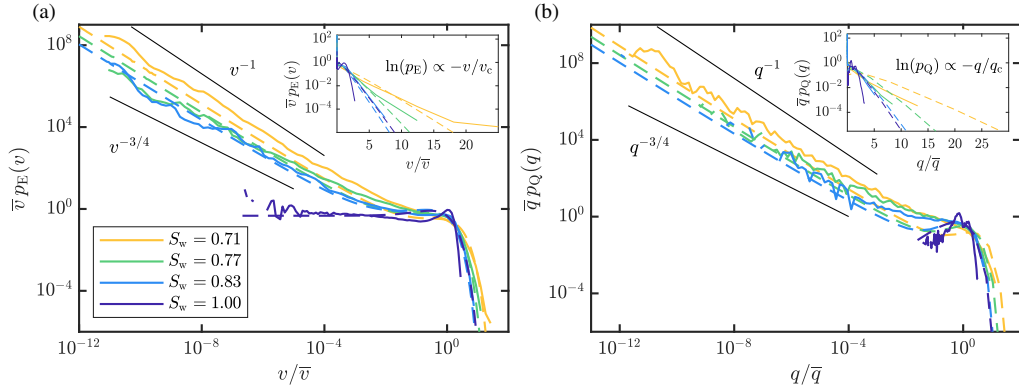


Figure 2.2: Numerical (continuous lines) and predicted (dashed lines) probability density functions (PDF) for (a) Eulerian velocities and (b) pore flow rates, normalized by their respective average values \bar{v} and \bar{q} , for $S_w = 1.00, 0.83, 0.77,$ and 0.71 . The log-log scale highlights the scaling of low magnitudes; the power law scalings are shown for visual reference. Semi-log insets highlight the exponential behavior at high magnitudes.

However, for $S_w = 1.00$, $p_Q(q)$ increases with q at low values instead of the plateau observed for $p_E(v)$. For $S_w = 1.00$, $p_Q(q)$ is well captured by the flow rate PDF in the backbone p_Q^b , which follows a gamma distribution,

$$p_Q^b(q) = \frac{q e^{-q/q_c}}{q_c^2}, \quad (2.1)$$

where the saturation-dependent characteristic flow rate q_c controls the exponential high-flow tailing. This is consistent with the random aggregation model of Alim et al. (2017), based on the random splitting and merging of flow throughout the pore network (Coppersmith 1996).

To model $p_Q(q)$ and $p_E(v)$ for $S_w < 1.00$, we quantify the flow statistics in backbone (p_Q^b) and dead-end (p_Q^d) regions. We first determine the ratio f of the area occupied by dead-end regions to the total area of the pore space (e.g., 0.2601 for $S_w = 0.71$, refer to Figure 2.6 in Appendix 2.A for the remaining S_w). We express $p_Q(q)$ as

$$p_Q(q) = f p_Q^d(q) + (1 - f) p_Q^b(q). \quad (2.2)$$

Next, we determine p_Q^d . Simulation data suggest that flow-rate magnitudes within dead-end regions decay exponentially with depth $0 \leq z \leq \ell$ (see Appendix 2.A, Figure 2.7), up to the total depth ℓ of the dead-end region, which

extends from the contact with the backbone to the far liquid–gas boundary (see inset in Figure 2.1d). Such exponential decay is consistent with the fundamental solutions of the Laplace equation for the propagation within the dead-end of the pressure perturbation applied from the boundary with the backbone (Bland 1965). We expect macroscopic pressure gradients within dead-ends regions to obey a Laplace equation resulting from Darcy’s law (Whitaker 1986). We thus approximate the flow rate decay along the depth as

$$q_d(z|\ell) \approx q_0 e^{-z/a_m} H(\ell - z), \quad (2.3)$$

where $q_0 = q_d(0|\ell)$ is the flow rate at the contact with the backbone and H is the Heaviside step function. Since this flow rate profile is monotonically decreasing, the associated PDF for a given q_0 and ℓ can be computed as (Aquino and Le Borgne 2021)

$$p_Q^d(q|\ell, q_0) = \left(\ell \frac{dq_d(z|\ell)}{dz} \Big|_{z=z_q(q)} \right)^{-1}, \quad (2.4)$$

where $z_q(q)$ is the point at which the flow has a given value q , i.e., $q_d[z_q(q)|\ell] = q$. Thus, inverting Eq. 2.3 for depth as a function of flow rate, computing $dq_d(z|\ell)/dz$, and substituting, Eq. 2.4 becomes

$$p_Q^d(q|\ell, q_0) = \frac{a_m}{\ell q} H(q_0 - q) H(q - q_0 e^{-\ell/a_m}), \quad (2.5)$$

for the dead-end flow-rate PDF $p_Q^d(\cdot|\ell, q_0)$, given maximum depth ℓ and flow rate $q_0 = q_d(0|\ell)$ at the entrance. Taking q_0 to be distributed according to Eq. 2.1 and averaging over the latter, we can now express the flow rate PDF in dead-ends given ℓ as

$$p_Q^d(q|\ell) = \int_0^\infty dq_0 p_Q^d(q|\ell, q_0) p_Q^b(q_0), \quad (2.6)$$

which after computing the integral leads to

$$p_Q^d(q|\ell) = \frac{a_m}{\ell q_c q} \left[e^{-q/q_c} (q + q_c) - \exp\left(-\frac{e^{\ell/a_m} q}{q_c}\right) (e^{\ell/a_m} q + q_c) \right]. \quad (2.7)$$

By approximating $\ell \approx \sqrt{A}$, with A the dead-end area, and averaging over areas, we obtain an expression for the PDF of dead-end flow rates,

$$p_Q^d(q) \approx \int_0^\infty dA p_Q^d(q|\sqrt{A}) p_A(A). \quad (2.8)$$

The PDF p_A of dead-end areas, defined for a given flow field such that $p_A(A) dA$ is the probability of a uniformly randomly chosen dead-end region to have area in an infinitesimal neighborhood dA of A , is shown in Figure 2.3 for each unsaturated flow field. The area PDFs were determined based on the flow field partitions, as shown in Figure 2.1 for $S_w = 0.83$ and $S_w = 0.71$. We approximate p_A by a Pareto PDF,

$$p_A(A) = \frac{\gamma}{a_m^2} \left(\frac{A}{a_m^2} \right)^{-1-\gamma} H(A - a_m^2), \quad (2.9)$$

where the exponent γ decreases with decreasing S_w , indicating broader dead-end area variability. The approximations thus obtained are plotted as dashed lines in Figure 2.3. We consider the minimum area of a dead-end region to be equal to the area of one pore throat, approximated as a_m^2 .

We can now expand the integrand in Eq. 2.8 using Eq. 2.9, obtaining

$$p_Q^d(q) \approx \int_0^\infty dA \frac{a_m}{q_c \sqrt{A}} e^{-q/q_c} p_A(A). \quad (2.10)$$

Computing this integral, and combining it with the expression for $p_Q^b(q)$ (Eq. 2.1) in Eq. 2.2, we deduce an expression for $p_Q(q)$. For $q \ll q_c$, the latter is controlled by the dead-end contribution as long as $f \neq 0$, corresponding to $S_w < 1.00$. Notice also that the nested exponential in Eq. 2.7 varies rapidly from zero to unity around $q = q_c e^{-\ell/a_m}$, so that it is well approximated by a cutoff for $A \approx \ell^2 > [a_m \ln(q_c/q)]^2$. This leads to

$$\begin{aligned} p_Q^d(q) &\approx \int_0^\infty dA \frac{a_m}{q_c \sqrt{A}} \left[1 - H \left(\left[a_m \ln \left(\frac{q_c}{q} \right) \right]^2 - A \right) \right] p_A(A), \\ &\approx \frac{2\gamma}{q(1+2\gamma)} \left[\ln \left(\frac{q_c}{q} \right) \right]^{-1-2\gamma}, \end{aligned} \quad q \ll q_c, \quad (2.11)$$

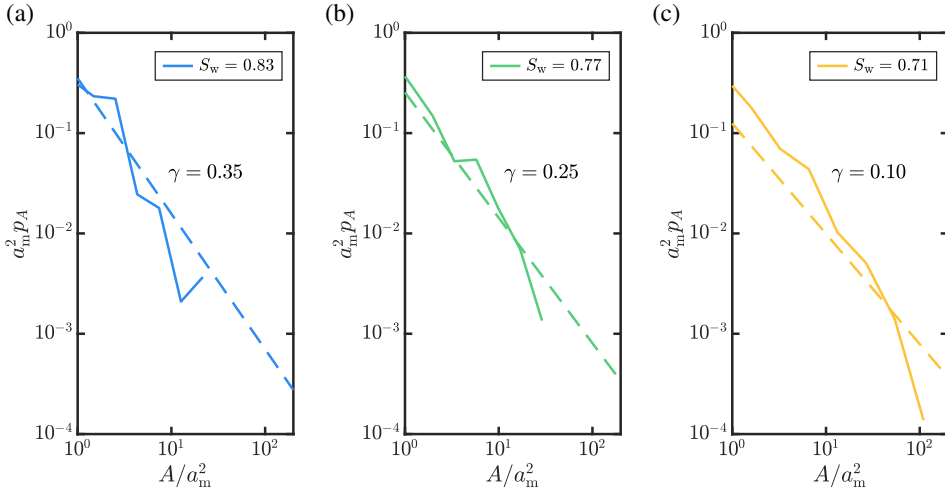


Figure 2.3: PDF of the dead-end areas p_A for (a) $S_w = 0.83$, (b) $S_w = 0.77$, and (c) $S_w = 0.71$. For all three cases, p_A is well approximated by a Pareto PDF (Eq. 2.9) describing power-law decay. Corresponding values of the fitting parameter γ describing a power law decay $\propto A^{-1-\gamma}$, which decreases with decreasing liquid phase saturation, are also shown. Quantities are non-dimensionalized with respect to the area a_m^2 associated with the average pore-throat aperture.

which, combined with Eqs. 2.1 and 2.2, leads to

$$p_Q(q) \approx \frac{2\gamma f}{q(1+2\gamma)} \left[\ln \left(\frac{q_c}{q} \right) \right]^{-1-2\gamma}. \quad (2.12)$$

Thus, our model predicts that for $S_w < 1.00$, $p_Q(q)$ scales for low flow rates as a power law, q^{-1} , corrected by a logarithmic factor, raised to a power controlled by $p_A(A)$ through the exponent γ . In the particular case $f = 0$, i.e., $S_w = 1.00$, Taylor expansion of p_Q^b (Eq. 2.1) for low q leads to $p_Q(q) \approx q/q_c^2$, linear in q . Proceeding similarly for $q \gtrsim q_c$, for which we must consider contributions from both $p_Q^b(q)$ and $p_Q^d(q)$, we obtain the exponential decay

$$p_Q(q) \approx \left[\frac{2\gamma f}{1+2\gamma} + (1-f) \frac{q}{q_c} \right] \frac{e^{-q/q_c}}{q_c}. \quad (2.13)$$

We now turn our attention to $p_E(v)$. It results from the combined effect of $p_Q(q)$ and the intra-throat variability arising from the local velocity profile within each throat. Thus, these two PDFs are related by

$$p_E(v) = \int_0^\infty dq p_Q(q) p_E(v|q), \quad (2.14)$$

where $p_E(\cdot|q)$ is the PDF of velocities associated with a pore throat characterized by q . Since pore throat widths are comparable in size to the channel thickness h , we consider the impact of this third dimension on the intra-pore, depth-averaged 2D velocity profile. The latter differs from the parabolic profile expected in a purely-2D scenario (see Appendix 2.B, Figure 2.8, for a plot of velocity profiles across the system). By approximating the pore throat as a cuboid channel of width a_m and thickness h , we express the velocity profile for Stokes flow over the channel thickness h as a series in the form (Bruus 2008)

$$v_x(y, z) = \frac{4h^2 \Delta p}{\pi^3 \mu L} \sum_{n, \text{odd}} \frac{1}{n^3} \left[1 - \frac{\cosh(n\pi \frac{y}{h})}{\cosh(n\pi \frac{a_m}{2h})} \right] \sin\left(n\pi \frac{z}{h}\right), \quad (2.15)$$

where μ is the viscosity of the liquid (wetting) phase, Δp is the pressure difference across the cuboid channel of length L , and the sum extends over odd values of n as indicated. Here we have set a local coordinate system at each pore throat, with x representing the local mean flow direction, the throat width running parallel to y , and z running along the channel thickness. Averaging this function over z values between 0 and h , we obtain

$$\langle v_x(y, z) \rangle_z = \frac{8h^2 \Delta p}{\pi^4 \mu L} \sum_{n, \text{odd}} \frac{1}{n^4} \left[1 - \frac{\cosh(n\pi \frac{y}{h})}{\cosh(n\pi \frac{a_m}{2h})} \right], \quad (2.16)$$

where $\langle \cdot \rangle$ denotes the mean value. Given the low variability of pore-throat sizes across the medium, we approximate throat widths by their average value a_m . For the dimensions of our porous medium (thickness h and average throat width a_m), this series is governed by its first term, reducing the expression to

$$\langle v_x(y, z) \rangle_z \approx \frac{h^2 \Delta p}{2\pi^4 \mu L} \left[1 - \frac{\cosh(2\pi \frac{y}{h})}{\cosh(\pi \frac{a_m}{h})} \right]. \quad (2.17)$$

The Eulerian velocity PDF associated with the velocity profile across a pore throat with local flow rate q is then (see Appendix 2.B.1, for further details)

$$p_E(v|q) = \frac{2h}{\pi a_m v_{\max}(q)} \frac{(C-1)H[v_{\max}(q) - v]}{\sqrt{[C - (C-1)v/v_{\max}(q)]^2 - 1}}, \quad (2.18)$$

where $C = \cosh[\pi a_m / (2h)]$, and $v_{\max}(q) = \alpha q / (h a_m)$ is the maximum velocity within the pore throat, with

$$\alpha = 2 \left(1 + \coth \left(\frac{\pi a_m}{4h} \right) \left[\coth \left(\frac{\pi a_m}{4h} \right) - \frac{4h}{\pi a_m} \right] \right)^{-1}. \quad (2.19)$$

For $S_w = 1.00$, the integral in Eq. 2.14 can then be approximated for $v \ll v_c$ and $v \gtrsim v_c = q_c / (a_m h)$, respectively, by using Eq. 2.1, as

$$p_E(v) \approx \frac{2h}{\pi a_m \alpha v_c} \tanh \left(\frac{\pi a_m}{4h} \right), \quad (2.20a)$$

$$p_E(v) \approx \frac{2h}{\alpha a_m v_c} \sinh \left(\frac{\pi a_m}{4h} \right) \sqrt{\frac{v}{\pi \alpha v_c}} e^{-\frac{v}{\alpha v_c}}. \quad (2.20b)$$

Equation 2.20a describes a low-velocity plateau, while Eq. 2.20b encodes exponential tailing at large velocities.

For $S_w < 1.00$, the previous derivation holds for the backbone component. Similar to $p_Q(q)$, $p_E(v)$ for $v \ll v_c$ is dominated by the dead-end regions, while for $v \gtrsim v_c$ the contribution of both backbone and dead-ends matters. The low-velocity behavior is controlled by low flow rates. For small q , $p_E(v|q)$ becomes arbitrarily narrow, because the maximum velocity is linear in q , see Eq. 2.18. Accordingly, $p_E(v)$ is well approximated for low v by setting $p_E(v|q) \approx \delta[v - q / (h a_m)]$ in Eq. 2.14, where $\delta(\cdot)$ is the Dirac delta, and by using Eq. 2.12 for $p_Q(q)$. We obtain, for $v \ll v_c$,

$$p_E(v) \approx \frac{2\gamma f}{v(1+2\gamma)} \left[\ln \left(\frac{v_c}{v} \right) \right]^{-1-2\gamma}. \quad (2.21)$$

Analogously, for $v \gtrsim v_c$, $p_E(v)$ can be computed using Eq. 2.13 for $p_Q(q)$, and Taylor expanding Eq. 2.18 for $v \approx v_{\max}(q)$, which leads to

$$p_E(v) \approx \left[\frac{2\gamma f}{1+2\gamma} \sqrt{\frac{\alpha v_c}{v}} + (1-f) \sqrt{\frac{v}{\alpha v_c}} \right] \frac{C_* e^{-\frac{v}{\alpha v_c}}}{\alpha v_c}, \quad (2.22)$$

where $C_* = 2h \sinh(\pi a_m / 4h) / (\sqrt{\pi} a_m)$. Note that for large h values compared to a_m , Eqs. 2.20a–2.22 reduce to expressions that correspond to those obtained under the assumption of a Poiseuille velocity profile (fully-2D case) (see Appendix 2.B.2, for a complete mathematical deduction).

Figure 2.2 shows the predictions (dashed lines) for both $p_Q(q)$ and $p_E(v)$. The model successfully captures the different regimes and scaling variation for the various S_w . The low-velocity plateau for $S_w = 1.00$ is also captured. The results shown here correspond to numerical computation of the full theoretical PDFs according to Eqs. 2.1, 2.2, 2.8, and 2.14. Further details on the regime scalings and parameter values can be found in Appendix 2.B, Figure 2.9.

2.4 PREDICTION OF ADVECTIVE TRANSPORT

Using the results of the particle tracking simulations (see Section 2.2.2), we compute (advective) dispersion $\sigma_x^2(t)$, as a function of time t , as the variance of longitudinal particle positions. Lower saturation induces larger particle dispersion due to the increased velocity heterogeneity, as discussed above. At early times, a ballistic regime, $\sigma_x^2 \sim t^2$ is observed in Figure 2.4 for all S_w , which then transitions to an asymptotic superdiffusive regime. The crossover time between the ballistic and asymptotic regimes is also larger for smaller S_w , i.e., the Lagrangian correlation length ζ_x of velocities along the mean flow direction increases with decreasing saturation (refer to Appendix 2.C, Figure 2.10, for correlation plots).

To develop a transport modeling framework that links the dispersion dynamics to hydrodynamics, we employ a CTRW approach (Berkowitz et al. 2006; Cortis and Berkowitz 2004; Dentz et al. 2016). The CTRW framework used here models transport in terms of Lagrangian particles taking fixed spatial steps of length ζ_x along the mean flow direction (s -Lagrangian sampling). Particle velocities remain constant over a step and are assumed to fully decorrelate between steps. They are sampled independently in each step from the s -Lagrangian velocity distribution, which is given by the flux-weighted $p_E(v)$, $p_s(v) = v p_E(v) / \bar{v}$ (Dentz et al. 2016). This approach captures the intermittent nature of the t -Lagrangian velocity signal through the distributed waiting times to cross the fixed distance ζ_x .

To assess the applicability of our theoretical model to predict advective transport, we employ $p_s(v)$ defined from the predicted $p_E(v)$ (dashed lines in Figure 2.2a) in the CTRW description. Figure 2.4 shows σ_x^2 computed from the resulting CTRW for each S_w (dashed lines), together with σ_x^2 computed from the particle tracking simulations. Dispersion is well predicted over both the ballistic

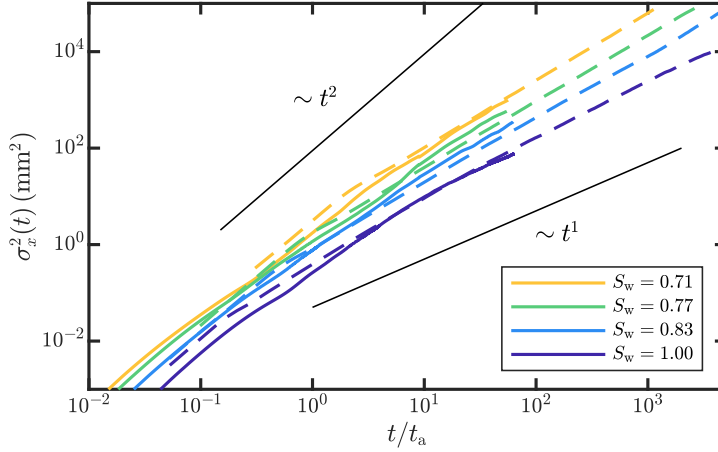


Figure 2.4: Advective dispersion σ_x^2 in time for $S_w = 1.00, 0.83, 0.77,$ and 0.71 . Time is normalized by the advective time $t_a = \lambda/\bar{v}$ over the mean pore size λ . The plot compares σ_x^2 from the particle tracking analysis (continuous lines) with σ_x^2 from a CTRW approach computed using the predicted velocity PDF $p_E(v)$ (dashed lines). Scalings for a ballistic ($\sigma_x^2 \sim t^2$) and a Fickian ($\sigma_x^2 \sim t^1$) regime are also displayed for reference.

and superdiffusive regimes, and so the impact of S_w on the temporal scaling. A slight overestimation of early-time dispersion is visible for $S_w = 1.00$, which might be explained by the assumption of full velocity decorrelation beyond ζ_x . Late-time dispersion is well captured in all cases, exhibiting more pronounced superdiffusive behavior for $S_w < 1.00$. Overall, these results support the suitability of both our theoretical description of velocity statistics and the CTRW to predict advective transport in unsaturated porous media, representing a major step towards predicting solute transport in such systems from the sole knowledge of the medium's geometry.

The CTRW model presented here provides a theoretical framework to quantify the relationship between dispersive scalings and velocity variability. In particular, the late-time scaling is controlled by the low-velocity behavior of $p_E(v)$. If $p_E(v)$ exhibits power-law decay near $v = 0$, $p_E(v) \sim v^{-\theta}$ with $0 < \theta < 1$, late-time dispersion scales like $\sigma_x^2 \sim t^{1+\theta}$ (Dentz et al. 2016), between the Fickian and ballistic limits $\sigma_x^2 \sim t$ and $\sigma_x^2 \sim t^2$. The scalings found here for saturated and unsaturated conditions correspond to two contrasting edge-cases. Under saturated conditions, $\theta = 0$ (Eq. 2.20a), which leads to logarithmically-enhanced Fickian dispersion (Dentz et al. 2016). Note that pure power-law decay characterized by $\theta \geq 1$ is not integrable near $v = 0$. In this sense, unsaturated

conditions are characterized by maximal variability of low velocities, described by logarithmic corrections to power-law decay with $\theta = 1$ (Eq. 2.21). This leads to logarithmically-inhibited ballistic dispersion. In light of these considerations, along with the fact that the unsaturated $p_E(v)$ is broader than for the saturated case (Figure 2.2), the apparent power-law scalings in Figure 2.4 vary slowly with time, as logarithmic corrections and the effect of progressively lower velocities come into play. A rigorous derivation of asymptotic dispersion scalings is beyond the scope of this work and will be presented elsewhere.

2.5 CONCLUSIONS AND OUTLOOK

Here we have presented a new theoretical framework for the prediction of pore-scale flow PDFs and advective transport capturing the impact of liquid-phase saturation. Results reveal that the introduction of an immiscible gas phase leads to a shift in the scaling of the velocity PDFs that induces a sharp transition to strongly anomalous transport. Under saturated conditions, dispersion is quasi-Fickian. In contrast, even under slightly unsaturated conditions, dispersion becomes quasi-ballistic. In practice, this superdiffusive dispersion behavior is sustained until low-velocity cutoffs introduced by additional processes, such as diffusion, become relevant. The long-term residence time of a particle in a dead-end region is eventually controlled by molecular diffusion, effectively cutting off extreme slow velocities (de Gennes 1983). While in the presence of diffusion the transport is thus always asymptotically Fickian at sufficiently late times, the dispersive scalings related to the velocity variability remain relevant over significant time scales. Our CTRW formulation also opens the door to the quantification of nontrivial scalings of dispersion (Aquino and Le Borgne 2021; Bijeljic and Blunt 2006).

The theoretical formulation developed here successfully predicts flow and velocity PDFs based only on a small set of parameters, which reflect characteristics of the porous medium (average pore throat width a_m and thickness h), the relative occupancy of backbone and dead-ends in the system (power-law tailing exponent γ and ratio of dead-end area to total pore-space area f), and flow properties (correlation length of longitudinal velocities ζ_x and tortuosity χ , along with the characteristic flow rate q_c , used to determine the characteristic velocity $v_c = q_c/(ha_m)$). While the values of these parameters depend on properties such as porosity and liquid phase saturation, we expect the uncovered transition in the velocity PDF and its impact on transport scaling properties to be robust.

We expect the power-law dead-end area distribution to hold for (quasi-)2D systems, independently of the detailed pore geometry. In particular, it holds for

fully 2D systems, and so does the spatial distribution of pore flow rates in dead-end regions (Eq. 2.3), providing good predictions for $h/a_m \gg 1$. In addition, we also expect it to persist in 3D systems, as is known to happen for both wetting and non-wetting phase cluster size distributions (Iglauer et al. 2012; Iglauer et al. 2010; Scheffer et al. 2021). These authors also report this behavior for wetting phase saturation degrees lower than 0.71, which we could not achieve in the present study, as they would approach the percolation threshold for the experimental medium. However, following previous works that report a decrease in dispersivity once the system is desaturated below the so-called critical saturation (Raouf and Hassanizadeh 2013), we hypothesize a decrease in the broadness of the velocity distribution through an increase in the dead-end area-PDF exponent γ for saturation degrees below that critical saturation. In addition, although the present study considers a high porosity (0.71), the distribution of non-wetting-phase cluster sizes still exhibits power-law behavior for porosity values as low as 0.11 (Iglauer et al. 2012; Iglauer et al. 2010; Scheffer et al. 2021). The effect of broader pore size variability (de Anna et al. 2017) under unsaturated conditions remains an important open question. Note, however, that even if a different functional dependency were observed for the dead-end area PDF, our new theoretical framework provides the means to quantify its impact on flow velocity distributions and transport. Furthermore, the upscaling of flow and transport presented here is a first step towards theoretical assessment of mixing and chemical reactions in unsaturated porous media, which are essential processes for the analysis and optimization of environmental and industrial systems.

BIBLIOGRAPHY

- Alim, K., S. Parsa, D. A. Weitz, and M. P. Brenner (2017). "Local pore size correlations determine flow distributions in porous media." In: *Physical Review Letters* 119, p. 144501.
- Andrade, Jr., J. S., M. P. Almeida, J. Mendes Filho, S. Havlin, B. Suki, and H. E. Stanley (1997). "Fluid flow through porous media: The role of stagnant zones." In: *Physical Review Letters* 79, pp. 3901–3904.
- Aquino, T. and T. Le Borgne (2021). "The diffusing-velocity random walk: a spatial-Markov formulation of heterogeneous advection and diffusion." In: *Journal of Fluid Mechanics* 910, A12.
- Aziz, R., V. Joekar-Niasar, and P. Martinez-Ferrer (2018). "Pore-scale insights into transport and mixing in steady-state two-phase flow in porous media." In: *International Journal of Multiphase Flow* 109, pp. 51–62.
- Barbier, E. (2002). "Geothermal energy technology and current status: An overview." In: *Renewable and Sustainable Energy Reviews* 6, pp. 3–65.
- Berkowitz, B., A. Cortis, M. Dentz, and H. Scher (2006). "Modeling non-fickian transport in geological formations as a continuous time random walk." In: *Reviews of Geophysics* 44, RG2003.
- Bijeljic, B. and M. J. Blunt (2006). "Pore-scale modeling and continuous time random walk analysis of dispersion in porous media." In: *Water Resources Research* 42, W01202.
- Bijeljic, B., S. Rubin, H. Scher, and B. Berkowitz (2011). "Non-fickian transport in porous media with bimodal structural heterogeneity." In: *Journal of Contaminant Hydrology* 120-121, pp. 213–221.
- Birkholzer, J. and C.-f. Tsang (1997). "Solute channeling in unsaturated heterogeneous porous media." In: *Water Resources Research* 33, pp. 2221–2238.
- Bland, D. R. (1965). *Solutions of Laplace's Equation*. Plymouth: Routledge.
- Bouwer, H. (2002). "Artificial recharge of groundwater: hydrogeology and engineering." In: *Hydrogeology Journal* 10, pp. 121–142.
- Bromly, M. and C. Hinz (2004). "Non-fickian transport in homogeneous unsaturated repacked sand." In: *Water Resources Research* 40, W07402.
- Bruus, H. (2008). *Theoretical Microfluidics - Oxford Master series in condenser matter physics*. Oxford University Press, pp. 48–51.

- Coppersmith, D. (1996). *Advances in Cryptology - EUROCRYPT '96, Lecture Notes in Computer Science*. Vol. 1070. Springer, Berlin. Chap. Small Root of a Univariate Modular Equation, pp. 155–165.
- Cortis, A. and B. Berkowitz (2004). “Anomalous transport in “classical” soil and sand columns.” In: *Soil Science Society of America Journal* 68, pp. 1539–1548.
- Datta, S. S., H. Chiang, T. S. Ramakrishnan, and D. A. Weitz (2013). “Spatial fluctuations of fluid velocities in flow through a three-dimensional porous medium.” In: *Physical Review Letters* 111, p. 064501.
- De Anna, P., T. Le Borgne, M. Dentz, A. M. Tartakovsky, D. Bolster, and P. Davy (2013). “Flow intermittency, dispersion, and correlated continuous time random walks in porous media.” In: *Physical Review Letters* 110, p. 184502.
- De Anna, P., B. Quaife, G. Biros, and R. Juanes (2017). “Prediction of the low-velocity distribution from the pore structure in simple porous media.” In: *Physical Review Fluids* 2, p. 124103.
- De Gennes, P. G. (1983). “Hydrodynamic dispersion in unsaturated porous media.” In: *Journal of Fluid Mechanics* 136, pp. 189–200.
- Dentz, M., P. K. Kang, A. Comolli, T. Le Borgne, and D. R. Lester (2016). “Continuous time random walks for the evolution of Lagrangian velocities.” In: *Physical Review Fluids* 1, p. 074004.
- Ferrari, A., J. Jiménez-Martínez, T. Le Borgne, Y. Meheust, and I. Lunati (2015). “Challenges in modeling unstable two-phase flow experiments in porous micromodels.” In: *Water Resources Research* 51, pp. 1381–1400.
- Haga, D., Y. Niibori, and T. Chida (1999). “Hydrodynamic dispersion and mass transfer in unsaturated flow.” In: *Water Resources Research* 35, pp. 1065–1077.
- Holzner, M., V. L. Morales, M. Willmann, and M. Dentz (2015). “Intermittent lagrangian velocities and accelerations in three-dimensional porous medium flow.” In: *Physical Review E* 92, p. 013015.
- Iglauer, S., M. A. Fernø, P. Shearing, and M. J. Blunt (2012). “Comparison of residual oil cluster size distribution, morphology and saturation in oil-wet and water-wet sandstone.” In: *Journal of Colloid and Interface Science* 375, pp. 187–192.
- Iglauer, S., S. Favretto, G. Spinelli, G. Schena, and M. J. Blunt (2010). “X-ray tomography measurements of power-law cluster size distributions for the nonwetting phase in sandstones.” In: *Physical Review E* 82, p. 056315.
- Jiménez-Martínez, J., P. de Anna, H. Tabuteau, R. Turuban, T. Le Borgne, and Y. Méheust (2015). “Pore-scale mechanisms for the enhancement of mixing in unsaturated porous media and implications for chemical reactions.” In: *Geophysical Research Letters* 42, pp. 5316–5324.

- Jiménez-Martínez, J., T. Le Borgne, H. Tabuteau, and Y. Méheust (2017). "Impact of saturation on dispersion and mixing in porous media: Photobleaching pulse injection experiments and shear-enhanced mixing model." In: *Water Resources Research* 53, pp. 1457–1472.
- Kang, P. K., P. de Anna, J. P. Nunes, B. Bijeljic, M. J. Blunt, and R. Juanes (2014). "Pore-scale intermittent velocity structure underpinning anomalous transport through 3-D porous media." In: *Geophysical Research Letters* 41, pp. 6184–6190.
- Kazemifar, F., G. Blois, D. C. Kyritsis, and K. T. Christensen (2016). "Quantifying the flow dynamics of supercritical CO₂–water displacement in a 2D porous micromodel using fluorescent microscopy and microscopic PIV." In: *Advances in Water Resources* 95, pp. 352–368.
- Lahav, O., M. Kochva, and J. Tarchitzky (2010). "Potential drawbacks associated with agricultural irrigation with treated wastewaters from desalinated water origin and possible remedies." In: *Water Science and Technology* 61, pp. 2451–2460.
- Le Borgne, T., D. Bolster, M. Dentz, P. de Anna, and A. Tartakovsky (2011). "Effective pore-scale dispersion upscaling with a correlated continuous time random walk approach." In: *Water Resources Research* 47, W12538.
- Morales, V. L., M. Dentz, M. Willmann, and M. Holzner (2017). "Stochastic dynamics of intermittent pore-scale particle motion in three-dimensional porous media: Experiments and theory." In: *Geophysical Research Letters* 44, pp. 9361–9371.
- Moroni, M., N. Kleinfelter, and J. H. Cushman (2007). "Analysis of dispersion in porous media via matched-index particle tracking velocimetry experiments." In: *Advances in Water Resources* 30, pp. 1–15.
- Nützmann, G., S. Maciejewski, and K. Joswig (2002). "Estimation of water saturation dependence of dispersion in unsaturated porous media: experiments and modelling analysis." In: *Advances in Water Resources* 25, pp. 565–576.
- Padilla, I. Y., T.-C. J. Yah, and M. H. Conklin (1999). "The effect of water content on solute transport in unsaturated porous media." In: *Water Resources Research* 35, pp. 3303–3313.
- Panfilov, M. (2010). "Underground storage of hydrogen: In situ self-organisation and methane generation." In: *Transport in Porous Media* 85, pp. 841–865.
- Raouf, A. and S. M. Hassanizadeh (2013). "Saturation-dependent solute dispersivity in porous media: Pore-scale processes." In: *Water Resources Research* 49, pp. 1943–1951.
- Scheffer, K., Y. Méheust, M. S. Carvalho, M. H. Mauricio, and S. Paciornik (2021). "Enhancement of oil recovery by emulsion injection: A pore scale analysis from

- X-ray micro-tomography measurements." In: *Journal of Petroleum Science and Engineering* 198, p. 108134.
- Sebilo, M., B. Mayer, B. Nicolardot, G. Pinay, and A. Mariotti (2013). "Long-term fate of nitrate fertilizer in agricultural soils." In: *Proceedings of the National Academy of Sciences* 110, pp. 18185–18189.
- Stoop, N., N. Waisbord, V. Kantsler, V. Heinonen, J. S. Guasto, and J. Dunkel (2019). "Disorder-induced topological transition in porous media flow networks." In: *Journal of Non-Newtonian Fluid Mechanics* 268, pp. 66–74.
- Tallakstad, K. T., G. Løvoll, H. A. Knudsen, T. Ramstad, E. G. Flekkøy, and K. J. Måløy (2009). "Steady-state, simultaneous two-phase flow in porous media: An experimental study." In: *Physical Review E* 80, p. 036308.
- Tang, J., M. Smit, S. Vincent-Bonnieu, and W. R. Rossen (2019). "New capillary number definition for micromodels: The impact of pore microstructure." In: *Water Resources Research* 55, pp. 1167–1178.
- Vanderborght, J. and H. Vereecken (2007). "Review of dispersivities for transport modeling in soils." In: *Vadose Zone Journal* 6, pp. 29–52.
- Whitaker, S. (1986). "Flow in porous media I: A theoretical derivation of Darcy's law." In: *Transport in Porous Media* 1, pp. 3–25.
- Wildenschild, D. and K. H. Jensen (1999). "Laboratory investigations of effective flow behavior in unsaturated heterogeneous sands." In: *Water Resources Research* 35, pp. 17–27.
- Winograd, I. (1981). "Radioactive waste disposal in thick unsaturated zones." In: *Science* 212, pp. 1457–1464.

SUPPLEMENTARY MATERIAL TO CHAPTER 2

This appendix has been published as Supplementary Material to: Velásquez-Parra, A., T. Aquino, M. Willmann, Y. Méheust, T. Le Borgne, & J. Jiménez-Martínez (2022). "Sharp transition to strongly anomalous transport in unsaturated porous media". In: *Geophysical Research Letters* 49, e2021GL096280. <http://doi.org/10.1029/2021GL096280>.

In this Supplementary Material, we present additional details and derivations regarding the results reported in Chapter 2. It is organized in three Appendixes. Appendix 2.A concerns additional results on the numerical velocity analysis for all analyzed saturation degrees. Further details on the derivation of the theoretical model for the prediction of the probability density function (PDF) of both velocities and flow rates through the pore throats are presented in Appendix 2.B. Finally, details on the performance and application of the model for the prediction of advective transport and dispersion dynamics are discussed in Appendix 2.C.

2.A POROUS MEDIUM STRUCTURE AND FLOW

Here, we present additional results on the flow fields obtained from the numerical Stokes flow simulations. The velocity fields for all analyzed saturation degrees are shown in Figure 2.5. The associated partition of the three unsaturated flow fields into a backbone of preferential flow paths, and dead-ends, or regions of low velocity, for the unsaturated cases is shown in Figure 2.6. Given the large velocity gradient at the boundaries between backbone and dead-ends, the regions distribution do not change significantly when varying the velocity threshold chosen for this partition.

We now turn our attention to the structure of dead-end regions in the three unsaturated flow cases. A representative example of the velocity variation occurring within a single dead-end region is presented in Figure 2.7. This describes an exponential decrease of velocities within the dead-end region starting from the point of contact with the backbone.

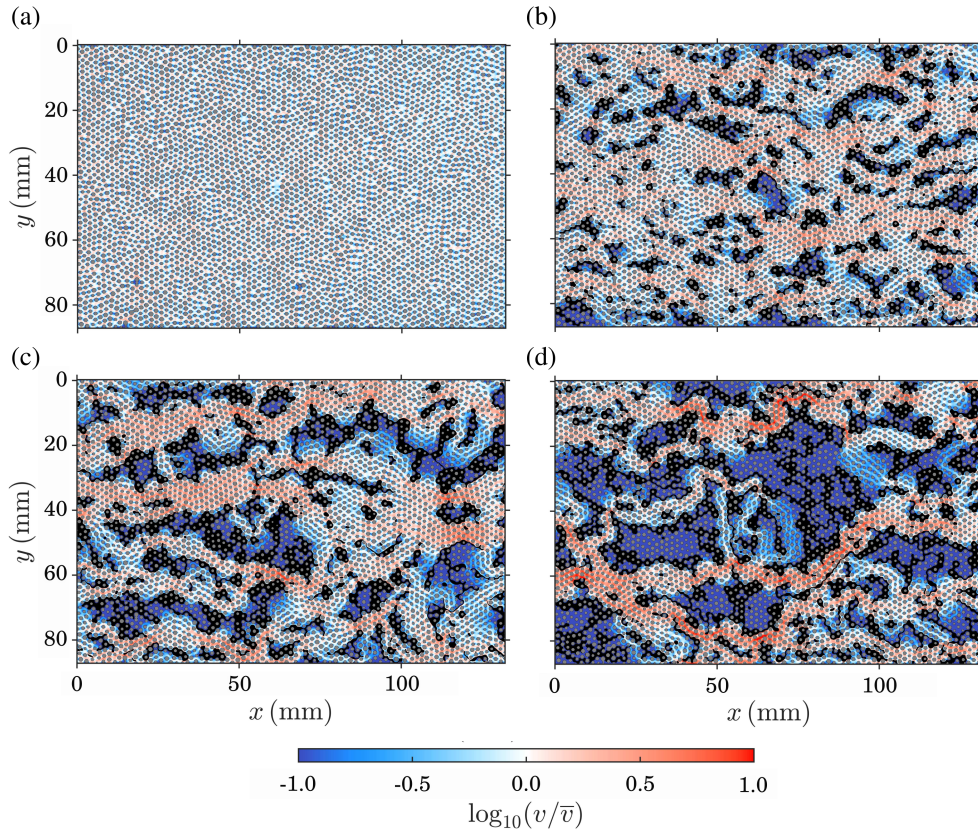


Figure 2.5: Velocity fields obtained from Stokes flow numerical simulations, displayed in terms of the velocity magnitude v normalized by its mean value \bar{v} , for (a) $S_w = 1.00$, (b) $S_w = 0.83$, (c) $S_w = 0.77$, and (d) $S_w = 0.71$. The color scale is common to all panels, with red colors indicating high velocities and blue colors low velocities. Regions where $\log_{10}(v/\bar{v}) \leq -1$ are shown in the darkest blue tone. The solid phase (circular obstacles) is shown in gray and air clusters in black. More accentuated backbone and dead-end regions are induced with decreasing liquid phase saturation.

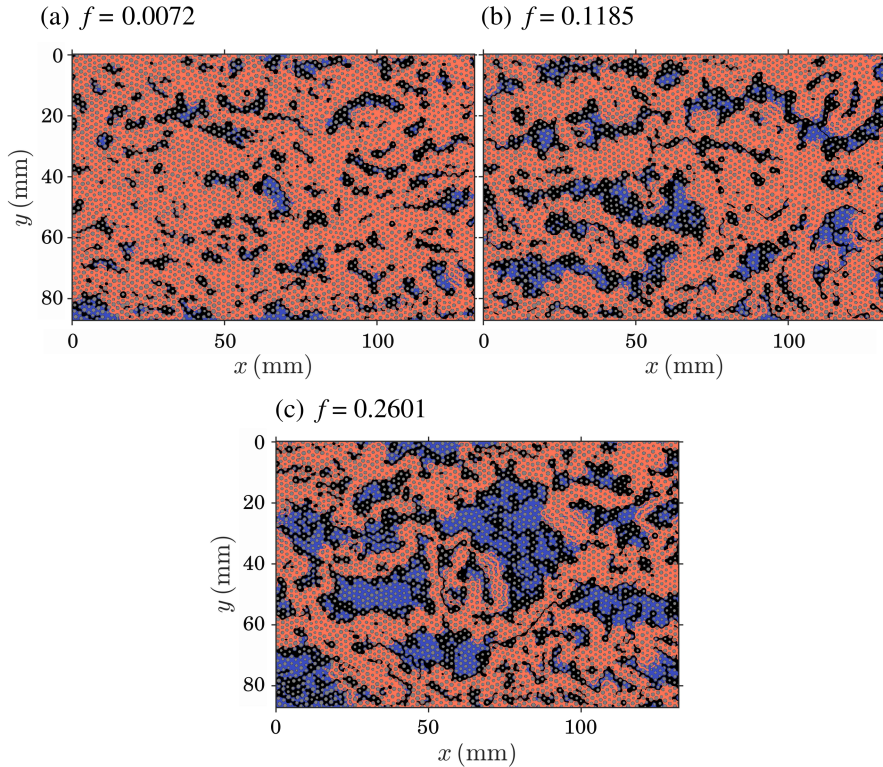


Figure 2.6: Partition of the velocity field for (a) $S_w = 0.83$, (b) $S_w = 0.77$, and (c) $S_w = 0.71$ into two types of flow structures: (i) backbone or preferential paths of high velocity, depicted in red, and (ii) dead-end regions or stagnation zones of low velocity, depicted in blue. The number and size of dead-ends increase as liquid phase saturation decreases. The ratio f of dead-end area to the total area of the pore space is reported for each case.

2.B THEORETICAL MODEL FOR FLOW AND VELOCITY PDFS

The assumptions and core of the approach behind our model for the flow and velocity PDFs are discussed in Section 2.3. Here, we provide some additional details on the derivations of some of our main results, specifically concerning the velocity PDF. We first provide details on the full model, corresponding to our main results, which takes into account three-dimensional effects due to the finite medium thickness h . We then discuss its two-dimensional limit $a_m/h \rightarrow 0$, in which the flow within pore throats reduces to a standard Poiseuille profile.

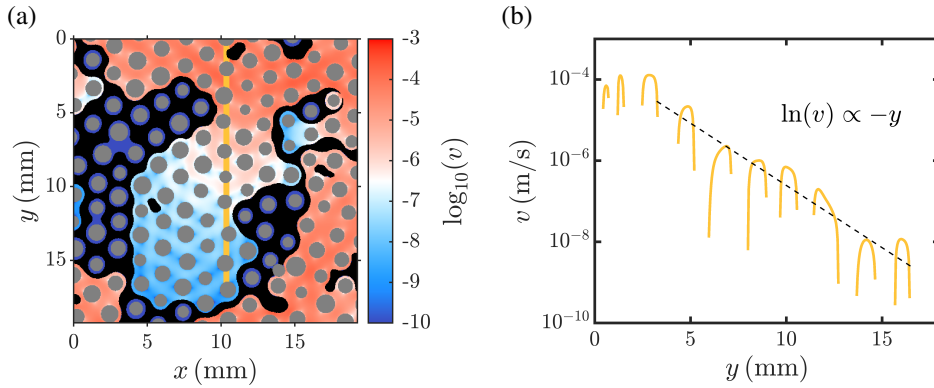


Figure 2.7: (a) Close view of the velocity field for $S_w = 0.71$, highlighting the velocity field within a dead-end region. An observation cross-section is depicted as a continuous line. (b) Velocity variation over the depth of a dead-end region, here parallel to the y -axis, along the observation cross-section shown in (a). The velocity decays exponentially as a function of depth.

2.B.1 Full formulation considering three-dimensional effects

The porous medium used in the numerical Stokes flow simulations (Jiménez-Martínez et al. 2017) (see Figure 2.5) has a pore throat width that is comparable in size to the channel thickness. Therefore, three-dimensional effects impact the intra-pore velocity profiles and the corresponding point statistics. Setting a local coordinate system at each pore throat, with x representing the local mean flow direction, the throat width running parallel to y , and z along the channel thickness, we analyze the resulting velocity profile over the y direction, averaged over the ensemble of pore throats (see Figure 2.8).

As mentioned in Section 2.3.2, we can express the velocity profile for Stokes flow over the channel thickness h for a pore throat, approximated as a cuboid channel of width a_m and thickness h , as the series shown in Eq. 2.15. Averaging this function over z values between 0 and h , we obtain Eq. 2.16. The velocity profile obtained with this expression is represented by the continuous line in Figure 2.8. For the dimensions of our porous medium (h and a_m), this series is governed by its first term, reducing the expression to Eq. 2.17. We are now in a position to derive a theoretical expression for the PDF of the depth-averaged

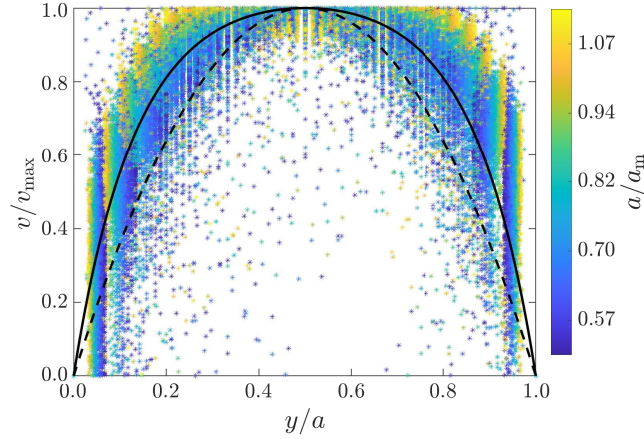


Figure 2.8: Spatial distribution of liquid-phase velocities v within each pore throat in the medium along the direction y transverse to the local main flow direction at each throat, under fully-saturated conditions ($S_w = 1.00$). Velocities are normalized by the maximum velocity v_{\max} at each pore throat and y coordinates are normalized by the corresponding pore throat size a . The plot highlights the variability of the velocity profile across pore throats. The color map represents the pore throat size, with dark blue tones corresponding to small pore throats and yellow colors representing large ones. The continuous line represents the mean velocity profile described by Eq. 2.16. The dashed line shows a parabolic (i.e., Poiseuille) velocity profile (Eq. 2.26), found only in the smaller pore throats.

velocity magnitudes in the x - y plane. Normalizing the previous result by the maximum depth-averaged velocity v_{\max} and then inverting for y , we obtain

$$y_v(v) = \frac{h}{2\pi} \operatorname{arccosh} \left[C - \frac{v}{v_{\max}} (C - 1) \right], \quad C = \cosh \left(\frac{\pi a_m}{2h} \right). \quad (2.23)$$

Following the same procedure as for Eq. 2.5, we obtain Eq. 2.18 for the velocity PDF $p_E(\cdot|q)$ given pore flow rate q . In order to characterize the maximum velocity in the pore $v_{\max}(q)$ as a function of the flow rate q , we multiply Eq. 2.18 by velocity v and integrate, which leads to the mean pore velocity

$$v_m(q) = \frac{v_{\max}(q)}{2} \left(1 + \coth \left(\frac{\pi a_m}{4h} \right) \left[\coth \left(\frac{\pi a_m}{4h} \right) - \frac{4h}{\pi a_m} \right] \right). \quad (2.24)$$

Relating the local flow rate q to the local mean velocity by $q = h a_m v_m(q)$, we find $v_{\max}(q) = \alpha q / (h a_m)$, with α a constant given by Eq. 2.19.

As discussed in the Section 2.3.2, using these results and those for the flow rate PDF together with Eq. 2.14 allows us to obtain analytical scalings for the low- and high-velocity dependencies of the Eulerian velocity PDF p_E by appropriate Taylor expansions. We note here that, for the range $v \gtrsim v_c$, we expand the integrand for $v - \alpha q / (ha_m) \ll 1$ (velocities near the maximum pore velocity), which corresponds to a pole of the integrand and provides the dominant contribution in this case. We obtain, in terms of the Meijer G function,

$$p_E(v) \approx \frac{\sqrt{2}\pi hv}{a_m v_c^2 \alpha^2} \left[G_{24}^{20} \left(\frac{v^2}{4v_c^2 \alpha^2} \middle| -\frac{1}{4}, \frac{1}{4}; -\frac{1}{2}, \frac{1}{2}, 0, 0 \right) - G_{24}^{20} \left(\frac{v^2}{4v_c^2 \alpha^2} \middle| -\frac{1}{4}, \frac{1}{4}; 0, 0, -\frac{1}{2}, \frac{1}{2} \right) \right]. \quad (2.25)$$

Expanding again for $v \gtrsim v_c$, we obtain the high-velocity behavior for the saturated case, Eq. 2.20b.

2.B.2 Two-dimensional limit

In two-dimensional porous media, the velocity profile within pore throats is typically well approximated by a Poiseuille profile (de Anna et al. 2017). We now show that this assumption is equivalent to the formulation described in Section 2.3.2, where we consider three-dimensional effects, in the limit of large medium thickness or small pore throats, $a_m/h \rightarrow 0$, when the flow dynamics are effectively two-dimensional. As shown in Figure 2.8, the Poiseuille profile provides a good fit across the smaller pore throats in our medium, but, for wider throats, three-dimensional effects become relevant. Note that the arguments leading to the flow rate PDF make no use of the flow profile within pores, and therefore p_Q remains unchanged. The presence of three-dimensional effects impacts only the velocity PDF p_E , although, as we now show, the functional scalings at low and high velocity remain unchanged.

First, assume that the velocity field within a pore throat is well approximated by a Poiseuille profile. Then, for a local flow rate q at the pore throat, the Eulerian velocity profile in the direction transverse to the flow is

$$v_E(v|q) = \frac{3q}{2a_m} \left(1 - \frac{y^2}{a_m^2} \right), \quad (2.26)$$

where the mean velocity within the pore throat is given by $v_m = ha_m q$ and the maximum velocity is equal to $3v_m/2$. Consider the case of fully-saturated

conditions. The intra-pore PDF associated with the Poiseuille flow profile is (Aquino and Le Borgne 2021)

$$p_E(v|q) = \frac{a_m H[3q/(2a_m) - v]}{3q \sqrt{1 - 2a_m v/(3q)}}. \quad (2.27)$$

In the limit $a_m/h \rightarrow 0$, we have $\alpha \rightarrow 2/3$ (Eq. 2.19), yielding the same result for the relationship between flow and maximum velocity mentioned previously for the full formulation. Substituting this in Eq. 2.18 and again taking the limit $a_m/h \rightarrow 0$, we obtain Eq. 2.27. This shows that intra-pore Poiseuille velocity profiles are a limit case of the general model derived in Section 2.3.2 and shortly expanded in Appendix 2.B.1.

Based on the definition of the overall velocity PDF $p_E(v)$, Eq. 2.14, and recalling that $p_Q(q)$ is given by Eq. 2.1 for the backbone, the global PDF can then be written in terms of the Meijer G function as

$$p_E(v) = \frac{\sqrt{\pi}}{3v_c} \frac{2v}{3v_c} G_{12}^{20} \left(\frac{2v}{3v_c} \middle| -\frac{1}{2}; -1, 0 \right), \quad (2.28)$$

where the characteristic velocity $v_c = q_c/(ha_m)$. For small velocities, $v \ll v_c$, this admits the series expansion

$$p_E(v) \approx \frac{1}{3v_c} \left[1 - \left(1 + \ln \left[\frac{2e^{2(\gamma_E-1)+F(-1/2)} v}{3v_c} \right] \right) \frac{v}{3v_c} \right], \quad (2.29)$$

where F is the digamma function, defined in terms of the Gamma function Γ as $F(x) = d \ln \Gamma(x) / dx$, and $\gamma_E \approx 0.5772$ is the Euler-Mascheroni constant. We have $F(-1/2) \approx 0.03649$. In particular, $p_E(v) \approx p_E(0) = 1/(3v_c)$ for sufficiently small v , which agrees with Eq. 2.20a when $a_m/h \rightarrow 0$. For large velocities, $v \gtrsim v_c$ we find

$$p_E(v) \approx \frac{1}{3v_c} \sqrt{\frac{2\pi v}{3v_c}} e^{-\frac{2v}{3v_c}}, \quad (2.30)$$

which is again equivalent to the limit $a_m/h \rightarrow 0$ of Eq. 2.20b. Thus, the high-velocity behavior remains exponential, and the low-velocity behavior remains flat.

Next, we examine unsaturated conditions. For low velocities, we can again approximate $p_E(v|q) \approx \delta[v - q/(ha_m)]$. Therefore, Eq. 2.21 remains valid without change. As before, the contribution of dead-end regions to the high-velocity behavior is controlled by the high-flow-rate behavior. The backbone contribution is proportional to Eq. 2.30. Proceeding similarly to the three-dimensional for-

mulation, and using Eq. 2.13 for the flow contribution of flow rates in dead-end regions for $q \gtrsim q_c$, we find

$$p_E(v) \approx \left[\frac{\gamma f}{1 + 2\gamma} \sqrt{\frac{3v_c}{v}} + (1 - f) \sqrt{\frac{v}{3v_c}} \right] \frac{\sqrt{2\pi}}{3v_c} e^{-\frac{2v}{3v_c}}, \quad (2.31)$$

which agrees with the limit $a_m/h \rightarrow 0$ of Eq. 2.22.

2.B.3 Model parameters and regime scalings

Table 2.1 summarizes the parameter values employed in our model results for the velocity and flow rate PDFs, as well as for the CTRW transport model discussed in Section 2.4 and in Appendix 2.C. In all cases, the average pore-throat width $a_m = 1.17$ mm, the medium thickness $h = 0.5$ mm, and the mean pore size $\lambda = 1.85$ mm, as measured.

As a verification of the low- and high-magnitude analytical scaling results, Figure 2.9 shows comparison of the numerical data from Stokes flow simulations, the full theoretical PDFs computed numerically from the general theoretical expressions as discussed in Section 2.3.2, and the regime scalings. Figure 2.9a concerns the velocity PDFs, with regime scalings given by Eqs. 2.20a, 2.20b, 2.21, and 2.22, whereas Figure 2.9b shows the flow-rate PDFs, with scalings according to Eqs. 2.1, 2.12, and 2.13.

2.C PARTICLE TRACKING SIMULATIONS AND THE CTRW MODEL

To assess the applicability of the theoretical model introduced in Section 2.3 for the prediction of advective transport, we employ a Continuous Time Random Walk model (CTRW). The CTRW description discussed in Section 2.4 corresponds to a set of stochastic recursion relations for the particle positions and times X_k and T_k at the completion of the k th step,

$$X_{k+1} = X_k + \zeta_x, \quad T_{k+1} = T_k + \tau_k, \quad (2.32)$$

where the initial position $X_0 = 0$, the initial time is $T_0 = 0$, ζ_x is the longitudinal (i.e., along the mean flow direction) correlation length, and τ_k is the transition time, or duration, associated with step k .

We determine ζ_x based on s -Lagrangian (i.e., sampled equidistantly along particle trajectories) velocity statistics obtained from linear interpolation of the t -Lagrangian trajectories. Correlation lengths increase with decreasing saturation;

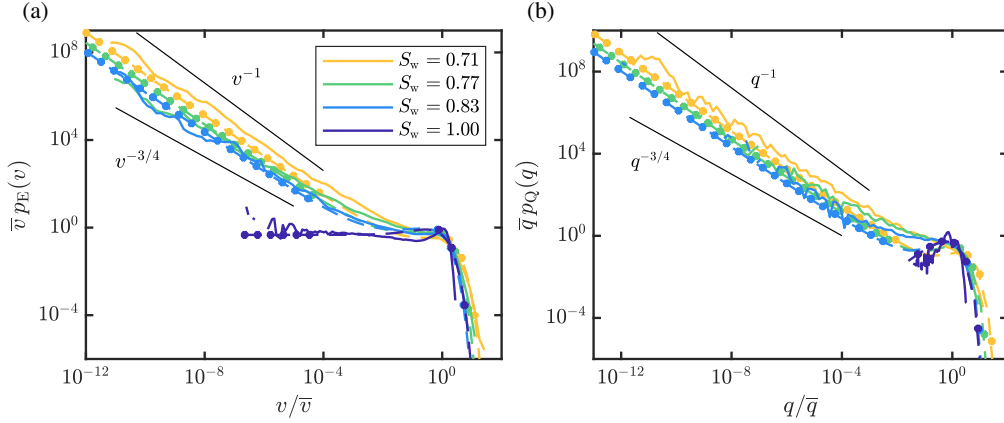


Figure 2.9: (a) Eulerian velocity PDFs and (b) local flow rate PDFs for all analyzed saturation degrees $S_w = 1.00, 0.83, 0.77,$ and 0.71 . Continuous lines represent the data from Stokes flow simulations; dashed lines represent full numerical computation of the integral representation of the theoretical PDFs discussed in Section 2.3.2; and circular markers represent the analytical low- and high-magnitude regime scalings. Plots are non-dimensionalized according to the mean velocity \bar{v} and the mean pore flow rate \bar{q} of the numerical data set, respectively.

the values obtained are given in Table 2.1. The corresponding auto-correlation functions, from where the values of ζ_x for each saturation are obtained, are shown in Figure 2.10.

The velocities V_k of a particle are assumed to be constant throughout each step k , and fully uncorrelated between steps, as an approximation of the Lagrangian correlation structure of the flow associated with the longitudinal correlation length ζ_x . Accordingly, for each step k , V_k is independently sampled from the equilibrium s -Lagrangian velocity PDF, which is given by $p_s(v) = v p_E(v) / \bar{v}$. The flux-weighting of the underlying Eulerian PDF is required by the fixed-distance sampling of particle velocities (Dentz et al. 2016). Note that the initial velocity V_0 is determined by the initial condition, which here is also flux-weighted. The transition time τ_k associated with each fixed longitudinal displacement depends on the current particle velocity and on its orientation with respect to the mean flow direction. The latter can be quantified in terms of the average tortuosity χ , determined as the ratio of average Eulerian velocity magnitudes to the average projection of Eulerian velocities along the mean flow direction. Values of tortuosity for each analyzed saturation degree are reported in Table 2.1.

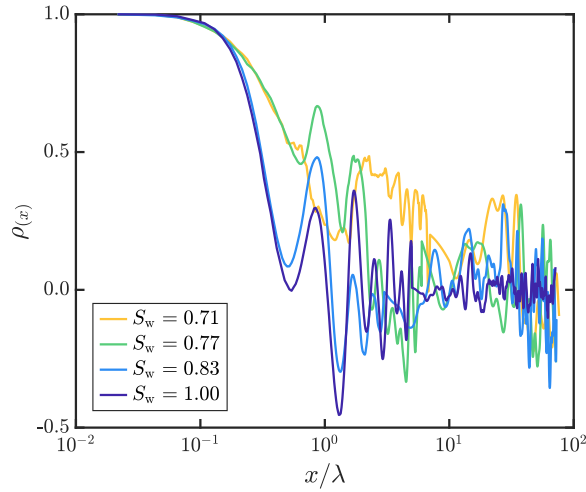


Figure 2.10: Auto-correlation functions ρ of the longitudinal velocities, as a function of longitudinal distance x normalized by the mean pore size λ , for $S_w = 1.00$, 0.83, 0.77, and 0.71.

The correlation length along streamlines, corresponding to the full particle displacement within a step, is then $\zeta = \chi \zeta_x$, and

$$\tau_k = \frac{\chi \zeta_x}{V_k}. \quad (2.33)$$

As discussed in Section 2.4, we employ the CTRW approach to compute the temporal evolution of the advective longitudinal dispersion σ_x^2 based on our predictions for the velocity PDF. Figure 2.11 shows additional comparisons to the results obtained from parameterizing the CTRW using the velocity PDF obtained directly from the simulated velocity field.

Table 2.1: Model parameters. The parameters employed to model the flow and velocity PDFs are the ratio f of dead-end areas to total pore space area, the Pareto exponent γ of the dead-end area PDF, and the characteristic pore flow rate q_c . The characteristic velocity $v_c = q_c / (ha_m)$ is also reported. The CTRW transport model requires the tortuosity χ and the longitudinal correlation length ζ_x of Lagrangian velocities.

S_w	f [-]	γ [-]	q_c [m ³ /s]	v_c [m/s]	χ [-]	ζ_x [λ]
1.00	0.000	—	1.19×10^{-11}	2.04×10^{-5}	1.10	0.45
0.83	0.072	0.35	2.90×10^{-12}	4.95×10^{-6}	1.18	1.10
0.77	0.119	0.25	4.82×10^{-12}	8.25×10^{-6}	1.23	2.23
0.71	0.260	0.10	9.65×10^{-12}	1.65×10^{-5}	1.29	6.70

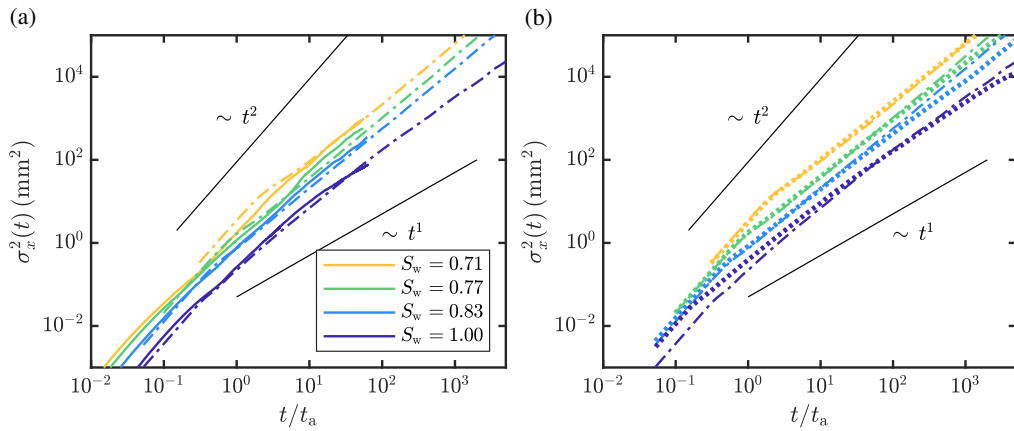


Figure 2.11: Temporal evolution of advective longitudinal dispersion σ_x^2 . Time has been non-dimensionalized by the advective time t_a for each saturation. (a) Comparison of dispersion from particle tracking simulations (continuous lines) with dispersion obtained from CTRW using the numerical Eulerian velocity PDFs (dash-dotted lines). (b) Comparison of σ_x^2 from CTRW using the numerical Eulerian velocity PDFs (dash-dotted lines) and from CTRW using the velocity PDFs from the theoretical model (dotted lines). Scalings for ballistic ($\sigma_x^2 \sim t^2$) and Fickian ($\sigma_x^2 \sim t^1$) regimes are shown as visual guides.

BIBLIOGRAPHY

- Aquino, T. and T. Le Borgne (2021). “The diffusing-velocity random walk: a spatial-Markov formulation of heterogeneous advection and diffusion.” In: *Journal of Fluid Mechanics* 910, A12.
- De Anna, P., B. Quaife, G. Biroso, and R. Juanes (2017). “Prediction of the low-velocity distribution from the pore structure in simple porous media.” In: *Physical Review Fluids* 2, p. 124103.
- Dentz, M., P. K. Kang, A. Comolli, T. Le Borgne, and D. R. Lester (2016). “Continuous time random walks for the evolution of Lagrangian velocities.” In: *Physical Review Fluids* 1, p. 074004.
- Jiménez-Martínez, J., T. Le Borgne, H. Tabuteau, and Y. Méheust (2017). “Impact of saturation on dispersion and mixing in porous media: Photobleaching pulse injection experiments and shear-enhanced mixing model.” In: *Water Resources Research* 53, pp. 1457–1472.

PHASE SATURATION CONTROL ON VORTICITY ENHANCES MIXING IN POROUS MEDIA

This chapter has been published on March 31 2024 as: Velásquez-Parra, A., F. Marone, R. Kaufmann, M. Griffa, & J. Jiménez-Martínez (2024). "Phase saturation control on vorticity enhances mixing in porous media". In: *Water Resources Research* 60, e2023WR036628. <http://doi.org/10.1029/2023WR036628>.

Key Findings:

- Lower liquid phase saturation induces stronger solute plume's front deformation, enhancing liquid-liquid mixing.
- Helical flow in the pore space is promoted by an increased convergence of flow streamlines.
- Vorticity-dominated deformation is enhanced as liquid phase saturation decreases.

Authors' contribution: *A. Velásquez-Parra*: conceptualization, data analysis, numerical analysis, paper writing; *F. Marone*: conceptualization, experimental work, paper writing; *R. Kaufmann*: conceptualization, experimental work; *M. Griffa*: conceptualization, experimental work, data analysis, supervision, paper writing; *J. Jiménez-Martínez*: conceptualization, experimental work, supervision, paper writing.

This is a post-print of the paper, differing from the published version only in terms of layout and formatting. Reprinted with permission from John Wiley & Sons Publications and the American Geophysical Union.

ABSTRACT

Mixing controls the fate of any solute entering porous media. Hence, an understanding of the involved processes is essential for assessing subsurface contamination and planning for its protection. However, the three-dimensional mechanisms dominating solute mixing in the presence of several fluid phases in the pore space, and their dependency on phase saturation degree (fraction of the pore volume occupied by a phase) are unknown. Here, we analyze solute mixing in unsaturated porous media at the pore scale using X-ray micro-tomography performed with synchrotron radiation at unprecedented temporal and spatial resolutions for such an investigation. Transport experiments through a synthetic, sand-like porous medium, followed in 4D using a contrast solution, are performed at different liquid phase saturation degrees. The results reveal larger solute's front deformation at lower saturation, which translates into an enhanced mixing with time. Using different topological indexes, defined based on a description of the liquid phase geometry and of the resulting hydrodynamics, we show an increase in the spatial convergence of flow streamlines at lower saturation, which, in turn, leads to a strengthened helical flow inside the liquid phase. Consequently, this increases the number of shear- and vorticity-dominated deformation regions, as characterized by larger negative and positive Q-criterion values, respectively. These findings represent a major step towards understanding the control of both saturation and the system's heterogeneity on solute mixing, essential, among others, to assess reactivity in porous media.

PLAIN LANGUAGE SUMMARY

The fate of any solute spreading through porous media, as it is the case for nutrients or pollutants entering the subsoil, is controlled by liquid-liquid mixing with the resident solution. However, it is still unknown which mechanisms control mixing in the presence of several fluid phases, as it occurs in the unsaturated region of soils. A combination of synchrotron 4D X-ray micro-tomography experiments with very high temporal and spatial resolutions, advanced 3D image analysis, and numerical simulations of flow, allowed to reveal an enhancement of the spatial convergence of flow streamlines at lower liquid phase content, i.e., at a lower fraction of the entire pore volume that is occupied by the liquid phase. This increases the number of shear- and vorticity-dominated flow regions, inducing an overall larger solute front deformation with time and rendering mixing more efficient. These findings can highly contribute to the assessment of mixing and reactions in natural porous media.

3.1 INTRODUCTION

Porous media in the environment often include several material phases within the pore space, both in liquid and gas form. In such a case, porous media are commonly referred to as unsaturated. Subsurface examples include soils, which act as a filter and buffer for contaminants (Burauel and Baßmann 2005), so as deep aquifers and exhausted hydrocarbon reservoirs, where geological sequestration of CO₂ is typically carried out (Szulczewski et al. 2012). In all these cases, flow and transport processes intrinsically occur at the micro-scale, within the liquid- or gas-filled voids (pores) between solid grains, whose size usually spans the range of a couple to hundreds of micrometers. In those locations, initially segregated miscible phases come into contact with each other and homogenize by the action of molecular diffusion through what is commonly referred to as mixing, increasing the volume occupied by the solute and smoothing out concentration gradients across their interface (Danckwerts 1952; Kitanidis 1994; Ottino 1989). However, our current understanding of the micro-scale coupling of flow dynamics and associated liquid-liquid mixing and reactive processes in unsaturated porous media is very limited, owing to both the complexities related to the presence of multiple phases and the difficulty in experimentally probing/observing these systems in real-time, in particular with visible light. The classical modelling approaches for solute transport in unsaturated porous media are often based on equivalent parameters (permeability, dispersion) derived from analogy with saturated conditions and on systematic *ad hoc* incorporation of a dependency on the phase saturation degree (the fraction of the pore volume occupied by a phase) (Simunek et al. 2008). However, expressing solute transport in terms of a bulk phase saturation value introduces inaccuracy due to the high degree of heterogeneity in these systems. Fundamentally, current large-scale (continuum) models (Simunek et al. 2008) cannot accurately predict the fate of chemicals and reactions (both liquid-liquid and liquid-solid) in unsaturated porous media because of the control exerted by pore-scale processes on mixing (Dentz et al. 2011; Li et al. 2017; Valdés et al. 2022).

Recent studies have attempted to identify and include the effect of this heterogeneity on flow and transport prediction across scales (Lasseux et al. 2021). 2D studies, mainly based on microfluidics experiments and pore-scale numerical simulations, have exposed signs of anomalous transport already in simplified, model system porous media (Bordoloi et al. 2022). Anomalous transport is usually characterized by breakthrough curves, i.e., time series of the solute concentration at a fixed location, that show early arrival and long tailing, describing

non-symmetric solute's plume spreading patterns and non-Fickian evolution of mixing in time (Berkowitz et al. 2006; de Anna et al. 2014; de Anna et al. 2013; Levy and Berkowitz 2003). Such behavior has been shown to be enhanced in unsaturated conditions (Hasan et al. 2019; Jiménez-Martínez et al. 2015; Jiménez-Martínez et al. 2017; Karadimitriou et al. 2016), given the increase in the system's heterogeneity, i.e., broader fluid flow velocity distributions (Velásquez-Parra et al. 2022). In particular, the presence of a second immiscible material phase in the pore space leads to both the formation of larger interface areas between mixing fluids and enhanced concentration gradients across them, rendering mixing more efficient (Jiménez-Martínez et al. 2015). New advances in imaging techniques such as magnetic resonance imaging (Lehoux et al. 2016; Markale et al. 2021), high-resolution laser imaging (Heyman et al. 2020), and X-ray micro-tomography (Boon et al. 2017; Hasan et al. 2020) have allowed expanding these observations to 3D systems, involving both artificial and real porous media. Advances in X-ray micro-tomography have increasingly enabled the imaging of rock- and soil-like samples and of flow and transport through them, both for real-time visualization of the physical processes themselves (Armstrong et al. 2016; Chen et al. 2021; Dobson et al. 2016; Hasan et al. 2020; Schlüter et al. 2016) and for supporting the development and validation of respective numerical investigations (Guédon et al. 2019; Kang et al. 2014; Puyguraud et al. 2021; Shih et al. 2022). These studies have unveiled important features of pore-scale flow and transport, such as intermittency of local velocities and accelerations, essential to be taken into account for improved model formulations (Kang et al. 2014). They have also provided relevant findings on the mechanisms behind non-Fickian scalings both of plume spreading over time (Puyguraud et al. 2021) and of pore-scale concentration distributions (Hasan et al. 2020). Such studies exemplify the potential of X-ray micro-tomography for flow and transport analyses. However, its use to study systematically similar processes in unsaturated porous media, at the pore scale, has not been fully explored yet. In particular, the control of saturation on solute plume deformation, as a driver of mixing, under nature-like conditions, remains an open question.

Under fully saturated conditions, 3D experimental studies at the Darcy scale have exposed the role of secondary flow motions, i.e., helical flow, on mixing enhancement (Chiogna et al. 2016). Twisted streamlines strongly deform the solute plume, increasing the surface for diffusive mass transport and enhancing plume dilution (Chiogna et al. 2016; Yu et al. 2015). Studies in 2D heterogeneous flow fields have highlighted the interplay of vorticity- and shear-dominated deformation areas in bending the solute plume and enhancing plume dilution, respectively (de Barros et al. 2012). In these cases, topological indicators such

as helicity density, reflecting the effect of vorticity on streamlines deformation, and indexes such as the Okubo-Weiss parameter (Okubo 1970; Weiss 1991) or the Q-criterion (Hunt et al. 1988), which can be used for characterizing both vorticity- and shear-dominated deformation regions, have been applied with success in mixing analyses. On the contrary, similar studies under unsaturated conditions have mainly drawn attention towards changes in the connectivity of the non-wetting phase during cycles of imbibition and drainage (Schlüter et al. 2016; Shih et al. 2022), and also during stages of constant saturation as a result of coalescence and snap-off events of trapped ganglia (Armstrong et al. 2016). The impact of saturation on wetting phase topology both in 2D and 3D model systems and its implications for flow and transport at the pore scale remain unanswered.

Here, we report a synergetic experimental and numerical 3D time-resolved (i.e., 4D) investigation and analysis of pore-scale solute mixing in unsaturated porous media. We show that lower saturation increases the spatial convergence of flow streamlines, allowing distant parcels of fluid to meet further downstream. This enhanced streamlines convergence leads to a strengthened helical flow, enhancing both shear- and vorticity-dominated flow deformation regions. We took advantage of synchrotron radiation-based X-ray micro-tomography experiments, performed with temporal and spatial resolutions unprecedented for such an investigation, to image in 4D a solute's concentration field. Such high resolutions, together with extensive 3D image analysis approaches, have allowed us to characterize the liquid phase topology and its effect on the system's hydrodynamics. Thus, we could systematically study the impact of liquid phase saturation and of fluid flow rates on mixing. Our results reveal that not only the bulk liquid phase saturation, but also its impact on both liquid phase topology and streamlines convergence, is fundamental for understanding and predicting the dynamics of contaminants and of geochemical cycles in soils.

3.2 METHODS

3.2.1 *Synchrotron X-ray micro-tomography experiments*

Results obtained from 4D synchrotron X-ray micro-tomography performed during transport experiments allowed the observation of real-time concentration changes inside the pore space of a soil-like sample, under different saturation degrees ($S_w = V_w/V_T$, where V_w is the volume occupied by the liquid phase and V_T is the total pore space volume). Experiments were carried out at the beamline for Tomographic Microscopy and Coherent Radiology Experiments

(TOMCAT) of the Swiss Light Source (SLS), located at the Paul Scherrer Institute (PSI), in Villigen, Switzerland. An artificial porous system, consisting of a sintered packing of irregularly shaped borosilicate glass grains (Hilgenberg GmbH), was used for all transport experiments. The cylindrical sample was 8 mm high and had a diameter of 4 mm, with a bulk porosity of 0.28, an intrinsic permeability of 10^{-10} m^2 , and an average pore size of $30 \text{ }\mu\text{m}$. It resembled a poorly graded sandy soil, with a relatively homogeneous pore size distribution (refer to Appendix 3.E, Figure 3.11, for the pore size distribution) and close to a spatial constant porosity. This represents a more realistic porous medium than the simplified porous systems consisting of spherical glass beads, usually employed in similar transport studies (Hasan et al. 2020; Heyman et al. 2020). A 3D rendering of the porous system's tomographic reconstruction together with the air phase hosted inside of the pore space is shown in Figure 3.1a for the experiment performed at a saturation degree $S_w = 0.82$.

The sample was placed inside a flow cell composed of three units: (i) a bottom conic cap allowing the separate and simultaneous injection of both the liquid and the gas (air) phases, (ii) a middle cylindrical casing, hosting the sample, and (iii) a top conic cap allowing the connection of the outlet line. The middle casing was internally coated with paraffin to avoid lateral flow and boundary effects. We fabricated each unit via 3D printing by stereo-lithography, using a photosensitive resin composed of acrylic monomers. The same pair of sample and flow cell was employed for all transport experiments. The pressure was constantly monitored during the experiments via two sensors (MPS by Elveflow) placed at the end of the inlet and outlet lines, respectively. A potassium iodine (KI) aqueous solution was used both as a tracer and as background, i.e., resident solution, albeit at different concentrations, namely, 0.06 M for the resident solution and 0.90 M for the injected tracer. The use of KI is justified in its lack of chemical reactivity with borosilicate glass and its high effective atomic number. This resulted in an optimal trade-off between X-ray absorption and phase contrast levels both between such a solution and air and between such a solution and the grain packing (Marone et al. 2020).

In the first stage, a simultaneous injection of both the gas (air) and the liquid phase (the aqueous solution) was performed until reaching a steady-state flow condition within the sample, i.e., until no large oscillations in the pressure difference between the inlet and outlet were registered. Then, the fluid pair injection was stopped, resulting in a static mixture of the two phases (Tallakstad et al. 2009a). The injection was performed with an automatically controlled syringe pump (Harvard Apparatus) at a constant flow rate. Transport experiments were carried out in a second stage with the goal of observing,

in real-time, the impact of both S_w and the flow rate, q , on solute transport and mixing. The tested flow rates included 0.125, 0.25, and 0.50 mm³ s⁻¹. We injected the tracer at low capillary numbers (ratio between viscous and capillary forces) to guarantee that the air (non-wetting phase) remained immobile during the tracer injection (Tallakstad et al. 2009b; Tang et al. 2019). We estimated an average (across experiments) capillary number $C_a = 2.67 \times 10^{-6}$, here defined as $C_a = \bar{v}\mu/\sigma$, where \bar{v} is the average flow velocity associated with every experiment and obtained through numerical simulations of flow, and μ and σ are the average dynamic viscosity, i.e., 8.65×10^{-4} kg m⁻¹s⁻¹ (Desnoyers and Perron 1972), and the average surface tension, i.e., 72.5 mN m⁻¹ (Ali et al. 2009), of the KI solution in the range of concentrations used in the experiment at a temperature of 25 °C, respectively. Table 3.1 summarizes the single C_a and \bar{v} values obtained for every experiment.

Very high spatial and temporal resolutions, unprecedented for transport studies in porous media, were essential for the purpose of this study, given the rapid nature of the observed processes. Each tomographic dataset consisted of $2016 \times 2016 \times 1100$ isotropic voxels of lateral size of 2.75 μm, acquired over a total time of 2.4 s (approximately 15% smaller voxel size and 60% faster acquisition time compared to similar studies (Hasan et al. 2020)). This included the time required for the acceleration, rotation (from 0° up to 180° around the cylindrical sample symmetry, vertical axis), and deceleration of the sample (1.2 s in total), during which a total of 500 angular projections, i.e., radiographs, of the sample were collected. In particular, the total tomographic acquisition time needed to be smaller than the time scales of the solute's advection and diffusion over the average pore size. The remaining 1.2 s were needed for rotating the sample back to a position of 0°. This was required since the inlet and outlet lines were connected without a slip ring, hence not allowing for an uninterrupted rotation of the sample. To avoid motion artifacts in the reconstruction, we made sure that the sample's movement during rotation with respect to the vertical axis was kept smaller than the voxel size. In addition, the acceleration and deceleration of the sample back and forth movement together with the achieved low capillary numbers, led to non-rotating flow conditions. The tomographic image acquisition was achieved by using almost monochromatic radiation at an energy of 21 keV, to be able to capture concentration gradients and to estimate quantitatively concentration values inside the pore space. Each experiment's set of results included a total of 250 tomograms, i.e., 250 time steps, for a total of eight experiments. This work focuses on the results from five of them. Before starting each experiment, we acquired 10 radiographs in the absence of the X-ray beam (so-called dark-current radiographs) and 100 of them in the presence of

the beam but with the sample out of the beam (so-called flat-field radiographs). Both sets of radiographs were then used for the usual dark-current and flat-field corrections of the sample's radiographs, at any successive point in the time series. We used as X-ray detector the system available at the TOMCAT beamline, consisting of (i) a 150 μm -thick LuAg:Ce scintillator screen, converting the X-ray photons into visible light ones; (ii) a high-efficiency visible light microscope, called macroscope (Bührer et al. 2019), which, in our case, was set to provide a $4\times$ geometrical magnification; and (iii) the high throughput GigaFRoST detection and read-out system (Marone et al. 2020), including a sCMOS chip as visible light photons detector (PCO.Dimax by PCO GmbH, with 11 μm physical pixel size). The detector's exposure time for acquiring each radiograph was 2 ms.

The tomograms were reconstructed using the beamline's software and hardware infrastructure, relying upon TOMCAT in-house-developed Fourier space re-gridding algorithm (Marone and Stampanoni 2012). In correspondence with each point in the tomographic time series, we reconstructed two types of tomograms. The first one assumed only X-ray absorption as the main image formation mechanism (contrast mechanism), using the Beer-Lambert law for relating radiographic pixel values to the linear projection of the X-ray linear attenuation coefficient along the respective ray hitting the detector at such pixel (Als-Nielsen and McMorro 2011). The second type of reconstruction assumed X-ray refraction as the main contrast source (so-called phase-contrast tomogram). In this case, the phase retrieval, i.e., the calculation of the linear projection of the real part of the X-ray index of refraction from the radiographic pixel value, was performed with an implementation of the algorithm proposed by Paganin et al. (2002), with an estimated ratio of real-to-imaginary parts of the complex-valued X-ray index of refraction, δ/β , of about 371. We note that at each time point during every experiment, our acquired tomographic datasets contained both X-ray absorption and refraction information. This was achieved by the sample being located at a distance from the detector, d_{S-D} , equal to 20 mm, which laid within the Fresnel diffraction region of the imaging configuration. Such downstream region past the object is where refraction effects on the X-ray beam propagation can be still exploited for the phase retrieval type based upon the cited approach by Paganin et al. (2002). At the mentioned X-ray photon energy of 21 keV, the Fresnel number, N_F , of the imaging configuration could be estimated as $N_F = l_d^2 / (\lambda d_{S-D}) \approx 25.6$, where λ is the X-ray wavelength (in vacuum) corresponding to 21 keV and l_d is the adopted level of detail of the sample. This was chosen equal to an upper bound of the effective, tomographic spatial resolution, being equal to twice the voxel size, $l_d = 5.5 \mu\text{m}$. By its definition, within the Fresnel diffraction region of the imaging configuration $N_F \geq 1$. The cited

phase retrieval approach by Paganin et al. (2002) requires $N_F \gg 1$, a condition well satisfied in our case. Images of the experimental setup and of the sample are shown in Appendix 3.E, Figure 3.12. As expanded in subsection 3.2.2, the experiments post-processing relied primarily on the phase-contrast tomograms.

3.2.2 Experimental concentration calibration

In addition to the high spatial and temporal resolutions, X-ray micro-tomography with almost monochromatic and highly spatially coherent synchrotron radiation allowed us to achieve a statistically robust mapping of image voxel values to actual solute concentration ones (expressed in molar, M). The experimental calibration of the tomograms' voxel values *versus* the solute's concentration values was achieved via a set of fourteen, single tomogram experiments. They involved the sample fully saturated with an aqueous KI solution at different concentration values, in the range from 0.06 M to 1.81 M. The obtained calibration curve, created following the procedure presented in Lavin et al. (2018) and in Bevington and Robinson (2003), describes a linear relationship between the directly measured voxel value and the corresponding solution concentration inside the liquid phase. It also describes a rather narrow confidence band (see Appendix 3.A, Figure 3.8a). The calibration curve was obtained by employing the 32-bit phase-contrast tomograms, considering only the regions occupied by the liquid phase, as obtained from segmentation (see Section 3.2.3). We chose the phase-contrast tomograms because they showed a smaller coefficient of variation of the voxel values in comparison with the absorption tomograms, i.e., a smaller ratio between the standard deviation computed from all voxels inside the liquid phase relative to their mean value. In general, we observed a slight heteroscedastic behavior of such voxel values across concentrations, with a slight increase in standard deviation towards the lower range of concentrations. Not much difference was observed between 32-bit and 16-bit tomograms, the latter obtained from the former by a coarser quantization of a 32-bit voxel value range chosen identical at any concentration, i.e., an identical dynamic range. However, we decided to use the 32-bit tomograms for the calibration and also for further analysis of the transport experiments since they are not affected by the dynamic range chosen for the image reconstruction. Hence, we could guarantee no bias in the calibration curve derivation as well as in any successive steps of the image analysis protocol described below. In addition to the linear mapping accuracy, the temporal stability of all components of the TOMCAT tomography beamline allowed for achieving high temporal consistency in such mapping. All these features further highlight the capabilities and advantages offered by

this experimental technique in studying transport processes at the pore scale. Further details on the mathematical derivation of the calibration curve and on the corresponding uncertainty analysis are presented in Appendix 3.A.

3.2.3 Image analysis

We defined an image analysis protocol for the post-processing of the transport experiment tomograms. Out of the 250 of them available per experiment, we applied such protocol to a total of 44 for the experiment performed at $q = 0.50 \text{ mm}^3 \text{ s}^{-1}$ and on an average of 65 of them for the remaining cases. We did not use, in any experiment, all 250 tomograms since the arrival, spreading, and mixing of the solute occurred only during specific time intervals shorter than the overall experiment duration. The latter was chosen long enough to be sure of always including enough duration to fully observe, and thus analyze, those processes. This is indicated in Table 3.1, which summarizes the total number of pore volumes, PV , i.e., the ratio of injected volume relative to the total volume of the liquid phase, injected over the chosen range of scans for every experiment. We first applied a 2D (XY planes, orthogonal to the cylindrical specimen's symmetry axis) non-local means denoising algorithm (Buades et al. 2005), implemented in the software Avizo (ThermoFisher Scientific 2022), on the full 32-bit tomographic slice stack of each one of those tomograms. No significant improvement was observed when applying the same algorithm in 3D. We then employed the Active Contours plugin available in the open source software Icy (version 2.1.3.0) (De Chaumont et al. 2012a; De Chaumont et al. 2012b) to generate a binary tomogram acting as a sample mask, i.e., to segment the sample's volume only. The latter is an 8-bit tomogram with only two possible voxel values: either 255, to indicate that a voxel is located inside the sample's volume, or 0, to indicate the opposite. Such sample mask allowed excluding the imaged areas surrounding the cylindrical sample from further analysis. Only one sample mask was generated per experiment. The remaining steps in the image analysis protocol were performed using the open-source software ImageJ (Schneider et al. 2012a; Schneider et al. 2012b), in particular, the Xlib plugin library (Münch 2022). We aimed at creating accurate phase material masks (i.e., binary 8-bit tomograms of the liquid, gas, and solid phases, respectively) of every analyzed tomogram, for extraction of single-phase image information. In the first step, we applied a K-means clustering algorithm (Lloyd 1982) on the 16-bit tomograms at each time instant. This aimed at associating all voxels belonging to every material phase to one single, distinct image voxel value. This was followed by a segmentation protocol, which also combined

artifacts removal (3D fill holes morphological operator) and background removal algorithms, resulting in corrected, binary masks for every material phase of the analyzed tomogram. The liquid phase binary mask was then used on the denoised version of the original 32-bit tomograms for extracting a final tomogram containing experimental information only in voxels belonging to this phase. This was performed in the same fashion for the air phase. The post-processing and analysis of the transport experiments were carried out using these final tomograms. A graphical summary of the image analysis protocol is shown in Appendix 3.A, Figure 3.7.

3.2.4 *Solute advance front reconstruction*

Our analysis of the mechanisms controlling the mixing behavior observed in the experimental results required the reconstruction of the solute plume's front. This was represented via the isosurface of 50% concentration ($c = 0.48$ M for the range of concentrations used in this study). To reconstruct this isosurface, we first used the software Paraview (Kitware 2023) to threshold the denoised 32-bit liquid phase tomograms and to extract single voxels belonging to the 49.8% – 50.2% concentration range. We created an analysis pipeline, implemented in Matlab (The MathWorks 2022), first to interpolate the obtained point cloud and to generate a continuous surface. We then corrected this surface using the liquid phase mask (see Section 3.2.3) to overwrite and set as image background all positions belonging to either the solid or the gas phase. The corresponding surface area was obtained by first triangulating the corrected isosurface using a moving observation window at the voxel scale of the images and then adding up the surface area of single triangular planes. Triangulation also allowed the generation of single *.stl files for reconstructing the corrected isosurface.

3.2.5 *Numerical simulations of flow*

Given the impossibility of obtaining a fully resolved velocity field from the experimental data only, we complemented our data set with additional 3D numerical simulations of flow. They consist in the solution of the Stokes flow equation for non-compressible flow for all experimental cases and also for the additional case $S_w = 1.00$. In these simulations, the spatial domain corresponded with the one occupied by the resident solution, thus the space throughout which transport and mixing occurred. Such spatial domain was obtained from a tomogram corresponding to a time step chosen at about half of each experiment

duration, via the image analysis workflow presented in the Appendix 3.A (see Figure 3.7 for a schematic summary of such workflow). Such digitized spatial domain was downsampled by a factor of five, compared with the original voxel size, thus leading to a spatial discretization scale of 13.75 μm . We also added the case $S_w = 1.00$ by using the tomogram of the entire sample's pore space. The tetrahedral meshing of the segmented liquid phase region was performed using the fTetWild algorithm (Hu et al. 2020) on these full-sample liquid phase masks. The obtained meshes were then imported into the Finite Elements Method software COMSOL Multiphysics for further analysis. Different boundary conditions were applied to simulate the same conditions tested during the experiments. They included a fixed inflow velocity at the inlet cross-section, a constant pressure at the outlet, and a no-slip boundary condition (zero velocity at the boundary) at all material interfaces. The use of the latter at the interface liquid-gas has been demonstrated to have a negligible impact, both in 2D and in 3D, on fluid flow velocity distributions in porous media (Guédon et al. 2019; Triadis et al. 2019). Further details on the numerical model setup can be found in Appendix 3.B. The main outputs of the simulations included resultant velocity magnitude and velocity tensor, vorticity tensor, shear rate tensor, and pressure at every node location. The values of such fields were extracted at a four-times smaller spatial resolution than that of the experimental data sets, i.e., over a regular grid of size 11 μm in all three principal directions. The results' post-processing revealed that PDFs of the listed fields' values experienced no significant variations when the numerical results were extracted at higher spatial resolutions. In the same fashion, no significant variations in the PDFs scalings were observed when using higher-resolution liquid phase masks for mesh generation. Both the resultant velocity fields and the vorticity magnitude fields obtained for every performed simulation are shown in Figures 3.9 and 3.10 of Appendix 3.B, respectively.

3.3 THEORETICAL CONCEPTS AND METRICS

3.3.1 Variance of the concentration field

The experimental concentration calibration allowed representing the tomographic datasets obtained from the synchrotron X-ray micro-tomography experiments as fields of solute concentration $c(\mathbf{x}, t)$ for every time step at every location of the pore space occupied by the liquid phase. We quantify mixing from these datasets in terms of concentration statistics, in particular through

computation of the variance of the concentration field $\sigma_c^2(t)$ at every time step t (Dentz et al. 2022; Jha et al. 2011). $\sigma_c^2(t)$ can be expressed as

$$\sigma_c^2(t) = \langle c(\mathbf{x}, t)^2 \rangle - \langle c(\mathbf{x}, t) \rangle^2, \quad (3.1)$$

where $\langle \cdot \rangle$ denotes the expected value over the entire ensemble of voxels in the liquid phase. σ_c^2 is thus a measure of the heterogeneity of the mixture, providing a good proxy for the amount of segregation existing between the resident solution and the continuously injected solute during the entire experiment duration.

3.3.2 Euler characteristic

Recent studies have highlighted the role of the topological complexity inherent to porous media in driving local fluid stretching, ultimately controlling transport, mixing, reactions, and biological processes occurring in porous systems (Lester et al. 2013; Lester et al. 2016). In order to assess this aspect, we first rely on a geometrical characterization of the wetting liquid phase topology, by means of the Euler characteristic χ , a topological invariant widely used in soil and porous systems research (Armstrong et al. 2019; Lester et al. 2016; Schlüter et al. 2016; Shih et al. 2022). In particular, it can be used to characterize the connectivity of the porous system, with strong implications on the divergence or convergence of streamlines, as it is directly linked to the dynamics of the skin friction field, i.e., to the occurrence of separation and reattachment points along boundary surfaces (Lester et al. 2016). It can be defined based on entities that describe a spatial region (Vogel 2002) (the pore space in this case) as

$$\chi = N - C + H, \quad (3.2)$$

where N is the number of isolated objects or clusters in the analyzed spatial domain, C is the number of redundant connections or loops, and H is the number of completely enclosed cavities. Negative values of χ describe a well-connected system, as it is usually the case for porous media, given that generally $N < C$ (Lester et al. 2016). Equation 3.2 can be expressed alternatively as a function of the number of voxels (n_c), faces (n_f), edges (n_e), and vertices (n_v) that form the 3D binary image representing the target geometrical domain (Michielsen and

De Raedt 2001), which in our case corresponds to the liquid wetting phase of every experiment. This results in

$$\chi = -n_c + n_f - n_e + n_v. \quad (3.3)$$

We used an optimized algorithm based on the immediate vicinity of every single voxel in the 3D binary tomogram of the segmented liquid phase, together with binary decision diagrams (Blasquez and Poiraudau 2003) for the computation of χ according to Eq. 3.3.

3.3.3 Helicity density

To further explore the impact of the liquid phase topology on flow streamlines, we also study the formation of secondary flows. In particular, we focus on the occurrence of helicity, a kinematical property that provides a quantitative measure of the spatial complexity of flow fields and that remains constant despite fluid deformation (Moffatt 1992; Sposito 2001). We quantify it through the helicity density h , which is expressed as the scalar product of the velocity vector (\vec{v}) and the vorticity vector ($\vec{\omega}$) fields

$$h = \vec{v} \cdot \vec{\omega}. \quad (3.4)$$

Both the velocity and vorticity fields were obtained from the numerical simulations of flow. The spatial distribution of both the resultant velocity magnitude and the vorticity magnitude over the entire pore space for all experiments are presented in Figures 3.9 and 3.10 of Appendix 3.B, respectively.

3.3.4 Q-Criterion

To further investigate the mechanisms controlling mixing in unsaturated porous media, we studied the control that the liquid phase saturation exerts on the interplay between the flow's shear deformation and the rotational one. The former results from local velocity differences along neighbouring streamlines, whereas the latter is induced by the occurrence of helical flow. For such purpose, we computed the Q-criterion (Hunt et al. 1988), an index that allows for vortex identification, suitable for the case of steady non-rotational flows (Haller 2005). It is expressed using the invariants of the 3D velocity gradient tensor, $\nabla\vec{v}$, i.e.,

the deformation rate tensor. It identifies a vortex whenever the second invariant, Q , of $\nabla\vec{v}$ is larger than zero, that is

$$Q = \frac{1}{2} (\|\mathbf{\Omega}\|^2 - \|\mathbf{S}\|^2) > 0, \quad (3.5)$$

where $\|\cdot\|$ indicates the Frobenius norm, $\mathbf{\Omega}$ is the non-symmetric portion of $\nabla\vec{v}$, i.e., the vorticity tensor, and \mathbf{S} is the symmetric counterpart of $\nabla\vec{v}$, i.e., the shear strain rate tensor (Hunt et al. 1988). Therefore, it can be used to locally quantify the excess of the rotation strain rate relative to the shear strain rate, hence hinting at the main mechanism behind local solute plume deformation. In addition, the Q -criterion also requires the pressure to be minimal compared to the ambient pressure inside the region identified as a vortex, as this guarantees that the neighbouring streamlines are indeed curved (Hunt et al. 1988).

3.4 RESULTS AND DISCUSSION

3.4.1 Lower saturation enhances mixing via a stronger solute front deformation

Results from five experiments are reported in this work, which cover saturation degrees spanning from 0.75 to 0.92 and tracer injection flow rates (q) ranging from $0.125 \text{ mm}^3 \text{ s}^{-1}$ to $0.50 \text{ mm}^3 \text{ s}^{-1}$. The latter values correspond to Péclet numbers, Pe , ranging from $Pe = 1.69$ to $Pe = 7.28$, respectively, where Pe represents the ratio between the characteristic time of diffusion and the characteristic time of advection over a characteristic length. It can be expressed as $Pe = \bar{v}\bar{\zeta}^2/2Da_t$, where \bar{v} is the mean flow velocity of every experiment; $D = 1.929 \times 10^{-9} \text{ m}^2 \text{ s}^{-1}$ is the average diffusion coefficient of the KI solution in the range of concentrations used in the experiment (Dunlop and Stokes 1951); $\bar{\zeta} = 30 \text{ }\mu\text{m}$ is the average pore size, computed from the distribution of pore sizes shown in Appendix 3.E, Figure 3.11; and $a_t \approx 15 \text{ }\mu\text{m}$ is the average pore throat size, approximated as one-fourth of the average glass beads diameter (Glover and Déry 2010). Table 3.1 summarizes the Pe numbers obtained for every experiment. Note that we have adopted $\bar{\zeta}$ as the characteristic length for advection, and a_t as the corresponding one for diffusion (Jiménez-Martínez et al. 2015; Markale et al. 2022). Figure 3.1b depicts the reconstructed concentration field for an experiment performed at $S_w = 0.82$ and at $q = 0.25 \text{ mm}^3 \text{ s}^{-1}$ at time $t = 50.4 \text{ s}$ after the tracer entered the sample, i.e., around 1/3 of the total experiment duration (refer to Movie S1 in the Supplementary Material, Appendix 3.D, for the entire time series). The combined effect of the porous medium heterogeneity and the presence of

S_w [-]	q [mm ³ s ⁻¹]	\bar{v} [$\times 10^{-4}$ m s ⁻¹]	Pe [-]	Ca [$\times 10^{-6}$]	PV [-]
1.00	0.250	1.49	2.32	1.78	-
0.92	0.250	1.85	2.88	2.21	5.13
0.89	0.250	1.49	2.31	1.77	5.00
0.82	0.250	1.96	3.05	2.34	5.44
0.76	0.500	4.68	7.28	5.58	7.84
0.75	0.125	1.09	1.69	1.30	3.33

Table 3.1: Summary of the flow characterization for all experiments reported in this study, and additionally also for the case $S_w = 1.00$, which was built up from the combination of the segmented tomograms of the liquid (KI solution) and the gas (air) phase. Values reported here were computed from the numerical flow simulations. Flow descriptors include the injection flow rate, q , the mean fluid flow velocity, \bar{v} , the Péclet number, Pe , the capillary number, Ca , and the total number of injected pore volumes during the entire experiment, PV . For the computation of both Pe and Ca , we used the average properties of the KI solution over the range of concentrations chosen for the experiments (0.06 M to 0.90 M) and at a temperature of 25 °C.

an immiscible-immobile phase manifests itself in the formation of preferential pathways, as highlighted in Figure 3.1b, which are usually referred to as the backbone of preferential flow (de Gennes 1983). This flow structure consists of channels of high velocity that allow for faster displacement of the tracer and for most of its transport.

We relied on the variance of the concentration field σ_c^2 (Dentz et al. 2022; Jha et al. 2011) to quantify and compare the mixing behavior across experiments. Figure 3.1c shows the variation in $\sigma_c^2 - \sigma_{c,t=0}^2$ over time, for all experiments, where $\sigma_{c,t=0}^2$ is the variance of the concentration field at time $t = 0$ s. This subtraction was applied to correct for some remaining noise in the tomograms at lower concentration values, right before starting the transport experiments, causing σ_c^2 at $t = 0$ s to slightly deviate from zero, i.e., when the entire porous space is occupied by the resident solution only. The results show an overall enhancement of mixing at lower S_w . All cases exhibit two clear phases. In the first phase at early times, both advection and diffusion contribute to solute transport, with the former controlling the increasing segregation of the two mixing liquids as the tracer enters the sample. This is reflected in an increase of σ_c^2 over time. Note here that the plume does not enter as a sharp front, since already some diffusion occurred at the inlet. A second phase begins at the stage of maximum

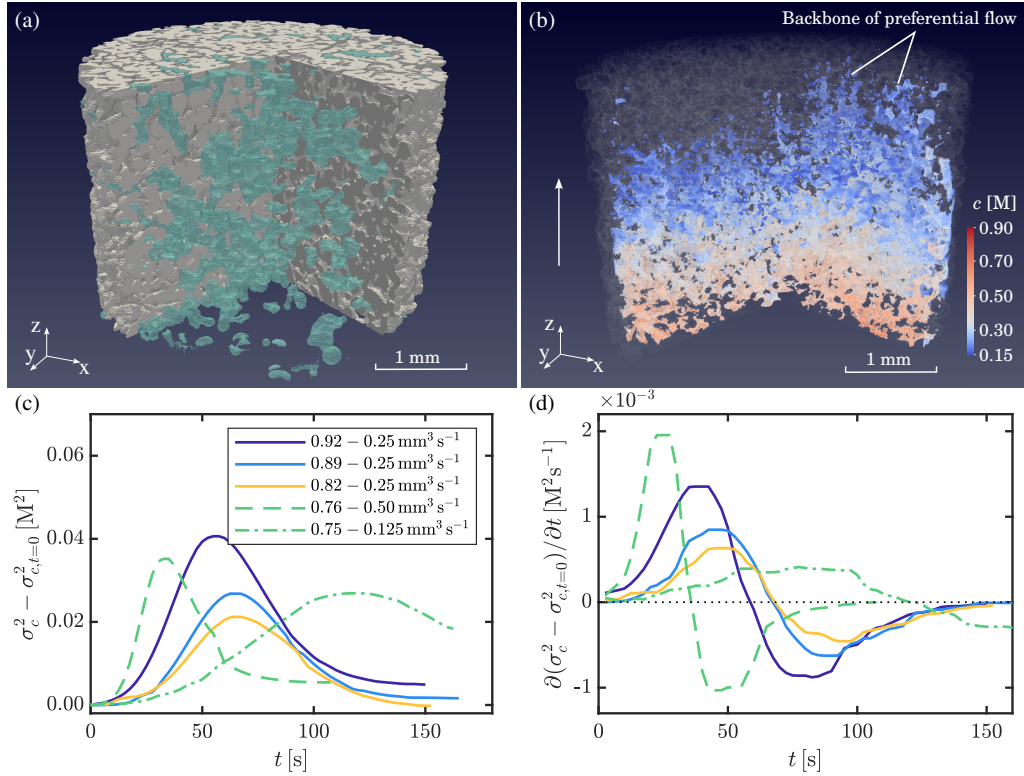


Figure 3.1: Concentration field and mixing quantification from synchrotron X-ray microtomography experiments. a) 3D reconstruction of the tested porous medium. Only three-quarters of the sample are displayed to allow the visualization of the gas phase (air, shown in cyan) inside of the pore space for the experiment performed at $S_w = 0.82$. b) Concentration field expressed in units of mole per unit of volume (molar concentration, M) for the experiment performed at $S_w = 0.82$ with a flow rate $q = 0.25 \text{ mm}^3 \text{ s}^{-1}$ at time $t = 50.4 \text{ s}$ after the tracer entered the sample. All concentration values lower than 0.15 M are not displayed for improved visualization. For the same purpose, the air phase is also not shown, whereas the solid phase of borosilicate glass grains is shown as grey transparency. Only three-quarters of the sample are displayed to better visualize the concentration differences inside the pore space. The white arrow indicates the main flow direction. The formation of a backbone of preferential flow is indicated on the upper right portion of the sample. c) Evolution of the variance of the concentration field, σ_c^2 , in time for all five transport experiments. The values of σ_c^2 have been corrected by the variance at time $t = 0 \text{ s}$, $\sigma_{c,t=0}^2$. d) Rate of change of σ_c^2 over time, $\partial(\sigma_c^2 - \sigma_{c,t=0}^2)/\partial t$, as computed from the results shown in panel c). For panels c) and d), different line types correspond to different injection flow rates, whereas different line colors correspond to different saturation degrees. Note that, in that regard and for facilitating experiment comparison, we have grouped together $S_w = 0.76$ and $S_w = 0.75$ given their very similar saturation degree.

segregation, i.e., highest $\sigma_c^2 - \sigma_{c,t=0}^2$, promoting the mixing of both tracer and resident solution. This reflects itself in a decreasing σ_c^2 in time. Results show that for the same q , lower S_w leads to smaller σ_c^2 , hence it induces a faster smoothing of the concentration gradients formed in the pore space during the transport process. At very similar S_w (less than 1% difference, i.e., cases $S_w = 0.76$ and $S_w = 0.75$), a higher q reduces the transit time of the solute, allowing for a more segregated condition to build up in the pore volume. This reflects itself in higher σ_c^2 values at early times, after which σ_c^2 rapidly decreases towards a well-mixed condition. Reducing q allows for diffusion to more effectively smooth out concentration gradients in the system before the plume has been largely dispersed. The latter point is better depicted when plotting $\sigma_c^2 - \sigma_{c,t=0}^2$ against the dimensionless time $\tau = t/t_{adv}$, where the advective time, $t_{adv} = \bar{\xi}/\bar{v}$, is the time required for the flow to bridge the average pore size $\bar{\xi}$ at the average flow velocity \bar{v} . This is shown in Appendix 3.E, Figure 3.13a, in which, after an identical increase of $\sigma_c^2 - \sigma_{c,t=0}^2$ in time for both $S_w = 0.76$ and $S_w = 0.75$, the latter case describes a lower maximum σ_c^2 .

The mixing analysis described so far can be further explained by taking a look at the derivative in time of the variance of concentration, $\partial(\sigma_c^2 - \sigma_{c,t=0}^2)/\partial t$, i.e., to the rate of change of segregation in time, as shown in Figure 3.1d. Under the same q , lower S_w described the lowest absolute $\partial\sigma_c^2/\partial t$ values among all cases tested experimentally, both in the phase of initial segregation and in the following diffusion dominated phase. The former can be explained by concentration gradients being enhanced in the liquid phase at lower S_w (Jiménez-Martínez et al. 2015; Markale et al. 2021) already at early times, resulting in a larger diffusive flux counteracting the segregation effect induced by advection. The latter is associated to incomplete mixing, i.e., the formation of not-fully mixed regions behind the plume's front, in which transport is mainly driven by diffusion, and whose formation is enhanced as saturation decreases (Markale et al. 2021).

The mechanism behind this mixing behavior is explained by looking at the evolution in time of the interface between the injected and the resident solution, i.e., at the plume's front where diffusion takes place. This interface between both mixing solutions can be analogously represented by the isosurface of 50% concentration ($c = 0.48$ M for the range of concentrations used in this study). Figure 3.2a shows such surface for $S_w = 0.92$ and $q = 0.25$ mm³ s⁻¹ at two specific time steps, $t = 30$ s shown in light red and $t = 60$ s shown in yellow (see Movie S2 in the Supplementary Material, Appendix 3.D, for the entire time series). The latter depicts an increase in the isosurface deformation as it moves through the sample, compared with an initial condition depicted by the former,

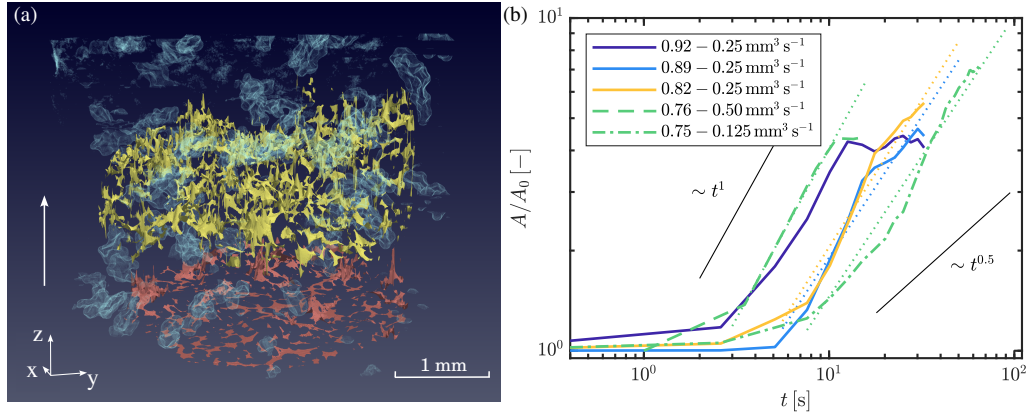


Figure 3.2: Analysis of the solute front deformation over time, as a function of the saturation degree. a) Deformation over time of the plume’s advancing front, here represented by the isosurface of 50% of concentration, shown at the time instants $t = 30$ s (in light red) and $t = 60$ s (in yellow), for the experiment performed at $S_w = 0.92$ and flow rate $q = 0.25 \text{ mm}^3 \text{ s}^{-1}$ (refer to Movie S2 in the Supplementary Material, Appendix 3.D, for a visualization of the entire time series). The solid phase of borosilicate glass grains is not displayed to improve the visualization, while the gas phase (air) is shown in semi-transparent cyan. The white arrow indicates the main flow direction. b) Temporal evolution of the area of the advancing front, A , normalized by the area computed at the initial time of the deformation analysis, A_0 . Different line types correspond to different injection flow rates, whereas different line colors correspond to different saturation degrees. Note that, in that regard and for facilitating experiment comparison, we have grouped together $S_w = 0.76$ and $S_w = 0.75$ given their very similar saturation degree. The respective power law fitting curves are displayed with dot lines for all cases except for $S_w = 0.92$, which is the only case that reaches a plateau at later times. Scalings for both a ballistic ($A/A_0 \sim t^1$) and a Fickian ($A/A_0 \sim t^{0.5}$) regime are displayed for visual reference.

when almost no deformation is visible. This feature is analyzed quantitatively in Figure 3.2b, which shows, for all experiments, the increase in time of the area, A , of the isosurface over the sample’s imaged length. For comparison, A has been divided by the corresponding value at the first time step considered in the analysis, A_0 . Note the shorter time range used for this analysis compared to the entire duration of the experiment, as reported in Figure 3.1c. That is because only time instants, at which the entire 50% concentration isosurface can be found inside the sample, are considered. Figure 3.2b shows that at high $S_w = 0.92$, the system still remains fairly homogeneous, causing a piston-like movement of the isosurface after some initial deformation has occurred, as indicated by

the plateau reached at long times (after $t \sim 11$ s) (Jiménez-Martínez et al. 2015). For lower S_w and under a constant q , we observed an enhancement of the isosurface deformation over time, manifested both in a larger maximum relative deformation and in a larger power-regression exponent (refer to Appendix 3.C, Table 3.2, for the magnitude of these exponents). The larger the volume of air in the pore space, the more the number of obstacles to be bypassed by the solute's plume to move through the system, enhancing the plume's dispersion and stretching. At very similar S_w , an increase of q leads to a higher rate of deformation in time. We hypothesize that the isosurface deformation will eventually reach a plateau at late times for all cases, given both the effect of diffusion recovering some of the deformation that occurred as the plume moves through the system and the finite size of the tested domain. In summary, both lower S_w and higher q enhance front deformation, increasing at a higher rate the interface area where mixing between the resident and the injected solution occurs. This translates into increased diffusive flux and enhanced mixing efficiency, i.e., smaller σ_c^2 (Jiménez-Martínez et al. 2015; Jiménez-Martínez et al. 2017). The results here reported show a super-diffusive scaling of A with time, in all cases, which highlights the non-Fickian nature of transport in unsaturated porous media (Jiménez-Martínez et al. 2017; Velásquez-Parra et al. 2022). Detailed information on the estimation and magnitude of the power-regression scalings shown in Figure 3.2b can be found in Appendix 3.C.

3.4.2 Dependence of mixing on hydrodynamics and air clusters volume

The different mixing regimes as a function of S_w can be further described by looking at the liquid flow velocities in the pore space. Figure 3.3a shows the probability density function (PDF), $p(v)$, obtained for the liquid flow velocity magnitude, v , as estimated for all cases from numerical simulations of flow. Further details on the numerical simulations are presented in the Methods section and in Appendix 3.B, where also a full visualization of the scalar field v is presented (see Figure 3.9). The velocity magnitude PDFs are characterized by two regimes, a power law-like behavior for low-velocity magnitudes, and an exponential scaling for high v -values, in agreement with both experimental and numerical results already reported in the literature (Datta et al. 2013; Guédon et al. 2019; Souzy et al. 2020; Velásquez-Parra et al. 2022). Note here the power law behavior obtained for the low-velocity range under fully saturated conditions, which reflects the role of the solid phase heterogeneity in leading to velocity magnitude PDFs that differ from those obtained in the presence of Poiseuille velocity distributions, as it is often the case in 2D analyses performed under

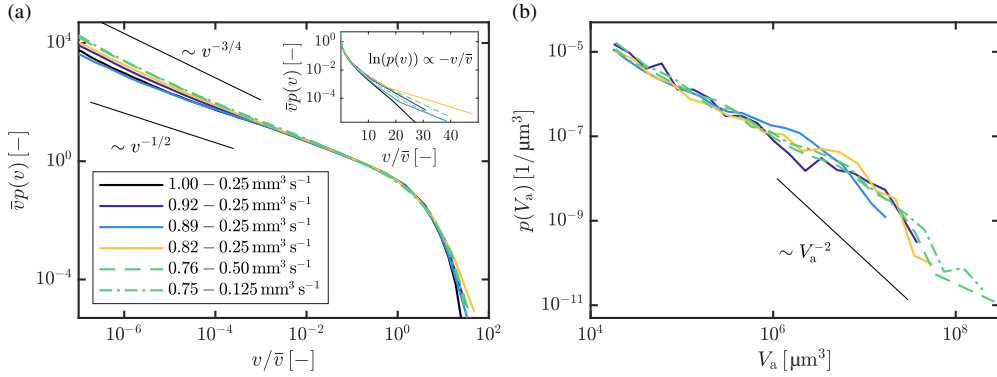


Figure 3.3: Hydrodynamic characterization and air clusters volume distribution as a function of saturation degree. a) Probability density function (PDF) of the liquid flow velocity magnitude, $p(v)$, computed in each case via 3D flow Finite Elements Method (FEM)-based numerical simulations. $p(v)$ has been normalized by the corresponding average velocity magnitude value, \bar{v} . $p(v)$ for the additional case $S_w = 1.00$ is also included. The Log-Log scale highlights the scaling of the low-velocity magnitudes, with exact power-law scalings also shown for visual reference only. A semi-Log plot is shown in the inset to display the exponential behavior at high-velocity magnitudes. b) PDF of the volume of air clusters, $p(V_a)$, for all experiments. $p(V_a)$ is expressed in units of μm^3 . The minimum volume considered corresponds to that of an average pore of size $\bar{\xi} = 30 \mu\text{m}$. The power-law scaling V_a^{-2} is shown for visual reference. In both panels, different line types correspond to different injection flow rates, whereas different line colors correspond to different saturation degrees. Note that, in that regard, we have grouped together $S_w = 0.76$ and $S_w = 0.75$ given their very similar saturation degree.

idealized conditions (de Anna et al. 2017). Lower S_w leads to a broader $p(v)$, characterized both by larger maximum velocities under constant q and by a larger $p(v)$ -value at lower velocity magnitudes. This reflects an enhancement of the so-called backbone, where large velocities are reached and through which most of the solute is transported, and of the so-called dead-ends of low velocities, which are less accessible for the solute (de Gennes 1983; Velásquez-Parra et al. 2022). Transport in these dead-ends is strongly influenced by molecular diffusion, as it is the main control on the solute's long residence times experienced in the presence of such low flow velocities. The enhancement of these two flow structures (backbone and dead-ends) translates into larger concentration gradients at their interface, in correspondence of lower S_w (Jiménez-Martínez et al. 2015), increasing the diffusive flux between them and further explaining the mixing enhancement.

Single differences in the trend described so far for $p(v)$ as a function of S_w are obtained for $S_w = 0.89$, which displays a less negative power law scaling for low velocities than $S_w = 0.92$. This difference is explained by the volume of air clusters inside the pore space, whose PDF $p(V_a)$ is shown in Figure 3.3b. Only volumes equal to or larger than the volume of an average pore, assumed equal to that of a sphere with a diameter equal to the estimated average pore size $\bar{\zeta} = 30 \mu\text{m}$, were considered, since they represent the gas phase hosted in the system by capillary forces. We observe a change in the $p(V_a)$ scaling at an air cluster volume $V_a \sim 1 \times 10^6 \mu\text{m}^3$, after which $p(V_a)$ shows for all cases a power law distribution with a scaling $p(V_a) \sim V_a^{-2}$ that very well matches previously published results obtained for 2D conditions (Jiménez-Martínez et al. 2017; Tallakstad et al. 2009b). This volume corresponds to that of a cluster with a size of approximately three average pore sizes. Counter-intuitively, Figure 3.3b depicts a narrower distribution for $S_w = 0.89$ than for $S_w = 0.92$, which translates into smaller air clusters in spite of the overall larger relative volume of air inside the pore space. This denotes a weaker effect of the air clusters at blocking the flow, leading to less enhancement of preferential pathways and dead-ends than for $S_w = 0.92$, as observed in its $p(v)$. For the remaining cases, a reduction of S_w leads to larger air cluster volumes as expected. These results point out the non-uniqueness of these multiphase systems and highlight the importance of both the air cluster volumes and their spatial distribution for defining the system's heterogeneity. These two elements further explain differences in the final area A of the 50%-concentration isosurface achieved under similar saturation degrees ($S_w \sim 0.75$; Figure 3.2b).

3.4.3 Backbone formation promotes helicity

To explain the mechanisms behind the isosurface deformation reconstructed from the experiments and presented in Figure 3.2a, we first characterise the liquid phase connectivity using as an index the Euler characteristic χ (see Eq. 3.2). Figure 3.4 shows a linear decrease of χ with decreasing S_w for the range of S_w considered in this work. Lower S_w thus improves the system's capacity for joining initially separated entities, due mainly to the formation of new redundant loops, i.e., larger C in Eq. 3.2. This promotes the spatial convergence of flow streamlines, increasing their tortuosity, as they now follow these newly opened loops and can connect to other distant pathways. Consequently, the formation of the preferential flow backbone is enhanced, as also shown by the increase of high velocities in the inset of Figure 3.3a. Similar variations of χ as a function of S_w have been observed for the connectivity of the non-wetting phase (Armstrong

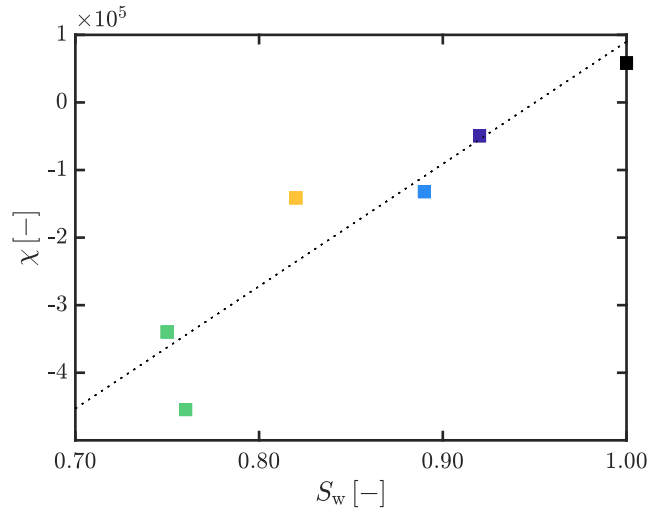


Figure 3.4: Euler characteristic, χ , of the liquid phase, as a function of saturation degree S_w , computed for every experiment at a single time step chosen at about half of its duration. Results were obtained in each case from binary tomographic images of the liquid phase of the entire sample (liquid phase mask, see Figure 3.7 in Appendix 3.A). A fully saturated condition $S_w = 1.00$ is also displayed for comparison. The best fitting line is displayed black dotted. The color criteria used for the markers follows the same one used in Figures 3.1c, 3.1d and 3.2b.

et al. 2016; Schlüter et al. 2016; Xu et al. 2020) and also of the wetting phase under imbibition-drainage cycles (Schlüter et al. 2016), although in simplified 3D geometries obtained with packed spherical (instead of irregularly shaped) glass beads. They also suggest an increase of χ at very low saturation degrees (not reached in this study) once non-wetting clusters start isolating portions of the wetting phase (Schlüter et al. 2016), i.e., increase in N in Eq. 3.2. Figure 3.4 also shows significant differences in χ for very similar saturation degrees ($S_w \sim 0.75$), further highlighting the topological non-uniqueness of unsaturated systems in spite of overall similar S_w .

The impact of the liquid phase connectivity changes expressed by χ on the flow streamlines is better understood by analysing the occurrence of secondary flows, i.e., helical flow, which we quantify by computing the helicity density h using Eq. 3.4. The scalar field h is directly related to the topology of the vorticity field itself (Moffatt 1992), as it reflects the linkage of vortex lines under a given flow field. This is of paramount importance for the analysis of streamlines deformation, as vorticity induces local rotation on streamlines around an axis

specified by the direction of $\vec{\omega}$, depending on the local orientation of the velocity field in reference to the vorticity one (Batchelor 2000; Sposito 2001). In particular, h has been used in Darcy-scale studies as a topological measure to showcase the occurrence of helical flow under anisotropic hydraulic conductivity fields both in homogeneous and heterogeneous porous media (Chiogna et al. 2016; Chiogna et al. 2014).

Figure 3.5a presents the absolute helicity density $\langle |h| \rangle$, averaged over the entire liquid phase, as a function of saturation degree. We have expanded our data set by performing additional numerical simulations to generate the flow field of every experimental saturation degree and also of the case $S_w = 1.00$ for every injection flow rate tested (keeping $C_a < 1.0$). Note that, for this purpose, we have grouped together $S_w = 0.75$ and $S_w = 0.76$ given their very similar magnitude, creating only one additional case for $S_w = 0.76$ at $q = 0.25 \text{ mm}^3 \text{ s}^{-1}$. All additional cases are displayed with circular markers, whereas the conditions tested experimentally are displayed with squared markers. Results indicate a linear increase of $\langle |h| \rangle$ as S_w decreases for the range of saturation degrees presented in this work. This indicates that the heterogeneity added to the system by the air clusters enhances the occurrence of helical flow in the liquid phase, which translates into an enhanced role of vortices in deforming flow streamlines. Figures 3.5b and 3.5c depict the case $S_w = 0.75$ and $q = 0.125 \text{ mm}^3 \text{ s}^{-1}$ as an example, where streamlines have been colored based on the local absolute helicity density and the air phase is shown in cyan. In Figure 3.5b, the occurrence of strong braiding is visible in the vicinity of an air bubble (see twisted ribbon arrow), which is linked to large $|h|$ -values. In contrast, streamlines travelling through the middle section of the nearby flow backbone describe low local $|h|$, showcasing no braiding and low deformation. Similarly, Figure 3.5c shows the convergence of two backbones into one common pore throat, with one group of streamlines experiencing large braiding and folding while bypassing air clusters, whereas the other group shows no distinctive deformation patterns and low $|h|$. Both cases illustrate the impact of the increased heterogeneity of the system and of the enhanced spatial convergence of streamlines, associated with lower S_w , on streamlines deformation, through mechanisms that have been described as main drivers of enhanced mixing and chaotic mixing behavior (Aref et al. 2017; Thiffeault and Finn 2006), namely braiding and folding. In particular, the occurrence of braiding has been strongly linked to the existence of non-zero helicity fields (Aref et al. 2017) and reflects characteristics of the flow topology (Thiffeault and Finn 2006). The occurrence of more twisted streamlines evidences the control of topology changes driven by saturation, as described in Figure 3.4, on the flow field.

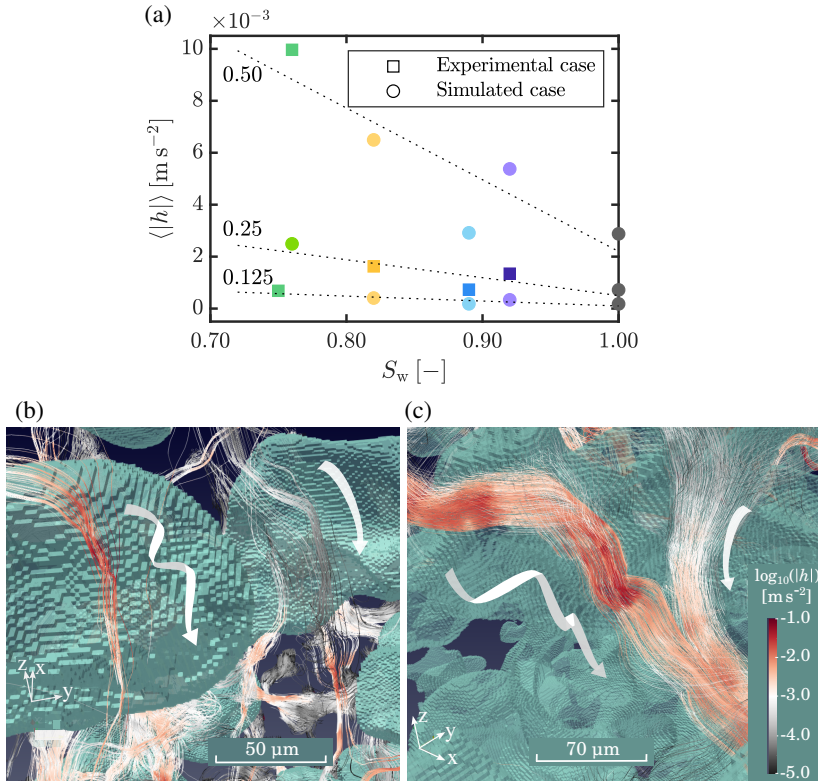


Figure 3.5: Analysis of the occurrence of helical flow in the pore space. a) Variation of the average absolute helicity density, $\langle |h| \rangle$, with S_w , for the three experimental injection flow rates $q = 0.125, 0.25$, and $0.50 \text{ mm}^3 \text{ s}^{-1}$. The conditions investigated experimentally are displayed with squared markers, whereas additional numerically simulated conditions are shown with circular markers. The dotted lines describe the linear trend obtained for the variation of $\langle |h| \rangle$ with S_w . The color criteria corresponds to that of Figures 3.1c, 3.1d and 3.2b. b) and c) show different streamlines deformation patterns induced by the occurrence and enhancement of helical flow in the system. These results correspond to the experiment performed at $S_w = 0.75$ and $q = 0.125 \text{ mm}^3 \text{ s}^{-1}$, with numerically generated streamlines colored based on the absolute local helicity ($\log_{10}(|h|)$) and with the air phase imaged experimentally displayed in semi-transparent cyan. The borosilicate glass grains are not displayed to improve visibility. White ribbon arrows describe the deformation pattern common to the different groups of streamlines: b) depicts the braiding of streamlines in the neighbourhood of an air bubble (see red streamlines on the left) and the absence of it for streamlines travelling along a backbone (see grey streamlines on the right); c) depicts the convergence of two groups of streamlines into the same backbone, with one group experiencing strong braiding and folding (red tones) and the other one showcasing no strong streamline deformation (grey tones).

Results also show an increase of $\langle |h| \rangle$ with increasing injection flow rate for a given saturation degree. In contrast, this dependency is not linear, given the larger growth rate of $\langle |h| \rangle$ with decreasing S_w for larger q . This trend can be deduced from Eq. 3.4, in which \vec{v} grows linearly, in the same proportion, with q , following the continuity equation. The increment of \vec{v} by a constant scalar function thus results in a linear growth of $\vec{\omega}$ in the same proportion. From the definition of h in Eq. 3.4, this renders the growth of $\langle |h| \rangle$ proportional to the square of the relative increase in q . Note also the narrower range of change in $\langle |h| \rangle$ for the data set corresponding to $S_w = 0.89$ (light blue markers) compared to the remaining cases. This is a consequence of the air clusters volume distribution shown in Figure 3.3b. Smaller air clusters impose fewer constraints on the flow field, hence causing less streamlines deformation.

3.4.4 Larger shear- and vorticity-dominated deformation at lower saturation degree

We now study the interplay between shear and rotational deformation on the local solute plume deformation by employing the Q -criterion (Hunt et al. 1988). We evaluated the scalar field Q expressed in Eq. 3.5, using the computed flow field. This allowed us to identify the regions where $Q > 0$, i.e., vorticity-dominated deformation, and those where $Q < 0$, i.e., shear-dominated deformation. Figure 3.6a reports the average of these two ensembles of positive and negative Q -values ($\langle Q \rangle$), respectively, over the entire liquid phase, as a function of saturation, for all tested injection flow rates. As previously explained for the computation of $\langle |h| \rangle$ in Figure 3.5a, we have included additional cases derived from numerical flow simulations, to obtain an estimate of Q for every experimental S_w at all three experimental q values. Note that we did not explicitly test the minimum pressure condition for every computed Q -value, since the curvature of flow streamlines is implicit in the occurrence of helical flow, as confirmed in Figure 3.5a.

The results show both a linear increase in the average positive Q -value and a linear decrease in the average negative Q -value with a reduction in saturation, similar to the behavior observed for $\langle |h| \rangle$ (Figure 3.5a). This indicates that the heterogeneity added by the presence of air in the system increases the magnitude of both shear strain rate and vorticity tensors. However, the increase of negative $\langle Q \rangle$ happens at a faster rate, pointing out a stronger enhancement of the shear strain deformation portion of the local deformation rate tensor. To complement these observations, Figure 3.6b shows the PDF of Q -values, $p(Q)$, for the experimental cases only, together with the case $S_w = 1.00$. Lower saturation degrees display a broader $p(Q)$, with larger positive and negative

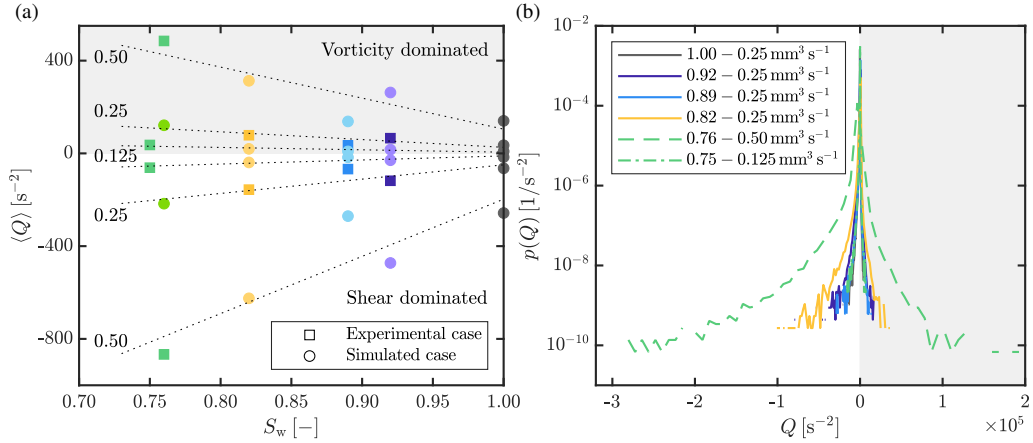


Figure 3.6: Impact of the saturation degree on how topology controls the solute plume deformation. a) Average positive and negative Q -criterion, $\langle Q \rangle$, as a function of S_w , for the three experimental injection flow rates, $q = 0.125, 0.25,$ and $0.50 \text{ mm}^3 \text{ s}^{-1}$. The conditions investigated experimentally are displayed with squared markers, whereas additional conditions, created numerically only, are shown with circular markers. The dotted lines describe the linear trends obtained for the variations of the respective indexes as a function of S_w . b) PDF of the Q -criterion, $p(Q)$, for the experimental cases only, plus the case $S_w = 1.00$, included for comparison. Different line types correspond to different injection flow rates, whereas different line colors correspond to different saturation degrees. Note that, in this regard, we have grouped together $S_w = 0.76$ and $S_w = 0.75$ given their very similar saturation degree. In both panels, we have indicated with grey shaded areas the range of Q -values associated to vorticity-dominated deformation.

values, which further confirms the behavior observed for $\langle Q \rangle$. $p(Q)$ also depicts a distribution skewed towards negative magnitudes that persists for all S_w considered in this work. From the two input variables, S_w and q , strong and non-monotonic variations in the skewness were observed only upon varying S_w , and not when varying q on the same system (see Appendix 3.E, Figure 3.14). Therefore, the system's heterogeneity arising from the presence and distribution of air is the main control on the relative occurrence of shear strain and vorticity-induced deformation. The skewness can even vary largely for very similar saturation degrees, as it occurs for the two cases $S_w = 0.75$ and $S_w = 0.76$. The former case displays a less skewed distribution, indicating that the solute plume deformation is no longer mainly associated to shear-induced stretching, but that more intensive bending is also taking place. This is reflected in the larger deformation of the 50%-concentration isosurface (plume's front deformation)

for $S_w = 0.75$ compared to $S_w = 0.76$ in spite of the very similar saturation (see Figure 3.2b). This interplay between shear-dominated and vorticity-dominated deformation corresponds to the stretching and folding deformation patterns that explain the occurrence of chaotic advection, as observed in previous studies on fully saturated conditions (Heyman et al. 2020; Lester et al. 2013).

Both shear- and vorticity-dominated deformations enhance the growth in time of the interface area between the resident and the injected solution, which contributes to a more efficient mixing through a faster dilution of the solute in the resident liquid phase. Both similar and contrasting mechanisms have been reported at the Darcy scale under fully saturated conditions. On the one side, numerical studies on 2D systems with heterogeneous permeability fields have pointed out the dominant role of shear-dominated regions in controlling solute plume dilution, while vorticity-dominated regions contributed significantly less (de Barros et al. 2012). On the other side, numerical 3D studies on anisotropic porous media have highlighted the role of folding and faster helical motion in enhancing dilution (Chiogna et al. 2016). Our results point out a combined effect of both shear-dominated and vorticity-dominated deformation regions on mixing enhancement. This is characterized by a generally larger contribution from shear, regardless of saturation, and by an increasing importance of vorticity as saturation decreases. These results agree with previous numerical studies at large scale that have shown the combined role of shear- and vorticity-dominated deformation regions on enhanced solute transport dynamics, highlighting the dominant role of pore-scale processes on large-scale observations (Geng et al. 2020). We further emphasize that the relative change in the indexes $\langle|h|\rangle$ and $\langle Q\rangle$ to a given relative change in saturation, as shown in Figures 3.5a and 3.6, is not unique, since it ultimately changes with heterogeneity, i.e., with the arrangement of material phases in the pore space. This has been shown in the non-unique change of connectivity in the system for very similar saturation degrees (see Figure 3.4 for $S_w = 0.75$ and $S_w = 0.76$). However, the trends shown here for the change of χ to S_w , and for $\langle|h|\rangle$ and $\langle Q\rangle$ as function of S_w , are expected to persist for the range of saturation degrees considered in this study. Figure 3.15 in Appendix 3.E further illustrates this point by comparing both $\langle|h|\rangle$ and $\langle Q\rangle$ to changes in χ based on the results plotted in Figures 3.4 to 3.6.

3.5 CONCLUSIONS

Taking advantage of 4D X-ray micro-tomography, performed with very high spatial and temporal resolutions at a synchrotron radiation X-ray imaging beamline, and of an extensive analysis of concentration and velocity vector fields

from both the respective experimental datasets and corresponding ones obtained from pore-scale numerical simulations, we have disentangled the mechanisms controlling mixing dynamics in unsaturated porous media under conditions relevant for natural systems. We reveal an enhancement of the mixing efficiency for lower saturation degrees, explained by the development of stronger helical flow. Lower saturation enhances the formation of the backbone of preferential flow via the convergence of different flow paths into preferential channels, resulting in more twisted streamlines, as reflected in a larger helicity density. By Q -criterion computations, we have shown that a lower wetting liquid phase saturation induces an enhancement of both shear- and vorticity-dominated deformation regions, with the former increasing at a faster rate and the latter becoming more relevant at lower saturation. This hints at the interplay between stretching and folding mechanisms (Heyman et al. 2020; Lester et al. 2013), especially at lower saturation degrees, as the main driver of the solute front deformation observed experimentally. Note also the strong impact of slightly unsaturated conditions on the solute front deformation and the mixing presented in this work. Further research will allow considering the effect of saturation degrees below the so-called critical saturation (Raouf and Hassanizadeh 2013), which are characterized by both a lower dispersivity (Raouf and Hassanizadeh 2013) and an increasing Euler characteristic (Schlüter et al. 2016) with decreasing S_w , on solute's deformation and mixing. We hypothesise contrasting trends to those presented here for such a range, i.e., weaker solute's front deformation and less efficient mixing as S_w decreases. Our results also indicate that the flow rate, i.e., fluid flow velocity magnitudes, is less relevant in the process of solute plume deformation and therefore a secondary control on mixing.

Solute mixing is relevant in natural and industrial systems, with applications ranging from soil remediation (Burauel and Baßmann 2005) to chemical reactors (Valdés et al. 2022). Our findings can contribute to the understanding of natural systems and assist in the design of industrial processes. The experimental and numerical framework we present can be a significant starting point to study the control of phase saturation on mixing dynamics with multiphase flow conditions (Berg et al. 2013), i.e., with the simultaneous displacement of both immiscible phases. While multiphase flow is expected to enhance mixing because of a new flow phenomenon, the control of phase saturation on mixing, documented and characterized in this study, is expected to persist. In particular, the inter-dependency between wetting and non-wetting phase topology and its variation in time has to be considered when addressing such flow conditions. The possibility to study dynamic processes within the ubiquitous multiphase systems at the relevant spatial and temporal scale using X-ray micro-tomography

opens up new research opportunities in further and more realistically studying similar systems under conditions that are very relevant in nature and for a wide spectrum of industrial applications. Aspects, such as temporal resolution, require special consideration and could potentially be further improved compared to the setup presented in this study, e.g., by enabling constant sample rotation during image acquisition and/or with the usage of more advanced sample rotation stages, allowing even faster rotation rates. However, for the purpose of vortex identification, the experiment design should consider any eventual additional rotational components to the flow derived from such conditions, demanding the use of rotation invariant vortex identification criteria (Haller 2005). In addition, newer technical advances could allow for a better compromise between the imaged field of view and achieved spatial resolution. Moreover, further optimization in the experimental protocol applied in this type of studies would contribute to optimizing beamtime usage, enabling both the accurate acquisition of replicates and the exploration of more experimental conditions (e.g., lower saturation degrees as those presented here). This would enrich the uncertainty quantification on similar data sets and applications. A robust image analysis protocol is also of paramount importance. We are confident that the protocol outlined in this study, and described in detail in Appendix 3.A, can find wider application for the correct visualization and segmentation of similar X-ray micro-tomography data sets involving real-time imaging of several material phases and/or a transported solute. Finally, while the porous geometry used in this study provided significant insights on mixing in unsaturated flows, further research on different geometries with additional sources of heterogeneity is still needed to understand the implications of our pore-scale findings on the response of large-scale systems. We believe that the scientific results and the novel experimental applications shown in this study will motivate the further study of similar processes, enriching our understanding of flow and transport in porous systems.

BIBLIOGRAPHY

- Ali, K., A. u. H. A. Shah, S. Bilal, and A. u. H. A. Shah (2009). "Surface tensions and thermodynamic parameters of surface formation of aqueous salt solutions: III. Aqueous solution of KCl, KBr and KI." In: *Colloids and Surfaces A: Physicochemical and Engineering Aspects* 337, pp. 194–199.
- Als-Nielsen, J. and D. McMorrow (2011). "Elements of modern X-ray physics." In: 2nd ed. John Wiley and Sons, Ltd. Chap. 1: X-rays and their interaction with matter.
- Aref, H., J. R. Blake, M. Budišić, S. S. Cardoso, J. H. Cartwright, H. J. Clercx, K. El Omari, U. Feudel, R. Golestanian, E. Guillard, G. F. Van Heijst, T. S. Krasnopolskaya, Y. Le Guer, R. S. MacKay, V. V. Meleshko, G. Metcalfe, I. Mezić, A. P. De Moura, O. Piro, M. F. Speetjens, R. Sturman, J. L. Thiffeault, and I. Tuval (2017). "Frontiers of chaotic advection." In: *Reviews of Modern Physics* 89, p. 025007.
- Armstrong, R. T., J. E. McClure, M. A. Berrill, M. Rücker, S. Schlüter, and S. Berg (2016). "Beyond Darcy's law: The role of phase topology and ganglion dynamics for two-fluid flow." In: *Physical Review E* 94, p. 043113.
- Armstrong, R. T., J. E. McClure, V. Robins, Z. Liu, C. H. Arns, S. Schlüter, and S. Berg (2019). "Porous media characterization using Minkowski functionals: theories, applications and future directions." In: *Transport in Porous Media* 130, pp. 305–335.
- Batchelor, G. K. (2000). *An Introduction to Fluid Dynamics*. Cambridge Mathematical Library. Cambridge University Press.
- Berg, S., H. Ott, S. A. Klapp, A. Schwing, R. Neiteler, N. Brussee, A. Makurat, L. Leu, F. Enzmann, J.-O. Schwarz, et al. (2013). "Real-time 3D imaging of Haines jumps in porous media flow." In: *Proceedings of the National Academy of Sciences of the United States of America* 110, pp. 3755–3759.
- Berkowitz, B., A. Cortis, M. Dentz, and H. Scher (2006). "Modeling non-fickian transport in geological formations as a continuous time random walk." In: *Reviews of Geophysics* 44, RG2003.
- Bevington, P. R. and D. K. Robinson (2003). *Data reduction and error analysis for the physical sciences*. New York, NY 10020: McGraw Hill Higher Education. Chap. Least-squares fit to a straight line.

- Blasquez, I. and J. Poiraud (2003). "Efficient processing of Minkowski functionals on a 3D binary image using binary decision diagrams." In: *Journal of WSCG* 11.
- Boon, M., B. Bijeljic, and S. Krevor (2017). "Observations of the impact of rock heterogeneity on solute spreading and mixing." In: *Water Resources Research* 53, pp. 4624–4642.
- Bordoloi, A. D., D. Scheidweiler, M. Dentz, M. Bouabdellaoui, M. Abbarchi, and P. de Anna (2022). "Structure induced laminar vortices control anomalous dispersion in porous media." In: *Nature Communications* 13, p. 3820.
- Buades, A., B. Coll, and J. M. Morel (2005). "A review of image denoising algorithms, with a new one." In: *Multiscale Modeling and Simulation* 4, pp. 490–530.
- Bührer, M., M. Stampanoni, X. Rochet, F. Büchi, J. Eller, and F. Marone (2019). "High-numerical-aperture microscope optics for time-resolved experiments." In: *Journal of Synchrotron Radiation* 26, pp. 1161–1172.
- Burauel, P. and F. Baßmann (2005). "Soils as filter and buffer for pesticides — experimental concepts to understand soil functions." In: *Environmental Pollution* 133, pp. 11–16.
- Chen, Y., H. Steeb, H. Erfani, N. K. Karadimitriou, M. S. Walczak, M. Ruf, D. Lee, S. An, S. Hasan, T. Connolley, N. T. Vo, and V. Niasar (2021). "Nonuniqueness of hydrodynamic dispersion revealed using fast 4D synchrotron X-ray imaging." In: *Science Advances* 7, eabj0960.
- Chiogna, G., O. A. Cirpka, and P. A. Herrera (2016). "Helical flow and transient solute dilution in porous media." In: *Transport in Porous Media* 111, pp. 591–603.
- Chiogna, G., M. Rolle, A. Bellin, and O. A. Cirpka (2014). "Helicity and flow topology in three-dimensional anisotropic porous media." In: *Advances in Water Resources* 73, pp. 134–143.
- Dankwerts, P. V. (1952). "The definition and measurement of some characteristics of mixtures." In: *Applied Scientific Research* 3, pp. 279–196.
- Datta, S. S., H. Chiang, T. S. Ramakrishnan, and D. A. Weitz (2013). "Spatial fluctuations of fluid velocities in flow through a three-dimensional porous medium." In: *Physical Review Letters* 111, p. 064501.
- De Chaumont, F., S. Dallongeville, N. Chenouard, N. Hervé, S. Pop, T. Provoost, V. Meas-Yedid, P. Pankajakshan, T. Lecomte, Y. Le Montagner, T. Lagache, A. Dufour, and J. C. Olivo-Marin (2012a). "Icy: An open bioimage informatics platform for extended reproducible research." In: *Nature Methods* 9, pp. 690–696.

- De Chaumont, F., S. Dallongeville, N. Chenouard, N. Hervé, S. Pop, T. Provoost, V. Meas-Yedid, P. Pankajakshan, T. Lecomte, Y. Le Montagner, T. Lagache, A. Dufour, and J. C. Olivo-Marin (2012b). *Icy: An open bioimage informatics platform for extended reproducible research. Version 2.1.3.0 [Software]*.
- De Anna, P., J. Jiménez-Martínez, H. Tabuteau, R. Turuban, T. Le Borgne, M. Derrien, and Y. Méheust (2014). "Mixing and reaction kinetics in porous media: An experimental pore scale quantification." In: *Environmental Science and Technology* 48, pp. 508–516.
- De Anna, P., T. Le Borgne, M. Dentz, A. M. Tartakovsky, D. Bolster, and P. Davy (2013). "Flow intermittency, dispersion, and correlated continuous time random walks in porous media." In: *Physical Review Letters* 110, p. 184502.
- De Anna, P., B. Quaipe, G. Biros, and R. Juanes (2017). "Prediction of the low-velocity distribution from the pore structure in simple porous media." In: *Physical Review Fluids* 2, p. 124103.
- De Barros, F. P., M. Dentz, J. Koch, and W. Nowak (2012). "Flow topology and scalar mixing in spatially heterogeneous flow fields." In: *Geophysical Research Letters* 39, p. L08404.
- De Gennes, P. G. (1983). "Hydrodynamic dispersion in unsaturated porous media." In: *Journal of Fluid Mechanics* 136, pp. 189–200.
- Dentz, M., J. J. Hidalgo, and D. Lester (2022). "Mixing in porous media: concepts and approaches across scales." In: *Transport in Porous Media* 146, pp. 5–53.
- Dentz, M., T. Le Borgne, A. Englert, and B. Bijeljic (2011). "Mixing, spreading and reaction in heterogeneous media: a brief review." In: *Journal of Contaminant Hydrology* 120, pp. 1–17.
- Desnoyers, J. E. and G. Perron (1972). "The viscosity of aqueous solutions of alkali and tetraalkylammonium halides at 25°C." In: *Journal of Solution Chemistry* 1, pp. 199–212.
- Dobson, K. J., S. B. Coban, S. A. McDonald, J. N. Walsh, R. C. Atwood, and P. J. Withers (2016). "4-D imaging of sub-second dynamics in pore-scale processes using real-time synchrotron X-ray tomography." In: *Solid Earth* 7, pp. 1059–1073.
- Dunlop, P. J. and R. H. Stokes (1951). "The diffusion coefficients of Sodium and Potassium iodides in aqueous solution at 25 C." In: *Journal of the American Chemical Society* 73, pp. 5456–5457.
- Geng, X., H. A. Michael, M. C. Boufadel, F. J. Molz, F. Gerges, and K. Lee (2020). "Heterogeneity affects intertidal flow topology in coastal beach aquifers." In: *Geophysical Research Letters* 47, e2020GL089612.

- Glover, P. W. and N. Déry (2010). "Streaming potential coupling coefficient of quartz glass bead packs: dependence on grain diameter, pore size, and pore throat radius." In: *Geophysics* 75, 1ND–Z138.
- Guédon, G. R., F. Inzoli, M. Riva, and A. Guadagnini (2019). "Pore-scale velocities in three-dimensional porous materials with trapped immiscible fluid." In: *Physical Review E* 100, p. 043101.
- Haller, G. (2005). "An objective definition of a vortex." In: *Journal of Fluid Mechanics* 525, pp. 1–26.
- Hasan, S., V. Joekar-Niasar, N. K. Karadimitriou, and M. Sahimi (2019). "Saturation dependence of non-Fickian transport in porous media." In: *Water Resources Research* 55, pp. 1153–1166.
- Hasan, S., V. Niasar, N. K. Karadimitriou, J. R. Godinho, N. T. Vo, S. An, A. Rabbani, and H. Steeb (2020). "Direct characterization of solute transport in unsaturated porous media using fast X-ray synchrotron microtomography." In: *Proceedings of the National Academy of Sciences of the United States of America* 117, pp. 23443–23449.
- Heyman, J., D. R. Lester, R. Turuban, Y. Méheust, and T. Le Borgne (2020). "Stretching and folding sustain microscale chemical gradients in porous media." In: *Proceedings of the National Academy of Sciences of the United States of America* 117, pp. 13359–13365.
- Hu, Y., T. Schneider, B. Wang, D. Zorin, and D. Panozzo (2020). "Fast tetrahedral meshing in the wild." In: *ACM Transactions on Graphics* 39, 117:1–117:18.
- Hunt, J., A. Wray, and P. Moin (1988). "Eddies, streams, and convergence zones in turbulent flows." In: *Center for Turbulence Research, Proceedings of the Summer Program*, pp. 193–208.
- Jha, B., L. Cueto-Felgueroso, and R. Juanes (2011). "Fluid mixing from viscous fingering." In: *Physical Review Letters* 106, p. 194502.
- Jiménez-Martínez, J., P. de Anna, H. Tabuteau, R. Turuban, T. Le Borgne, and Y. Méheust (2015). "Pore-scale mechanisms for the enhancement of mixing in unsaturated porous media and implications for chemical reactions." In: *Geophysical Research Letters* 42, pp. 5316–5324.
- Jiménez-Martínez, J., T. Le Borgne, H. Tabuteau, and Y. Méheust (2017). "Impact of saturation on dispersion and mixing in porous media: Photobleaching pulse injection experiments and shear-enhanced mixing model." In: *Water Resources Research* 53, pp. 1457–1472.
- Kang, P. K., P. de Anna, J. P. Nunes, B. Bijeljic, M. J. Blunt, and R. Juanes (2014). "Pore-scale intermittent velocity structure underpinning anomalous transport through 3-D porous media." In: *Geophysical Research Letters* 41, pp. 6184–6190.

- Karadimitriou, N. K., V. Joekar-Niasar, M. Babaei, and C. A. Shore (2016). "Critical role of the immobile zone in non-Fickian two-phase transport: A new paradigm." In: *Environmental Science and Technology* 50, pp. 4384–4392.
- Kitanidis, K. (1994). "The concept of the dilution index." In: *Water Resources Research* 30, pp. 2011–2026.
- Kitware, I. (2023). *Paraview. Version: 5.10.0 [Software]*.
- Lasseux, D., F. Valdés-Parada, and B. Wood (2021). "Recent developments in upscaling and characterization of flow and transport in porous media." In: *Advances in Water Resources* 150, p. 103886.
- Lavin, A., J. De Vicente, M. Holgado, M. F. Laguna, R. Casquel, B. Santamaria, M. V. Maigler, A. L. Hernandez, and Y. Ramirez (2018). "On the determination of uncertainty and limit of detection in label-free biosensors." In: *Sensors* 18, p. 2038.
- Lehoux, A. P., S. Rodts, P. Faure, E. Michel, D. Courtier-Murias, and P. Coussot (2016). "Magnetic resonance imaging measurements evidence weak dispersion in homogeneous porous media." In: *Physical Review E* 94, p. 053107.
- Lester, D. R., G. Metcalfe, and M. G. Trefry (2013). "Is chaotic advection inherent to porous media flow?" In: *Physical Review Letters* 111, p. 174101.
- Lester, D. R., M. G. Trefry, and G. Metcalfe (2016). "Chaotic advection at the pore scale: Mechanisms, upscaling and implications for macroscopic transport." In: *Advances in Water Resources* 97, pp. 175–192.
- Levy, M. and B. Berkowitz (2003). "Measurement and analysis of non-Fickian dispersion in heterogeneous porous media." In: *Journal of Contaminant Hydrology* 64, pp. 203–226.
- Li, L., K. Maher, A. Navarre-Sitchler, J. Druhan, C. Meile, C. Lawrence, J. Moore, J. Perdrial, P. Sullivan, A. Thompson, et al. (2017). "Expanding the role of reactive transport models in critical zone processes." In: *Earth-Science Reviews* 165, pp. 280–301.
- Lloyd, S. (1982). "Least squares quantization in PCM." In: *IEEE Transactions on Information Theory* 28, pp. 129–137.
- Markale, I., G. M. Cimmarusti, M. M. Britton, and J. Jiménez-Martínez (2021). "Phase saturation control on mixing-driven reactions in 3D porous media." In: *Environmental Science and Technology* 55, pp. 8742–8752.
- Markale, I., A. Velásquez-Parra, A. Alcolea, and J. Jiménez-Martínez (2022). "Mixing controlled adsorption at the liquid-solid interfaces in unsaturated porous media." In: *Transport in Porous Media* 146, pp. 159–175.
- Marone, F. and M. Stampanoni (2012). "Regridding reconstruction algorithm for real-time tomographic imaging." In: *Journal of Synchrotron Radiation* 19, pp. 1029–1037.

- Marone, F., C. M. Schlepütz, S. Marti, F. Fousseis, A. Velásquez-Parra, M. Griffa, J. Jiménez-Martínez, K. J. Dobson, and M. Stampanoni (2020). "Time resolved in situ X-Ray tomographic microscopy unraveling dynamic processes in geologic systems." In: *Frontiers in Earth Science* 7, p. 346.
- Michielsen, K. and H. De Raedt (2001). "Integral-geometry morphological image analysis." In: *Physics Reports* 347, pp. 461–538.
- Moffatt, H. K. (1992). "Helicity in laminar and turbulent flow." In: *Annual Review Fluid Mechanics* 24, pp. 281–312.
- Münch, B. (2022). *Xlib library of ImageJ plugins*.
- Okubo, A. (1970). "Horizontal dispersion of floatable particles in the vicinity of velocity singularities such as convergences." In: *Deep-Sea Research and Oceanographic Abstracts* 17, pp. 445–454.
- Ottino, J. M. (1989). *The Kinematics of mixing: stretching, chaos, and transport*. Cambridge, England: Cambridge University Press.
- Paganin, D., S. C. Mayo, T. E. Gureyev, P. R. Miller, and S. W. Wilkins (2002). "Simultaneous phase and amplitude extraction from a single defocused image of a homogeneous object." In: *Journal of Microscopy* 206, pp. 33–40.
- Puyguiraud, A., P. Gouze, and M. Dentz (2021). "Pore-scale mixing and the evolution of hydrodynamic dispersion in porous media." In: *Physical Review Letters* 126, p. 164501.
- Raouf, A. and S. M. Hassanizadeh (2013). "Saturation-dependent solute dispersivity in porous media: Pore-scale processes." In: *Water Resources Research* 49, pp. 1943–1951.
- Schlüter, S., S. Berg, M. Rücker, R. T. Armstrong, H.-J. Vogel, R. Hilfer, and D. Wildenschild (2016). "Pore-scale displacement mechanisms as a source of hysteresis for two-phase flow in porous media." In: *Water Resources Research* 52, pp. 2194–2205.
- Schneider, C. A., W. S. Rasband, and K. W. Eliceiri (2012a). *ImageJ. Version: 2.3.051 [Software]*.
- Schneider, C. A., W. S. Rasband, and K. W. Eliceiri (2012b). "NIH Image to ImageJ: 25 years of image analysis." In: *Nature Methods* 9, pp. 671–675.
- Shih, Y. H., S. Y. Hsu, Q. Z. Huang, K. Lamorski, M. C. Hu, C. W. Tsao, C. Sławiński, and N. Shokri (2022). "Euler characteristic during drying of porous media." In: *Drying Technology* 40, pp. 781–795.
- Simunek, J., M. T. van Genuchten, and M. Sejna (2008). "Development and applications of the HYDRUS and STANMOD software packages and related codes." In: *Vadose Zone Journal* 7, pp. 587–600.

- Souzy, M., H. Lhuissier, Y. Méheust, T. Le Borgne, and B. Metzger (2020). "Velocity distributions, dispersion and stretching in three-dimensional porous media." In: *Journal of Fluid Mechanics* 891, A16.
- Sposito, G. (2001). "Topological groundwater hydrodynamics." In: *Advances in Water Resources* 24, pp. 793–801.
- Szulczewski, M. L., C. W. MacMinn, H. J. Herzog, and R. Juanes (2012). "Lifetime of carbon capture and storage as a climate-change mitigation technology." In: *Proceedings of the National Academy of Sciences of the United States of America* 109, pp. 5185–5189.
- Tallakstad, K. T., H. A. Knudsen, T. Ramstad, G. Løvoll, K. J. Måløy, R. Toussaint, and E. G. Flekkøy (2009a). "Steady-state two-phase flow in porous media: statistics and transport properties." In: *Physical Review Letters* 102, p. 074502.
- Tallakstad, K. T., G. Løvoll, H. A. Knudsen, T. Ramstad, E. G. Flekkøy, and K. J. Måløy (2009b). "Steady-state, simultaneous two-phase flow in porous media: An experimental study." In: *Physical Review E* 80, p. 036308.
- Tang, J., M. Smit, S. Vincent-Bonnieu, and W. R. Rossen (2019). "New capillary number definition for micromodels: The impact of pore microstructure." In: *Water Resources Research* 55, pp. 1167–1178.
- The MathWorks, I. (2022). *MATLAB version: 9.13.0 (R2022b)*. Natick, Massachusetts, United States.
- ThermoFisher Scientific, I. (2022). *Avizo*.
- Thiffeault, J. L. and M. D. Finn (2006). "Topology, braids and mixing in fluids." In: *Philosophical Transactions of the Royal Society A: Mathematical, Physical and Engineering Sciences* 364, pp. 3251–3266.
- Triadis, D., F. Jiang, and D. Bolster (2019). "Anomalous dispersion in pore-scale simulations of two-phase flow." In: *Transport in Porous Media* 126, pp. 337–353.
- Valdés, J. P., L. Kahouadji, and O. K. Matar (2022). "Current advances in liquid–liquid mixing in static mixers: a review." In: *Chemical Engineering Research and Design* 177, pp. 694–731.
- Velásquez-Parra, A., T. Aquino, M. Willmann, Y. Méheust, T. Le Borgne, and J. Jiménez-Martínez (2022). "Sharp transition to strongly anomalous transport in unsaturated porous media." In: *Geophysical Research Letters* 49, e2021GL096280.
- Vogel, H.-J. (2002). "Topological characterization of porous media." In: *Morphology of Condensed Matter. Physical and Geometry of Spatially Complex Systems*. Ed. by K. Mecke and D. Stoyan. Springer.
- Weiss, J. (1991). "The dynamics of enstrophy transfer in two-dimensional hydrodynamics." In: *Physica D: Nonlinear Phenomena* 48, pp. 273–294.

- Xu, R., M. Prodanović, and C. Landry (2020). "Pore-scale study of water adsorption and subsequent methane transport in clay in the presence of wettability heterogeneity." In: *Water Resources Research* 56, e2020WR027568.
- Yu, Y., G. Chiogna, O. A. Cirpka, P. Grathwohl, and M. Rolle (2015). "Experimental evidence of helical flow in porous media." In: *Physical Review Letters* 115, p. 194502.

SUPPLEMENTARY MATERIAL TO CHAPTER 3

This appendix has been published as Supplementary Material to: Velásquez-Parra, A., F. Marone, R. Kaufmann, M. Griffa, & J. Jiménez-Martínez (2024). "Phase saturation control on vorticity enhances mixing in porous media". In: *Water Resources Research* 60, e2023WR036628. <http://doi.org/10.1029/2023WR036628>.

This Supplementary Material provides additional insights into the post-processing of the experimental results and numerical results reported in Chapter 3. Appendix 3.A presents a detailed description of the concentration calibration for the proper interpretation of the tomographic datasets. In addition, Appendix 3.B presents further details on the 3D numerical simulations of flow, while Appendix 3.C explains the power-law regression method performed for the evolution of the isosurface deformation, i.e., solute plume's front deformation. Figures 3.7 to 3.15 and Table 3.2 expand on the experimental protocol and on the post-processing of the experimental results, and show a summary of the results obtained from the numerical simulations. Furthermore, a description of the two Movies belonging to the Supplementary Material, which show the evolution in time of both the solute mixing and of the isosurface deformation as obtained from the 4D synchrotron X-ray micro-tomography experiments, is presented.

3.A EXPERIMENTAL CONCENTRATION CALIBRATION

The experiment calibration aimed at establishing a direct relationship between the concentration of KI in the liquid phase and the phase contrast values on the voxels of the reconstructed tomograms. This allows estimating the tracer's concentration at any location inside the pore space region occupied by the liquid phase and at any given time during the transport experiments. Note that the procedure described here could also be applied for calibrating the KI concentration to the adsorption values of the reconstructed tomograms. To achieve a calibration curve, we performed fourteen tomographic measurements of the entire sample, in each case after full saturation with an aqueous KI solution

at a different concentration, ranging between 0.06 M and 1.81 M. Thirteen of those were further used for creating the calibration curve, covering the range 0.06 M to 0.90 M. The difference between the two latter values was the chosen concentration difference between the resident solution and the tracer. In correspondence with each concentration solution, the phase contrast tomogram was reconstructed and post-processed using the same image analysis protocol described within the article and summarized graphically in Figure 3.7. With such a protocol, we could extract the 3D information of the liquid phase regions alone. The protocol led to a final data set of approximately 3×10^8 voxel values per calibration tomogram. Note here that certain regions of the resulting tomograms were excluded from this data set, in order not to jeopardize the calibration curve generation, as they would introduce additional uncertainty. These included regions occupied by the paraffin used to coat the flow cell, located at the borders of the sample, which were wrongly clustered by the K-means algorithm as part of the liquid phase. Additionally, we also excluded the first layer of voxels located at the boundaries with the solid phase, which contained spurious artifacts common in phase contrast tomograms at the boundaries between distinct material phases (so-called edge enhancement artifacts).

We used the procedure described in Lavin et al. (2018) and Bevington and Robinson (2003) to create a calibration curve via linear regression of the obtained calibration data, according to the model

$$V = ac + b, \quad (3.6)$$

where V is the tomographic voxel value (i.e., phase contrast intensity), c is the solute concentration, and a and b are the parameters of the linear regression model. We also relied on the statistical calibration approach described in Lavin et al. (2018) to quantify the uncertainty of the concentration values derived from the calibration curve. In both cases, we considered the liquid phase voxel values obtained from each calibration tomogram as a set of independent, measured signal realizations (measured statistical ensemble). We characterized every calibration point by the mean (V_i) and standard deviation (S_{V_i}) of such an ensemble (see Figure 3.8a). We also defined a representative statistical sample size (n) for this ensemble, i.e., the number of voxels that, after random sampling, could be considered representative of the entire population. For this purpose, we adopted the median absolute deviation from the median value (MAD) as the statistical metric for the representativeness decision criterion, given its smaller sensitivity to statistical sample outliers. We computed the increase in the MAD of a sample of voxel values as a function of the sample size for every tomogram

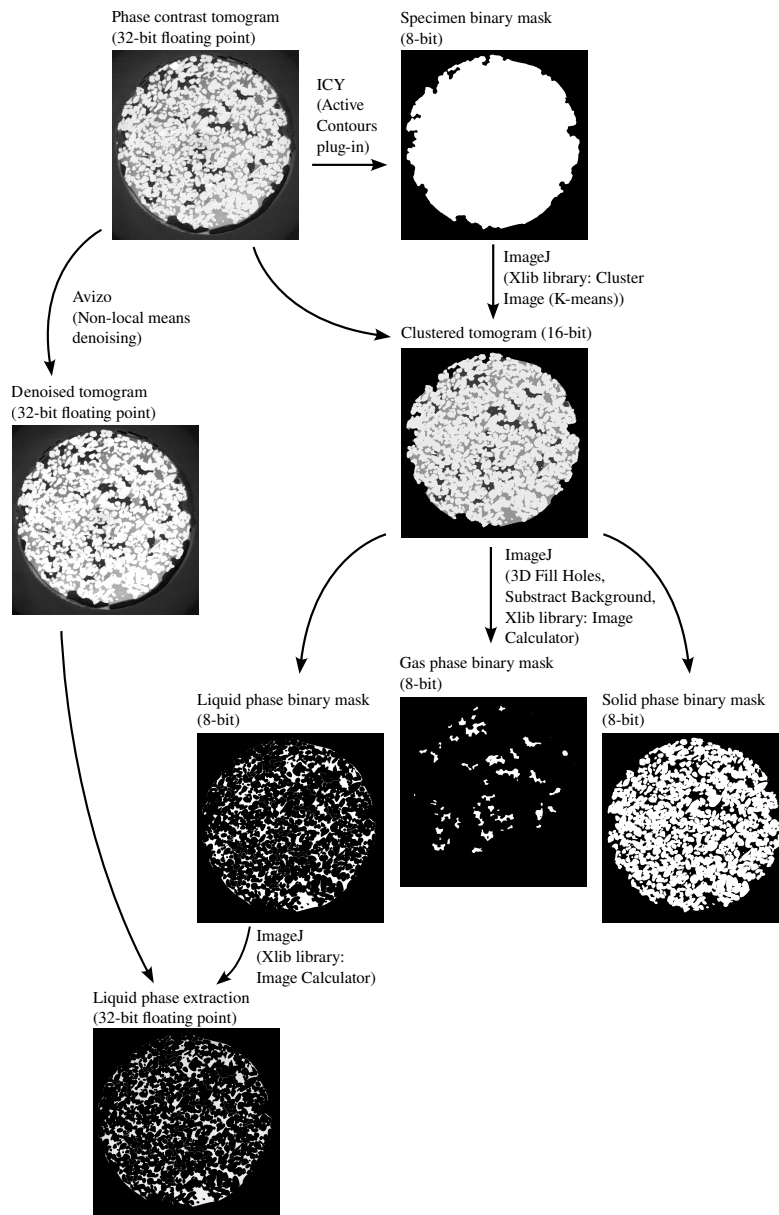


Figure 3.7: Graphical summary of the image analysis protocol used for the post-processing and quantitative evaluation of the reconstructed transport experiments. The protocol was also used for the analysis of the calibration tomograms. All processes depicted here were performed in 3D, i.e., considering all slices in the image stack representing every tomogram, hence taking into account 3D connectivity and continuity of the different material phases. For every step, both the software used and the corresponding plugin(s) are listed.

independently. Such statistical samples were created by randomly choosing voxels from the corresponding liquid phase calibration tomogram. The results are presented in Figure 3.8b for all calibration experiments. They indicate that the MAD stabilizes and reaches a plateau around a sample size of 500 voxels, for all cases, which allowed us to define $n = 500$ voxels.

The parameterization of the linear relationship between voxel value and concentration was achieved by minimizing the weighted sum of the deviations between the sample and the fitted values, i.e., a traditional least-squares fit. Here we assumed that the uncertainty of the concentrations, i.e., the uncertainty associated with the preparation of the injected solution, was negligible, compared to that resulting from the tomographic acquisition. For each calibration tomogram, we also hypothesized that the voxel value of the liquid phase, as a random variable, followed a Gaussian distribution, i.e., that the representative statistical sample of size n was drawn from a Gaussian distribution. We used the Kolmogorov-Smirnov test to provide some ground for this hypothesis. The null hypothesis was in this case that the measured liquid phase voxel values were independent samples from a Gaussian distribution. The results of such a test indicate a Kolmogorov-Smirnov metric equal to zero for all concentration cases. In addition, the corresponding p -values reached values not lower than 0.2 in all cases, which are considerably larger than 0.05, the significance level we chose (95% confidence interval used in the hypothesis test). Thus, with such a confidence interval, the null hypothesis could not be rejected in any concentration case. These results helped us reinforce our assumption that the sampled values were as if actually drawn from a Gaussian distribution.

The linear regression parameters a and b are defined for a total of N calibration points (i.e., in this case, tomograms) as

$$a = \frac{1}{\Delta} \begin{vmatrix} \sum_{i=1}^N \frac{1}{S_{V_i}^2} & \sum_{i=1}^N \frac{V_i}{S_{V_i}^2} \\ \sum_{i=1}^N \frac{c_i}{S_{V_i}^2} & \sum_{i=1}^N \frac{c_i V_i}{S_{V_i}^2} \end{vmatrix}, \quad (3.7)$$

$$b = \frac{1}{\Delta} \begin{vmatrix} \sum_{i=1}^N \frac{V_i}{S_{V_i}^2} & \sum_{i=1}^N \frac{c_i}{S_{V_i}^2} \\ \sum_{i=1}^N \frac{c_i V_i}{S_{V_i}^2} & \sum_{i=1}^N \frac{c_i^2}{S_{V_i}^2} \end{vmatrix}, \quad (3.8)$$

$$\Delta = \begin{vmatrix} \sum_{i=1}^N \frac{V_i}{S_{V_i}^2} & \sum_{i=1}^N \frac{c_i}{S_{V_i}^2} \\ \sum_{i=1}^N \frac{c_i}{S_{V_i}^2} & \sum_{i=1}^N \frac{c_i^2}{S_{V_i}^2} \end{vmatrix}, \quad (3.9)$$

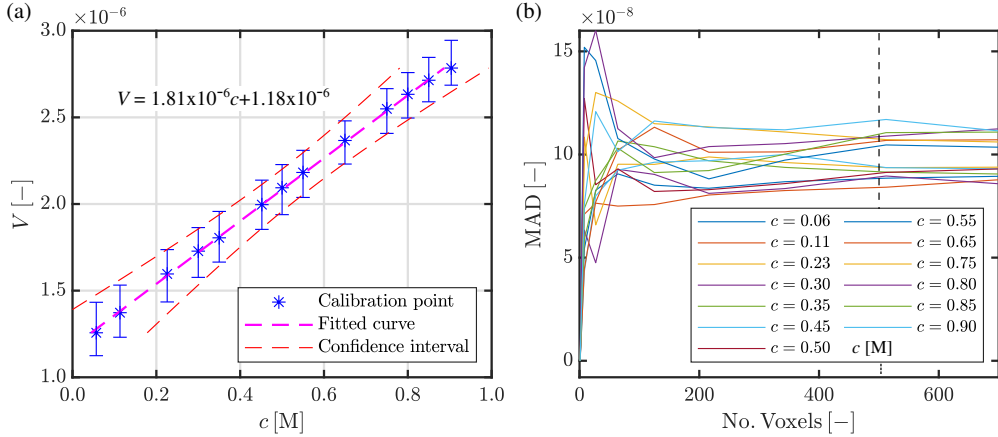


Figure 3.8: Summary of the experiment calibration process. a) Calibration curve relating the tomographic voxel value (i.e., phase contrast intensity), V , and the solute concentration, c , obtained following the procedure described in Appendix 3.A. All thirteen pairs of points used for the calibration are shown in blue markers and represent the average voxel value of the calibration tomogram, V_i , and their corresponding concentration values. The error bars represent the standard deviation of the voxel values, S_{V_i} , for every calibration tomogram. The obtained linear relationship is shown in the magenta dashed line. Red dashed lines represent the 99% confidence intervals obtained for the concentration estimation. The resulting linear equation is also shown. b) Variation in the median absolute deviation from the median value (MAD) of a sample of voxel values, with the increasing number of sampled voxels. This was used for estimating the representative statistical sample size, to be used for defining the confidence intervals shown in a). MAD-values stabilize around a value of 500 voxels for all cases.

where c_i is the concentration of the i -th calibration tomogram and $|\cdot|$ denotes the determinant of the resulting matrix. Such calculation resulted in the following calibration curve

$$V = 1.81 \times 10^{-6}c + 1.18 \times 10^{-6}, \quad (3.10)$$

which was further used to convert the voxel values in the experimental tomogram into their corresponding concentrations ones.

The uncertainty of any concentration value calculated by Eq. 3.10, (u_c), was estimated by standard error propagation calculation (Lavin et al. 2018). We considered the uncertainties, u_a and u_b , of the regression parameters (refer to Lavin et al. (2018) for their full expressions) as well as that of the voxel values, u_V , to be plugged into the calibration curve. The latter uncertainty can be expressed as the standard error of the mean, i.e., $u_V = S_V/n$. Given that we do

not have replicates of every experiment, we estimated u_V using the calibration data set, since we can assume every calibration voxel value as an independent measurement. We chose S_V as the maximum of the standard deviations of the thirteen calibration data sets, given their slightly heteroscedastic nature, and we adopted $n = 500$ as explained from Figure 3.8b. Based upon all these working definitions, we could compute u_c as

$$u_c = k \left[\frac{1}{a} \sqrt{\frac{S_V}{n} + u_b^2 + \left(\frac{b-y}{a}\right)^2 u_a^2} + 2 \left(\frac{y-b}{a}\right) u_a u_b r(a,b) \right], \quad (3.11)$$

where $k = 3$, to set a confidence interval of 99%, and $r(a,b)$ represents the correlation coefficient between the parameters a and b .

Figure 3.8a depicts the calibration curve obtained from the procedure described so far. The data from the calibration tomograms exhibited a very clear voxel value *versus* concentration linear relationship, with a Pearson's correlation coefficient of 0.9996. The depicted error bars represent the standard deviation of every calibration point, S_{Vi} . The confidence intervals (red dashed line) result from adding and subtracting u_c to any given concentration value in the analyzed range. The results show slightly larger uncertainties toward the extreme concentration values.

3.B NUMERICAL FLOW SIMULATIONS

Numerical simulations of steady-state flow through the liquid phase were performed for every case analyzed experimentally, and additionally also for the fully saturated condition. They were performed using the Finite-Elements-Method (FEM) software COMSOL Multiphysics 6.0. Given the steady-state flow conditions imposed in the experiment, only one tomogram per experiment was employed to build up the simulation spatial domain. This is further supported by the observation of no significant variations in the liquid phase geometry during the experiment, as the saturation degree was preserved in each case at all imaged time instants. An experiment tomogram at approximately half of the whole experiment duration was thus chosen for this purpose.

The computational spatial domain was created based on the liquid phase binary mask obtained for the chosen tomogram (see Figure 3.7). We generated a finite element tetrahedral mesh based on this tomographic data set using the open-source algorithm fTetWild (Hu et al. 2020). To reduce the computational demands, we decreased the resolution of the input binary masks by a factor

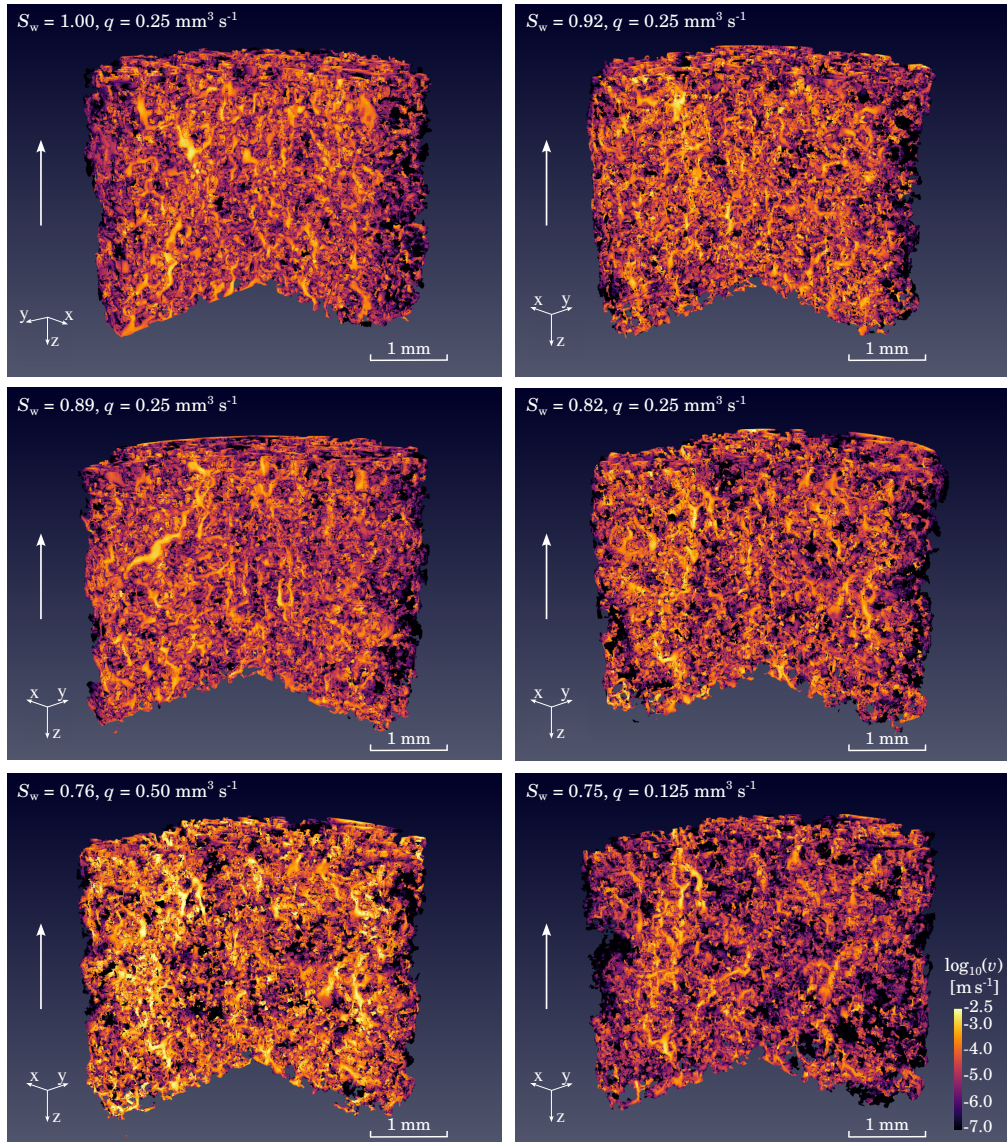


Figure 3.9: Scalar fields of the resultant velocity magnitude in the liquid phase obtained from the steady-state Stokes flow simulations, displayed as the logarithm of the velocity magnitude v , $\log_{10}(v)$. The color bar is common to all panels, with lighter colors depicting larger velocity magnitudes. Regions where $\log_{10}(v) < -7.0$ are depicted in black and those where $\log_{10}(v) > -2.5$ are shown in the brightest yellow. All five experimental cases are shown together and described by their corresponding liquid phase saturation degree S_w and injection flow rate q . The fully saturated case $S_w = 1.00$ is also shown for reference. Three-quarters of the sample are displayed in all cases to better visualize the inner flow structures. The white arrows indicate the main flow direction.

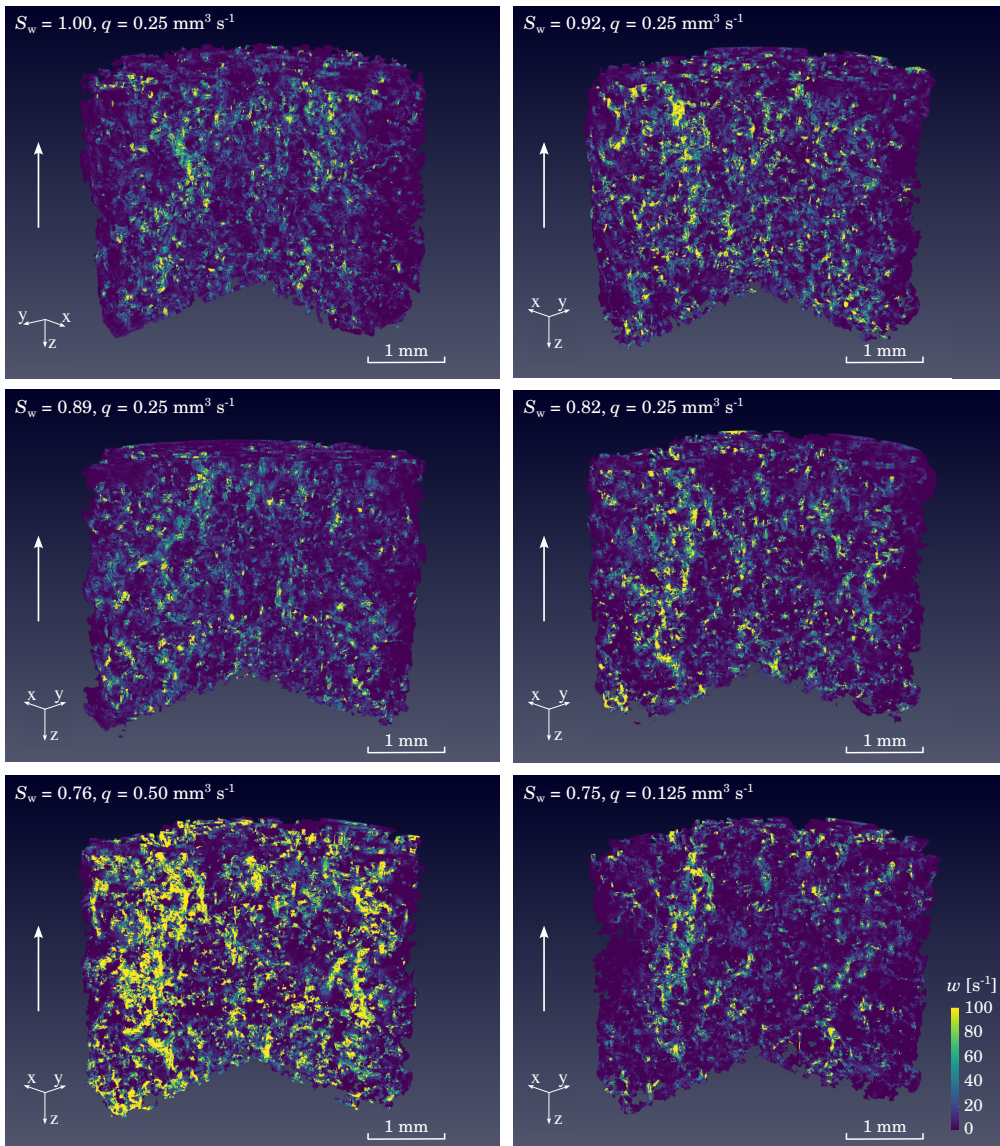


Figure 3.10: Scalar fields of the vorticity magnitude ω in the liquid phase obtained from the steady-state Stokes flow simulations. The color bar is common to all panels, with lighter colors depicting larger vorticity magnitudes. Regions where $\omega > 100 \text{ s}^{-1}$ are shown in the brightest yellow. All five experimental cases are shown together and described by their corresponding liquid phase saturation degree S_w and injection flow rate q . The fully saturated case $S_w = 1.00$ is also shown for reference. Three-quarters of the sample are displayed in all cases to visualize the inner scalar field magnitudes better. The white arrows indicate the main flow direction.

of five, i.e., a final voxel size of $13.75\ \mu\text{m}$ in all three principal directions. This was supported by comparing results obtained from simulations built up with meshes generated with higher-resolution binary masks. In particular, these did not expose significant variations in the probability density functions of the target variables. The final meshes were then imported into COMSOL Multiphysics, where a Stokes flow simulation was set up. This aimed at simulating the exact same flow conditions present during the experiment. We did this by assigning a constant velocity at the inlet, resulting from the relationship between the injection flow rate used during the corresponding experiment and the pore space cross-section area at the bottom of the sample. In addition, we also defined a pressure difference inside the sample, i.e., between the inlet and outlet, equal to the constant pressure measurement registered during the tracer injection phase of the experiment. This amounts to a pressure difference ranging from $\Delta p = 0.31\ \text{Pa}$ for the injection flow rate $q = 0.125\ \text{mm}^3\ \text{s}^{-1}$ up to $\Delta p = 1.23\ \text{Pa}$ for $q = 0.50\ \text{mm}^3\ \text{s}^{-1}$. We used a no-slip boundary condition at the interface between all material phases, i.e., the fluid velocity was set to zero at the boundaries. The use of this boundary condition at the interface liquid-gas has been demonstrated to have a negligible impact, both in 2D and in 3D, on fluid flow velocities in porous media (Guédon et al. 2019; Triadis et al. 2019). The resulting velocity and vorticity fields (magnitude thereof) are shown in Figures 3.9 and 3.10 for all six cases, respectively. Such renderings depict the strong local velocity variations caused by the porous medium's local heterogeneity. The effects of a lower saturation degree on the flow field are also visible. The development of a clearer backbone of preferential pathways (see, for example, the $S_w = 0.82$ case), as well as the development of larger and more abundant dead-ends of low velocities (see more abundant darker regions for the $S_w = 0.75$ case), are recognized.

The main outputs of the numerical flow simulations included local values of the liquid velocity magnitude, the velocity tensor, the vorticity tensor, the shear rate tensor, and the pressure fields. They were extracted at a scale of $11\ \mu\text{m}$, i.e., four times smaller spatial resolution than that of the experiments.

3.C POWER FUNCTION REGRESSION OF THE EVOLUTION IN TIME OF THE SOLUTE PLUME'S FRONT DEFORMATION

The experimental results allowed the reconstruction of the solute plume's front at every time instant imaged during the experiments, for all conditions tested. The front was represented by the isosurface of the 50% of concentration, whose area, A , was computed and plotted against time, t , as shown in Section 3.4.1, Figure 3.2b. The results indicate a power law increase of A/A_0 in time, where

A_0 corresponds to the isosurface area at time $t = 0$ s. This occurs for all cases, except for the experiment performed at a saturation degree $S_w = 0.92$ and an injection flow rate $q = 0.25 \text{ mm}^3 \text{ s}^{-1}$, which shows a plateau at late times. We performed a regression on the data series displaying a power law trend to follow the function

$$Y = \beta t^\alpha, \quad (3.12)$$

where $Y = A/A_0$, and β and α are the power function parameters. The regression was performed using the least-squares method over the linear equation

$$\ln Y = \ln \beta + \alpha \ln t, \quad (3.13)$$

that is, over the logarithmic values of Y and t . Considering $\tilde{Y} = \ln Y$ and $\tilde{t} = \ln t$, the regression parameters β and α can then be expressed as

$$\alpha = \frac{(n \sum_{i=1}^n \tilde{Y}_i \tilde{t}_i - \sum_{i=1}^n \tilde{Y}_i \sum_{i=1}^n \tilde{t}_i)}{(n \sum_{i=1}^n \tilde{t}_i^2 - (\sum_{i=1}^n \tilde{t}_i)^2)}, \quad (3.14)$$

$$\beta = \frac{(\sum_{i=1}^n \tilde{Y}_i - \alpha \sum_{i=1}^n \tilde{t}_i)}{n}, \quad (3.15)$$

where n is the total number of data points included in the regression. The results of the regression for all experimental cases are summarized in Table 3.2. They describe an increase in the exponent α both for a decrease in S_w under constant q , and also for an increase in q at very similar S_w (less than 1% difference, i.e., cases $S_w = 0.76$ and $S_w = 0.75$). This indicates a faster isosurface deformation in time for such conditions.

3.D MOVIE CAPTIONS

3.D.1 *Movie S1.*

Evolution in time of the concentration field for the transport experiment performed at $S_w = 0.82$ with a flow rate $q = 0.25 \text{ mm}^3 \text{ s}^{-1}$. The video depicts initially the spatial distribution of the three material phases, with the liquid phase shown in blue, the air phase shown in cyan, and the solid phase displayed in light grey. Subsequently, the entrance and movement of the tracer inside the pore space is depicted as a concentration field, expressed in units of mole per unit of volume (molar concentration, M). All concentration values lower than 0.15 M are not displayed for improved visualization. For the same purpose, the

S_w [-]	q [mm ³ s ⁻¹]	β	α	R^2
0.89	0.250	0.270	0.848	0.961
0.82	0.250	0.268	0.883	0.965
0.76	0.500	0.387	1.019	0.998
0.75	0.125	0.209	0.842	0.963

Table 3.2: Results of the regression performed for the evolution in time of the area A of the isosurface of 50% of concentration, i.e., solute plume's front. The regression follows the equation $Y = \beta t^\alpha$, where $Y = A/A_0$, being A_0 the isosurface area at time $t = 0$ s, and β and α are the parameters of the power function. The regression was performed using the least-squares method over the logarithmic values of Y and t , that is, over the linear equation $\ln Y = \ln \beta + \alpha \ln t$ (see Appendix 3.C). The Pearson correlation coefficient, R^2 , obtained in every case for the regression is also reported. Results indicate an increase in the power law scaling, α , due to both a decrease in saturation degree, S_w , under constant injection flow rate of the solute, q , and an increase in q at very similar S_w .

air phase is also not shown, whereas the solid phase of borosilicate glass grains is shown as grey transparency. Note that only 3/4 of the sample is displayed to observe concentration gradients inside of the sample. The white arrow indicates the main flow direction.

3.D.2 *Movie S2.*

Deformation over time of the plume's advancing front, here represented by the isosurface of 50% of concentration, for the experiment performed at $S_w = 0.92$ and flow rate $q = 0.25$ mm³ s⁻¹. The video depicts initially the spatial distribution of the three material phases, with the liquid phase shown in blue, the air phase shown in cyan, and the solid phase displayed in light grey. Subsequently, the plume's advancing front is shown, starting from an almost undeformed condition close to the inlet, in which the plane covers the cross-section of the liquid phase, transitioning to conditions of increased deformation at later times, up until the isosurface reaches the outlet. Different surface colors represent different time steps. The solid phase of borosilicate glass grains is not displayed to improve the visualization, while the gas phase (air) is shown in semi-transparent cyan. The white arrow indicates the main flow direction.

3.E ADDITIONAL SUPPLEMENTARY MATERIAL

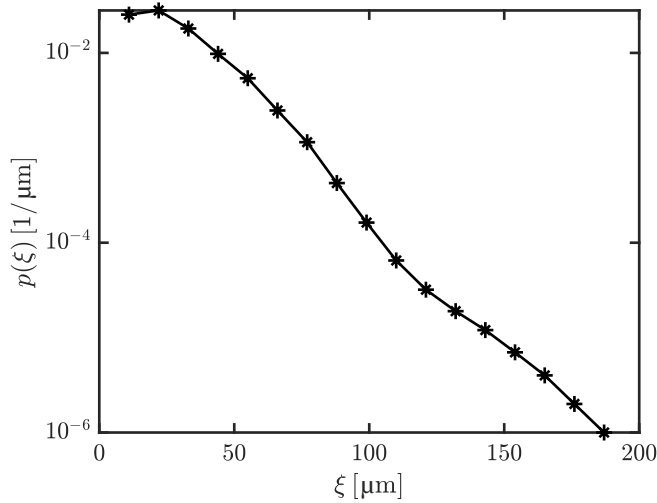


Figure 3.11: Probability density function, $p(\xi)$, of the pore size, ξ , computed for the porous medium made of sintered irregularly shaped borosilicate glass grains, used in all transport experiments. A 3D rendering of the tomographic reconstruction of the entire sample is shown in Figure 3.12b. The distribution was obtained by using the Pore Size Distribution algorithm, available on the Xlib plugin library (Münch 2022) on the free-source software ImageJ. From this distribution, we computed the average pore size, $\bar{\xi} = 30 \mu\text{m}$.

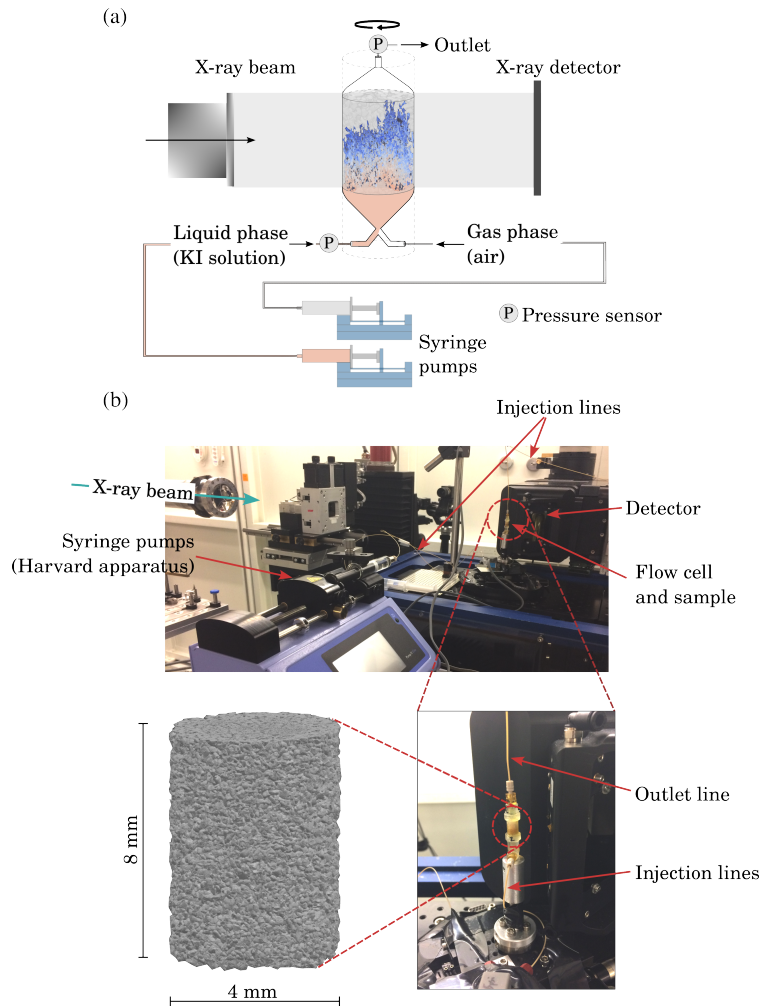


Figure 3.12: Setup for the transport experiments + X-ray tomography measurements, as implemented at the TOMCAT beamline of the Swiss Light Source (SLS), Paul-Scherrer Institute (Villigen, Switzerland). a) Shows a schematic representation of the experimental setup, with an indication of the two injection lines, and the installation of pressure sensors both at the inlet and at the outlet lines. b) Shows, in the upper panel, the general setup and the porous medium sample location relative to the X-ray beam. The lower right panel shows a close-up of the flow cell, with the gas and liquid injection lines at the bottom, the outlet line at the top, and the central cylindrical part containing the sample. A 3D rendering of the tomographic reconstruction of the entire sample is shown in the lower left panel, depicting the heterogeneous shape of the solid grains, with the whole sample resembling a sandy soil in terms of grain size and bulk porosity.

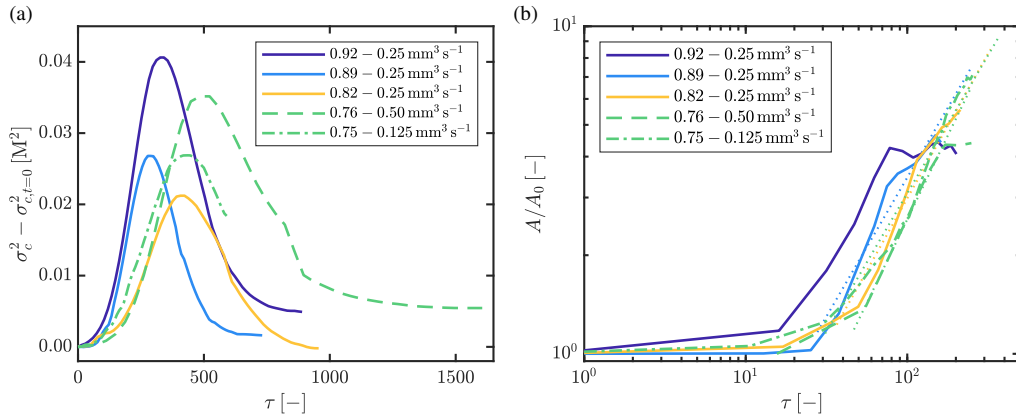


Figure 3.13: Alternative representation of the experimental results. a) Variance of the concentration field, σ_c^2 , against the dimensionless time, τ , for all five transport experiments. The values of σ_c^2 have been corrected by the variance at time $t = 0$ s, $\sigma_{c,t=0}^2$. τ is expressed as $\tau = t/t_{\text{adv}}$, where the advective time $t_{\text{adv}} = \bar{\xi}/\bar{v}$ is the time required for the flow to bridge the average pore size $\bar{\xi}$ at the average flow velocity \bar{v} . b) Evolution over the dimensionless time τ of the area of the advancing front, A , normalized by the area computed at the initial time of the deformation front, A_0 . The respective power law fitting curves are displayed with dot lines for all cases except for $S_w = 0.92$, which is the only case that reaches a plateau at later times. On both panels, different line types correspond to different injection flow rates, whereas different line colors correspond to different saturation degrees. Note that, in that regard and for facilitating experiment comparison, we have grouped together $S_w = 0.76$ and $S_w = 0.75$ given their very similar saturation degree.

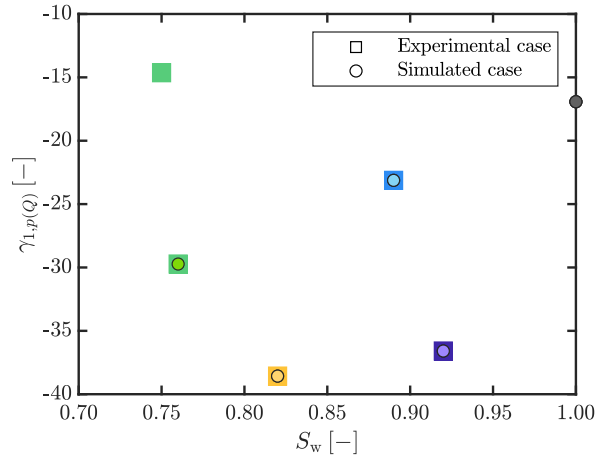


Figure 3.14: Skewness, $\gamma_{1,p(Q)}$, of the probability density function of the Q -criterion as a function of the liquid phase saturation degree S_w . Cases tested experimentally are displayed with squared markers. Additional cases derived from numerical flow simulations to generate one flow field for every combination of saturation degree and injection flow rate, q , tested experimentally are included and shown in circular markers. Note that, for this purpose, we have grouped together $S_w = 0.75$ at $q = 0.50 \text{ mm}^3 \text{ s}^{-1}$ and $S_w = 0.76$ at $q = 0.125 \text{ mm}^3 \text{ s}^{-1}$ given their very similar saturation degree, meaning that we simulated only one additional case for $S_w = 0.76$ at $q = 0.25 \text{ mm}^3 \text{ s}^{-1}$. This grouping is also reflected in the color criteria of the markers, which corresponds to that used in Section 3.4 (see Figure 3.6) and represents the saturation degree plotted on the x -axis. However, $S_w = 0.75$ and $S_w = 0.76$ are not considered identical conditions in terms of saturation, given the different spatial arrangement of air clusters inside the pore space obtained in both cases. Results indicate that $\gamma_{1,p(Q)}$ is exclusively controlled by the saturation degree, i.e., the spatial heterogeneity of the porous medium, whereas changes in the imposed flow conditions on the same system do not affect the skewness of the distribution. The latter behavior is observed in the overlapping between the squared and circular markers. This concludes on the exclusive control of saturation, and in particular of the spatial distribution of the gas phase (air) in the pore space, on defining the main mechanism locally deforming the solute plume as it spreads through the pore space, i.e., shear-dominated or vorticity-dominated deformation.

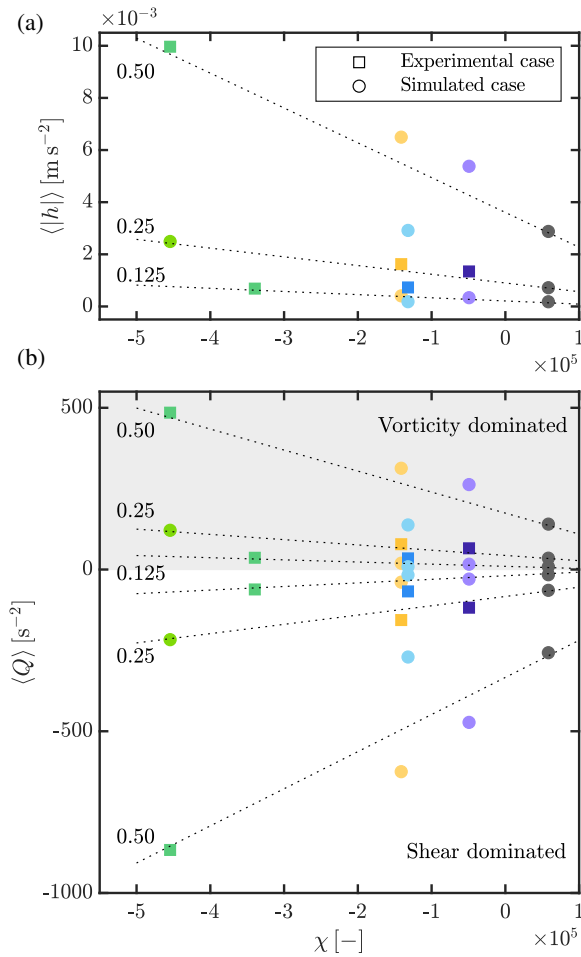


Figure 3.15: Variations in the mechanisms of flow deformation as function of connectivity. a) Variation of the average absolute helicity density, $\langle |h| \rangle$, with the Euler characteristic χ , for the three experimental injection flow rates $q = 0.125, 0.25, \text{ and } 0.50 \text{ mm}^3 \text{ s}^{-1}$. b) Average positive and negative Q -criterion, $\langle Q \rangle$, as a function of χ , for the three experimental injection flow rates, $q = 0.125, 0.25, \text{ and } 0.50 \text{ mm}^3 \text{ s}^{-1}$. The grey shaded area indicates the range of Q -values associated with shear-dominated deformation. On both panels, the conditions investigated experimentally are displayed with squared markers, whereas additional numerically simulated conditions are shown with circular markers. The dotted lines describe the linear trend obtained for the variation of both metrics with χ . The color criteria corresponds to that employed in Section 3.4.

BIBLIOGRAPHY

- Bevington, P. R. and D. K. Robinson (2003). *Data reduction and error analysis for the physical sciences*. New York, NY 10020: McGraw Hill Higher Education. Chap. Least-squares fit to a straight line.
- Guédon, G. R., F. Inzoli, M. Riva, and A. Guadagnini (2019). “Pore-scale velocities in three-dimensional porous materials with trapped immiscible fluid.” In: *Physical Review E* 100, p. 043101.
- Hu, Y., T. Schneider, B. Wang, D. Zorin, and D. Panozzo (2020). “Fast tetrahedral meshing in the wild.” In: *ACM Transactions on Graphics* 39, 117:1–117:18.
- Lavin, A., J. De Vicente, M. Holgado, M. F. Laguna, R. Casquel, B. Santamaria, M. V. Maigler, A. L. Hernandez, and Y. Ramirez (2018). “On the determination of uncertainty and limit of detection in label-free biosensors.” In: *Sensors* 18, p. 2038.
- Münch, B. (2022). *Xlib library of ImageJ plugins*.
- Triadis, D., F. Jiang, and D. Bolster (2019). “Anomalous dispersion in pore-scale simulations of two-phase flow.” In: *Transport in Porous Media* 126, pp. 337–353.

4

CHAOTIC ADVECTION AND CHAOTIC MIXING IN UNSATURATED POROUS MEDIA

This chapter has been submitted on March 19 2024 as: Velásquez-Parra, A., F. Marone, M. Griffa, & J. Jiménez-Martínez (2024). "Chaotic transport of solutes in unsaturated porous media". In: *Environmental Science and Technology*.

Key Findings:

- The presence of an immiscible phase within the pore space further promotes chaotic dynamics in solute transport and mixing.
- Lower liquid phase saturation increases the exponential growth rate of mixing.
- Larger fluid flow velocities increase the exponential growth rate of solute plume's deformation with time.

Authors' contribution: *A. Velásquez-Parra:* conceptualization, numerical analysis, data analysis, paper writing; *F. Marone:* conceptualization, paper writing; *M. Griffa:* conceptualization, data analysis, paper writing; *J. Jiménez-Martínez:* conceptualization, supervision, paper writing.

This is a pre-print of the submitted version of the paper, differing from it in terms of title, layout, and formatting. The Conclusions section has been slightly extended.

ABSTRACT

Unsaturated porous media, characterized by the combined presence of several immiscible fluid phases in the pore space, are highly relevant systems in nature, as they control the fate of contaminants and the availability of nutrients in the subsoil. However, a full understanding of the mechanisms controlling mixing in such systems is still missing. Using fully resolved 3D numerical simulations of flow and transport, based on X-ray tomograms of a porous medium at different degrees of liquid (wetting) phase saturation, we show the occurrence of chaotic dynamics in the deformation of the solute's plume, as characterized by computed chaos metrics (Lyapunov exponents), and in the mixing of the injected solute. This is enhanced at lower saturation and is sustained even under diffusion-relevant conditions over the medium's length, in which case it is also strengthened by larger flow velocities. Our results highlight the dominant role of the system's spatial heterogeneity, increased by the presence of an immiscible phase (e.g., air), on the solute's mixing efficiency. This represents a stepping stone for the assessment of mixing and reactions in unsaturated porous media.

PLAIN LANGUAGE SUMMARY

The unsaturated region of soils, located between the soil surface and the groundwater level, mediates the effects of processes taking place in the atmosphere on the subsoil and on the groundwater sources located deeper in the ground. Gaining a better understanding of the mechanisms controlling the transport and mixing dynamics of solutes in that region is thus essential for assessing and predicting the fate of contaminants and nutrients entering the pore space. Here, we present a numerical investigation of both the control of the saturation degree, i.e., the fraction of the pore volume occupied by water, and the imposed flow conditions on the solute plume's deformation and on the solute's degree of mixing with the resident pore water. We identify chaotic dynamics for these two metrics, characterized by exponential growths with travel distance. They are strengthened both upon reduction in the degree of saturation and upon increase in the magnitude of the imposed flow, i.e., liquid flow velocities. This highlights the dominant role of the system's spatial heterogeneity, increased by the presence of air, on the solute's mixing efficiency, with strong implications for the assessment of chemical reactions in subsurface environments.

4.1 INTRODUCTION

Natural processes occurring in the atmosphere, together with anthropogenic actions mainly related to agricultural and industrial activities, are the main contributors to the entry of solutes into the subsoil. This includes both nutrients and contaminants, whose fate is largely controlled by processes taking place in the unsaturated region of soils, i.e., the uppermost soil layer, which is characterized by the presence of more than one material phase (water and air) in the pore space. This region is thus of paramount importance for a wide range of environmental and industrial applications, including groundwater and soil remediation (Cunningham et al. 2003; Lahav et al. 2010; Sebiló et al. 2013; Williams et al. 2009), radioactive waste disposal (Winograd 1981), and energy storage (Barbier 2002). A full assessment of these applications and further technical advances for their optimization have remained elusive due to the still incomplete understanding of the mechanisms controlling the mixing of solutes under such so-called unsaturated conditions. In particular, the control of the degree of liquid phase saturation, i.e., the fraction of pore volume occupied by the liquid phase, on both the solute's plume stretching and the associated dilution within the resident aqueous phase remains unknown. This is largely due to the highly complex physical heterogeneity and spatial organization of the fluid phases, i.e., the liquid- or gas-filled voids, at the pore scale, which ultimately control mixing (Dentz et al. 2011; Li et al. 2017; Valdés et al. 2022), and which are not accounted for in classical transport formulations at the continuum (Darcy) scale (Simunek et al. 2008).

Recent studies (Lester et al. 2013) have unveiled how the inherent nature of porous media promotes chaotic flow dynamics, changing the paradigm of porous media transport for both environmental and industrial applications. This dynamics is characterized by fluid tracer particles whose distance diverges exponentially in time under the presence of a given flow field, resulting in complex fluid particle trajectories (Aref 1984; Aref et al. 2017; Ottino 1989). This causes large deformation in the advected solute, enhancing mixing through a rapid generation of small-scale structures over which diffusive mass transfer occurs more efficiently (Aref 2002). Signs of chaotic advection and chaotic mixing in porous media have been observed at the Darcy scale, both from experimental (Yu et al. 2015) and numerical studies (Chiogna et al. 2015; Chiogna et al. 2016; Chiogna et al. 2014; Cirpka et al. 2015; de Barros et al. 2012; Ye et al. 2020) performed on fully saturated systems. They have highlighted the occurrence, under the presence of an anisotropic permeability tensor, of helical flow and twisting streamlines (Bakker and Hemker 2004; Chiogna et al. 2014;

Yu et al. 2015), which have resulted in both enhanced plume deformation, i.e., larger surface for diffusive mass transfer, and faster dilution. They have been complemented by direct quantification of solute plume deformation. This has been achieved, on the one side, via vortex identification indexes (de Barros et al. 2012), which allow discerning between shear- and vorticity-dominated deformation flow regions in the pore space. On the other side, streamlines deformation has been directly quantified through kinematic metrics (Chiogna et al. 2015; Chiogna et al. 2016; Cirpka et al. 2015; Ye et al. 2020), leading to the identification of stretching and folding events along single streamlines, both of which are hallmarks of chaotic advection. While all these studies have considered steady-state flow conditions, enhanced mixing resulting from chaotic solute deformation has also been identified on experimental Darcy-scale investigations under oscillatory flow (Zhang et al. 2009), aiming at improving contaminant remediation. The high environmental relevance of this chaotic dynamics has also been exposed in large-scale studies, in which the optimal *in situ* flow conditions required for inducing chaotic flow in the subsoil have been investigated, with the aim of both optimizing groundwater remediation (Cho et al. 2019; Mays and Neupauer 2012; Neupauer et al. 2014) and improving biodegradation (Bagtzoglou and Oates 2007).

For long time, the study of chaotic mixing in porous media at the pore scale has been predominantly centered around numerical analyses, given the difficulty of experimentally accessing and probing these systems at the required spatial and temporal scales. Recently, high-resolution laser imaging, via high-precision refractive-index matching, was applied successfully for imaging the evolution of a low-diffusivity fluorescent dye in a 3D column of transparent borosilicate spheres, allowing for the reconstruction of the plume deformation over distance (Heyman et al. 2021; Heyman et al. 2020). Results revealed the key role of grain contacts in inducing intense stretching and folding of the solute plume, leading to chaotic advection. A similar technique was also employed recently for the experimental reconstruction of velocity fields through high-resolution particle tracking. These experimentally determined fields were further applied for the numerical investigation of the stretching history of fluid material lines, which are defined as segments joining non-diffusive tracers initially located close to each other (Souzy et al. 2020). Results revealed the exponential growth over time of these material lines, characteristic of chaos. Purely numerical investigations have further cast light on the physical mechanisms controlling this chaotic behavior in porous media. They have highlighted the role of the intrinsic topological complexity of 3D porous systems in inducing continuous separation and reattachment of the advected fluid at the contacts with solid

interfaces, which induces local stretching and folding events (Lester et al. 2014; Lester et al. 2016a). This is specifically related to the formation of stagnation points of zero skin friction on the surface of those interfaces, giving place to both stable and unstable manifolds, which induce considerable fluid stretching downstream (Lester et al. 2014; Lester et al. 2016a). More recent numerical pore-scale investigations have addressed further implications of chaotic mixing on reactive processes, more specifically on heterogeneous (liquid-solid) reactions (Aquino et al. 2023). They have emphasized the role of chaos in allowing the solute to efficiently explore the pore space, which thus renders reaction at the liquid-solid interfaces more efficient. All pore-scale studies summarised so far have exclusively focused on the study of fully saturated systems. To our knowledge, similar pore-scale studies on the occurrence of chaos under the presence of more than one material phase in the pore space, such as the unsaturated region of soils, have not been reported yet. Recent findings have been able to characterize the impact of the saturation degree on the occurrence of helical flow in the pore space, and have highlighted its important role in altering the associated vorticity field and enhancing streamlines deformation in the form of intense folding and braiding (Velásquez-Parra et al. 2024). However, an investigation of the systematic impact of liquid phase saturation on chaotic advection and chaotic mixing through direct quantification of chaotic stretching and mixing rates has not been reported yet.

Here, we present a numerical investigation of chaotic advection and chaotic mixing in unsaturated porous media at the pore scale. We take advantage of images obtained from previous synchrotron X-ray micro-tomography experiments of a porous medium resembling a sandy soil (Marone et al. 2020; Velásquez-Parra et al. 2024) to build up realistic numerical simulations of flow and transport. We investigate the occurrence of chaotic advection and chaotic mixing under different saturation degrees and different flow rates, both under low-diffusivity and diffusion-relevant conditions. We identify a previously unknown dependency of the strength of chaotic advection on liquid phase saturation, expressed both by an increasing rate of the exponential stretching of the injected plume with travel distance and by a larger Lyapunov exponent, as the degree of liquid phase saturation decreases. This behavior reflects itself in an enhanced mixing across the sample, which persists even in the presence of relevant diffusion rates over the sample's length, leading to sustained chaotic mixing. We also analyze the dependency of mixing on the imposed flow conditions, with larger flow rates inducing larger exponential mixing rates with travel distance. Our results reveal important features of the control of liquid phase saturation on chaotic advection and chaotic mixing in porous media, which represents a stepping stone for

better understanding and predicting solute transport and mixing under relevant conditions for environmental and industrial systems.

4.2 MATERIALS AND METHODS

The present work is based on 3D numerical simulations of steady flow and transport, i.e., unchanging in time, which are rooted in 4D synchrotron X-ray micro-tomography experiments performed in previous investigations for the analysis of mixing in unsaturated porous media (Marone et al. 2020; Velásquez-Parra et al. 2024). From those experiments, we obtained 3D high-resolution (in space and time) tomographic datasets of a porous medium resembling a sandy soil at different saturation degrees, S_w . See Marone et al. (2020) and Velásquez-Parra et al. (2024) for details about both the porous medium cylindrical sample itself (a packing of sintered borosilicate glass particles), the aqueous solution occupying its pore space, and the time-lapse X-ray micro-tomography settings. The imaged portion of the sample was approximately 3 mm high (along the flow direction) and had a diameter of 4 mm, with a relatively homogeneous pore size distribution (Velásquez-Parra et al. 2024), a bulk porosity of 0.28, an intrinsic permeability of 10^{-10} m², and an average pore size, $\bar{\xi}$, of 30 μ m. By post-processing the obtained images, we were able to create the binary tomograms of the three single material phases forming the tested sample (solid, liquid, and gas) at high spatial resolutions (with a voxel size of 2.75 μ m) (Marone et al. 2020; Velásquez-Parra et al. 2024). The numerical simulations were set up using only the binary tomograms of the aqueous liquid phase, whose geometry reflects the spatial arrangement of both the solid phase (the irregular borosilicate glass particles) and the gas phase (air clusters) trapped in the pore space. To reduce the computational demands of our numerical investigation, these tomograms were downsampled by a factor of four, compared to the initial voxel size, for a final spatial discretization with a voxel size of 11 μ m. Finite element tetrahedral meshes were generated from these final images using the fTetWild algorithm (Hu et al. 2020), for a total of five distinct conditions, representing $S_w = 1.00, 0.92, 0.89, 0.82$ and 0.76.

The 3D numerical simulations were performed using the Finite Elements Method software Comsol Multiphysics. Flow simulations were based on the solution of the steady-state Stokes equation, which is valid for flows exclusively controlled by viscous dissipation, i.e., Reynolds numbers, $Re \ll 1.0$. We set boundary conditions that aimed at mimicking the experimental conditions employed in the reference study (Velásquez-Parra et al. 2024). They included a fixed inflow velocity at the inlet located on one end of the sample, which

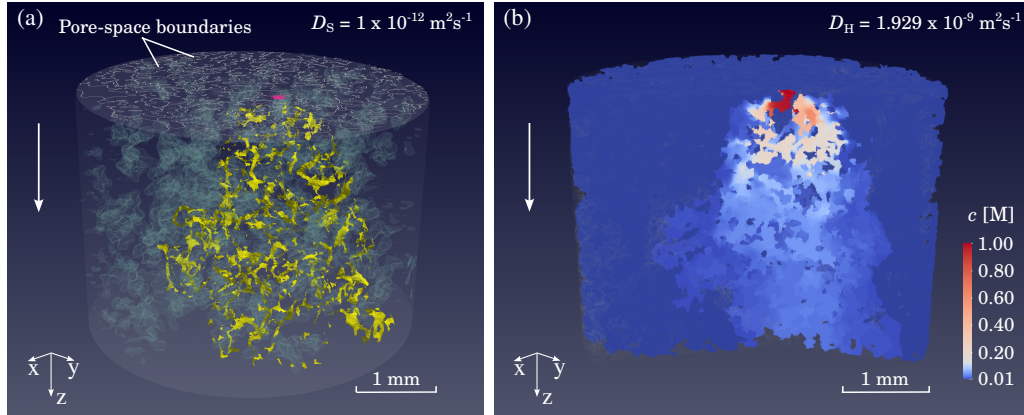


Figure 4.1: Main outputs from the two steady-state transport scenarios solved numerically. Results for a porous medium with a saturation degree $S_w = 0.82$ and with an injection flow rate $q_1 = 0.125 \text{ mm}^3 \text{ s}^{-1}$ are displayed. a) Solute's plume deformation, i.e., deformation of the isosurface of the 1% of concentration, 3D-rendered in yellow, as reconstructed from the low-diffusivity transport scenario ($D_S = 1 \times 10^{-12} \text{ m}^2 \text{ s}^{-1}$). In addition, the air phase volume is 3D-rendered in transparent cyan and the porous medium boundaries are shown as a transparent cylinder. The pore space boundaries on the inlet's cross section are highlighted in white, with the surface region of the chosen injection pore on the inlet's cross-sectional plane highlighted in magenta. b) Solute's concentration field inside the sample, expressed in units of solute moles per unit of volume (molar concentration, M), as obtained from the diffusive transport scenario ($D_H = 1.929 \times 10^{-9} \text{ m}^2 \text{ s}^{-1}$). All concentration values below 0.01 M are displayed in the darkest blue. In addition, only the solid phase's volume is 3D-rendered in transparent grey. Only three-quarters of the sample are displayed to improve the visualization of the concentration gradients inside the sample. In both panels, the white arrow indicates the main flow direction. See Figures 4.5, 4.7 and 4.8 in the Appendix, for the remaining cases.

was computed from the relationship between the injected flow rate, q , and the pore-space cross-sectional area at the inlet. A total of three flow conditions, $q_1 = 0.125$, $q_2 = 0.250$ and $q_3 = 0.500 \text{ mm}^3 \text{ s}^{-1}$ were simulated for each S_w . We also set a constant pressure at the outlet, as measured during the reference experiments and ranging from $\Delta P = 0.31 \text{ Pa}$ for q_1 to $\Delta P = 1.23 \text{ Pa}$ for q_3 . A no-slip boundary condition (zero velocity at the boundary) was also set at all material interfaces. The use of the latter at the interface liquid-gas has been demonstrated to have a negligible impact, both in 2D and in 3D, on fluid flow velocity distributions in porous media (Guédon et al. 2019; Triadis et al. 2019).

Steady-state transport simulations employed the flow fields obtained from the Stokes flow simulations. They were aimed at observing the steady-state spreading and mixing of a solute plume inside the unsaturated porous sample. The simulated resident (low potassium iodine concentration) and injected (higher potassium iodine concentration) solutions corresponded to those employed in the reference experiments. The higher concentration solution was punctually injected with a constant concentration $c_0 = 1.0 \text{ M}$, over the area of a pore body located towards the center of the sample's inlet. For every combination of S_w and q , we simulated two mixing scenarios, (i) a low-diffusivity case, characterized by the solute's diffusion coefficient, $D_S = 1 \times 10^{-12} \text{ m}^2\text{s}^{-1}$ (one order of magnitude smaller than that previously used for the study of chaotic advection; (Heyman et al. 2020)), and (ii) a diffusive case with $D_H = 1.929 \times 10^{-9} \text{ m}^2\text{s}^{-1}$, the latter of which matched the conditions tested in the reference experiment (Dunlop and Stokes 1951; Velásquez-Parra et al. 2024). These two scenarios allowed us to study the occurrence of chaotic advection and chaotic mixing under both low-diffusivity and diffusion-relevant conditions, respectively. The numerical work presented here thus amounts to a total of thirty 3D steady-state simulations of flow and transport.

4.3 RESULTS AND DISCUSSION

The two transport scenarios considered in the numerical simulations allowed the investigation of the impact of the system's heterogeneity, characterized through S_w , and of the imposed flow conditions, as expressed by q , on the solute's plume deformation and mixing in the pore space. A 3D visualization of both these results is shown in Figure 4.1 for the case $S_w = 0.82$ with $q_1 = 0.125 \text{ mm}^3\text{s}^{-1}$. Figure 4.1a shows the deformation of the solute plume in its travel through the unsaturated porous medium from the point of injection, as reconstructed from the low-diffusivity transport simulations (see Appendix 4.A, Figure 4.5, for the remaining cases), whereas Figure 4.1b depicts the concentration field inside the pore space as obtained from the diffusive transport scenario (see Appendix 4.B, Figures 4.7 and 4.8 for a comparison of such fields for the remaining S_w under low, q_1 , and high, q_3 , flow rates). Both these scenarios, for every combination of S_w and q tested, can be characterized by the Péclet number, Pe , where Pe represents the ratio between the characteristic time of diffusion and the characteristic time of advection over a characteristic length. It can be expressed as $Pe(D_i) = \bar{v}\bar{\xi}^2/2D_i a_t$, where \bar{v} is the mean flow velocity of every tested condition, D_i is either D_S or D_H , depending on the simulated scenario, and $a_t \approx 15 \text{ }\mu\text{m}$ is the average pore throat size, approximated as one-fourth of

$S_w [-]$	q_1			q_2			q_3		
	\bar{v}	$Pe(D_H)$	$Pe(D_S)$	\bar{v}	$Pe(D_H)$	$Pe(D_S)$	\bar{v}	$Pe(D_H)$	$Pe(D_S)$
1.00	0.753	1.17	2259	1.506	2.34	4519	3.012	4.68	9036
0.92	0.931	1.45	2794	1.862	2.89	5587	3.724	5.79	11173
0.89	0.769	1.20	2309	1.539	2.40	4617	3.078	4.79	9234
0.82	1.016	1.58	3048	2.027	3.15	6082	4.067	6.33	12202
0.76	1.153	1.79	3454	2.302	3.58	6908	4.604	7.16	13813

Table 4.1: Summary of the flow and transport characterization for all thirty conditions reported in this study based on results of the numerical flow simulations. These conditions are characterized by the saturation degree, S_w , the injection flow rate, q , with $q_1 = 0.125$, $q_2 = 0.250$ and $q_3 = 0.500 \text{ mm}^3 \text{ s}^{-1}$, and the diffusion coefficient, D_i , where $D_H/D_S \approx 2000$. Reported descriptors include the mean fluid flow velocity, \bar{v} , expressed in units of $\times 10^{-4} \text{ m s}^{-1}$, and the dimensionless Péclet numbers, $Pe(D_H)$ and $Pe(D_S)$, linked to the two transport scenarios defined by D_H and D_S , respectively.

the average glass beads diameter (Glover and Déry 2010). Note that we have adopted $\bar{\zeta}$ as the characteristic length for advection, and a_t as the corresponding one for diffusion (Jiménez-Martínez et al. 2015; Markale et al. 2022). Values for \bar{v} and Pe are summarized in Table 4.1 for all tested conditions.

4.3.1 Solute plume deformation as a function of saturation

The solute's plume deformation was investigated based on the results from the low-diffusivity simulations, i.e., using D_S , $Pe(D_S) > 2000$. They allowed observing the changes in the plume's shape, both in longitudinal (along the z -axis) and transversal direction, induced by the action of stretching and folding, which could be preserved given the negligible role of diffusion. We represented the plume's deformation by reconstructing the concentration field's isosurface at a value of 1% of the injected tracer concentration (1.0 M) using the computed concentration field (refer to Appendix 4.A for further details on the isosurface generation). We use this isosurface as an approximation of the solute's front where both the injected and the resident solutions meet. As an example, Figure 4.1a shows the case $S_w = 0.82$ and q_1 (refer to Appendix 4.A, Figure 4.5, for a visualization of the remaining conditions), in which the location of the air clusters in the pore space is also shown. The trapped air clusters act as obstacles for the flow, increasing the system's heterogeneity and altering its connectivity

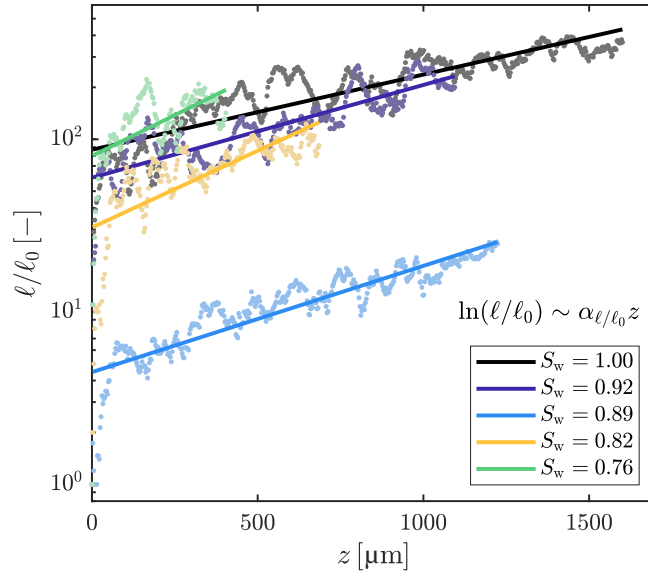


Figure 4.2: Evolution of the relative length of the solute's plume front, ℓ/ℓ_0 , with travel distance along the z -axis, for all pairs of conditions S_w - q considered in this study. All the results stemmed from the low-diffusivity simulations, i.e., performed with a diffusion coefficient $D_S = 1 \times 10^{-12} \text{ m}^2\text{s}^{-1}$, in which no variation in ℓ/ℓ_0 upon changes in q for the same S_w was observed. The plume's front is represented through the isosurface of the concentration field with value equal to 1% of the injection concentration (1.0 M). ℓ represents the plume's length over an x - y cross-sectional plane at a certain z . The results have been expressed as a relative deformation by dividing ℓ by the isosurface length at $z = 0 \text{ }\mu\text{m}$, ℓ_0 . This explains the offset along the y -axis for all the curves. Results for every observation plane are shown as markers, whereas the corresponding exponential regressions are shown as continuous lines. Different colors correspond to different saturation degrees. In both panels, the type of scaling described by ℓ/ℓ_0 as a function of z is displayed.

and flow field (Velásquez-Parra et al. 2024). The results show a strong deformation of the solute's plume, visible already right below the injection point, which leads to a rapid increase of the surface area of the mixing interface along the main flow direction.

We quantified the plume's transversal deformation for every condition S_w - q . For this purpose, we sliced the reconstructed isosurface (see Figure 4.1a) with an x - y plane moving along z at a spatial step equal to the voxel size of the reference tomograms ($2.75 \text{ }\mu\text{m}$). We then computed the length of the isosurface, ℓ , on each one of these cross-sectional planes, by adding together the length of the single curve elements resulting from this intersection (refer to Appendix 4.A, Figure 4.6,

for a schematic of this process). The ensemble of all ℓ -values quantified for every moving plane reflects the occurrence of plume's transversal stretching and folding, as the solute moves along the main longitudinal flow direction (Heyman et al. 2020). Figure 4.2 shows the evolution of ℓ/ℓ_0 along z for all tested conditions, where ℓ_0 is the isosurface length at the inlet plane, i.e., at $z = 0$ μm . The offset of the data sets along the y -axis of such plot, especially visible for $S_w = 0.89$, is due to the different ℓ_0 , i.e., different injection pore, obtained for every saturation degree. Note that the data sets have been truncated at the z -coordinate at which the plume has touched the outer boundaries of the sample, since this constrained the growth of ℓ further downstream. For all cases, the results describe an exponential increase of ℓ/ℓ_0 over z , which sets in after an initial fast increase of ℓ/ℓ_0 over the length of a few pores. This exponential trend indicates the occurrence of chaotic dynamics in the stretching of the solute plume, as it moves through the pore space. We quantify this trend by performing an exponential regression on the obtained results (shown as a continuous line in Figure 4.2a) following the equation

$$Y = \beta e^{\alpha z}, \quad (4.1)$$

where Y represents the studied quantity, and β and α are the corresponding regression parameters. Refer to Appendix 4.B for a detailed description of the regression procedure. In general, ℓ/ℓ_0 increases faster with decreasing S_w , reflecting the effect of the larger spatial heterogeneity in the pore space at lower saturation degrees in inducing a larger solute's plume deformation. The latter effect of S_w is already known and has been described in previous studies. However, such studies did not focus on assessing the presence or the absence of chaotic deformation scalings, either because they concerned non-chaotic systems (Jiménez-Martínez et al. 2015) or because they did not account for the the plume's transversal stretching (Velásquez-Parra et al. 2024) in such assessment. The latter is essential for quantifying the effects of the connected pore branches and mergers (Lester et al. 2013), responsible for fluid separation and fluid convergence, respectively, and of their transverse orientation to each other, on the stretching history of material lines. They are associated with the occurrence of stable and unstable manifolds (Lester et al. 2013), whose transverse intersection is a condition for the generation of chaotic advection (Metcalf et al. 2022). Our results also showed no variation in ℓ/ℓ_0 upon variation in q for any given S_w . This is explained by the large Pe , thus confirming that the computed isosurface deformation was not affected by diffusive effects, preserving the plume's stretching and folding events occurring in the pore space.

4.3.2 Solute mixing as function of saturation

We explored the effects of the plume's exponential stretching on mixing by quantifying the increase of the mixing volume along the main flow direction. The mixing volume was defined as the pore volume occupied by the injected solute, i.e., where the concentration c satisfied the condition $0.01 < c < 0.99$ (de Anna et al. 2014). We plotted the area of the intersection of the mixing volume with the x - y plane at any z position, called in the following M_V . We observed that the exponential growth identified for the plume's stretching under low-diffusivity conditions is sustained also for the growth of the associated mixing volume, $M_V(D_S)$. This is shown in Figure 4.3a, which also depicts an increasing rate of exponential growth of $M_V(D_S)$ with a saturation decrease, as determined using Eq. 4.1 and also observed for ℓ/ℓ_0 (Figure 4.2). These results reflect the close relationship of both processes and expose the control of saturation on chaotic mixing. A stronger solute plume's stretching increases the interface area between both miscible solutions (the resident and the injected one), enhancing the diffusive flux across it and rendering mixing more efficient. As also observed for ℓ/ℓ_0 , q did not seem to impact at all the growth of $M_V(D_S)$, given the large Pe numbers considered.

Next, we investigated the effects of diffusion on the mixing volume. Diffusion might counteract the strong plume deformation shown before, by inducing coalescence of the stretched solute lamellas, thus impacting the mixing efficiency in the system. We did this by analyzing the results of the numerical simulations performed under diffusion-relevant conditions, i.e., using D_H , and by comparing them to those discussed before for the low-diffusivity scenario. Figures 4.3b and 4.3c show the increase of $M_V(D_H)$ along z for $S_w = 0.92$ and $S_w = 0.76$, respectively. We only present these two cases for simplicity (see Appendix 4.B, Figure 4.9, for the remaining S_w values). However, the analysis described in the following applies to the remaining saturation degrees as well. The results indicate an asymptotic exponential growth of the mixing volume over the longitudinal travel distance for this diffusive scenario as well. The already discussed impact of S_w on $M_V(D_S)$ (see Figure 4.3a) persists also for $M_V(D_H)$, characterized by a larger increase in M_V at lower saturation degrees. This chaotic scaling for mixing also exists upon variations in the flow field induced by changes in q (see Figures 4.3b and 4.3c), albeit with changes in the exponential scaling. In general, lower q induces larger values for the mixing volume over the entire sample. This is expected, since lower q increases the transit time of the solute inside the pore space, allowing diffusion to more effectively smooth out concentration gradients. This leads to a larger volume occupied by the solute

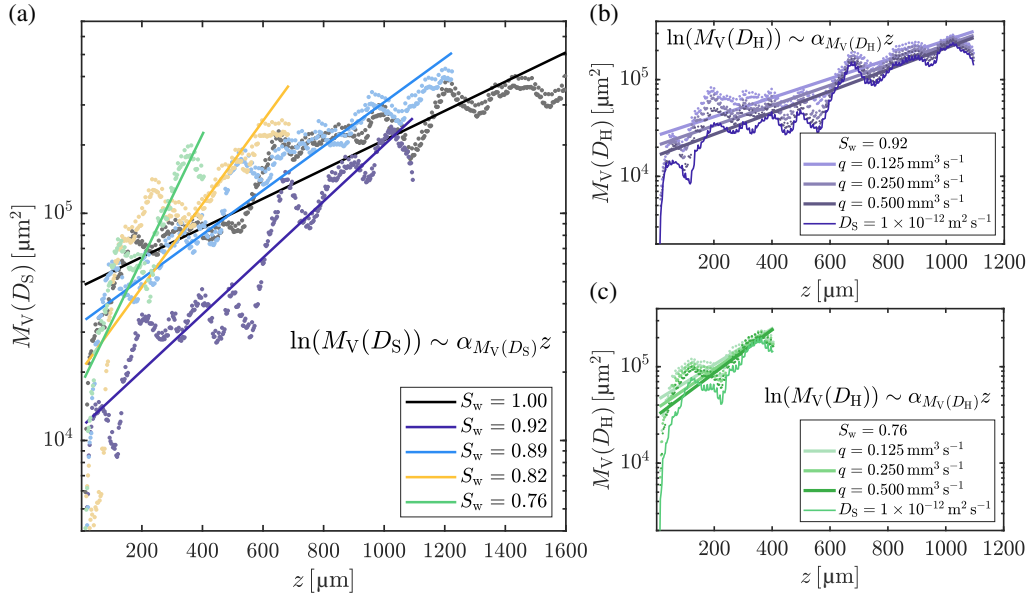


Figure 4.3: Mixing analysis for the two transport scenarios considered in this work. a) Evolution of the mixing volume, $M_V(D_S)$, along the main flow direction, z , for all tested S_w cases based on the transport scenario defined by $D_S = 1 \times 10^{-12} \text{ m}^2 \text{ s}^{-1}$. Values for M_V have been computed over an x - y cross-section plane moving along z . Different colors correspond to different S_w values. b) and c) Evolution of $M_V(D_H)$ along z for $S_w = 0.92$ and $S_w = 0.76$, respectively, based on results for the transport scenario defined by $D_H = 1.929 \times 10^{-9} \text{ m}^2 \text{ s}^{-1}$. Results for the three tested flow rates are shown in different colors. In addition, the evolution of M_V along z for the low-diffusivity case D_S (i.e., $M_V(D_S)$) is shown also in each panel for comparison. In all panels, results for every observation plane along z are shown as markers, whereas the corresponding exponential regressions are shown as continuous lines.

plume along the main flow direction. In both panels, the increase of M_V for the corresponding D_S case is shown as a reference. As expected, all cases simulated with D_H present, at almost any z , higher M_V values than those obtained in the corresponding D_S cases.

4.3.3 Control of saturation on the chaos strength

We now assess quantitatively the impact of the saturation degree on the chaotic dynamics exposed in Sections 4.3.1 and 4.3.2. This is done by comparing the dependency of the exponential regression parameter α , computed from Eq. 4.1

for the regressions shown in Figures 4.2 and 4.3, on the saturation degree. The results are presented in Figures 4.4a to 4.4c for all conditions tested. Note that variation in α upon a change in q was only obtained for $M_V(D_H)$, as seen in Figure 4.3b and 4.3c. Overall, we observe an increase in α with decreasing S_w for all three metrics, although the range of variation across metrics is different. α_{ℓ/ℓ_0} , associated to the solute plume's deformation, shows a far smaller range of change upon the same relative change in saturation compared to $\alpha_{M_V(D_S)}$ and $\alpha_{M_V(D_H)}$. This indicates that only a small relative increase in the plume stretching rate can induce far larger changes in the mixing rate. This point is further illustrated in Appendix 4.C, Figure 4.10, where $\alpha_{M_V(D_S)}$ has been plotted against α_{ℓ/ℓ_0} for all S_w -values. It can be explained by the larger plume's deformation inducing an increase of both the interface area between the injected and the resident solution and the concentration gradients across this interface (Heyman et al. 2020; Jiménez-Martínez et al. 2015; Le Borgne et al. 2013), both of which contribute to the enhancement of the diffusive flux across the system.

The control of the flow conditions on the exponential scalings is observed only in Figure 4.4c for $M_V(D_H)$, i.e., for low Pe , where every q has been assigned a different marker. Results show that $\alpha_{M_V(D_H)}$ increases with q for the range of saturation degrees considered in our study. In addition, the relative difference in scaling over the range of flow rates analyzed also becomes larger as S_w decreases. Both of these results can be explained by the interplay between the advective and the diffusive time upon change in q , whose effect can be seen in the evolution of $M_V(D_H)$ in Figures 4.3b and 4.3c. On the one hand, larger advective times associated with lower q translate into a stronger effect of diffusion at increasing the volume occupied by the solute after a given travel length. This is visible already after short travel distances from the inlet. On the other hand, larger q increases the advective travel length associated with the diffusive time over a measurable characteristic length, e.g., the size of a voxel. This allows for a stronger stretching of the interface before being smoothed out by diffusion, leading to an increased diffusive flux at larger z . Both of these effects reflect themselves in the difference of $M_V(D_H)$ for different q values under constant S_w , as z increases. Note also the occurrence of exponential growth in $M_V(D_H)$ for Péclet numbers as low as 1.17 (see Table 4.1 for $S_w = 1.00$ and q_1). This Pe is lower than that reported by Heyman et al. (2020) as a lower bound for the development of incomplete pore-scale mixing and chaotic advection, as defined for a porous medium composed of spherical glass beads of different sizes. Our results highlight the strong impact on the development of chaotic dynamics of the intrinsic spatial heterogeneity of our porous medium, which is composed of irregularly shaped glass particles, resembling natural porous media. For the

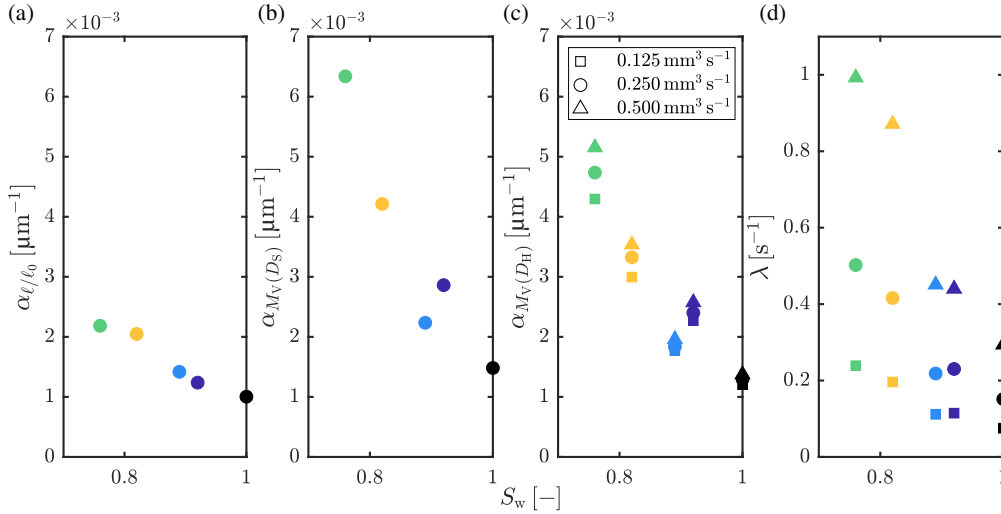


Figure 4.4: Variation of the exponential scaling rate parameter, α , as function of the saturation degree, S_w , for the different injection flow rates, q , as obtained from the regression performed on the results of the numerical simulations of transport for a) the relative increase in plume's deformation (isosurface transversal deformation), ℓ/ℓ_0 , b) the mixing volume for the low-diffusivity scenario, $M_V(D_S)$, and c) the mixing volume for the diffusive scenario, $M_V(D_H)$. d) Variation in the Lyapunov exponent, λ , as function of S_w and q , computed from the data in a) as $\lambda = \alpha_{\ell/\ell_0} \bar{v}$. The color labelling corresponds to that employed in Figures 4.2 and 4.3. Different markers are assigned to different flow rates.

unsaturated cases, not only the saturation but also the spatial distribution of the air clusters can explain the chaos strength. For instance, the slightly smaller growth rate of M_V with z for $S_w = 0.89$ compared to $S_w = 0.92$ is a consequence of the narrower distribution of air cluster volumes of the former, as shown in Velásquez-Parra et al. (2024) (see Chapter 3, Figure 3.3b). The gas phase is less effective at blocking the advance of the plume, inducing an overall slower exponential increase in the mixing volume across the sample.

To better characterize the chaotic behavior exhibited from our results, we use our plume deformation data to compute the Lyapunov exponent, λ . This index measures the rate of exponential growth of a material line with time (Ottino 1990), serving as a proxy for characterizing the strength of chaotic dynamics in the system (Lester et al. 2016a). It is expressed as

$$\lambda = \lim_{t \rightarrow \infty} \frac{1}{t} \ln \frac{\ell(t)}{\ell_0}, \quad (4.2)$$

that is, based on the variation of ℓ/ℓ_0 with time. We can express our results as a function of time by employing the mean flow velocity \bar{v} of each case, such that $t = z/\bar{v}$. Following Eq. 4.1, we can then rewrite the Lyapunov exponent as $\lambda = \alpha_{\ell/\ell_0} \bar{v}$. Figure 4.4d shows the obtained values for λ for all saturation degrees and flow rates tested. We observe a strong impact of the saturation degree on the strength of chaos, with λ increasing largely as S_w decreases for the range of saturation degrees considered in our study. This further reinforces the strong impact of an increase in the system's spatial heterogeneity on the development of chaos in the pore space. In contrast to α_{ℓ/ℓ_0} , λ displays a dependency on the flow rate, with values ranging from 0.075 for $S_w = 1.00$ and q_1 , up to 0.994 for $S_w = 0.76$ and q_3 . In addition, the range of λ values upon variation in q increases significantly with decreasing S_w . That is because \bar{v} strongly increases with decreasing S_w . To our knowledge, this is the first time that Lyapunov exponents for transport studies in unsaturated porous media have been reported. Previous studies have focused exclusively on the occurrence of chaos under fully saturated conditions. They have reported values for λ ranging from 0.18 and 0.21, which were derived from an experimental study performed with a similar tracer injection to that implemented in our study (Heyman et al. 2021; Heyman et al. 2020), up to values of 0.47, estimated based on the stretching rate of material lines advected numerically on an experimentally resolved flow field (Souzy et al. 2020). Both of these studies employed a discrete porous system consisting of spherical glass beads, less heterogeneous than the porous medium used in this study. We obtained Lyapunov exponents between 0.075 and 0.294 for $S_w = 1.00$ for the range of flow rates tested, in close agreement with the range of values reported in Heyman et al. (2021).

Previous studies have also reported Lyapunov exponents calculated with respect to the number of coupled pore branches bridged by the flow, λ_b (Carrière 2007; Lester et al. 2013), instead of time. λ_b can be expressed as

$$\lambda_b = \lambda \Delta t_b, \quad (4.3)$$

where Δt_b is the average residence time of the solute in a pore branch, i.e., locations of critical separation of fluid lines commonly found in the vicinity of solid boundaries (Lester et al. 2016b). These are linked together according to the system's topology, thus largely influencing solute transport and mixing (Lester et al. 2016a). We approximate the average branch size, a_b , as function of the average pore size, $\bar{\zeta}$, as $a_b \approx 2\bar{\zeta}$, leading to $\Delta t_b \approx 2\bar{\zeta}/\bar{v}$. This yields values for λ_b ranging as low as 0.06 for $S_w = 1.00$ and q_1 , up to 0.13 for $S_w = 0.76$ and q_3 , which are in line with previously reported values of $\lambda_b = 0.1178$ for open

porous networks formed by randomly connected pore branches and mergers (Lester et al. 2013). Note that this approximation is based on the average pore size, which was defined from the pore space under full saturation. A more rigorous derivation of λ_b would require an exact estimation of a_b , which takes into account the larger variability in the local branch size resulting from the presence of air clusters of different sizes across the pore space. These are known to block sections of the pore space, leading to the formation of stagnation zones of low flow velocity (de Gennes 1983; Jiménez-Martínez et al. 2015; Velásquez-Parra et al. 2022), which increase the streamlines' tortuosity and can lead to the formation of larger pore branches compared to those approximated based on $\bar{\zeta}$. Furthermore, future investigations should also focus on the design of numerical or experimental protocols for the uncertainty quantification of these exponents with the goal of offering a more quantitative validation of the occurrence and strength of chaos in porous media.

4.4 CONCLUSIONS AND OUTLOOK

In this work, we present a systematic study of the impact of a second immiscible (non-wetting) phase in the pore space on the transport dynamics of an injected solute. We have focused both on the deformation experienced by the solute's plume as it is advected by the underlying flow field, characterized by stretching and folding of the plume's front, and on the mixing dynamics (between the injected solute and the resident solution) resulting from that deformation. The results reveal an exponential growth with travel distance for both cases. The occurrence of chaos, typically studied under low-diffusivity conditions (Heyman et al. 2020; Souzy et al. 2020), persists even in the presence of diffusion-relevant conditions for the length scale of the whole porous medium studied. In addition, the growth rates of deformation and of mixing increase upon a decrease of saturation, for the range of S_w values here reported. This reveals stronger chaotic dynamics of the transported solute due to the increase in heterogeneity arising from the presence and distribution of air within the porous space. This translates into more efficient mixing under unsaturated conditions. In addition, a higher mean fluid flow velocity, as expressed here by an increase in the imposed flow rates, also leads to stronger exponential growth of the mixing volume. These results are in line with those obtained from the reference transport experiments, from which the images used to set up this numerical analysis were obtained, and where an increase in the mixing efficiency both for lower S_w and larger q under diffusion relevant conditions were reported (Velásquez-Parra et al. 2024).

Further research should aim at understanding these dynamics at saturation degrees even lower than those considered here, which are also of high relevance for several natural systems. In particular, the impact of large changes in pore space topology below the so-called critical saturation, under which the system's dispersivity has been shown to decrease (Raouf and Hassanizadeh 2013), should be investigated. At very low S_w , the flow field is strongly channelized by very dominant preferential pathways, through which most of the solute will be transported. This could inhibit the solute's plume deformation and the development of chaotic dynamics in the pore space. In addition, similar investigations under multiphase flow conditions, i.e., under the simultaneous movement of the wetting and immiscible non-wetting phase, would further contribute to understanding the chaotic dynamics under conditions commonly found in the subsoil and in several other applications. We believe that the results presented here will find application in the assessment and prediction of homogeneous and heterogeneous reactions in unsaturated porous media. In particular, they can be exploited in large-scale groundwater remediation (Cho et al. 2019; Mays and Neupauer 2012; Neupauer et al. 2014) and biodegradation processes (Bagtzoglou and Oates 2007), in which first advances on the successful application of chaotic mixing have been reported. We believe that our results will motivate further research of similar processes under even more complex systems and conditions.

BIBLIOGRAPHY

- Aquino, T., T. Le Borgne, and J. Heyman (2023). "Fluid-solid reaction in porous media as a chaotic restart process." In: *Physical Review Letters* 130, p. 264001.
- Aref, H. (1984). "Stirring by chaotic advection." In: *Journal of Fluid Mechanics* 143, pp. 1–21.
- Aref, H. (2002). "The development of chaotic advection." In: *Physics of Fluids* 14, pp. 1315–1325.
- Aref, H., J. R. Blake, M. Budišić, S. S. Cardoso, J. H. Cartwright, H. J. Clercx, K. El Omari, U. Feudel, R. Golestanian, E. Guoillart, G. F. Van Heijst, T. S. Krasnopolskaya, Y. Le Guer, R. S. MacKay, V. V. Meleshko, G. Metcalfe, I. Mezić, A. P. De Moura, O. Piro, M. F. Speetjens, R. Sturman, J. L. Thiffeault, and I. Tuval (2017). "Frontiers of chaotic advection." In: *Reviews of Modern Physics* 89, p. 025007.
- Bagtzoglou, A. C. and P. M. Oates (2007). "Chaotic advection and enhanced groundwater remediation." In: *Journal of Materials in Civil Engineering* 19, pp. 75–83.
- Bakker, M. and K. Hemker (2004). "Analytic solutions for groundwater whirls in box-shaped, layered anisotropic aquifers." In: *Advances in Water Resources* 27, pp. 1075–1086.
- Barbier, E. (2002). "Geothermal energy technology and current status: An overview." In: *Renewable and Sustainable Energy Reviews* 6, pp. 3–65.
- Carrière, P. (2007). "On a three-dimensional implementation of the Baker's transformation." In: *Physics of Fluids* 19, p. 118110.
- Chiogna, G., O. A. Cirpka, M. Rolle, and A. Bellin (2015). "Helical flow in three-dimensional nonstationary anisotropic heterogeneous porous media." In: *Water Resources Research* 51, pp. 261–280.
- Chiogna, G., O. A. Cirpka, and P. A. Herrera (2016). "Helical flow and transient solute dilution in porous media." In: *Transport in Porous Media* 111, pp. 591–603.
- Chiogna, G., M. Rolle, A. Bellin, and O. A. Cirpka (2014). "Helicity and flow topology in three-dimensional anisotropic porous media." In: *Advances in Water Resources* 73, pp. 134–143.
- Cho, M. S., F. Solano, N. R. Thomson, M. G. Trefry, D. R. Lester, and G. Metcalfe (2019). "Field trials of chaotic advection to enhance reagent delivery." In: *Groundwater Monitoring and Remediation* 39, pp. 23–39.

- Cirpka, O. A., G. Chiogna, M. Rolle, and A. Bellin (2015). "Transverse mixing in three-dimensional nonstationary anisotropic heterogeneous porous media." In: *Water Resources Research* 51, pp. 241–260.
- Cunningham, A. B., R. R. Sharp, R. Hiebert, and G. James (2003). "Subsurface biofilm barriers for the containment and remediation of contaminated groundwater." In: *Bioremediation Journal* 7, pp. 151–164.
- De Anna, P., J. Jiménez-Martínez, H. Tabuteau, R. Turuban, T. Le Borgne, M. Derrien, and Y. Méheust (2014). "Mixing and reaction kinetics in porous media: An experimental pore scale quantification." In: *Environmental Science and Technology* 48, pp. 508–516.
- De Barros, F. P., M. Dentz, J. Koch, and W. Nowak (2012). "Flow topology and scalar mixing in spatially heterogeneous flow fields." In: *Geophysical Research Letters* 39, p. L08404.
- De Gennes, P. G. (1983). "Hydrodynamic dispersion in unsaturated porous media." In: *Journal of Fluid Mechanics* 136, pp. 189–200.
- Dentz, M., T. Le Borgne, A. Englert, and B. Bijeljic (2011). "Mixing, spreading and reaction in heterogeneous media: a brief review." In: *Journal of Contaminant Hydrology* 120, pp. 1–17.
- Dunlop, P. J. and R. H. Stokes (1951). "The diffusion coefficients of Sodium and Potassium iodides in aqueous solution at 25 C." In: *Journal of the American Chemical Society* 73, pp. 5456–5457.
- Glover, P. W. and N. Déry (2010). "Streaming potential coupling coefficient of quartz glass bead packs: dependence on grain diameter, pore size, and pore throat radius." In: *Geophysics* 75, 1ND–Z138.
- Guédon, G. R., F. Inzoli, M. Riva, and A. Guadagnini (2019). "Pore-scale velocities in three-dimensional porous materials with trapped immiscible fluid." In: *Physical Review E* 100, p. 043101.
- Heyman, J., D. R. Lester, and T. Le Borgne (2021). "Scalar signatures of chaotic mixing in porous media." In: *Physical Review Letters* 126, p. 34505.
- Heyman, J., D. R. Lester, R. Turuban, Y. Méheust, and T. Le Borgne (2020). "Stretching and folding sustain microscale chemical gradients in porous media." In: *Proceedings of the National Academy of Sciences of the United States of America* 117, pp. 13359–13365.
- Hu, Y., T. Schneider, B. Wang, D. Zorin, and D. Panozzo (2020). "Fast tetrahedral meshing in the wild." In: *ACM Transactions on Graphics* 39, 117:1–117:18.
- Jiménez-Martínez, J., P. de Anna, H. Tabuteau, R. Turuban, T. Le Borgne, and Y. Méheust (2015). "Pore-scale mechanisms for the enhancement of mixing in unsaturated porous media and implications for chemical reactions." In: *Geophysical Research Letters* 42, pp. 5316–5324.

- Lahav, O., M. Kochva, and J. Tarchitzky (2010). "Potential drawbacks associated with agricultural irrigation with treated wastewaters from desalinated water origin and possible remedies." In: *Water Science and Technology* 61, pp. 2451–2460.
- Le Borgne, T., M. Dentz, and E. Villermanx (2013). "Stretching, coalescence, and mixing in porous media." In: *Physical Review Letters* 110, p. 204501.
- Lester, D. R., G. Metcalfe, and M. G. Trefry (2013). "Is chaotic advection inherent to porous media flow?" In: *Physical Review Letters* 111, p. 174101.
- Lester, D. R., G. Metcalfe, and M. G. Trefry (2014). "Anomalous transport and chaotic advection in homogeneous porous media." In: *Physical Review E* 90, p. 063012.
- Lester, D. R., M. G. Trefry, and G. Metcalfe (2016a). "Chaotic advection at the pore scale: Mechanisms, upscaling and implications for macroscopic transport." In: *Advances in Water Resources* 97, pp. 175–192.
- Lester, D. R., M. Dentz, and T. Le Borgne (2016b). "Chaotic mixing in three-dimensional porous media." In: *Journal of Fluid Mechanics* 803, pp. 144–174.
- Li, L., K. Maher, A. Navarre-Sitchler, J. Druhan, C. Meile, C. Lawrence, J. Moore, J. Perdrial, P. Sullivan, A. Thompson, et al. (2017). "Expanding the role of reactive transport models in critical zone processes." In: *Earth-Science Reviews* 165, pp. 280–301.
- Markale, I., A. Velásquez-Parra, A. Alcolea, and J. Jiménez-Martínez (2022). "Mixing controlled adsorption at the liquid-solid interfaces in unsaturated porous media." In: *Transport in Porous Media* 146, pp. 159–175.
- Marone, F., C. M. Schlepütz, S. Marti, F. Fuisseis, A. Velásquez-Parra, M. Griffa, J. Jiménez-Martínez, K. J. Dobson, and M. Stampanoni (2020). "Time resolved in situ X-Ray tomographic microscopy unraveling dynamic processes in geologic systems." In: *Frontiers in Earth Science* 7, p. 346.
- Mays, D. C. and R. M. Neupauer (2012). "Plume spreading in groundwater by stretching and folding." In: *Water Resources Research* 48.
- Metcalfe, G., D. Lester, and M. Trefry (2022). "A primer on the dynamical systems approach to transport in porous media." In: *Transport in Porous Media* 146, pp. 55–84.
- Neupauer, R. M., J. D. Meiss, and D. C. Mays (2014). "Chaotic advection and reaction during engineered injection and extraction in heterogeneous porous media." In: *Water Resources Research* 50, pp. 1433–1447.
- Ottino, J. M. (1989). *The Kinematics of mixing: stretching, chaos, and transport*. Cambridge, England: Cambridge University Press.
- Ottino, J. M. (1990). "Mixing, chaotic advection, and turbulence." In: *Annual Review Fluid Mechanics* 22, pp. 207–254.

- Raouf, A. and S. M. Hassanizadeh (2013). "Saturation-dependent solute dispersivity in porous media: Pore-scale processes." In: *Water Resources Research* 49, pp. 1943–1951.
- Sebilo, M., B. Mayer, B. Nicolardot, G. Pinay, and A. Mariotti (2013). "Long-term fate of nitrate fertilizer in agricultural soils." In: *Proceedings of the National Academy of Sciences* 110, pp. 18185–18189.
- Simunek, J., M. T. van Genuchten, and M. Sejna (2008). "Development and applications of the HYDRUS and STANMOD software packages and related codes." In: *Vadose Zone Journal* 7, pp. 587–600.
- Souzy, M., H. Lhuissier, Y. Méheust, T. Le Borgne, and B. Metzger (2020). "Velocity distributions, dispersion and stretching in three-dimensional porous media." In: *Journal of Fluid Mechanics* 891, A16.
- Triadis, D., F. Jiang, and D. Bolster (2019). "Anomalous dispersion in pore-scale simulations of two-phase flow." In: *Transport in Porous Media* 126, pp. 337–353.
- Valdés, J. P., L. Kahouadji, and O. K. Matar (2022). "Current advances in liquid–liquid mixing in static mixers: a review." In: *Chemical Engineering Research and Design* 177, pp. 694–731.
- Velásquez-Parra, A., F. Marone, R. Kaufmann, M. Griffa, and J. Jiménez-Martínez (2024). "Phase saturation control on vorticity enhances mixing in porous media." In: *Water Resources Research* 60, e2023WR036628.
- Velásquez-Parra, A., T. Aquino, M. Willmann, Y. Méheust, T. Le Borgne, and J. Jiménez-Martínez (2022). "Sharp transition to strongly anomalous transport in unsaturated porous media." In: *Geophysical Research Letters* 49, e2021GL096280.
- Williams, K., A. Kemna, M. J. Wilkins, and J. Druhan (2009). "Geophysical monitoring of coupled microbial and geochemical processes during stimulated subsurface bioremediation." In: *Environmental Science and Technology* 43, pp. 6717–6723.
- Winograd, I. (1981). "Radioactive waste disposal in thick unsaturated zones." In: *Science* 212, pp. 1457–1464.
- Ye, Y., G. Chiogna, C. Lu, and M. Rolle (2020). "Plume deformation, mixing, and reaction kinetics: An analysis of interacting helical flows in three-dimensional porous media." In: *Physical Review E* 102, p. 013110.
- Yu, Y., G. Chiogna, O. A. Cirpka, P. Grathwohl, and M. Rolle (2015). "Experimental evidence of helical flow in porous media." In: *Physical Review Letters* 115, p. 194502.
- Zhang, P., S. L. Devries, A. Dathe, and A. C. Bagtzoglou (2009). "Enhanced mixing and plume containment in porous media under time-dependent oscillatory flow." In: *Environmental Science and Technology* 43, pp. 6283–6288.

SUPPLEMENTARY MATERIAL TO CHAPTER 4

This appendix has been submitted as Supplementary Material to: Velásquez-Parra, A., F. Marone, M. Griffa, & J. Jiménez-Martínez (2024). "Chaotic transport of solutes in unsaturated porous media". In: *Environmental Science and Technology*.

This Supplementary Material presents additional results obtained from the numerical transport simulations, with the aim of allowing further comparison of the main outputs of the study for the different saturation degrees, S_w , and injection flow rates, q , tested. Appendix 4.A presets detailed information on the reconstruction and quantification of the solute's plume deformation, while Appendix 4.B provides details on the exponential regressions applied for most of the numerical results of this study. These results are further summarized in Figures 4.5 to 4.10, and include: (i) the reconstruction of the injection plume's deformation for all S_w , as obtained from the low-diffusivity transport simulations, together with a schematic of the methodology used for its quantification, (ii) the concentration fields obtained for every S_w at different q -values, resulting from the simulations performed for the diffusive transport scenario, and (iii) the evolution of the mixing volume over distance for all S_w - q combinations. Finally, Tables 4.2 and 4.3 summarize the results of the exponential regressions.

4.A RECONSTRUCTION AND QUANTIFICATION OF THE SOLUTE'S PLUME DEFORMATION

In order to assess the deformation of the solute plume along the main longitudinal flow direction (z -axis, see Figure 4.5), starting from the point of injection, we reconstructed the interfacial surface (or manifold) that outlines the plume. This corresponds to the interface between the injected, more concentrated solution, and the resident, less concentrated one, where both solutions meet and mix with each other. We represent this interface by the isosurface of the concentration scalar field characterized by a concentration, c , of 1% of the value $c_0 = 1.0$ M at the injection region, i.e., isosurface of 1% of concentration. This threshold thus acts as the lowest concentration bound for the region where mixing can

occur, helping delineate the volume occupied by the plume across the pore space (de Anna et al. 2014). We reconstruct this isosurface using the results of the numerical simulations performed for the low-diffusivity transport scenario, i.e., with a diffusion coefficient $D_S = 1 \times 10^{-12} \text{ m}^2\text{s}^{-1}$. Under these conditions, we guarantee that the longitudinal and transversal deformation components of the plume are preserved over the length of the sample, i.e., diffusion has not yet smoothed out the plume's front. This is further confirmed by the high Péclet numbers achieved ($Pe \geq 2259$ for all low-diffusivity conditions tested, see Section 4.3, Table 4.1), reflecting the overall larger diffusive times over the length of a pore throat compared to the corresponding advective times over the characteristic length of a pore body. This diffusive time is even larger than the average travel time across the entire length of the sample for all simulated conditions. To reconstruct this isosurface, we exported the concentration field obtained from the simulation for any of the tested S_w - q combinations, at a spatial resolution of $11 \mu\text{m}$ in all three principal directions. We then extracted all positions displaying a concentration in the range $0.9\% - 1.1\%$ of the injected value c_0 . We created an analysis pipeline, implemented in Matlab, first to interpolate the obtained point cloud and to generate a continuous surface. We proceeded to correct this continuous surface by removing all locations occupied by either the solid or the gas phase, through comparison with the tomograms of the liquid phase. They were the images used for creating the input geometries of the numerical simulations (Marone et al. 2020; Velásquez-Parra et al. 2024). We finally triangulate the resulting isosurface using a moving observation window of the same size as the spatial resolution of the concentration fields. Triangulation also allowed the generation of single *.stl files for representing the corrected isosurface, as shown in Figure 4.5 for all five saturation degrees tested.

The quantification of the solute's plume deformation was performed based on the isosurfaces generated with the aforementioned methodology. It aimed at estimating the amount of transverse deformation experienced by the solute as it spread and dispersed across the pore space. We performed this by slicing the reconstructed isosurfaces with a x - y plane moving along the main longitudinal direction (z -axis) at fixed space steps equal to the pixel resolution of the reference tomographs ($2.75 \mu\text{m}$). This yields a set of x - y planes containing single curve elements resulting from this intersection, which, as an ensemble, represent the amount of transversal deformation, i.e., transverse stretching and folding, experienced by the solute's plume over travel distance. The length of every single curve element is computed by counting the number of grid points in the concentration field that form it, for which an unitary size equal to the resolution of the concentration fields ($11 \mu\text{m}$) can be defined. The total solute

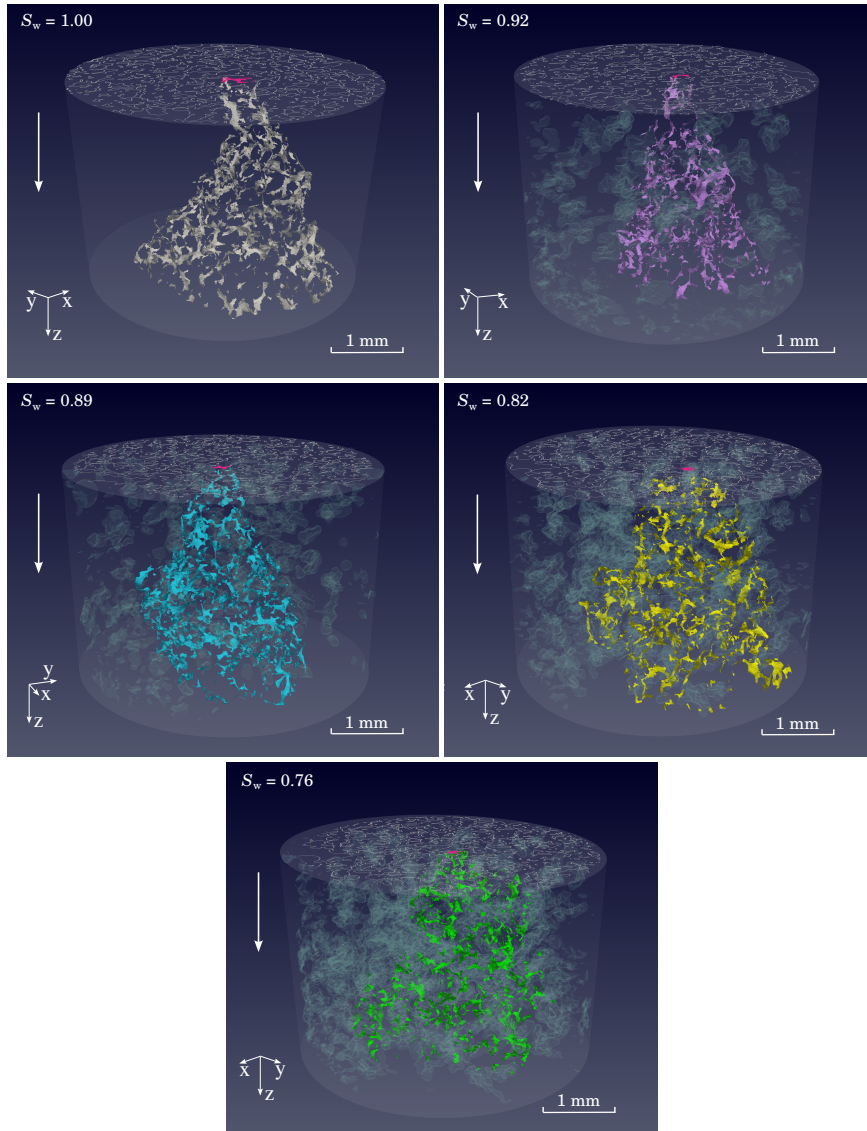


Figure 4.5: Solute's plume deformation, i.e., deformation of the isosurface of the 1% of concentration, as reconstructed from the numerical simulations performed for the low-diffusivity transport scenario ($D_S = 1 \times 10^{-12} \text{ m}^2 \text{ s}^{-1}$), for all five saturation degrees considered in this study. In all cases, the air phase is shown in cyan transparency, the sample boundaries are shown as a transparent cylinder, and the inlet's cross section at the top is shown in white, where the injection pore is highlighted in magenta. The color assigned to every isosurface in each panel corresponds to the color map employed in Section 4.3 for every saturation degree. The white arrows represent the main flow direction.

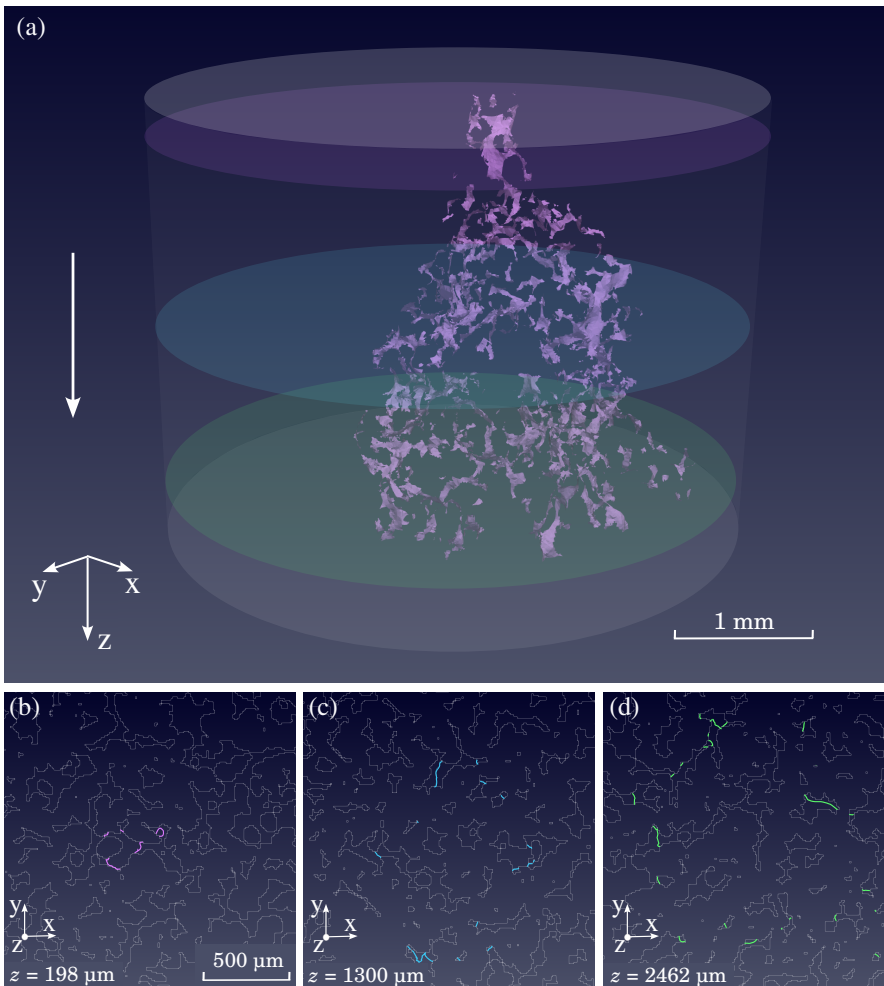


Figure 4.6: Graphical summary of the quantification of the solute's plume deformation, i.e., deformation of the isosurface of the 1% of concentration. a) Isosurface generated for the porous medium characterized by a saturation degree $S_w = 0.92$. The systems bounds are depicted as a transparent cylinder, and three x - y planes, located along z at $198 \mu\text{m}$ (purple), $1300 \mu\text{m}$ (blue), and $2642 \mu\text{m}$ (green) from the injection point, are displayed. The white arrow represents the main flow direction. b), c), and d) show the 2D sections resulting from the intersection of these three x - y planes with the porous medium, respectively. They show the resulting pore space cross section as white lines, and the intersection with the isosurface of the 1% of concentration as single curves in the same color as the corresponding plane. The ensemble of these single curves represent the transverse deformation of the plume across the pore space. The length scale in panel b) is common for panels b), c), and d).

plume's deformation for a given x - y plane is then the sum of the length of these single elements. Figure 4.6 shows a schematic of this pipeline. Figure 4.6a depicts the isosurface generated for the porous medium with a saturation degree $S_w = 0.92$, and three x - y planes located at three different z -coordinates. Figures 4.6b to 4.6d show the 2D intersections resulting from slicing the system with each one of these three planes. The transverse isosurface deformation on each case is represented by the single colored curve elements located inside some of the intersected pore bodies.

4.B EXPONENTIAL FUNCTION REGRESSIONS

The post-processing of the numerical simulations allowed the quantification of both the deformation of the solute's plume and of the mixing volume across the sample. Results showed an exponential trend for the growth of both variables as a function of the travel length along the main longitudinal flow direction. We characterize this trend by performing exponential function regressions on both of these data sets for all the simulated conditions, that is, for all S_w - q combinations both for the low-diffusivity and the diffusive transport scenarios. The exponential function can be written as

$$Y = \beta e^{\alpha z}, \quad (4.4)$$

where β and α are the corresponding regression parameters, and Y represents the target quantity, which, in this study, could represent the isosurface deformation ℓ/ℓ_0 or the mixing volume M_V . The corresponding regression was obtained by applying the least-squares method over a linearization of Eq. 4.4, expressed as

$$\ln Y = \ln \beta + \alpha z, \quad (4.5)$$

that is, considering the logarithmic values of Y . By adopting $\tilde{Y} = \ln Y$, the regression parameters α and β can be written as

$$\alpha = \frac{(n \sum_{i=1}^n \tilde{Y}_i z_i - \sum_{i=1}^n \tilde{Y}_i \sum_{i=1}^n z_i)}{(n \sum_{i=1}^n z_i^2 - (\sum_{i=1}^n z_i)^2)}, \quad (4.6)$$

$$\beta = \frac{(\sum_{i=1}^n \tilde{Y}_i - \alpha \sum_{i=1}^n z_i)}{n}, \quad (4.7)$$

where n is the total number of data points per data set. We applied Eqs. 4.6 and 4.7 to the evolution over distance of: (i) the isosurface deformation ℓ/ℓ_0 for

$S_w [-]$	ℓ/ℓ_0			$M_V(D_S)$		
	α_{ℓ/ℓ_0}	β_{ℓ/ℓ_0}	sMAPE	$\alpha_{M_V(D_S)}$	$\beta_{M_V(D_S)}$	sMAPE
1.00	0.0010	86.94	0.097	0.0015	4.77	0.105
0.92	0.0012	59.87	0.093	0.0029	1.14	0.111
0.89	0.0014	4.470	0.082	0.0022	3.30	0.096
0.82	0.0020	30.80	0.121	0.0042	2.04	0.203
0.76	0.0022	79.99	0.121	0.0063	1.76	0.132

Table 4.2: Summary of the exponential regression (see Eq. 4.4) performed on the results obtained from the numerical simulations for the low-diffusivity transport scenario, for all saturation degrees considered. Two main data sets are included, namely, the isosurface deformation, ℓ/ℓ_0 , and the mixing volume, $M_V(D_S)$. Both of them did not show any dependency on the injection flow rate, q , given the high Péclet numbers achieved, $Pe(D_S) > 2000$. Reported variables include the exponential regression parameters α_{ℓ/ℓ_0} and $\alpha_{M_V(D_S)}$ [μm^{-1}], and β_{ℓ/ℓ_0} [-] and $\beta_{M_V(D_S)}$ [$\times 10^4 \mu\text{m}^2$], and also the dimensionless symmetric Mean Absolute Percentage Error (sMAPE).

the low-diffusivity scenario, (ii) the mixing volume for the low-diffusivity scenario, $M_V(D_S)$, and (iii) the mixing volume for the diffusive transport scenario, $M_V(D_H)$, for all five saturation degrees considered in this study. Note that only the latter case showed a dependency on the injection flow rate, q , given the lower Péclet numbers achieved (see Figures 4.7 and 4.8 for a 3D visualisation of these concentration fields for the highest and the lowest injection flow rate considered). Therefore, the regression for $M_V(D_H)$ as a function of z was applied for each combination S_w - q , as presented in Figure 4.9. Tables 4.2 and 4.3 summarize the regression parameters obtained for both ℓ/ℓ_0 and M_V for the low-diffusivity and diffusive transport scenarios, respectively. They also summarize the values of symmetric Mean Absolute Percentage Error (sMAPE), used as Goodness-of-Fit measure for evaluating the regressions. It is expressed as

$$\text{sMAPE} = \frac{1}{n} \sum_{i=1}^n \frac{|Y_{i,f} - Y_i|}{|Y_{i,f}| + |Y_i|}, \quad (4.8)$$

where $|\cdot|$ denotes the absolute value, and $Y_{i,f}$ is the predicted value for the variable Y_i . Note that the large spatial heterogeneity of the pore space led to constant oscillations in the evolution of both ℓ/ℓ_0 and $M_V(D_H)$ over the course of a few pores, as observed in Figures 4.2 and 4.3 in Section 4.3, which reflected itself in the regression.

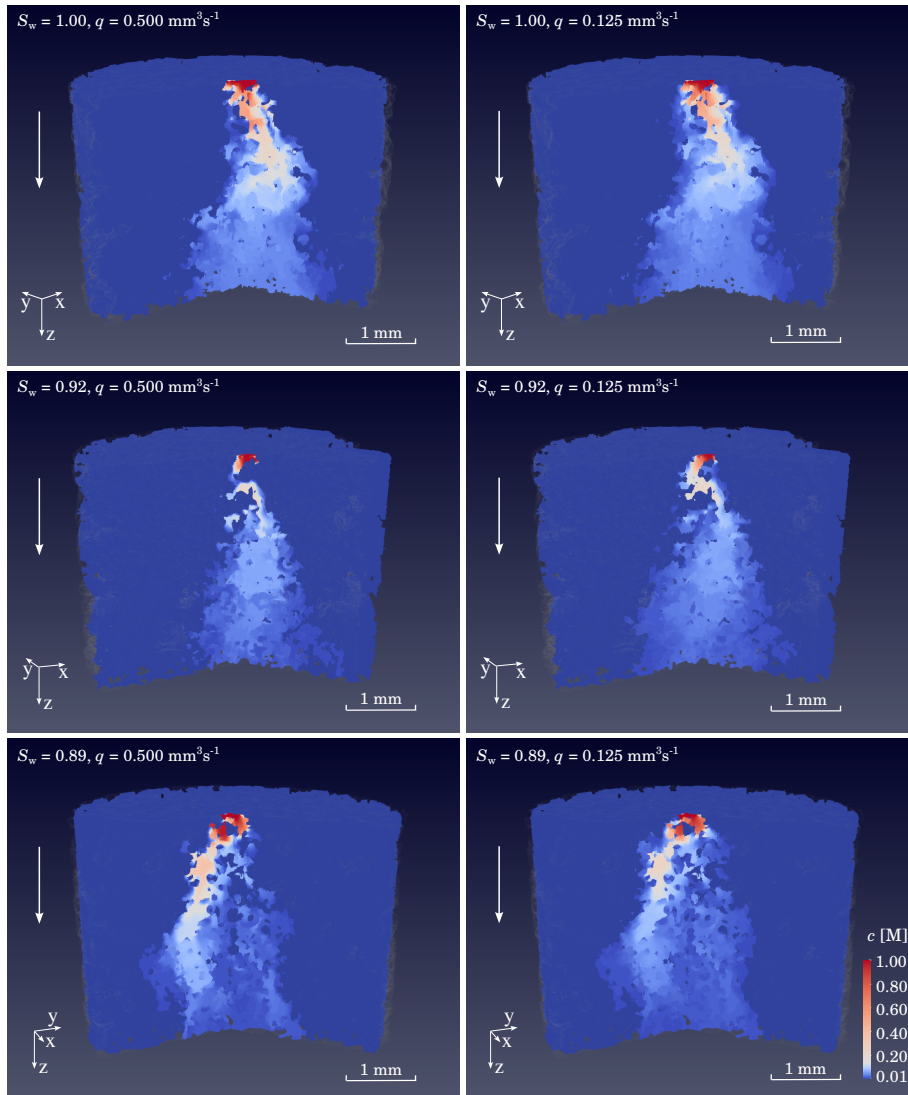


Figure 4.7: Concentration field inside of the porous medium, expressed in units of mole per unit of volume (M), for the saturation degrees $S_w = 1.00$, 0.92 , and 0.89 , as obtained from the numerical simulations performed for the diffusive transport scenario ($D_H = 1.929 \times 10^{-9} \text{ m}^2 \text{ s}^{-1}$). For all cases, results for the highest flow rate, $q_1 = 0.500 \text{ mm}^3 \text{ s}^{-1}$, and for the lowest one, $q_3 = 0.125 \text{ mm}^3 \text{ s}^{-1}$, are shown in the left and the right column, respectively. The color bar is common to all panels, where all concentration values below 0.01 M are displayed in the darkest blue. In addition, only the solid phase is shown in grey transparency, and only three-quarters of the sample are shown to better visualize the concentration gradients inside the sample. The white arrows represent the main flow direction.

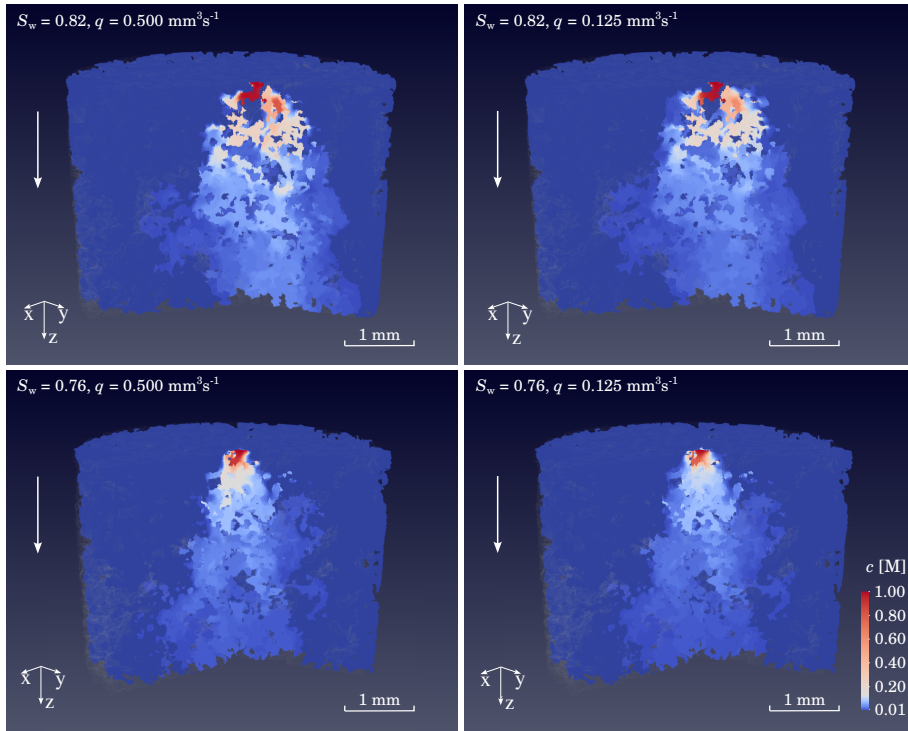


Figure 4.8: Concentration field inside of the porous medium, expressed in units of mole per unit of volume (M), for the saturation degrees $S_w = 0.82$ and 0.76 , as obtained from the numerical simulations performed for the diffusive transport scenario ($D_H = 1.929 \times 10^{-9} \text{ m}^2\text{s}^{-1}$). For all cases, results for the highest flow rate, $q_1 = 0.500 \text{ mm}^3\text{s}^{-1}$, and for the lowest one, $q_3 = 0.125 \text{ mm}^3\text{s}^{-1}$, are shown in the left and the right column, respectively. The color bar is common to all panels, where all concentration values below 0.01 M are displayed in the darkest blue. In addition, only the solid phase is shown in grey transparency, and only three-quarters of the sample are shown to better visualize the concentration gradients inside the sample. The white arrows represent the main flow direction.

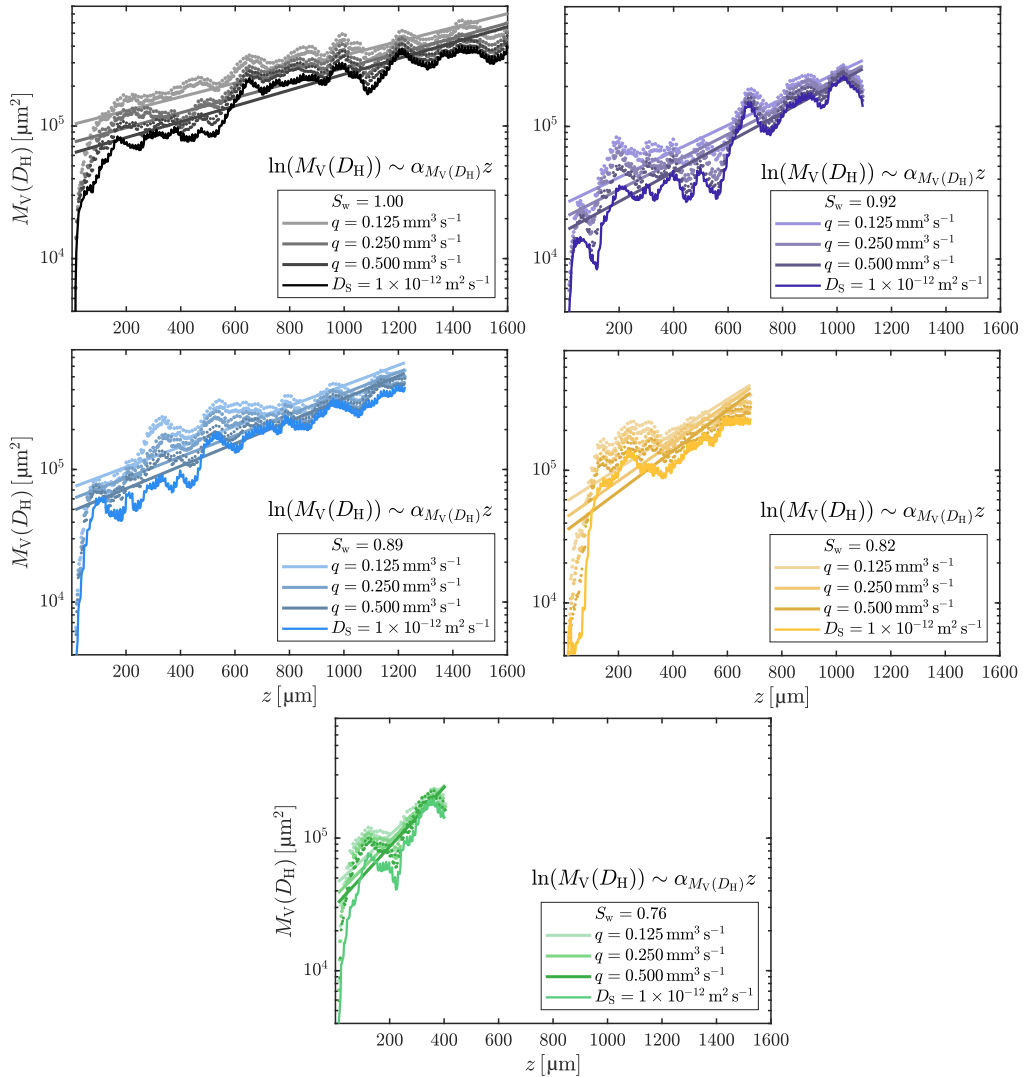


Figure 4.9: Evolution of the mixing volume, $M_V(D_H)$, along the main flow direction, z , for all five saturation degrees considered in the study, based on the results of the numerical simulations for the diffusive transport scenario defined by $D_H = 1.929 \times 10^{-9} \text{ m}^2 \text{ s}^{-1}$. Values for $M_V(D_H)$ have been computed over a x - y cross-section plane moving along z , and are displayed as markers in every panel. The corresponding exponential regressions are shown as continuous lines. In each panel, results for the three tested flow rates are shown in different colors. In addition, the evolution of M_V along z for the low-diffusivity case D_S is also shown for comparison in each case.

$S_w [-]$	$M_V(D_H)$								
	$q_1 = 0.125 \text{ mm}^3\text{s}^{-1}$			$q_2 = 0.250 \text{ mm}^3\text{s}^{-1}$			$q_3 = 0.500 \text{ mm}^3\text{s}^{-1}$		
	$\alpha_{M_V(D_H)}$	$\beta_{M_V(D_H)}$	sMAPE	$\alpha_{M_V(D_H)}$	$\beta_{M_V(D_H)}$	sMAPE	$\alpha_{M_V(D_H)}$	$\beta_{M_V(D_H)}$	sMAPE
1.00	0.0012	10.24	0.086	0.0013	7.50	0.095	0.0014	6.22	0.099
0.92	0.0023	2.62	0.111	0.0024	2.07	0.112	0.0026	1.62	0.121
0.89	0.0018	7.30	0.115	0.0018	5.98	0.099	0.0020	4.84	0.082
0.82	0.0030	5.68	0.159	0.0033	4.29	0.167	0.0035	3.40	0.181
0.76	0.0043	4.46	0.103	0.0047	3.66	0.113	0.0052	3.08	0.122

Table 4.3: Summary of the exponential regression (see Eq. 4.4) performed on the results obtained from the numerical simulations for the diffusive transport scenario, namely, the mixing volume, $M_V(D_H)$. Results for all five saturation degrees, S_w , and for all three injection flow rates, q_1 , q_2 , and q_3 , considered in the study are reported. For each data set, the exponential regression parameters, $\alpha_{M_V(D_H)}$ [μm^{-1}], and $\beta_{M_V(D_H)}$ [$\times 10^4 \mu\text{m}^2$], together with the dimensionless symmetric Mean Absolute Percentage Error (sMAPE), are reported.

4.C ADDITIONAL SUPPLEMENTARY MATERIAL

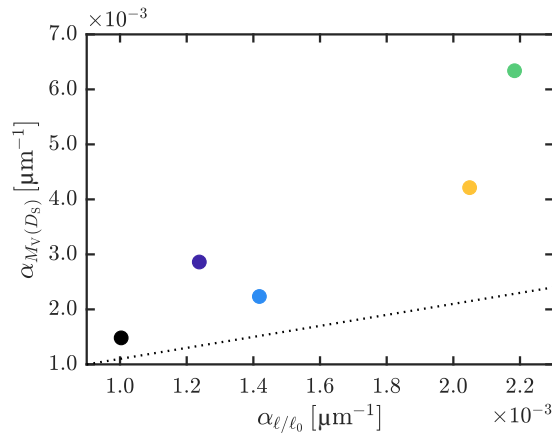


Figure 4.10: Comparison between the computed exponential regression parameters α_{ℓ/ℓ_0} and $\alpha_{M_V(D_S)}$, obtained from the isosurface deformation ℓ/ℓ_0 , and the mixing volume, $M_V(D_S)$, data sets for every saturation degree, respectively. Both data sets are linked to the low-diffusivity transport scenario. The dashed line corresponds to the linear equation of unitary slope. Results expose the large variation induced on the exponential growth rate of the mixing volume over travel distance upon a small change in the corresponding growth rate of the isosurface deformation.

BIBLIOGRAPHY

- De Anna, P., J. Jiménez-Martínez, H. Tabuteau, R. Turuban, T. Le Borgne, M. Derrien, and Y. Méheust (2014). "Mixing and reaction kinetics in porous media: An experimental pore scale quantification." In: *Environmental Science and Technology* 48, pp. 508–516.
- Marone, F., C. M. Schlepütz, S. Marti, F. Füsseis, A. Velásquez-Parra, M. Griffa, J. Jiménez-Martínez, K. J. Dobson, and M. Stampanoni (2020). "Time resolved in situ X-Ray tomographic microscopy unraveling dynamic processes in geologic systems." In: *Frontiers in Earth Science* 7, p. 346.
- Velásquez-Parra, A., F. Marone, R. Kaufmann, M. Griffa, and J. Jiménez-Martínez (2024). "Phase saturation control on vorticity enhances mixing in porous media." In: *Water Resources Research* 60, e2023WR036628.

DISCUSSION, CONCLUSIONS AND OUTLOOK

This chapter summarizes and discusses the key findings of this Doctoral thesis, highlighting the main scientific contributions leading to answering the research questions proposed in Chapter 1 and positioning them in the context of the current research in the field. In addition, future research ideas based on these main outputs and on the state-of-the-art summarized in Chapter 1 are discussed.

5.1 GENERAL DISCUSSION

5.1.1 *Control of liquid phase saturation on both fluid flow and solute dispersion in porous media*

Research Question No. 1 was addressed primarily based on the methodology and results outlined in Chapter 2. The performed numerical analysis of fluid flow in a 2.5D porous medium at different saturation degrees ($S_w = 1.00, 0.83, 0.77$ and 0.71) allowed identifying the main mechanisms shaping the flow field and controlling solute dispersion under unsaturated conditions. The well-known double flow structure (de Gennes 1983; Holzner et al. 2015), characterized by the combined presence in the pore space of a backbone of preferential flow and dead-end regions of low velocity, was observed in our studies and showed to be clearly enhanced at lower saturation. This enhancement was mainly visible in a stronger backbone formation, as hinted from the larger flow velocities displayed in the PDF of Eulerian velocities ($p_E(v)$) with lower S_w , and in larger dead-end regions, as revealed in the sharp transition in the power-law scaling of the low-velocity magnitudes observed in $p_E(v)$ after only a slight desaturation. In particular, these low-velocity zones were identified as a key morphological feature shaping the flow and transport response in the system, and were characterized by the PDF of the area of dead-end regions in all tested systems. Furthermore, particle

tracking simulations also exposed the non-stagnant nature of these regions, since particles reaching them still experienced purely advective flow motions over the time-scale of the analysis. This agrees with more recent studies that have exposed the vortex-like flow patterns inside these regions (Bordoloi et al. 2022). As a consequence of this highly heterogeneous flow field, particle spreading exhibited super-diffusive non-Fickian scalings over more than five time-decades for all tested conditions. These power-law scalings were also impacted upon changes in saturation, increasing from a quasi-Fickian scaling for $S_w = 1.00$ up to a quasi-ballistic trend for $S_w = 0.71$. This mechanism, by which the saturation degree conditions the formation of high- and low-velocity regions, consequently shaping the flow and transport response in the system, was exploited in the formulation of a theoretical framework for the prediction of the flow distribution and, ultimately, of the dispersion scalings as a function of saturation. This theoretical model stemmed from the simple hypothesis that the entire PDF of flow rates across the system, $p_Q(q)$, must originate from the added contributions of the backbone, $p_Q^b(q)$, and of the dead-ends, $p_Q^d(q)$, whose combination is controlled by the ratio of the total area occupied by dead-ends relative to the entire pore space area. This basic linear combination, expanded with both power-law definitions for the distribution of dead-end areas and an analytical solution for describing the velocity profile within a pore throat, allowed the successful prediction of $p_E(v)$ and $p_Q(q)$ as a function of saturation. Its main feature lies in its dependency on only a few parameters describing the pore space morphology, such as the average pore throat width, the relative occupancy of dead-ends in the pore space, and the scaling of the dead-ends area PDF. Therefore, it represents a major contribution to the prediction of flow in unsaturated porous media from structural properties of the pore space. The model's versatility is highlighted in its application in combination with a Continuous Time Random Walk model (Berkowitz et al. 2006; Cortis and Berkowitz 2004; Dentz et al. 2016) for the successful prediction of the scaling of superdiffusive particle dispersion as a function of saturation. The aforementioned large variation of the latter from a quasi-Fickian to a quasi-ballistic trend was very well captured by the proposed formulation.

The results here presented consider purely advective transport, hence allowing for particles trapped in dead-end regions to only leave such zones because of the action of very low flow velocities. In practice, the action of diffusion would eventually control the long-term response of the system by introducing low-velocity cutoffs that would define the residence time of particles in such locations (de Gennes 1983). As a consequence, the long-time dispersion scaling for all tested saturation degrees will eventually reach a Fickian condition. Never-

theless, the non-Fickian dispersion regimes here presented remain relevant over considerable time scales, especially as saturation decreases and the associated heterogeneous flow field allows for larger solute dispersion to develop over a given time scale. This has strong implications for additional processes, such as chemical reactions. For cases characterized by reaction times larger than the solute advective time over a characteristic length, the strong solute dispersion achieved at early and middle time scales would increase the interface where reactants would meet, conditioning the reaction product formation, both for homogeneous (liquid-liquid) and heterogeneous (liquid-solid) reactions. In the case of faster reactions, the enhanced dispersion would effectively lead to a larger spreading of the reaction front (Markale et al. 2021). We also hypothesize changes in the obtained trends when reaching very low saturation degrees, following previous studies that have hinted at a decrease in dispersivity below a so-called critical saturation (Raouf and Hassanizadeh 2013; Zhuang et al. 2021). Very low S_w values would dramatically enhance the flow separation in the system in the form of larger flow backbones and dead-ends, causing the pore space to resemble a fully saturated system, in which both flow and advective transport are mainly occurring along a few clearly differentiated pathways. Nevertheless, the power-law PDF of dead-end areas obtained in our study is expected to persist under such low saturation conditions. This is suggested by studies that have addressed the non-wetting phase cluster size distributions for systems with values of saturation as low as $S_w = 0.11$, which preserve the power-law dependency identified also at higher S_w values (Iglauer et al. 2012; Iglauer et al. 2010; Scheffer et al. 2021). Moreover, the proposed theoretical framework excels by its versatility in case a different functional form is identified, since it provides the means to quantify and to integrate such new dependency in the flow and transport prediction.

5.1.2 *Control of saturation on solute mixing and solute plume deformation*

Chapter 2 dealt with the study of transport from a purely advective approach, which allowed gaining a mechanistic understanding of the impact of an additional immiscible gas phase in the pore space on the liquid flow field, and ultimately on the dispersion of a solute in the liquid phase. To provide a full description of solute transport, we focused our attention on the process of mixing in the remaining of the doctoral thesis, keeping in mind the insights inferred from our 2.5D study. In particular, Research Question No. 2 is addressed based on the experimental and numerical results presented and discussed in Chapter 3. Synchrotron X-ray micro-tomography allowed observing experimentally

the evolution in time of a miscible solute injected in a nature-like porous system at different saturation degrees ($S_w = 0.92, 0.89, 0.82, 0.76,$ and 0.75) and at different solute flow rates ($q = 0.125, 0.25,$ and $0.50 \text{ mm}^3\text{s}^{-1}$). The results evidenced the enhancement of the mixing efficiency in the system upon both a decrease in the saturation degree and an increase in the injection flow rate. The same dependency was observed in the deformation experienced by the solute front, which directly conditions the rate of mixing, as it represents the surface where the diffusive mass flux between the miscible solutions occurs. This close interplay between solute front deformation and mixing rates matches previous findings reported on 2.5D fully saturated (de Anna et al. 2014) and unsaturated systems (Jiménez-Martínez et al. 2015). It was also found in the results presented in Chapter 4 based on numerical transport simulations performed on the same geometries here discussed, albeit after adopting a punctual injection. The latter depicted an increase in the rate of growth of the mixing volume upon a decrease in saturation, which was also reflected in a similar trend for the growth rate of plume's transversal deformation over travel distance. This interplay also very well reflects the insights gained from Chapter 2 on the impact of saturation on the flow field and solute dispersion. Lower saturation enhances solute dispersion through the stronger formation of backbones of preferential flow and dead-ends of low velocity, as hinted from the reconstructed experimental concentration fields and confirmed by the corresponding Stokes flow numerical simulations. This induces a larger solute front deformation, resulting in a larger mixing interface and, thus, in a faster smoothing out of the concentration gradients formed in the pore space. As a consequence of this mechanism, systems tested at the same injection flow rate showcased an overall smaller segregation of the mixing fluids, i.e., a smaller variance of the concentration field, upon a decrease in S_w . The control of the residence time of the solute in the system on mixing was visible when comparing experiments performed at the same S_w but at different q . Larger injection flow rates reduced the residence time of the solute in the sample, allowing for a larger solute dispersion before diffusion effectively smoothed out concentration differences over a measurable characteristic length. This reflected itself in a larger segregation between both miscible fluids at early times compared with lower q -values, which then dropped faster towards a fully mixed condition as diffusion took over.

The topological investigation carried out on the tested porous media helped unveil the physical mechanisms behind the experimental observations, as motivated by recent studies concluding on the dominant role of pore-space topology on shaping flow and transport in porous systems (Lester et al. 2013; Lester et al. 2016). This was based on both an analysis of the tomographic datasets

generated for the liquid phase only, and on the numerical Stokes flow simulations performed for every condition tested experimentally. This investigation exposed the strong impact of the pore space heterogeneity on solute transport. Lower saturation translated into changes in the pore space connectivity through the formation of new redundant loops, i.e., possible pathways connecting two locations in the pore space (Vogel 2002), as reflected in the decreasing Euler characteristic, χ , upon reduction in S_w . This improved the system's capacity to join initially separated entities through the formation of more tortuous pathways, leading to enhanced streamlines convergence and explaining the stronger backbone formation characteristic of low saturation degrees. Further analysis into this mechanism led to the identification of an enhancement of secondary flow motions in the pore space as a result of this increased convergence. This was revealed by quantification of the helicity density across the system, using the velocity and vorticity fields generated from the numerical flow simulations. Results revealed a linear increase in the average absolute helicity density, $\langle |h| \rangle$, in the pore space with decreasing S_w , for the range of saturation degrees considered in our study. Moreover, an increase in the injection flow rate also resulted in enhanced $\langle |h| \rangle$. These results led to the conclusion that the increased convergence of streamlines promotes the occurrence of helicity in the pore space. The numerical analysis also indicated that large values of $\langle |h| \rangle$ were linked with locations close to air clusters, where strong streamline deformation in the form of folding and braiding was observed. This hinted at the local occurrence of different fluid flow deformation mechanisms across the system in relation to the increased heterogeneity added by the air phase. The quantification of vortex identification criteria, such as the Q -criterion (Hunt et al. 1988), allowed addressing this aspect, with the aim of explaining the enhanced solute plume deformation observed experimentally at lower S_w . Q -criterion computations showed both a linear increase in the average positive Q values across the system, i.e., vorticity-dominated deformation, and a linear decrease in the average negative Q , i.e., shear-dominated deformation, at lower saturation degrees, for the range of S_w considered in our study. This translates into an enhancement of both the vorticity and the shear strain rate component of the local deformation tensor as a result of the increased heterogeneity in the system. However, the increase in the latter occurred at a faster rate, indicating a more dominant role of shear in inducing flow and solute deformation in the pore space. This was also inferred from the PDF of Q values in the liquid phase, which depicted a distribution skewed towards negative values for all conditions tested. Nevertheless, this skewness reduced at the lowest S_w tested, hinting at

the increased importance of rotational deformation, i.e., in the form of folding and braiding, as saturation keeps decreasing.

The results reported in Chapter 3 helped answer Research Question No. 2 by providing an extensive investigation of the physical mechanisms behind solute mixing in unsaturated porous media. In summary, the increase in heterogeneity in the pore space at lower saturation degrees altered the connectivity in the system, enhancing streamlines convergence and promoting the backbone formation. The resulting larger tortuosity and more twisted streamlines promoted helicity across the system, with large values of helicity density linked to intense braiding and folding, as observed locally along streamlines. This suggested the co-existence of different deformation mechanisms in the pore space, which was quantified through Q -criterion computations. Results revealed a larger contribution of shear to the overall deformation of the solute, regardless of saturation, and an increasing importance of vorticity-dominated deformation as saturation decreased. This interplay explains the larger solute plume deformation quantified from the experiments, and thus, the enhanced mixing efficiency measured at lower S_w . Similar investigations on fully saturated conditions at the Darcy scale had reported either a dominant role of shear (de Barros et al. 2012) or of vorticity (Chiogna et al. 2016) on both solute deformation and enhanced dilution. Our results point out a combined effect of both deformation mechanisms, as also suggested from studies performed at large scale (Geng et al. 2020), highlighting the role of pore-scale processes driving large-scale observations.

5.1.3 Chaotic advection and chaotic mixing in unsaturated porous media

The folding and braiding patterns observed in the streamlines generated from the numerical flow simulations discussed in Section 5.1.2 suggested the occurrence of chaotic dynamics on the spreading and mixing of the solute plume. These two types of deformation have been closely associated with non-zero helicity fields (Aref et al. 2017) and with the occurrence of exponential stretching of traverse materials lines (Metcalf et al. 2022). In addition, chaotic dynamics have been shown to be inherent to the high topological complexity of porous media (Lester et al. 2013). However, the solute plume deformation quantified from the synchrotron X-ray micro-tomography experiments and shown in Chapter 3 depicted an algebraic scaling over time. This is explained by the type of solute injection carried out in these experiments. A mass entry in the system distributed over the entire inlet's cross-section constrained the solute plume's front deformation analysis from the experimental data to the quantification of mainly longitudinal components of deformation. As some reference studies have

suggested (Heyman et al. 2020; Lester et al. 2013; Metcalfe et al. 2022; Yu et al. 2015), transversal plume deformation and lateral mass exchange are relevant elements to be considered in chaos investigations.

To answer Research Question No. 3 and to provide a full picture of the mechanisms leading to enhanced mixing in unsaturated porous media, we complemented our experimental study with steady-state numerical simulations of flow and transport (see Chapter 4). They addressed the aforementioned shortcoming in our experimental analysis by implementing a punctual injection towards the middle of the inlet, allowing the quantification of the lateral deformation component of the plume (Heyman et al. 2020). The latter was also achieved by adopting low-diffusivity conditions, implemented numerically by choosing a low diffusion coefficient for the mixing solutions. Results indicated the occurrence of exponential growth rates for the solute's plume deformation over travel distance. This rate was enhanced by a reduction in the saturation degree of the system, revealing not only the occurrence of chaotic advection under unsaturated conditions, but also the enhancement of such dynamics upon loss of saturation. Using the mixing volume, M_V , as a proxy for mixing quantification, results revealed the same exponential growth scaling for the evolution of M_V over travel distance. This scaling was sustained even under diffusion-relevant conditions for the dimensions of the tested domain, which were investigated in a second set of simulations by mimicking the conditions of the reference experiments (see Chapter 3). In addition, the exponential growth rate of M_V also increased at lower S_w . These results confirmed the impact of the pore space heterogeneity in inducing chaotic dynamics in the solute's mixing. Adopting diffusion-relevant conditions, i.e., low Péclet numbers, also allowed addressing the dependency of the chaotic mixing dynamics on the imposed flow conditions. For systems at the same saturation degree, results showed an increasing exponential growth rate of the mixing volume over distance with increasing flow rate. Overall, the numerical analysis of chaos further confirmed the same dependencies observed from the experimental work discussed in Chapter 3, that is, both mixing and solute deformation are enhanced upon both a decrease in saturation and an increase in the injection flow rate. The dominant role of the pore space heterogeneity in controlling the transport response is further highlighted in these results, specifically in how the short-ranged increase in the exponential growth rate of the solute plume's deformation as S_w decreased led to a far larger increase in the growth rate of the mixing volume.

The quantification of the solute plume's deformation under low-diffusivity conditions allowed yielding values for the Lyapunov exponents, λ , expressed as a function of time. They served as a direct measure of the strength of chaos

in the system and allowed comparing some of our results with those already reported in literature (Heyman et al. 2021; Heyman et al. 2020; Lester et al. 2013; Souzy et al. 2020). In contrast to the growth rate of solute plume deformation over distance, λ displayed a stronger increase upon a reduction in the saturation degree and it showed a dependency on the injection flow rate, increasing with larger q under constant saturation. Our results indicated the occurrence of chaos already at Péclet numbers smaller than those reported as lower bound for the occurrence of incomplete pore-scale mixing and chaotic advection, as defined from a simplified porous system composed of spherical glass beads (Heyman et al. 2020). This suggested the strong impact of the intrinsic pore space heterogeneity of the porous medium, which in our study had a closer resemblance to a natural porous system than in the reference studies (Heyman et al. 2020; Souzy et al. 2020), on the development of this chaotic dynamics. To our knowledge, this study represents the first time that a systematic study of the impact of saturation on the strength of chaotic dynamics in porous systems is reported. The obtained results further expand our understanding of the mechanisms behind solute transport and mixing in such conditions, and could support the application of chaotic mixing on large-scale problems involving the unsaturated regions of soils, such as groundwater remediation (Cho et al. 2019; Mays and Neupauer 2012; Neupauer et al. 2014) and biodegradation (Bagtzoglou and Oates 2007).

5.2 CONCLUSIONS AND CONTRIBUTIONS TO THE RESEARCH FIELD

This doctoral thesis presents and discusses exciting results in the study of flow and transport in unsaturated porous media, which contribute largely to the current state of the research in the field. The focus of the present thesis on both the physical mechanisms controlling these processes and their quantification provides the means for extending their application beyond the particular porous systems here tested. This includes for example fully saturated systems; porous systems also hosting a liquid and a gas phase in the pore space, albeit at lower degrees of saturation; or porous media containing fluids different than those explored in this study both for the non-wetting phase and the wetting phase, such as oil-brine systems relevant in CO₂ sequestration and injection (Jiménez-Martínez et al. 2016), or non-Newtonian fluids often encountered in industrial and medical applications (Seybold et al. 2021).

In the context of fluid flow analyses, some studies have attempted to effectively predict flow redistribution in porous media (Alim et al. 2017; de Anna et al. 2017; Holzner et al. 2015), with no particular studies addressing the case of unsaturated

conditions. The theoretical model shown in Chapter 2 attempts to bridge this gap by providing a theoretical framework for the prediction of flow and velocity probability density functions based on morphological characteristics of the pore space, among other parameters reflecting the control of heterogeneity on flow. It also outlines the physical mechanisms controlling such flow distributions, which serve as a foundation for further investigations that might focus on porous media of different characteristics and on different conditions than those tested here, i.e., different pore size distributions, lower porosity, or lower saturation degrees. This thesis also expands on the successful application of well-established models, such as the Continuous Time Random Walk model (Berkowitz et al. 2006; Cortis and Berkowitz 2004; Dentz et al. 2016), for the prediction of solute advective transport in unsaturated systems.

The present work also offers important advances in the mechanistic understanding of mixing in unsaturated porous media. In particular, the control of liquid phase saturation on both the occurrence and the strength of chaos has not been reported before. Furthermore, both the enhancement of secondary flow motions, i.e., helical flow, and the interplay between shear and rotational deformation components enhancing solute plume deformation as a function of saturation provide an integral description of the impact of pore space heterogeneity on flow and transport. These findings can find wider application across different scales. This includes millifluidic and/or pore-scale studies addressing additional physical processes, such as homogeneous or heterogeneous chemical reactions (Aquino et al. 2023; Markale et al. 2021) and solute transport under multiphase flow conditions, i.e., with simultaneous movement of several phases within the pore space. Also the optimization in the design of static mixers, often operated under laminar flow conditions (Valdés et al. 2022), and large-scale applications, such as groundwater remediation (Mays and Neupauer 2012; Neupauer et al. 2014) and biodegradation (Bagtzoglou and Oates 2007), in which the optimization of the mixing efficiency in the subsoil is desired, could benefit from the findings here reported.

Finally, this doctoral thesis presents a very important contribution to the use of synchrotron X-ray micro-tomography for the study of flow and transport in porous media. The high temporal resolutions achieved by the use of high-energy synchrotron radiation enabled the real-time imaging of solute spreading and mixing, contributing to the very small number of studies addressing such processes with similar methodologies (Chen et al. 2021; Hasan et al. 2020). Our experimental protocol could also be extended to studies carried out in laboratory X-ray facilities, in which high-resolution steady-state analysis could also be performed based on the current technical advances in X-ray imaging.

Additionally, the image analysis pipeline outlined in Chapter 3 could find wider application in the post-processing of synchrotron data involving the imaging of several material phases, being effectively implemented using open-source software. Moreover, this study further showcases the compatibility of combined experimental and numerical investigations for an integral approach to the study of complex physical processes in challenging natural and industrial systems.

5.3 OUTLOOK AND POSSIBLE FUTURE RESEARCH DIRECTIONS

The investigation presented in this doctoral thesis opens the door for the study of additional research questions and processes of high environmental and industrial relevance in natural and industrial porous media. This relates both to the scientific output presented here and to the experimental and numerical tools successfully applied for the observation and quantification of flow and transport under unsaturated conditions. The results presented in Chapters 2, 3, and 4 shared the commonality of investigating these processes in systems with saturation degrees as low as $S_w \sim 0.70$. Only a few similar transport studies at the pore scale have achieved lower saturation values. Markale et al. (2021) report values as low as 0.43 on an experimental investigation using Magnetic Resonance Imaging, whereas Hasan et al. (2020) achieved saturation degrees as low as 0.53 also using synchrotron X-ray micro-tomography, albeit on a simpler porous medium composed of spherical glass beads. Even though the saturation degree achieved experimentally is ultimately conditioned by the morphological characteristics of the tested porous medium, as its percolation threshold is approached, **the study of saturation degrees lower than those reported here could provide additional insights on flow and transport on conditions very relevant in nature and industry.** In particular, numerical and experimental investigations have reported a decrease in dispersivity below a so-called critical saturation (Raoof and Hassanizadeh 2013; Zhuang et al. 2021), which could translate into changes in the trends and scalings reported in this work. Such an investigation would benefit from the adoption of 3D conditions, in which potentially lower S_w -values could be reached. This would require the implementation of optimized techniques to induce desaturation in the sample, potentially different from those outlined in the experimental protocol of this study. Pore-scale studies using synchrotron X-ray micro-tomography for two-phase flow investigations (Armstrong et al. 2016; Schlüter et al. 2016) have reported on the use of fractional flow during the saturation phase, allowing reaching saturation values as low as $S_w \sim 0.10$. In addition, methods derived from soil triaxial testing to control the sample's degree of saturation based on a combination of back pressure, applied

directly to the pore volume, and an isotropic cell pressure, applied externally on the sample, could be further explored, since they would allow knowing the exact saturation degree of the tested sample prior to the injection of the solute.

An additional common feature of the experimental and numerical analyses presented here is the consideration of the non-wetting gas (air) phase as a fixed additional obstacle for flow, altering the heterogeneity of the system. This is a condition commonly found on deeper layers of the unsaturated region of soils, which are less disturbed by atmospheric processes. **However, the consideration of multiphase flow conditions, in which all fluid phases hosted in the pore space move simultaneously, represents a natural progression from the study here presented.** This would mimic the behavior of upper soil layers shortly after rain following dry periods, in which the incoming liquid phase would interact with and displace the existing air phase. It also represents processes commonly found in deeper aquifers, where CO₂ sequestration is commonly carried out, albeit in the presence of an oil phase. Several of the research questions here addressed remain open for the case of multiphase flow. The simultaneous movement of both fluid phases would induce transient conditions on the heterogeneity of the system, resulting in different fluid flow dynamics than those described here. This will potentially lead to stronger intermittent flow across the pore space, which is known to dominate the transport response of the system (de Anna et al. 2013; Kang et al. 2014). As a consequence, both the solute deformation dynamics and the resulting mixing efficiency in the system would likely be further enhanced. Particular attention should be given to the strength of chaos under such conditions, given the additional degree of freedom associated with locally transient flow regimes. **Addressing these research gaps, either through numerical or experimental 2.5D or 3D studies, also opens the door for the investigation of chemical reactions between the different material phases in the system in the presence of simultaneously moving fluid phases.** This would allow assessing additional processes directly derived from solute mixing, providing also an indirect proxy for mixing quantification and solute plume deformation, and expanding on previous research both on homogeneous (Markale et al. 2021) and heterogeneous (Aquino et al. 2023; Markale et al. 2022) chemical reactions. The investigations proposed here are linked to numerous experimental and numerical challenges. From an experimental point of view, the application of techniques such as X-ray micro-tomography would require extensive preliminary work for the proper selection of the injected wetting and non-wetting phases, and of their corresponding concentrations, such that the contrast between all imaged material phases is preserved over time. Other types of imaging techniques such as MRI would be required for reactive transport

experiments, as previous studies have successfully implemented (Markale et al. 2021). Additional tuning parameters include the ratio between the injection flow rates of both fluid phases, such that the target processes can be captured within the temporal resolutions available from the experimental setup. This applies also to the selection of adequate reaction kinetics in the case of reactive transport experiments. The high computational demands for the numerical investigation of multiphase flow on 3D systems should also be considered.

Further research should also aim at the up-scaling and/or application of some of the findings here reported on large-scale systems. For the particular case of chaotic advection and chaotic mixing, some studies have reported advances on the generation of chaotic flow conditions in the subsoil from large-scale investigations, aimed both at groundwater remediation (Mays and Neupauer 2012; Neupauer et al. 2014) and at biodegradation (Bagtzoglou and Oates 2007). The numerical and experimental investigations performed in these studies have relied on the assumption of fully saturated conditions. The enhancement in the strength of chaos at lower saturation degrees reported here could motivate further research at the field scale aimed at taking advantage of the unsaturated region of soils for the aforementioned applications.

The achieved goal of this doctoral thesis, consisting of providing a mechanistic understanding of the control of saturation on both fluid flow and solute transport and mixing in porous media, has provided valuable tools for carrying out similar investigations across spatial scales and will likely motivate further research of related processes on other complex systems of high environmental and industrial relevance.

BIBLIOGRAPHY

- Alim, K., S. Parsa, D. A. Weitz, and M. P. Brenner (2017). "Local pore size correlations determine flow distributions in porous media." In: *Physical Review Letters* 119, p. 144501.
- Aquino, T., T. Le Borgne, and J. Heyman (2023). "Fluid-solid reaction in porous media as a chaotic restart process." In: *Physical Review Letters* 130, p. 264001.
- Aref, H., J. R. Blake, M. Budišić, S. S. Cardoso, J. H. Cartwright, H. J. Clercx, K. El Omari, U. Feudel, R. Golestanian, E. Guillard, G. F. Van Heijst, T. S. Krasnopolskaya, Y. Le Guer, R. S. MacKay, V. V. Meleshko, G. Metcalfe, I. Mezić, A. P. De Moura, O. Piro, M. F. Speetjens, R. Sturman, J. L. Thiffeault, and I. Tuval (2017). "Frontiers of chaotic advection." In: *Reviews of Modern Physics* 89, p. 025007.
- Armstrong, R. T., J. E. McClure, M. A. Berrill, M. Rücker, S. Schlüter, and S. Berg (2016). "Beyond Darcy's law: The role of phase topology and ganglion dynamics for two-fluid flow." In: *Physical Review E* 94, p. 043113.
- Bagtzoglou, A. C. and P. M. Oates (2007). "Chaotic advection and enhanced groundwater remediation." In: *Journal of Materials in Civil Engineering* 19, pp. 75–83.
- Berkowitz, B., A. Cortis, M. Dentz, and H. Scher (2006). "Modeling non-fickian transport in geological formations as a continuous time random walk." In: *Reviews of Geophysics* 44, RG2003.
- Bordoloi, A. D., D. Scheidweiler, M. Dentz, M. Bouabdellaoui, M. Abbarchi, and P. de Anna (2022). "Structure induced laminar vortices control anomalous dispersion in porous media." In: *Nature Communications* 13, p. 3820.
- Chen, Y., H. Steeb, H. Erfani, N. K. Karadimitriou, M. S. Walczak, M. Ruf, D. Lee, S. An, S. Hasan, T. Connolley, N. T. Vo, and V. Niasar (2021). "Nonuniqueness of hydrodynamic dispersion revealed using fast 4D synchrotron X-ray imaging." In: *Science Advances* 7, eabj0960.
- Chiogna, G., O. A. Cirpka, and P. A. Herrera (2016). "Helical flow and transient solute dilution in porous media." In: *Transport in Porous Media* 111, pp. 591–603.
- Cho, M. S., F. Solano, N. R. Thomson, M. G. Trefry, D. R. Lester, and G. Metcalfe (2019). "Field trials of chaotic advection to enhance reagent delivery." In: *Groundwater Monitoring and Remediation* 39, pp. 23–39.

- Cortis, A. and B. Berkowitz (2004). "Anomalous transport in "classical" soil and sand columns." In: *Soil Science Society of America Journal* 68, pp. 1539–1548.
- De Anna, P., J. Jiménez-Martínez, H. Tabuteau, R. Turuban, T. Le Borgne, M. Derrien, and Y. Méheust (2014). "Mixing and reaction kinetics in porous media: An experimental pore scale quantification." In: *Environmental Science and Technology* 48, pp. 508–516.
- De Anna, P., T. Le Borgne, M. Dentz, A. M. Tartakovsky, D. Bolster, and P. Davy (2013). "Flow intermittency, dispersion, and correlated continuous time random walks in porous media." In: *Physical Review Letters* 110, p. 184502.
- De Anna, P., B. Quaife, G. Biros, and R. Juanes (2017). "Prediction of the low-velocity distribution from the pore structure in simple porous media." In: *Physical Review Fluids* 2, p. 124103.
- De Barros, F. P., M. Dentz, J. Koch, and W. Nowak (2012). "Flow topology and scalar mixing in spatially heterogeneous flow fields." In: *Geophysical Research Letters* 39, p. L08404.
- De Gennes, P. G. (1983). "Hydrodynamic dispersion in unsaturated porous media." In: *Journal of Fluid Mechanics* 136, pp. 189–200.
- Dentz, M., P. K. Kang, A. Comolli, T. Le Borgne, and D. R. Lester (2016). "Continuous time random walks for the evolution of Lagrangian velocities." In: *Physical Review Fluids* 1, p. 074004.
- Geng, X., H. A. Michael, M. C. Boufadel, F. J. Molz, F. Gerges, and K. Lee (2020). "Heterogeneity affects intertidal flow topology in coastal beach aquifers." In: *Geophysical Research Letters* 47, e2020GL089612.
- Hasan, S., V. Niasar, N. K. Karadimitriou, J. R. Godinho, N. T. Vo, S. An, A. Rabbani, and H. Steeb (2020). "Direct characterization of solute transport in unsaturated porous media using fast X-ray synchrotron microtomography." In: *Proceedings of the National Academy of Sciences of the United States of America* 117, pp. 23443–23449.
- Heyman, J., D. R. Lester, and T. Le Borgne (2021). "Scalar signatures of chaotic mixing in porous media." In: *Physical Review Letters* 126, p. 34505.
- Heyman, J., D. R. Lester, R. Turuban, Y. Méheust, and T. Le Borgne (2020). "Stretching and folding sustain microscale chemical gradients in porous media." In: *Proceedings of the National Academy of Sciences of the United States of America* 117, pp. 13359–13365.
- Holzner, M., V. L. Morales, M. Willmann, and M. Dentz (2015). "Intermittent lagrangian velocities and accelerations in three-dimensional porous medium flow." In: *Physical Review E* 92, p. 013015.

- Hunt, J., A. Wray, and P. Moin (1988). "Eddies, streams, and convergence zones in turbulent flows." In: *Center for Turbulence Research, Proceedings of the Summer Program*, pp. 193–208.
- Iglauer, S., M. A. Fernø, P. Shearing, and M. J. Blunt (2012). "Comparison of residual oil cluster size distribution, morphology and saturation in oil-wet and water-wet sandstone." In: *Journal of Colloid and Interface Science* 375, pp. 187–192.
- Iglauer, S., S. Favretto, G. Spinelli, G. Schena, and M. J. Blunt (2010). "X-ray tomography measurements of power-law cluster size distributions for the nonwetting phase in sandstones." In: *Physical Review E* 82, p. 056315.
- Jiménez-Martínez, J., P. de Anna, H. Tabuteau, R. Turuban, T. Le Borgne, and Y. Méheust (2015). "Pore-scale mechanisms for the enhancement of mixing in unsaturated porous media and implications for chemical reactions." In: *Geophysical Research Letters* 42, pp. 5316–5324.
- Jiménez-Martínez, J., M. L. Porter, J. D. Hyman, J. W. Carey, and H. S. Viswanathan (2016). "Mixing in a three-phase system : Enhanced production of oil-wet reservoirs by CO₂ injection." In: *Geophysical Research Letters* 43, pp. 196–205.
- Kang, P. K., P. de Anna, J. P. Nunes, B. Bijeljic, M. J. Blunt, and R. Juanes (2014). "Pore-scale intermittent velocity structure underpinning anomalous transport through 3-D porous media." In: *Geophysical Research Letters* 41, pp. 6184–6190.
- Lester, D. R., G. Metcalfe, and M. G. Trefry (2013). "Is chaotic advection inherent to porous media flow?" In: *Physical Review Letters* 111, p. 174101.
- Lester, D. R., M. G. Trefry, and G. Metcalfe (2016). "Chaotic advection at the pore scale: Mechanisms, upscaling and implications for macroscopic transport." In: *Advances in Water Resources* 97, pp. 175–192.
- Markale, I., G. M. Cimmarusti, M. M. Britton, and J. Jiménez-Martínez (2021). "Phase saturation control on mixing-driven reactions in 3D porous media." In: *Environmental Science and Technology* 55, pp. 8742–8752.
- Markale, I., A. Velásquez-Parra, A. Alcolea, and J. Jiménez-Martínez (2022). "Mixing controlled adsorption at the liquid-solid interfaces in unsaturated porous media." In: *Transport in Porous Media* 146, pp. 159–175.
- Mays, D. C. and R. M. Neupauer (2012). "Plume spreading in groundwater by stretching and folding." In: *Water Resources Research* 48.
- Metcalfe, G., D. Lester, and M. Trefry (2022). "A primer on the dynamical systems approach to transport in porous media." In: *Transport in Porous Media* 146, pp. 55–84.
- Neupauer, R. M., J. D. Meiss, and D. C. Mays (2014). "Chaotic advection and reaction during engineered injection and extraction in heterogeneous porous media." In: *Water Resources Research* 50, pp. 1433–1447.

- Raouf, A. and S. M. Hassanizadeh (2013). "Saturation-dependent solute dispersivity in porous media: Pore-scale processes." In: *Water Resources Research* 49, pp. 1943–1951.
- Scheffer, K., Y. Méheust, M. S. Carvalho, M. H. Mauricio, and S. Paciornik (2021). "Enhancement of oil recovery by emulsion injection: A pore scale analysis from X-ray micro-tomography measurements." In: *Journal of Petroleum Science and Engineering* 198, p. 108134.
- Schlüter, S., S. Berg, M. Rücker, R. T. Armstrong, H.-J. Vogel, R. Hilfer, and D. Wildenschild (2016). "Pore-scale displacement mechanisms as a source of hysteresis for two-phase flow in porous media." In: *Water Resources Research* 52, pp. 2194–2205.
- Seybold, H. J., U. Eberhard, E. Secchi, R. L. Cisne, J. Jiménez-Martínez, R. F. Andrade, A. D. Araújo, M. Holzner, and J. S. Andrade (2021). "Localization in flow of non-Newtonian fluids through disordered porous media." In: *Frontiers in Physics* 9, p. 635051.
- Souzy, M., H. Lhuissier, Y. Méheust, T. Le Borgne, and B. Metzger (2020). "Velocity distributions, dispersion and stretching in three-dimensional porous media." In: *Journal of Fluid Mechanics* 891, A16.
- Valdés, J. P., L. Kahouadji, and O. K. Matar (2022). "Current advances in liquid-liquid mixing in static mixers: a review." In: *Chemical Engineering Research and Design* 177, pp. 694–731.
- Vogel, H.-J. (2002). "Topological characterization of porous media." In: *Morphology of Condensed Matter. Physical and Geometry of Spatially Complex Systems*. Ed. by K. Mecke and D. Stoyan. Springer.
- Yu, Y., G. Chiogna, O. A. Cirpka, P. Grathwohl, and M. Rolle (2015). "Experimental evidence of helical flow in porous media." In: *Physical Review Letters* 115, p. 194502.
- Zhuang, L., A. Raoof, M. G. Mahmoodlu, S. Biekart, R. de Witte, L. Badi, M. T. van Genuchten, and K. Lin (2021). "Unsaturated flow effects on solute transport in porous media." In: *Journal of Hydrology* 598, p. 126301.

CURRICULUM VITAE

JOURNAL PUBLICATIONS

1. Marone, F., C. M. Schlepütz, S. Marti, F. Füsseis, **A. Velásquez-Parra**, M. Griffa, J. Jiménez-Martínez, K. J. Dobson, & M. Stampanoni (2020). Time Resolved *in situ* "X-ray tomographic microscopy unraveling dynamic processes in geologic systems." In: *Frontiers in Earth Science* 7, 346. <http://doi.org/10.3389/feart.2019.00346>
2. **Velásquez-Parra, A.**, T. Aquino, M. Willmann, Y. Méheust, T. Le Borgne, & J. Jiménez-Martínez (2022). "Sharp transition to strongly anomalous transport in unsaturated porous media." In: *Geophysical Research Letters* 49, e2021GL096280. <http://doi.org/10.1029/2021GL096280>.
3. Aquino. T., & **A. Velásquez-Parra** (2022). "Impact of velocity correlations on longitudinal dispersion in space-Lagrangian advective transport models." In: *Physical Review Fluids* 7, 024501. <http://doi.org/10.1103/PhysRevFluids.7.024501>
4. Markale, I., **A. Velásquez-Parra**, A. Alcolea, & J. Jiménez-Martínez (2023). "Mixing controlled adsorption at the liquid-solid interfaces in unsaturated porous media." In: *Transport in Porous Media* 146, 159-175. <http://doi.org/10.1007/s11242-022-01747-x>
5. **Velásquez-Parra, A.**, F. Marone, R. Kaufmann, M. Griffa, & J. Jiménez-Martínez (2024). "Phase saturation control on vorticity enhances mixing in porous media." In: *Water Resources Research* 60, e2023WR036628. <http://doi.org/10.1029/2023WR036628>.
6. **Velásquez-Parra, A.**, F. Marone, M. Griffa, & J. Jiménez-Martínez (2024). "Chaotic transport of solutes in unsaturated porous media". In: *Environmental Science and Technology*.¹

¹ Submitted for publication.

CONFERENCE CONTRIBUTIONS

- **Velásquez-Parra, A.**, Marone, F., Kaufmann, R., Griffa, M., & Jiménez-Martínez, J. : Topological control on flow and transport in unsaturated porous media from temporally resolved 3D X-ray computed micro tomography. *15th Annual International Conference on Porous Media - Interpore 2023*, Edinburgh, Scotland, May 22-25, 2023.
- **Velásquez-Parra, A.**, Marone, F., Kaufmann, R., Griffa, M., & Jiménez-Martínez, J. : Water saturation impact on solute front deformation from temporally resolved 3D X-ray micro-computed tomography. *American Geophysical Union Fall Meeting 2022*, Chicago, IL, USA, December 12-16, 2022.
- **Velásquez-Parra, A.**, Marone, F., Kaufmann, R., Griffa, M., & Jiménez-Martínez, J. : Water saturation impact on solute front deformation and plume's advective dispersion from temporally resolved 3D X-ray micro-computed tomography. *Gordon Research Conference: Flow and transport in permeable media*, Les Diablerets, Switzerland, July 16-22, 2022.
- **Velásquez-Parra, A.**, Aquino, T., Willmann, M., Méheust, Y., Le Borgne, T., & Jiménez-Martínez, J. : Sharp transition to strongly anomalous transport in unsaturated porous media - Modelling and prediction. *European Geophysical Union General Assembly 2022*, Vienna, Austria, May 23-27, 2022.
- **Velásquez-Parra, A.**, Marone, F., Kaufmann, R., Griffa, M., & Jiménez-Martínez, J. : Water saturation impact on flow and transport at pore-scale from temporally resolved 3D X-ray micro-computed tomography. *5th Cargèse Summer School on flow and transport in porous and fractured media*. Cargèse, France, July 20-31, 2021
- **Velásquez-Parra, A.**, Willmann, M., Méheust, Y., Le Borgne, T., & Jiménez-Martínez, J. : Effects of spatial heterogeneity on flow and transport in variably saturated porous media. *11th Annual Meeting - Interpore 2019*, Valencia, Spain, May 6-10, 2019.